TESIS DOCTORAL

Programa de Doctorado en Ciencias de la Tierra

JOINT ACTIVE AND PASSIVE SEISMIC TOMOGRAPHY IN ACTIVE VOLCANOES: THE CASE OF STUDY OF MT. ETNA, AND FURTHER IMPLICATIONS IN ACTIVE VOLCANIC REGIONS.

ALEJANDRO DÍAZ MORENO

UNIVERSIDAD DE GRANADA

AÑO 2016

Editor: Universidad de Granada. Tesis Doctorales
Autor: Alejandro Díaz Moreno
ISBN: 978-84-9163-048-7
URI: http://hdl.handle.net/10481/44572

TESIS DOCTORAL

Joint Active and Passive Seismic Tomography in active volcanoes: The case of study of Mt. Etna, and further implications in active volcanic regions.

REALIZADA POR:

Alejandro Díaz Moreno

Directores:

Dr. Jesús M. Ibáñez Godoy

Dra. Mª Araceli García Yeguas

Dr. Isaac Álvarez Ruiz

Departamento de Física Teórica y del Cosmos

Instituto Andaluz de Geofísica y Prevención de Desastres Sísmicos

Universidad de Granada

Joint Active and Passive Seismic Tomography in active volcanoes: The case of study of Mt. Etna, and further implications in active volcanic regions.

Alejandro Díaz Moreno

Palabras Clave: Tomografía Sísmica velocidad, sísmica activa, propagación ondas,

El doctorando / The *doctoral candidate* **[Alejandro Díaz Moreno]** y los directores de la tesis / and the thesis supervisor/s: **[Jesús M. Ibáñez Godoy, MªAraceli García Yeguas e Isaac Álvarez Ruiz]**

Garantizamos, al firmar esta tesis doctoral, que el trabajo ha sido realizado por el doctorando bajo la dirección de los directores de la tesis y hasta donde nuestro conocimiento alcanza, en la realización del trabajo, se han respetado los derechos de otros autores a ser citados, cuando se han utilizado sus resultados o publicaciones.

/

Guarantee, by signing this doctoral thesis, that the work has been done by the doctoral candidate under the direction of the thesis supervisor/s and, as far as our knowledge reaches, in the performance of the work, the rights of other authors to be cited (when their results or publications have been used) have been respected.

Lugar y fecha / Place and date:

Granada a 28 Julio 2016

Director/es de la Tesis / *Thesis supervisor/s;* Doctorando / *Doctoral candidate*:

Jesús M. Ibáñez

Isaac M. Alvarez Ruiz

Alejandro Díaz

Firma / Signed

Firma / Signed

AGRADECIMIENTOS

Esta tesis de doctorado ha sido realizada gracias al apoyo de numerosas personas, instituciones y proyectos a los que quiero formalmente agradecer en estas primeras palabras del trabajo.

Entre los proyectos que han facilitado que esta tesis llegue a buen cabo se encuentran el Subprograma de Ayudas FPI-MICINN BES-2012-051822 del Ministerio de Economía y Competitividad que me ha financiado durante los 4 años en los que se ha desarrollado este proyecto de investigación. Agradecer al proyecto EPHESTOS (CGL2011-29499-C02-01), al que estaba ligada la mencionada beca FPI y que gracias a su financiación se pudieron llevar a cabo muchas de las tareas requeridas durante el trabajo. Otros proyectos de investigación han participado de manera fundamental en el desarrollo del presente trabajo, como son los proyectos europeos MEDSUV.ISES (Seventh Framework Program for research, technological development and demonstration under grant agreement No 308665) y EUROFLEET2 (Seventh Framework Programme, Grant Agreement n° 312762), los proyectos españoles COCSABO (COC-DI-2011-08), KNOWAVES TEC2015-68752-R (MINECO/FEDER) y CGL2015-67130-C2-2. Además agradecer enormemente al grupo de investigación de la Junta de Andalucía RNM-104 de Geofísica y Sismología.

Son numerosas las instituciones que han colaborado a lo largo de estos 4 años tanto españoles como extranjeras y que por tanto quiero agradecer y mencionar en estas páginas. Al Departamento de Física Teórica y Del Cosmos y al Instituto Andaluz de Geofísica y Prevención de Desastres Sísmicos (IAG) de la Universidad de Granada que me han acogido como becario predoctoral de investigación y que me han facilitado los medios y la infraestructura donde desarrollar mi trabajo de investigación. Al programa de doctorado de Ciencias de la Tierra bajo la tutela del cuál presento este trabajo. Entre las instituciones de fuera de España a las que debo mostrar mi agradecimiento por su innegable e incalculable apoyo son al Departamento de Ciencias de la Tierra y Océanos de la Universidad de Liverpool, del Reino Unido (Department of Earth and Ocean Sciences, University of Liverpool), al Instituto de Geología del Petróleo y Geofísica de la Academia de las Ciencias en Novosibirsk, Rusia (Institute of Petroleum Geology and Geophysics, SB RAS, Novosibirsk), al Instituto Nacional de Geofisica y Vulcanologia de Italia y su sección en Catania (INGV-OE) (Istituto Nazionale di Geofisica e Vulcanologia- Sezione di Catania-Osservatorio Etneo), y a la Base Antártica Española (BAE) Gabriel de Castilla gestionada por el Ejercito de Tierra Español.

Este trabajo de investigación no se habría podido llevar a cabo sin la realización de una serie de estancias de investigación a las que debo agradecer. Mi primera estancia en la Universidad de Liverpool (bajo la dirección del profesor S. De Angelis) me permitió sentar las bases de algunas de las publicaciones que han permitido dar avalar esta tesis doctoral. La estancia de casi tres meses en el Instituto de Geología del Petróleo y Geofísica de Novosibirsk tanto en Siberia como en Kamchatka (bajo la dirección del profesor I. Koulakov) me permitió y aprender la metodología y algoritmos necesarios para desarrollar el software de inversión tomográfica conjunta que presentamos en este trabajo, así como participar en una campaña de campo para la instalación de una red sísmica. Gracias a los programas de estancias breves del Ministerio de Economía y Competitividad, asociadas al programa FPI realicé dos estancias de cuatro meses (EEBB-I-14-07983; EEBB-I-15-09512) cada una en el INGV-OE (bajo la dirección del profesor D. Patanè) que me permitieron: en la primera, participar activamente en la experimento de sísmica activa TOMO-ETNA, y en la segunda, obtener e interpretar los resultados de inversión tomográfica, base de esta tesis, obtenidos a partir de los datos de TOMO-ETNA. Como complemento a mi formación realicé una estancia de dos meses en la BAE Gabriel de Castilla en la Isla de Decepción durante la cual nos encargamos de la vigilancia activa de la actividad sismo-volcánica del volcán de Decepción.

En primer lugar a mis directores de tesis, Jesús M. Ibáñez Godoy, Mª Araceli García Yeguas e Isaac Álvarez Ruiz por su entera disposición y su incalculable ayuda para llevar a buen puerto este trabajo. Agradecer su ayuda en cada uno de los pasos de esta tesis, desde sus comienzos hasta sus últimos retoques.

Agradecer también director del IAG, el catedrático José Morales Soto y al director del Departamento de Física Teórica y del Cosmos, José Santiago Pérez, por acogerme en dichas instituciones y poner a mi disposición el material y la infraestructura de apoyo necesaria. Agradecer a Silvio de Angelis, profesor de la Universidad de Liverpool por acogerme y dirigirme en mi estancia en Liverpool y formarme en la metodología de análisis del parámetro *b* utilizada en esta tesis. Agradecer al profesor Ivan Koulakov, director del laboratorio Modelado Sísmico Directo e Inverso del Instituto de Geología y Geofísica del Petróleo de Novosibirsk, por enseñarme la metodología necesaria para el desarrollo del software de inversión tomográfica, fundamental para el buen desarrollo de esta tesis. Agradecer también a Andrey Jakovlev por su ayuda en el desarrollo de dicho software. Agradecer a Domenico Patanè, investigador del INGV-OE, por acoger y dirigir mis estancias en Catania. Agradecer a Ornella Cocina, Luciano Zuccarello y Graziella Barberi, investigadores del INGV-OE por dedicarme su tiempo durante mi estancia en Catania y por su ayuda para resolver todos los problemas que fueron surgiendo. Agradecer a Eugenio Privitera como director del INGV-OE, por acoger mi estancia en dicha institución. A

Giuseppe Puglisi como Investigador principal del proyecto MEDSUV.ISES. A Javier Almendros por dirigir mi estancia en la BAE Gabriel de Castilla en Isla Decepción, de la cual aprendí no sólo a analizar y vigilar la actividad sismo-volcánica en tiempo real, sino también a gestionar las posibles crisis volcánicas. Agradecer a todo el personal investigador, técnico y de administración del IAG: Teresa Teixidó, José Peña, Jaime Vílchez, Antonio Martos, Javier Moreno, José Manuel López, Mercedes Feriche, Benito Martín, Paco Vidal, Carolina Aranda, Gerardo Alguacil, Alfonso Ontiveros, Enrique Carmona, Inmaculada Serrano, Francisco Carrión, Flor de Lis Mancilla, Daniel Stich, Federico Torcal, Rosa Martín, Janire Prudencio, Luciana Bonato, Rafael Abreu, Evelyn Núñez, José Ángel López, Vanessa Jiménez, Guillermo Cortés y Antonio Molina. Son personas con las que he compartido estos cuatro años y que en un modo u otro han aportado su granito de arena (espero no olvidar a nadie).

Gracias al Departamento de Teoría de la Señal, Telemática y Comunicaciones con su directora Mª Carmen, Benítez Ortúzar a la cabeza. Gracias a Isaac Álvarez, Luz García, Ángel de la Torre, Manolo Titos…por todo su apoyo y paciencia al enseñarme un mundo desconocido hasta el momento para mí, la programación. Agradeceros vuestra inestimable ayuda y trabajo en todo el procesado de datos, sin vosotros hubiera sido imposible terminar todo a tiempo. Sin duda creo que nuestra colaboración ha sido y será muy productiva y espero poder seguir colaborando con vosotros mucho tiempo. Estoy seguro de que a partir de ahora sacaremos mucho más partido a todo el trabajo de pre-procesado que tanto tiempo nos ha llevado.

Gracias a todos aquellos que participaron en el experimento TOMO-ETNA porque sin ellos no hubiéramos podido llevar a cabo este ambicioso proyecto que tanto trabajo costó y que ahora está empezando a dar los primeros de muchos frutos. Entre ellos al Geophysical Instrument Pool Potsdam (GIPP)" del GFZ (Potsdam), por proporcionarnos las estaciones sísmicas. Además, agradecer a las siguientes instituciones por su colaboración durante el experimento: Dipartimento Regionale della Protezione Civile, Regione Siciliana; Dipartimento Azienda Regionale Foreste Demaniali, Ufficio Provinciale de Catania; Ente Parco dell'Etna; Unidad de Tecnología Marina-CSIC en Barcelona (Spain); Stato Maggiore Marina (Italian Navy General Staff), CINCNAV (Command in Chief of the Fleet) y Marisicilia (Navy Command of Sicily); Guardia Costera de Messina y Riposto; y por facilitar la obtención de los permisos de navegación para los Buques Oceanográficos a las oficinas de Extranjería de España e Italia. También agradecer a todos los propietarios de terrenos privados donde se instalaron estaciones por su ayuda y desinteresada colaboración.

A nivel personal son muchas las personas a las que debo agradecer su apoyo y ayuda. A mi director de tesis Jesús, le debo agradezco todo y más, no puedo poner por escrito todo y cuanto

has hecho por mí en estos cuatro años que sin lugar a dudas están entre los mejores de mi vida. Me has enseñado a ser mejor investigador y mejor persona, y gracias por tener tu despacho siempre abierto aún a las 7:30 de la mañana para un becario con su libreta. Gracias por todas las oportunidades que me has dado de viajar y conocer mundo, sin duda han dado sus frutos a nivel investigador y a nivel personal me han ayudado a madurar como persona. Gracias por darme la confianza para trabajar y tomar responsabilidades bajo tu tutela. Gracias por confiar siempre en esta tesis y en encontrar siempre una salida a cualquier problema. Gracias por compartir tu experiencia y sabiduría conmigo, sin duda eres un ejemplo a seguir (¡al menos ya puedo decir que sé prepara diapositivas igual que tú!

Gracias a Araceli por su apoyo y consejos sobre todo al comienzo, cuando no sabía ni usar Matlab ni Linux, gracias a tu comprensión y ayuda he llegado hasta aquí. Gracias por tu paciencia con mi impaciencia cuando las cosas iban lentas al principio.

Gracias a Isaac por su extremada paciencia con un *muggle* de la programación. Me has enseñado mucho, no sólo a programar, sino a pensar como programador, que no es fácil para un geólogo… Gracias por no volverte loco con tanto filtro, tanto formato extraño… por esas decimas antes o después….

Gracias a Ivan Koulakov porque sin su ayuda para desarrollar el programa de tomografía, no podríamos haber terminado este trabajo…. Y porque bajo mi punto de vista no pudo haber escogido nombre mejor para el programa… ¡ha sido todo un "parto"! Gracias también por la oportunidad de trabajar con vosotros en Kamchatka y acogerme como a uno más. Aprovecho para agradecer también a Andrey, Sergey, Arseny, Pasha, Evgeny y todos los componentes del grupo de Novosbirsk por su ayuda durante mi estancia en Rusia.

A Luciano y Ornella por acogerme en Catania con tanto cariño. Por vuestra ayuda para organizar TOMO-ETNA, vuestra paciencia con mi "itañol" por enseñarme vuestra cultura y gastronomía (benditas granitas…). Además de apreciaros como investigadores os considero mis amigos. ¡Habéis conseguido que sea obligatorio volver a Catania al menos una vez al año!

Gracias a Janire por toda su ayuda durante estos cuatro años, por compartir a Jesús, con un nuevo becario recién llegado. Por tu ayuda e impresionante labor en TOMO-ETNA a pesar de las dificultades. Por todos esos momentos buenos y no tan buenos, y por todas esas granitas. ¡Muchas Gracias!

Gracias a Pepe, Paco, Benito, Rafa, Merche… por todos los desayunos juntos en los que arreglamos el mundo. Gracias a Edoardo del Pezzo y Francesca Bianco por sus ánimos y su apoyo, y por confiar en que este trabajo iba a salir adelante.

Gracias a mis compañeros antárticos, Enrique, Vanessa, Lorenzo, Amós, Belén, Mirenchu, Mariano, Javier, Luis y a todos los militares. Por toso los momentos que compartimos y que espero que volvamos a compartir pronto.

A todos mis amigos/as, los que siempre han estado y a los recién llegados, con los que he compartido todo o parte de estos cuatro maravillosos e inolvidables años, llenos de buenos y no tan buenos momentos, por ser un gran apoyo cuando las cosas no salían y alegraros cuando sí. ¡Gracias por todo el apoyo moral!

Por último y no menos importante, a mi familia, en especial a mis padres y hermano, por abrir la luz en este camino, por apoyarme y darme ánimos en todos y cada uno de los pasos que he ido dando. Gracias por encontrar siempre las palabras de aliento que he necesitado en cada momento. Gracias por lo que se ve y por lo que no se ve, gracias a cómo me habéis educado estoy aquí ahora, así que esta tesis es tan mía como vuestra. Gracias por darme la oportunidad de estar aquí terminando estas palabras de agradecimiento. Espero poder seguir viendo volcanes y erupciones por todo el mundo para seguir contándooslo. A vosotros en especial os dedico esta tesis (y perdón por escribirla en inglés jeje).

A mi padre, a mi madre y a mi hermano;

ÍNDICE

CONTENTS

RESUMEN EXTENDIDO

Los objetivos de esta Tesis Doctoral se basan en dos pilares fundamentales: i) obtención de un modelo de velocidad realista y tridimensional de la región que comprende el volcán Mt. Etna, el archipiélago de las Islas Eolias y las áreas circundantes, a partir de la inversión tomográfica conjunta de datos de sísmica activa y pasiva; ii) Aplicaciones avanzadas de los modelos de velocidad para el estudio de los mecanismos físicos que controlan la sismicidad en volcanes. Para la obtención del modelo tomográfico conjunto se han utilizado los datos obtenidos mediante un complejo experimento de sísmica activa y pasiva llamado TOMO-ETNA. Los datos han sido posteriormente analizados y procesados utilizando novedosos algoritmos de procesado de señales. Una vez analizados los datos sísmicos se procesan mediante un nuevo software tomográfico desarrollado ad-hoc para esta Tesis Doctoral. Dicho código se llama Passive Active Ray Tomography Software (PARTOS), y permite la inversión conjunta y simultánea de datos de sísmica activa y pasiva. Por último, Se resalta un estudio avanzado basado en el cálculo del parámetro b, en la localización precisa de terremotos, y en el cálculo de curvas de difusividad para la serie sismo-volcánica de El Hierro 2011-13, a partir de un modelo de velocidad tomográfico tridimensional que permite interpretar de manera novedosa la distribución y evolución de la sismicidad volcánica.

Capítulo 1. Introducción, Motivación y Estado del Arte

Los volcanes y los seres humanos están vinculados desde que se tiene registro. Los innumerables beneficios que aportan los volcanes a la vida diaria nos hacen acercarnos una y otra vez a ellos pese a los peligros que conlleva. Existen a lo largo de la historia numerosas muestras del poder de los fenómenos volcánicos y cómo estos son capaces de modelar el relieve, destruir poblaciones e incluso modificar el clima a nivel global (Santorini, Vesubio, Toba, etc.).

Gracias a los avances científicos, en la actualidad, podemos predecir con bastante eficacia la reactivación de un episodio volcánico. Disciplinas como la geoquímica, la

geodesia, el magnetismo, la gravimetría o la sismología se encargan de la vigilancia volcánica. Una de las claves de una vigilancia sólida es utilizar modelos lo más realista posibles de la estructura interna del volcán en cuestión. Para ello, la tomografía sísmica se presenta como una herramienta fundamental a la hora de obtener modelos estructurales 3D en velocidad o atenuación del interior de los volcanes, identificando heterogeneidades y anomalías laterales.

Uno de los volcanes más activos del mundo y sin duda el más monitorizado es el Etna, Sicila (Italia). Este volcán representa una oportunidad única para la aplicación de las técnicas ya comentadas debido a su casi-continua actividad y a la cantidad de poblaciones que se extienden en sus faldas. A raíz de esto, en 2014 se llevó a cabo un ambicioso experimento llamado TOMOETNA, dentro del proyecto europeo MEDSUV.ISES, que pretende el estudio del Etna y las regiones circundantes aunando las bondades de la sísmica activa y la pasiva.

TOMOETNA generó una enorme cantidad de datos sísmicos de alta calidad que han sido analizados utilizando algoritmos de tratamiento automático de señales que nos han permitido realizar de manera fiable y rápida una selección de tiempos de viaje de ondas P (picking) que son la base de la tomografía sísmica en velocidad.

Paralelamente hemos desarrollado un código tomográfico que nos permite invertir simultáneamente datos de picking de terremotos (tomografía pasiva) y de fuentes sísmicas activas (tomografía activa). Este programa se conoce como PARTOS (Passive Active Ray Tomographic Software) y ha sido utilizado para obtener por primera vez en el Etna una tomografía conjunta activa-pasiva. El resultado de esta inversión es un modelo de velocidad de ondas P en 3D realista y que cubre toda la región del noreste de Sicilia, incluyendo el volcán Etna y el archipiélago de las Islas Eolias.

No obstante, la tomografía sísmica no es únicamente un fin, sino que es la base de un gran número de trabajos posteriores que requieren de un modelo realista y detallado de la región. Es el caso de las localizaciones sísmicas de precisión que permiten estudiar con detalle distintas zonas sismogenéticas y que, a su vez, permiten realizar estudios de los patrones de la sismicidad, como son el parámetro *b* y el estudio de la difusividad de

los enjambres sísmicos, o estudios de migración de estrés provocado por intrusiones magmáticas (fracturación hidráulica).

Capítulo 2. Marco Geofísico, Geodinámico y Vulcanológico del volcán Mt. Etna, Islas Eolias y Áreas Circundantes

El volcán Mt. Etna es considerado un volcán laboratorio debido a su casi continua actividad, su fácil accesibilidad, y su cercanía de numerosas poblaciones. Por ello, existe hoy en día una intensa vigilancia de la actividad del volcán que comprende un gran número de disciplinas como son la volcanología, petrología, geoquímica, magnetismo, geodesia, gravimetría o sismología.

Este despliegue científico tiene dos vertientes fundamentales: la vigilancia volcánica en tiempo real y la investigación. La vigilancia permite alertar a la población y a los servicios de protección civil ante cualquier reactivación volcánica. La investigación utiliza la gran base de datos multidisciplinar que se genera día a día para avanzar en el conocimiento de la estructura y la dinámica del Etna y exportarla a otros volcanes.

Hoy en día, aún existe controversia acerca de la estructura interna del Etna y el origen del magma. En el capítulo 2 realizamos un repaso a las actuales teorías y proponemos un modelo unificado.

Capítulo 3. Experimento TOMOETNA. Campaña marina y terrestre de sísmica activa

En verano de 2014 se realizó un complejo experimento de sísmica activa en Sicilia. El experimento llamado TOMO-ETNA, forma parte del proyecto europeo MEDSUV, y pretende estudiar en detalle la compleja estructura interna del volcán Etna, el archipiélago de las Islas Eolias, y la relación entre ambas regiones volcánicas. Para ello, se realizaron más de 16.000 disparos de aire comprimido efectuados desde el BIO Sarmiento de Gamboa de España, con el apoyo de la Marina Naval Italiana que puso a disposición el Buque ‘Galatea’, y de una nave oceanográfica griega llamada ‘Aegeo’. El experimento TOMO-ETNA, constó de dos ramas fundamentales: actividad en mar y en tierra. La actividad marina se centró en: i) el despliegue de 27 sismómetros de fondo oceánico (OBS); ii) llevar a cabo dos campañas de sísmica, una de refracción y otra de reflexión; iii) realizar perfiles magnéticos; y iv) obtener imágenes del fondo marino

mediante el uso de un robot (ROV), entre otras actividades. El equipo de tierra, en cambio, se ocupó del despliegue y mantenimiento de una red sísmica temporal de cerca de 100 estaciones de corto periodo y de banda ancha que, junto con la red sísmica permanente ya instalada en Sicilia, formaron una red de 267 estaciones sísmicas que se encargaron de registrar no sólo las explosiones realizadas a mar, sino toda la sismicidad natural que pudiera ocurrir durante los 4 meses que duró instalada la red.

Dicho experimento, detallado en el capítulo 3, generó una gran base de datos con más de tres millones de señales sísmicas incluyendo señales de sísmica activa y el registro de más de 400 terremotos ocurridos en tal periodo. Dicha base de datos, que contiene datos de sísmica activa y pasiva, fue la base para el desarrollo de la primera tomografía sísmica en velocidad que integra simultáneamente fuentes activas y pasivas en el Etna, la cual se presenta en esta Tesis Doctoral.

Capítulo 4. 4. Avances en la estimación automática de llegadas de ondas sísmicas de tipo P

Para obtener dicha tomografía sísmica, en primer lugar se debieron obtener los tiempos de llegada de la onda P. Detectar correctamente la llegada de las ondas sísmicas generadas por terremotos o por fuentes artificiales, es un paso crítico para asegurar la bondad y calidad de los futuros análisis que se realicen, desde una localización preliminar del evento hasta estudios de atenuación o tomografías. En la mayoría de estos casos, la detección de la llegada de las ondas P y S se realiza de forma manual, siendo un operador experto quien se encarga de dicho procesado. El picking manual, por tanto tiene las ventajas de que es supervisado por un operador experto y que se revisa cada señal de manera independiente aplicando los filtros necesarios. Por tanto, en una base de datos sísmica relativamente pequeña el uso del picking manual es altamente recomendable. Sin embargo, el procesado manual tiene sus inconvenientes, y es que no todos los expertos sismólogos coinciden siempre en el momento exacto de la llegada de la onda P al aplicar distintos criterios (cruce por cero, superar un umbral de ruido, etc.). A esto, se le suma posibles condicionantes externos como el cansancio, o fatiga tras varias horas realizando el mismo proceso. Además, si se da el caso de que varios operadores trabajan con la misma base de datos dicho cambio de criterio puede ser importante. Por estas razones

desde hace décadas, la comunidad científica está centrando gran parte de sus esfuerzos en desarrollar algoritmos de picking automático de ondas sísmicas ya sean ondas P o S. Siguiendo este argumento, dichos nuevos algoritmos se basan en la necesidad de analizar grandes bases de datos sísmicas en poco tiempo, siguiendo siempre un mismo criterio. En el capítulo 4 de esta tesis, proponemos un detallado estado del arte en cuanto a los nuevos avances en picking automático se refiere y describimos en profundidad uno de estos algoritmos, que hemos utilizado para el análisis y la detección de las llegadas de las ondas P de los datos generados por el experimento TOMO-ETNA.

Capítulo 5. Software de Tomografía Activa y Pasiva Conjunta (PARTOS)

Las tomografías sísmicas activas y pasivas se han realizado tradicionalmente por separado. Sin embargo, no podemos desdeñar la potencialidad de una inversión conjunta que nos permita sumar la información suministrada por ambas. En este sentido, complementar la información en profundidad que ofrecen los terremotos con las ventajas de conocer la hora origen y la localización de las fuentes sísmicas activas permite mejorar considerablemente la información estructural del área en cuestión.

El proceso de inversión conjunta de datos activos y pasivos se ha realizado en muy pocas ocasiones. Si bien es cierto, existen unos pocos ejemplos de interpretaciones conjuntas de datos sísmicos activos y pasivos como los realizados en el complejo Vesubio-Campi Flegrei con las imágenes de tomografía pasiva de la misma región; o el en la región de Java Central (Indonesia). Estos trabajos permitieron demostrar la potencialidad de esta metodología en su aplicación para distintas áreas volcánicas.

En el capítulo 5 de esta Tesis se describe un nuevo software desarrollado en colaboración con el profesor Ivan Koulakov de la Universidad de Novosibirsk (Rusia), que permite la inversión simultánea de datos de sísmica activa y pasiva. Dicho programa, llamado Passive Active Ray TOmography Software (PARTOS), procesa por separado los datos únicamente durante la fase de localización de las fuentes, ya que requieren un procesado diverso. Una vez relocalizadas las fuentes sísmicas, se analizan conjuntamente ambas bases de datos proporcionando una imagen tomográfica conjunta que combina las ventajas de ambas técnicas.

PARTOS se ha desarrollado utilizando como base dos códigos tomográficos bien conocidos y ampliamente utilizados en todo el mundo que son LOTOS y ATOM-3D.

Capítulo 6. Tomografía Sísmica en Velocidad de Ondas P Conjunta Activa Pasiva del Volcán Mt. Etna, Islas Eolias y Áreas Circundantes

En el capítulo 6 mostramos los principales resultados de la inversión tomográfica conjunta de los datos obtenidos durante el Experimento TOMO-ETNA. Para ello, primero discutimos la importancia de los modelos de velocidad de partida. A continuación, y antes de mostrar las imágenes finales, mostramos los test sintéticos que nos permiten asegurar y demostrar la calidad y fiabilidad de los resultados. Estos test incluyen checkerboards verticales y horizontales, Jackknifing tests, e inversiones sintéticas utilizando modelos de anomalía libre. Posteriormente mostramos los mapas de densidad de rayos que muestran la cobertura de rayos del área invertida para, finalmente, mostrar e interpretar los resultados tomográficos utilizando tanto cortes verticales como horizontales. Este esquema lo seguimos para cada una de las tres regiones que distinguimos. Cada una de las cuáles es invertida de manera independiente, incluyendo un modelo de velocidad inicial ad-hoc. Estas regiones son: i) Área de Experimento TOMO-ETNA; ii) Archipiélago de las Islas Eolias; y iii) Volcán Mt. Etna. En estas regiones destacamos e interpretamos una serie de anomalías de velocidad de ondas P, en base a estudios regionales y locales previos. Muchas de estas anomalías corresponden con estructuras ya descritas por otros autores como son la el sistema de fallas conocido como "Aeolian-Tindari-Letojanni Fault System" (ATLFS) que cruza el noreste de Sicilia con dirección NW-SE, o el "High Velocity Body" (HVB) localizado ligeramente al sureste de los cráteres principales del volcán Mt. Etna. Destacamos también la presencia de una serie de anomalías no interpretadas en bibliografía y para las que proponemos una interpretación preliminar a falta de estudiarlas más en detalle como parte de los trabajos futuros.

Capítulo 7. Un ejemplo de Aplicaciones Avanzadas: El Análisis de la Serie Sísmica Asociada a la Actividad Volcánica en la Isla de El Hierro 2011-13, a la luz de Modelos Estructurales de Alta Definición

Como ya se ha comentado anteriormente, la tomografía sísmica no es el fin último de un trabajo, sino que sirve de base fundamental para realizar otros muchos estudios avanzados. En el capítulo 7 mostramos algunos de estos estudios posteriores a la tomografía que permiten avanzar en el conocimiento ya no sólo de la estructura, sino de la dinámica de los fenómenos volcánicos. La relocalización de precisión es un paso inmediato a la obtención de un modelo de velocidad realístico y en 3D que permite localizar con mucha mayor fidelidad los enjambres sísmicos y facilita la interpretación geodinámica de los mismos. En este sentido, presentamos una localización sísmica de precisión utilizando la serie sísmica registrada en la Isla de El Hierro (España) durante la crisis sismo-volcánica ocurrida en 2011-13, aplicando algoritmos probabilísticos no lineales (NonLinLoc) y algoritmos de relocalización relativa (HypoDD).

A su vez, una localización precisa permite realizar nuevos estudios en detalle para entender la dinámica sísmica de la región, en especial en volcanes donde se acostumbra a relacionar directamente la sismicidad con la migración del magma. Sin embargo, existen otras posibilidades como la sismicidad causada por la migración de estrés relacionada a su vez con intrusiones magmáticas en conductos cerrados. A este tipo de sismicidad se le conoce como sismicidad inducida por fracturación hidráulica y en este capítulo presentamos un estudio en detalle de la sismicidad asociada a la crisis volcánica ocurrida en la isla de El Hierro (Canarias, España) en el período 2011-2013.

Capítulo 8. Conclusiones

Las principales conclusiones que podemos extraer de esta Tesis Doctoral son:

- TOMO-ETNA es probablemente el experimento de sísmica active-pasiva conjunto más complejo llevado a cabo en el mundo, especialmente si consideramos el número de proyectos internacionales, países y personas involucradas.
- AMPA es un nuevo algoritmo robusto, rápido, adaptable y fiable que nos permite procesar los 3.000.000 de señales sísmicas en pocas horas, calculando al mismo tiempo una serie de parámetros de calidad que nos permiten filtrarlas.

- El software de tomografía conjunta active pasiva (PARTOS) ha sido desarrollado específicamente para analizar los datos del experimento TOMO-ETNA. Es probablemente la primera vez que un código de tomografía conjunta tan robusto y potente se pone abiertamente a disposición de la comunidad científica.
- Presentamos imágenes tomográficas de alta resolución para tres regiones de gran relevancia científica: i) Noreste de Sicilia, incluyendo Mar Jónico y Mar Tirreno (Región 1); ii) Archipiélago de las Islas Eolias (Región 2); y iii) Volcán Mt. Etna (Región 3).
- La calidad, robustez, y estabilidad de los modelos de velocidad resueltos están demostrados mediante numerosos test sintéticos.
- Se presenta un completo caso de estudio en el que se utiliza un modelo de velocidad como partida para realizar estudios avanzados que incluyen:
    - Estimación del parámetro *b*.
    - Localización sísmica de precision utilizando algorítmos de localización probabilística no-linear y relativa.
    - Cálculo de curvas de difusividad.
- La fracturación hidráulica puede considerarse un importante mecanismo de control de la migración sísmica y de stress en áreas volcánicas, especialmente cuando se producen intrusiones magmáticas.

ABSTRACT

The objectives of this PhD Thesis are based on two main legs: i) Obtaining a realistic, three-dimensional velocity model of the region comprising Mt. Etna volcano, Aeolian Island Archipelago, and surrounding areas, by using joint active and passive tomographic inversion; ii) Performing advanced applications of velocity models focused on the study of the physical mechanisms controlling seismicity on volcanoes. For obtaining the tomographic velocity model we used seismic data provided by a complex active seismic experiment known as TOMO-ETNA. Data, including active and passive seismic signals, has been further analysed using new signal processing algorithms. Once analysed, seismic data is processed applying a new ad-hoc developed software for joint active passive seismic tomography (PARTOS). Finally, we propose an advanced study based on b value calculation, precise seismic locations, and diffusivity curves calculations of the seismicity related to the El Hierro 2011-13 seimo-volcanic crisis. This study requires as a priori information a realistic 3D velocity model, and allows us to reinterpret the distribution and evolution of seismic swarms on volcanoes.

Chapter 1. Introduction. Motivation and State of Art

Volcanoes and humanity have been bonded since the beginning of times. The uncountable benefits volcanoes provide, make us to stay near them even though their associated risks. Volcanic phenomena are capable of modelling relief, destroy populations and even modify global climate. There are many examples of these consequences along history (e.g., Santorini, Vesusvius, Toba, etc).

Recent scientific advances predict with high accuracy rate a volcanic unrest. Disciplines such as geochemistry, geodesy, magnetism, gravimetry or seismology, are in focused on volcanic surveillance and monitoring. One of the keys of a robust and efficient surveillance is the use of realistic structural models of the volcano. Thus, seismic tomography appears as an essential tool for obtaining internal structural 3D models in

velocity or attenuation of the volcanoes interior, identifying lateral heterogeneities and anomalies.

One of the most active volcanoes in the World, and certainly the most monitorized, is Mt. Etna volcano in Sicily (Italiy). Due to the almost-persistent volcanic activity, and the high population living nearby, it represents a unique opportunity for the application of the mentioned geophysical techniques. In 2014 an ambitious active seismic experiment named TOMOETNA took place. It was conceived under the framework of MEDSUV.ISES European project and intended to study of Mt. Etna volcano and surrounding areas merging active and passive seismic data.

TOMOETNA provided a huge high quality database that has been analysed using automatic signal processing algorithms that has allowed us to detect trustfully, with low time consuming, seismic P-waves first arrivals (picking). These first arrivals picking are the base of seismic velocity tomography.

At the same time, we developed a new tomographic code that performs simultaneous joint inversion of seismic travel times using both active and passive seismic data. This Passive Active Ray Tomographic Software (PARTOS) has been implemented in order to obtain for the first time in Mt. Etna and surrounding areas, a joint active passive seismic tomography. Resulting from this inversion we obtained a 3D realistic P-wave velocity model for Mt. Etna and surrounding areas, including Aeolian Island Archipelago.

However, tomographic model are not the final result, but the initial step of several advanced applications that require realistic 3D detailed velocity models. This is the case of precise seismic locations that enlighten different seismogenetic zones and permit the study of seismic patterns such as: i) *b* value analysis; ii) diffusivity curves calculations; or iii) seismic stress migration analysis, caused by magmatic intrusions, among others (hydraulic fracturing).

Chapter 2. Geophysical, Geodynamic and Volcanological framework of Mt. Etna volcano, Aeolian Islands and surrounding areas

Mt. Etna volcano is considered a laboratory volcano due to its almost-persistent volcanic activity, easy accessibility, and the highly populated surrounding areas. Indeed,

Mt. Etna volcano has the largest volcanic monitoring network in the World, comprising a wide variety of disciplines including volcanology, petrology, geochemistry, geodesy, magnetism, gravimetry or seismology, among others.

Such an intense monitoring is based on two different legs: surveillance and research. Volcanic surveillance permits warning civil protection services and population when a volcanic unrest begins. Volcanic research takes the huge multidisciplinary database provided daily by the monitoring network to improve the current knowledge of volcanic internal structure and dynamics at Mt. Etna and export it to other worldwide volcanic regions.

Nowadays, the internal structure and magma origin and storage of Mt. Etna is still controversial. Along Chapter 2 we discuss the main existent theories and merge them, and proposing a unifying model.

Chapter 3. TOMOE-ETNA Experiment. Joint marine and on land seismic active survey

During summer 2014 a complex active seismic survey took place in Sicily, Italy. The experiment named TOMO-ETNA, was conceived in the framework of the European Project MEDSUV.ISES and was aimed to study in detail the complex and controversial internal structure of Mt. Etna volcano, AEOLIAN Island Archipelago and surrounding areas. Therefore, more than 16,000 air-gun shots were fired as active seismic sources from the Oceanographic Vessel “Sarmiento de Gamboa”, with the support of the Italian Navy and the Oceanographic Vessel “Galatea” and the Greek Oceanographic Vessel “Aegeo”. The survey was divided in two main legs: Marine and On land activities. Marine survey was focused on: i) 27 Ocean Bottom Seismometers (OBS) deployment; ii) Wide-Angle refraction Seismic (WAS) and Multi-Channel Seismic reflection (MCS) surveys; iii) Carry out magnetic profiles and; iv) imaging and sampling of ocean bottom using Remotely Operated Vehicle (ROV), among others. On land activities occupy on the deployment and maintenance of a temporal seismic network of almost 100 short period and broad-band seismic stations. This temporal network combined with the existent permanent broad-band network operated by the Istituto Nazionale di Geofisica e Vulcanologia Osservatorio Etneo (INGV-OE) provided a 267-station seismic network to

register the active sources generated by the air-guns. Additionally, this seismic network recorded the natural seismicity of the region during a period of 4 months, in order to complement the active sources with passive seismic data.

TOMO-ETNA experiment, described in Chapter 3, provided a huge database with more than 3,000,000 seismic signals including active data and more than 400 earthquakes. This dataset was the base of the first joint active passive seismic velocity tomography in Mt. Etna and surrounding areas that is presented in this PhD Thesis.

Chapter 4. Advances on the automatic estimation of the P-wave onset time

The first step of this promising seismic tomography was the travel time calculation for the P-waves. Identifying correctly the seismic wave's onset for both active and passive signals, is a crucial matter to ensure the quality of the further analyses. Usually, this estimation has been performed manually by an expertise human operator. The operator analyses each trace individually or in small groups using a variety of filters to detect the seismic wave onset as precisely as possible. Therefore, for small databases it is highly recommended to use this procedure as the experience of the operator is essential. Nonetheless, for larger datasets, manual picking may be inconvenient due to several factors: i) Expertise own criteria (zero-crossing point, threshold, etc.); ii) Tiredness becomes an important factor when analysing large amounts of data and it could end up in biased P-wave onset readings; iii) different operators analysing the same dataset, may lead to different results. In order to avoid these inconveniencies, since few decades ago, the scientific community is focusing on developing trustful and robust algorithms that could identify the seismic wave's arrivals, both P- and S-waves, using always the same criteria and with low time consuming. This chapter reviews the state of art of some of the most important advances on this field, and describes in detail one of these algorithms. The selected algorithm has been used to analyse and automatically identify the P-wave seismic onsets of the TOMO-ETNA experiment database.

Chapter 5. Passive Active Ray Tomography Software (PARTOS)

Active and passive seismic tomographies have been carried out historically independently. However, the potentiality of a joint inversion summing advantages of both techniques must be taken into account. Combining information in depth provided by

natural seismicity with the a priori information regarding location and time origin of the active seismic sources leads to a considerably improvement on the internal structure information of the study area.

Merging active and passive seismic data has been carried out few times. Though, there are some joint interpretations using both datasets performed at Vesusvius and Campi Flegrei area; and in Central Java (Indonesia).

This chapter describes a new software developed in collaboration with the University of Novosibirsk. This code, named Passive Active Ray TOmography Software (PARTOS), permits simultaneous joint inversion of active and passive seismic data. The algorithms implemented process independently the data only during the step of preliminary source location, as each type of data requires different processing. Once the relocation is performed, both dataset are merged and analysed as one during the rest of the inversion.

PARTOS has been developed using two well-known and widely used tomographic algorithms that are LOTOS and ATOM-3D.

Chapter 6. Joint active and passive P-waves seismic tomography of Mt. Etna volcano, Aeolian Islands and related geodynamic region

In this chapter we show the main joint tomography results, obtained using the TOMO-ETNA experiment dataset. Firstly, we discuss the importance of the starting velocity models. Then, before showing the final images, we illustrate the synthetic tests carried out. These synthetic analyses allowed us to confirm the quality and reliability of the resulting images. Among them we present vertical and horizontal checkerboards, jackknifing and free anomaly tests. Moreover, we plot the ray density maps denoting the ray coverage of the inverted area. Finally, we show and interpret the joint inversion tomographic images by using horizontal and vertical sections. This scheme is repeated with each of three independent regions. Each of them is inverted independently, including the use of an ad-hoc starting velocity model. These regions are: i) TOMO-ETNA Experiment area; ii) Aeolian Islands Archipelago; and iii) Mt. Etna Volcano. We discuss the interpretation of a series of P-wave velocity anomalies found in these regions, based on previous regional and local studies. Many of these anomalies correspond to well-

known structures, widely discussed in previous works, such as the "Aeolian-Tindari-Letojanni Fault System" (ATLFS) that crosses the northeastern Coast of Sicily with a NW-SE direction, or the "High Velocity Body" (HVB) located slightly southeastern form MT. Etna central craters. We highlight additional anomalies that have never been enlightened or interpreted in previous studies. Indeed, we present a preliminary interpretation of them, while further investigation must be done in future works.

Chapter 7. An example of an Advanced Application: The analysis of The 2011–2013 seismic series associated to the volcanic activity of El Hierro Island on the light of a 3D high definition structural model

Seismic tomography is presented along the Thesis not just as an ending study, but as the base for further advanced studies. This chapter is a review of some of these studies that allow us to improve our knowledge of the internal structure of a volcano and the related dynamics of the volcanic phenomena. Precise location of seismicity is a further natural step after seismic tomography, as it permits to localize the events using a realistic 3D velocity model that takes into account lateral heterogeneities. Indeed, we present a precise location of the seismicity occurred at El Hierro Island (Spain), during the 2011-13 seismo-volcanic crisis, by applying two different algorithms: i) Non-linear probabilistic location algorithms (NonLinLoc) and; ii) relative location algorithms (HypoDD).

Additionally, the precise location permits to carry out further analyses to enlighten the seismic dynamic of a region. Especially in volcanoes, seismicity is often interpreted as magma migration, while other mechanisms may act. Magmatic intrusions in close conduits may cause seismicity due to stress migration, known as hydraulic fracturing induced seismicity. Along this chapter we propose a deep interpretation on the seismicity recorded at El Hierro applying this advanced studies.

Chapter 8. Conclusions

The main conclusions of this PhD Thesis are:

- TOMO-ETNA Experiment is probably the most complex active-passive seismic survey carried out in the world. Especially when we consider the number of involved people, countries, international projects, etc.

- AMPA algorithm is a new fast, robust adaptable and reliable algorithm that allows us the processing of all three million seismic signals in few hours, providing also a set of quality assessment parameters.
- Joint Active Passive Ray Tomography Software (PARTOS) has been developed ad-hoc for the TOMO-ETNA experiment dataset. It is probably the first time that such robust and powerful joint active passive tomography software has been developed and openly shared within the scientific community.
- High resolution tomographic images are presented for three different relevant regions: i) North-eastern Sicily, comprising Ionian and Thyrrenian Seas (Region 1); ii) Aeolian Islands Archipelago (Region 2); and iii) Mt. Etna Volcano (Region 3).
- Stability, robustness and quality of the solutions are proved throughout a series of synthetic tests.
- We present a complete case of study using seismic velocity models as the base for further advanced applications. This study comprise the use of several procedures:
    - *B*-value estimation.
    - Seismic precise location using relative and probabilistic non-linear algorithms.
    - Estimation of diffusivity curves.
- Hydraulic fracturing can be considered as an important mechanism controlling stress and seismic migration in volcanic areas, especially when magma intrusions occurred.

PRÓLOGO

La importancia del estudio y control volcánico se debe a la estrecha relación que existe entre humanos y volcanes. En los últimos 20-30 años se ha avanzado muchísimo en predicción de erupciones volcánicas, y, aunque no se pueda predecir erupciones al 100%, sí se tiene una gran fiabilidad en lo que se conoce como "Alerta Temprana" ("Early Warning"). Este procedimiento no es una predicción en sí, sino el resultado del análisis de un conjunto de observables. Este análisis permite establecer un modelo de evolución del estado del volcán y por tanto servir de aviso a las autoridades de que está teniendo lugar una reactivación volcánica, ya sea a partir de indicadores sísmicos, geoquímicos, de deformación, etc. Una alerta temprana efectiva permite poner en marcha mecanismos de evacuación de poblaciones y mitigación de daños que pueden salvar muchas vidas. Para que sea efectiva, la alerta se debe basar en un análisis en tiempo real de multitud de parámetros geofísicos y geoquímicos.

Una de las claves de estos protocolos es el uso modelos lo más realistas posibles de la estructura interna del volcán en cuestión. Para ello, la sismología y en especial la tomografía sísmica se presentan como herramientas fundamentales a la hora de obtener modelos 3D en velocidad o atenuación de las estructuras volcánicas, identificando heterogeneidades y anomalías laterales. Estos modelos se suelen obtener a través del análisis de terremotos o de fuentes sísmicas artificiales como generadores de señales sísmicas, aunque recientemente también se están utilizando técnicas como el análisis del ruido sísmico. Las fuentes artificiales se suelen usar generalmente en ambientes con sismicidad no homogénea en tiempo y espacio. Además, disponemos a priori la localización y tiempo origen de la señal sísmica, información que tendríamos que calcular a posteriori en el caso de los terremotos. El uso de fuentes sísmicas artificiales está limitado por varios factores entre los que se encuentra su alto coste económico y la dificultad de utilizar la fuente sísmica más adecuada. Generalmente, se trata de evitar fuentes invasivas que requieran modificar el terreno. Pese a estas limitaciones se complementan a la perfección con la información obtenida a través de la sismicidad, homogeneizando la resolución y distribución espacial de las fuentes sísmicas.

Con sus ventajas e inconvenientes, ambos métodos se han utilizado tradicionalmente por separado, y raro es el caso en el que se realizan interpretaciones conjuntas (ej. Campi Flegrei, Java, etc.). Sin embargo existe una gran potencialidad en estudiar ambas metodologías conjuntamente ya que podemos aunar sus ventajas y compensar sus debilidades. El caso ideal es el de un uso conjunto de ambas técnicas, ya que nos permite realizar una "instantánea" de la estructura interna del volcán sin que esta se vea afectada por la dinámica magmática. Este uno de los pilares fundamentales de esta Tesis Doctoral.

El caso del volcán Etna, conocido mundialmente por su actividad y su intensa monitorización, se presenta como una oportunidad única para aplicar una tomografía de fuentes activas ya que junto a su alta sismicidad, nos permitirá realizar una "instantánea" de su estructura interna. Bajo el marco del proyecto europeo MED-SUV, se consigue llevar a cabo un ambicioso experimento de sísmica activa llamado TOMO-ETNA, en el que cabe destacar la colaboración distintas instituciones internacionales y un gran número de investigadores de todo el mundo. Esto ha dado lugar a un sólido consorcio de investigación que ha permitido el éxito de dicho proyecto. El experimento TOMOETNA tiene lugar en la región nororiental de Sicilia, con el objetivo de obtener un modelo de velocidad que contemple las anomalías y heterogeneidades laterales que presenta una región tan compleja en la que se encuadran: i) 2 grandes grupos volcánicos (el Etna y las islas Eolias); ii) cadenas metamórifcas como la Maghrebí-Peloritana o iii) cuencas sedimentarias como el Plateau Hybleo. TOMOETNA parte con la idea, no sólo de realizar una tomografía activa, sino de complementarla con la información de sísmica pasiva presente y aunar por primera vez en esta región sísmica activa y pasiva. El primer resultado, es una enorme base de datos de más de tres millones de señales sísmicas de alta calidad, que deben ser procesados posteriormente.

Gracias a la colaboración interdisciplinar que mantenemos con otros grupos de investigación (Ej. Departamento de Teoría de la Señal, Telemática y Comunicaciones, Universidad de Granada), hemos implementado un sistema automático de detección de primeras llegadas de fases sísmicas (picking, de aquí en adelante) específico para nuestra base de datos. Dicho picking automático nos permite detectar los tiempos de llegada de

las ondas P en muy poco tiempo, con una muy alta fiabilidad y un criterio común, evitando las incertidumbres asociadas al picking manual.

La colaboración internacional que hemos establecido a partir de TOMOETNA, ha permitido desarrollar un software de inversión tomográfica conjunta ad-hoc. Dicho trabajo se ha llevado a cabo con la colaboración del Instituto de Geología y Geofísica del Petróleo de Novosirbisk (Rusia). Dicho software se describe en esta Tesis Doctoral y se utiliza para el análisis de los datos obtenidos en el experimento TOMOETNA, invirtiendo conjuntamente los datos de fuentes sísmicas pasiva y activa.

El éxito del experimento TOMOETNA, el algoritmo automático de picking y el programa de inversión tomográfica conjunta, no implica que llevar a cabo una tomografía sísmica sea sencillo. Existen numerosos factores a tener en cuenta cuando se realiza un estudio similar y que han determinado que hasta el momento no todos los volcanes activos cuenten con un estudio detallado de su estructura interna. Entre estos condicionantes se pueden encontrar la logística, los costes, o el personal humano que debe participar. Por ello, el éxito de esta Tesis Doctoral se basa también en la gran colaboración nacional e internacional, interdisciplinar y transversal entre distintas instituciones, departamentos, universidades, etc.

Es importante remarcar que no consideramos la tomografía sísmica no como el fin último de un trabajo, sino que sirve de base fundamental para realizar otros muchos estudios avanzados. Por ello, presentamos un claro ejemplo de cómo la tomografía, sirve de base para otros estudios avanzados que permiten avanzar en el conocimiento ya no sólo de la estructura interna, sino de la dinámica de los fenómenos volcánicos. Generalmente, los modelos interpretativos que estudian la evolución sísmica en volcanes se basan en dónde se localizan los terremotos y cuáles son los mecanismos físicos que los generan. En el caso de los volcanes, estos mecanismos pueden ser fundamentalmente por movimiento del magma o por procesos de emplazamiento del mismo. Así, la localización de precisión es una aplicación avanzada, que parte de la obtención de un modelo de velocidad realista y en 3D, que permite localizar con mucha mayor precisión los enjambres sísmicos y facilita la interpretación geodinámica de los mismos. En este sentido, presentamos una localización de precisión utilizando algoritmos probabilísticos

no lineales y algoritmos de localización relativa que nos permiten avanzar en el conocimiento de los mecanismos físicos responsables de la sismicidad.

1. INTRODUCCIÓN. MOTIVACIÓN Y ESTADO DEL ARTE

1.1. Volcanes

Los volcanes son posiblemente una de las expresiones de la naturaleza más fascinantes y sobrecogedoras, transmitiendo miedo, admiración y beneficios al hombre desde la antigüedad. Así, la relación hombre-volcán se encuentra en la propia naturaleza humana, con numerosas manifestaciones del papel jugado por ésta en la historia (De Boer & Sanders, 2002). Nos ilustran cómo es el interior de la Tierra y cómo se forman algunas rocas. Englobar a todos los volcanes dentro de una misma definición es complicado debido a la gran variedad de lugares donde se pueden encontrar y las diferentes tipologías (según su morfología, origen, frecuencia de actividad, composición, etc.). Quizás, una de las descripciones que más se acerque sea la de Francis & Oppenheimer (2004), que los define como "*La manifestación en la superficie de un planeta o satélite de procesos térmicos internos a través de la emisión en superficie de productos sólidos, líquidos o gaseosos*".

1.1.1. Volcanes y Humanidad

La humanidad se ha sentido siempre atraída por los volcanes, no sólo por su belleza y espectacularidad, sino por proporcionar una tierra fértil sobre la que cultivar y asentar poblaciones. Además, son fuente fundamental de vapor de agua, facilitando el acceso al agua, indispensable para la vida, a través de acuíferos, aguas hidrotermales, etc. Muchas de las betas minerales de cobre, plomo y cinc, entre otros, se originaron a partir de procesos volcánicos y por tanto se pueden encontrar cerca de volcanes. Pese a ello, el hecho de vivir junto a un volcán puede representar un gran número de amenazas para la población. Dichas desventajas son consecuencia de los procesos de actividad que van desde coladas de lava, fuentes de lava, caída de cenizas, flujos piroclásticos, lahares, etc. y que pueden afectar de manera local, regional e incluso global a la vida humana.

Estas consecuencias negativas en la población se deben fundamentalmente a la falta de conocimiento del ser humano de los fenómenos naturales asociados a los volcanes. A continuación repasamos algunas de las erupciones volcánicas que más repercusión han tenido sobre la población, desde escala local a global. Ejemplos de este tipo de consecuencias volcánicas a escala local existen muchos, y muy bien conocidos por el público en general (De Boer & Sanders, 2002). Un ejemplo es la erupción del

Vesubio que sepultó Pompeya y Herculano en el año 79 matando a miles de personas, o la erupción del volcán Nevado del Ruiz en 1985 que destruyó el pueblo de Armero causando la muerte de decenas de miles de personas a causa de los lahares. Un impacto a escala regional lo tuvo por ejemplo la erupción del Krakatoa en 1883, que se escuchó a miles de kilómetros de distancia y que destruyó la isla de Krakatoa provocando un tsunami que arrasó más de 160 pueblos de islas vecinas matando a más de 40.000 personas. Otro ejemplo es el de la erupción de Thera hace 3.500 años, que provocó la desaparición de la isla de Thera debido al colapso de la caldera. Hoy en día conocemos dicha caldera de 6x11 km de diámetro como Santorini. Dicha erupción expulsó cerca de 60 km^3 de material volcánico. Más recientemente, el Eyjafjallajokull en 2010 provocó con sus nubes de cenizas el caos en la actividad aérea en Europa durante varias semanas.

Existen algunos ejemplos de erupción de una magnitud tal, que sus efectos se hicieron notar en todo el globo. Son el caso del volcán Tambora (Indonesia) cuya erupción y posterior colapso de la caldera en 1815 provocaron tal cantidad de cenizas que cubrieron por completo la atmósfera terrestre dando lugar un descenso de las temperaturas que acabó dando nombre al verano de 1816 como "el año sin verano". Por último existen los llamados "supervolcanes" (ej. Yellowstone, Toba), que se conocen en base a los registros y la datación de antiguas erupciones. En el caso de Toba (Indonesia), productos volcánicos (fundamentalmente cenizas) datados hace en torno a 75.000 años, ocupan una extensión de miles de kilómetros. Esta mega-erupción se relaciona con una de los más importantes descensos de la población mermándola a unos 10.000 individuos, marcando un hito en la evolución humana. Además, en estos años la temperatura media en la Tierra descendió varios grados. Por otro lado, Yellowstone (EE.UU) presenta depósitos lávicos de un mismo periodo eruptivo que ocupan varios miles de km^2. Dicho periodo eruptivo tuvo lugar hace alrededor de 2,5 millones de años y fue de una magnitud similar al de Toba.

1.1.2. Volcanes y Vigilancia

Los avances científicos permiten que en la actualidad la predicción de una erupción sea bastante acertada, permitiendo mitigar los posibles perjuicios y daños que ésta pueda provocar en una población. Para ello, sin embargo, se requiere un profundo

estudio y una constante vigilancia del volcán. Un estudio y control eficaces en un volcán implica afrontarlo desde diferentes puntos de vista y complementar distintas metodologías para poder establecer sistemas de Alerta Temprana ("Early Warning"), (e.g., Kamo et al., 1994, Leonard et al., 2008, Tilling, 2011). Son muchas las disciplinas que actualmente proporcionan una información imprescindible a la hora de predecir una hipotética erupción. A continuación describimos brevemente algunas de las aportaciones de dichas técnicas en el campo de la vigilancia volcánica y del estudio de los volcanes:

i) *Geoquímica*: Se dedica tanto al análisis de los gases emitidos en fumarolas como a analizar los cambios en la composición del agua en lagos, pozos o ríos cercanos al volcán. Los cambios en la composición de los gases emitidos, ya sea de manera difusa en toda la superficie del volcán (Chiodini et al., 2001) o a través de fumarolas (Granieri et al., 2006) pueden indicar un cambio en la composición del magma por un aporte de magma joven o directamente un ascenso de magma y por tanto la cercanía de un posible evento eruptivo. Los principales gases que se analizan actualmente son el He, CO_2, SO_2, Ra, etc. (Pérez et al., 2007, 2012, Padilla et al., 2013). Un aspecto fundamental en la geoquímica es el estudio de los ratios entre distintos gases o isótopos de un mismo elemento que proveen indicaciones del estado del magma, su contenido en gases o la profundidad a la que se encuentra.

ii) *Geodesia*: El análisis de la deformación del suelo mediante técnicas GPS o de interferometría laser (INSAR), permiten en la actualidad medir variaciones milimétricas del suelo en cualquiera de las 3 componentes. En volcanes, estas variaciones espaciales de un punto en el terreno se relacionan con inflaciones y deflaciones del sistema volcánico, apertura de diques, etc. que pueden implicar a su vez el ascenso de magma hacia la superficie o vaciado del reservorio magmático (Dvorak & Dzurisin, 1997; Fialko et al., 2001; Dzurisin, 2006; Sturkell et al., 2006).

iii) *Magnetismo*: Las propiedades magnéticas de ciertos minerales, supusieron un apoyo fundamental a la teoría de placas al evidenciar la distinta polaridad magnética de las rocas que forman la corteza oceánica según la

polaridad magnética terrestre. Además técnicas recientes permiten detectar la intrusión de diques y el enfriamiento de los mismos (Johnston, 1997; Michel & Zlotnicki, 1998; Cassidy et al., 2007, Ort et al., 2015).

iv) *Gravimetría*: Una de las grandes aportaciones de este campo para la vigilancia volcánica es el análisis de las variaciones en el valor de la aceleración de la gravedad. Dichas variaciones se miden en el tiempo para una serie de puntos. Esto permite detectar las intrusiones magmáticas, apertura de diques, y ascenso de magma en general, llegue, o no, a la superficie (Rymer & Brown, 1986; Kauahikaua et al., 2000; Furuya et al., 2003; Battaglia et al., 2008a).

v) *Sísmología*: El estudio de la sismicidad en ambientes volcánicos es de vital importancia ya que ésta es uno de los precursores eruptivos más frecuentes y evidentes. La sismicidad registrada en volcanes puede ser de varias tipologías según su origen, tal y como describe McNutt (2005), que los clasifica en: a) Eventos Volcano-Tectónicos de alta frecuencia (Volcano-Tectonic o VT), similares a los terremotos puramente tectónicos pero originados en ambientes volcánicos; b) Eventos de largo período (Long Periodo o LP) y de muy largo período (Very Long Periodo o VLP) (LP, VLP), producidos por la interacción de fluidos (magmáticos y/o hidrotermales); c) Explosiones volcánicas, con contenido en frecuencias del rango de los infrasonidos; estos eventos se producen también por la interacción de fluidos con el medio volcánico; d) Tremor volcánico, caracterizado como una señal de baja frecuencia prolongada en el tiempo (desde pocos segundos hasta días) (Chouet, 1996a; Chouet, 2003; Zobin, 2011; De Barros et al., 2012; Chouet & Matoza, 2013). Las mencionadas señales tienen distintos orígenes, por lo que existen disciplinas independientes para estudiar cada tipo de señal, permitiendo analizar distintos aspectos del sistema volcánico. Una de estas técnicas es la tomografía sísmica, que trataremos en profundidad a lo largo de esta Tesis Doctoral.

La vigilancia volcánica se basa fundamentalmente en la relación entre los observables y los modelos físicos que describen la dinámica interna. Para ello, debemos

conocer lo que sucede en el interior de la Tierra y cómo se comporta, y así tratar de predecir el fenómeno antes de que ocurra. En la actualidad, el conocimiento del interior terrestre se ha alcanzado únicamente mediante medidas indirectas que proporcionan modelos estructurales 3D. Con algunas de las disciplinas descritas anteriormente se pueden inferir estructuras en 3D del interior de la Tierra utilizando distintos parámetros físicos. A modo de ejemplo destacamos las aportaciones de la Gravimetría y su modelado de las anomalías de densidad (Fig.1.1.a) (Bonaccorso et al., 2011); el Magnetismo, modelando las anomalías magnéticas del terreno (Fig.1.1.b) (Blanco-Montenegro et al., 2011); o la Tomografía Sísmica, que estudia el comportamiento de las ondas sísmicas para derivar modelos estructurales en 3D (Fig.1.1.c) (García-Yeguas et al., 2014).

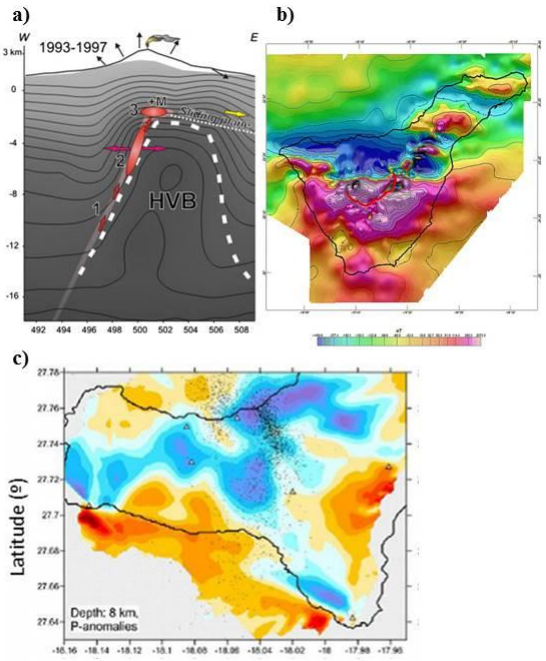

Figure 1.1 *a) Modelo ilustrativo de la estructura del Etna a partir de datos gravimétricos (Bonaccorso et al., 2011);b) Mapa de anomalías magnéticas de Tenerife*

(Blanco-Montenegro et al., 2011); c) Tomografía sísmica de la Isla de El Hierro (Garcia-Yeguas et al., 2014).

1.2. Técnica para inferir el interior de la Tierra usando ondas sísmicas: Tomografía Sísmica

La tomografía sísmica se presenta en la actualidad como una de las herramientas más potentes y robustas para el estudio de la estructura profunda de los volcanes (Lees, 2007). La tomografía, "imagen en capas" traducido literalmente, siendo un método para obtener una imagen de regiones no accesibles de manera directa, ha sido utilizada entre otros como método para "ver" partes internas de organismos vivos, otros planetas, y en la que se centra este trabajo, el interior de la Tierra. (Lees, 2007). Zonas de subducción, grandes fallas y volcanes son algunas de las principales estructuras geológicas que se pueden estudiar en detalle utilizando esta técnica desde que se desarrollara en el campo de la sismología a mediados de los 70 (Aki et al., 1974). Sus comienzos en sismología estuvieron más enfocados hacia estudios regionales utilizando telesismos donde la resolución a pequeña escala era aún bastante limitada. Una tomografía sísmica se realiza a partir de los tiempos de viaje de las ondas P y S que atraviesan dicha región y que se registran en una serie de estaciones sísmicas instaladas en torno al mismo (Iyer, 1993). Estos tiempos de viaje se comparan con los tiempos de viaje teóricos calculados con un modelo de velocidad inicial (generalmente bastante simplificado). Si el parámetro estadístico que nos muestra su aproximación con los tiempos de viaje observados no se considera adecuado se calcula un nuevo modelo de velocidad que se ajuste mejor a los tiempos de viaje observados. Esto se conoce como el método inverso ya que a partir de los resultados tratamos de inferir aquello que los produce. Centrándonos en su aplicación en volcanes, no fue hasta mediados de los 80 cuando se tuvieron las herramientas y algoritmos necesarios para su aplicación. Probablemente, la primera tomografía de un volcán fue la propuesta por Thurber (1984), en la cual el autor invierte las llegadas de las ondas P para determinar la estructura interna en velocidad del volcán Kilauea (Hawaii). El principal resultado de esta tomografía fue una anomalía de baja velocidad y asísmica bajo el volcán que se interpretó como la cámara magmática del Kilauea. Desde entonces, se han realizado numerosos trabajos en los que se estudia la estructura interna de un

volcán utilizando la tomografía sísmica, que permite "iluminar" estructuras profundas de un sistema volcánico que de otra manera serían inaccesibles. Sin lugar a dudas, detectar posibles zonas de acumulación de magma es uno de los principales objetivos de estos estudios, pero no siempre accesible ni realista debido a la complejidad de este tipo de estudios en volcanes. Entre otras causas, depende enormemente del tipo de volcán, la profundidad de dichas zonas de acumulación y el contenido en gases del magma, pero sobre todo, depende de la sismicidad asociada el volcán. Generalmente, los resultados obtenidos de una tomografía sísmica son anomalías, respecto a un modelo teórico, tanto positivas como negativas, de los valores de velocidad de las ondas P y/o de las ondas S y /o del ratio Vp/Vs. Durante los comienzos de las tomografías sísmicas en volcanes, los datos que se utilizaban eran generalmente telesismos, y se realizaban estudios de escala regional debido a la ausencia de redes sísmicas en volcanes suficientemente densificadas y a la poca o ausente sismicidad en muchos volcanes (Koulakov, 2013). Algunos ejemplos de estas tomografías a mayor escala son: Toomey & Foulger, (1989), en Islandia; Dawson et al., (1987), en Long Valley, California (EE.UU); Zhao & Hasegawa, (1993), en Japón, Koulakov et al., (2006) en India, o Koulakov et al., (2009) en Europa. Con el tiempo, los avances en instrumentación (Havskov & Alguacil, 2016) han permitido densificar las redes sísmicas y mejorar considerablemente la vigilancia de muchos volcanes. Esto lleva a estudios más locales, centrados en un único volcán.

La tomografía sísmica, tal cómo se describe anteriormente, se desarrolló basándose en el uso de los terremotos como fuente sísmica y se conoce como tomografía sísmica pasiva. La gran ventaja del uso de terremotos como fuente sísmica se relaciona con el amplio rango de profundidades a las que ocurren. De esta manera, se pueden realizar estudios a distintas escalas, según el tipo de terremoto que utilicemos, ya sea local, regional o telesismo. Sin embargo, el uso de terremotos como fuente sísmica no siempre es posible, ya que sólo se podrán utilizar en regiones donde la sismicidad sea elevada y tenga una distribución adecuada. Precisamente, los volcanes se suelen encuentrar en regiones sísmicamente poco activas o con sismicidad irregular en el tiempo, por lo que no siempre es posible utilizar la tomografía sísmica pasiva en estas regiones.

Para solventar esta necesidad, entre otras, se comienzan a utilizar fuentes artificiales como generadoras de ondas P. Dichas señales artificiales se pueden generar con la ayuda de cañones de aire comprimido, explosiones, caída de grandes masas, etc. (Koulakov & Shapiro 2015). Este método conocido como tomografía sísmica activa, tiene la desventaja del precio, ya que suele ser bastante caro organizar un experimento de sísmica activa (Ver Anexos 1-4). Sin embargo, acumula un gran número de ventajas entre las que se encuentra el conocer con absoluta precisión tanto la localización como la hora origen en la que se generan dichas señales sísmicas. En contraposición a los terremotos, de los cuáles la única información "a priori" que se tiene, son las llegadas de las ondas P y S a las distintas estaciones. Es a partir de esas llegadas, cuando se localiza el terremoto y se calcula su hora origen. Otra importante diferencia entra ambos tipos de fuente es el área que cubren, en el caso de las fuentes artificiales se generan en su mayoría en la superficie o a muy poca profundidad, por lo que el área que cubren los rayos hasta las estaciones sísmicas es generalmente superficial, llegando hasta 5-10 km de profundidad según el caso. Por lo que su uso, no resuelve estructuras demasiado profundas, pero en cambio, si el número de fuentes es grande, se puede obtener una gran resolución de los primeros kilómetros de la corteza. Por otro lado, los terremotos tienen un espectro mucho más amplio pudiendo originarse a cientos de kilómetros bajo la superficie terrestre, permitiendo que la tomografía resuelva profundidades mayores con buena resolución.

En el Capítulo 5 de esta tesis se discute detalladamente la metodología seguida para realizar una tomografía sísmica, tanto activa como pasiva y la combinación de ambas. A continuación, y para ilustrar lo ya comentado y presentar el estado del arte actual acerca de la tomografía sísmica en volcanes, ya sea activa o pasiva, en los próximos párrafos se describen los más importantes y recientes trabajos realizados en este campo, incluyendo distintos volcanes y distintas escalas, separándolos según hayan utilizado sismicidad natural o fuentes artificiales.

1.2.1. Tomografías de velocidad usando sismicidad pasiva

El número de tomografías realizadas utilizando la sismicidad natural como fuente sísmica es muy grande, y se ha desarrollado exponencialmente desde su comienzo en los

70. A continuación describimos algunas de las tomografías sísmicas pasivas más relevantes realizadas en volcanes en los últimos 20 años (Figure 1.2).

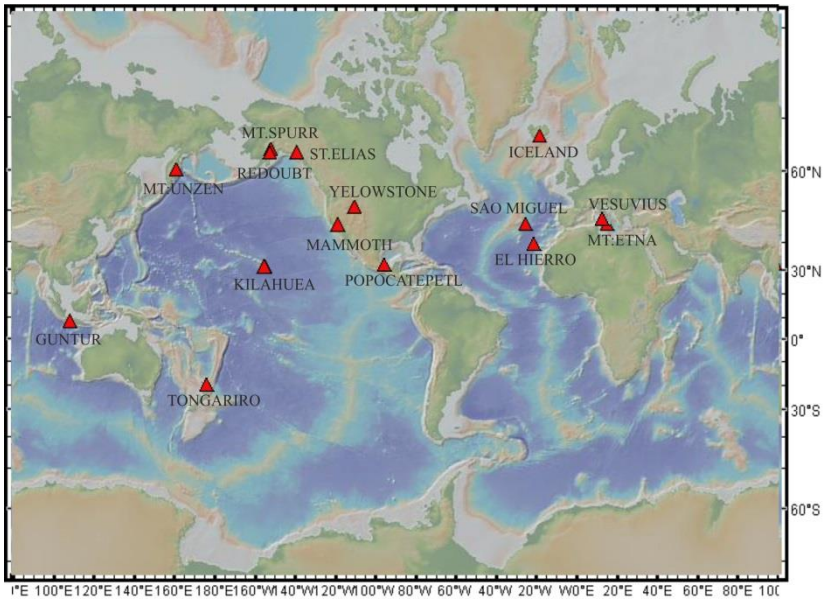

Figure 1.2 *Mapa del mundo con la localización de los volcanes donde se han realizado estudios de tomografía usando sísmica pasiva en los últimos 20 años.*

Japón, como una de las regiones volcánicas más activas del mundo, es el objetivo de numerosos estudios en volcanes, debido, entre otros factores, a la alta concentración de población cercana a los volcanes. En 2002, Zhao et al., (2002) analizaron la estructura en velocidad del volcán Unzen usando como base de datos la sismicidad regional registrada durante 116 años. Dicho estudio les permitió inferir la influencia de los fluidos y el magma con la ocurrencia de grandes terremotos, localizando una gran cantidad de terremotos de gran magnitud dentro o cerca de una anomalía de baja velocidad.

Zandomeneghi et al., (2008), realizo un estudio tomográfico local de la isla de Sao Miguel (Archipiélago de las Azores) a partir de las llegadas de las ondas P de 289 terremotos registrados durante 4 meses en 2003 por una red sísmica temporal de 20 sensores instalada para dicho propósito. Los principales resultados de este estudio son la interpretación de una serie de anomalías de baja velocidad que los autores relacionan con

campos hidrotermales y con zonas altamente fracturadas; en contraposición, aparecen zonas de alta velocidad que relacionan con densos cuerpos plutónicos.

En 2014 se estudiaron los volcanes de Kilauea y Mauna Loa en Hawaii aprovechando la sismicidad registrada en la zona (Lin et al., 2014a, 2014b). Como en casos anteriores, las anomalías negativas de velocidad se asociaron a la presencia de volátiles y sedimentos altamente fracturados. En ambos volcanes se detectó la presencia de las anomalías positivas de velocidad bajo las principales calderas. En este caso se partió de una base de datos compuesta por cerca de 53.000 eventos registrados entre 1992 y 2009. Una de las ventajas de un estudio tomográfico como este, es la posibilidad de utilizar el modelo 3-D más realista de velocidades para realizar posteriores relocalizaciones de la sismicidad.

La península de Kamchatka (Rusia) es una de las zonas con mayor concentración de volcanes activos del planeta y es el foco de numerosos estudios tomográficos para conocer la estructura interna en velocidad de la corteza. Es una región cuya importancia geológica es mayúscula pues se encuentra muy cerca de la zona de subducción del Pacífico, por lo que no sólo hay una gran cantidad de volcanes sino que la sismicidad registrada en la zona suele ser abundante y de gran magnitud. Se han presentado tomografías regionales que incluyen gran parte de la península de Kamchatka, como el complejo volcánico de Kluchevskoy (Koulakov et al., 2011, 2013a, 2016). En todos estos casos, se ha considerado la sismicidad local y regional, es decir no sólo aquellos terremotos VT ligados directamente a la dinámica volcánica sino también aquellos cuyo origen se encuentra en la zona de subducción de la placa Pacífica, permitiendo alcanzar resoluciones hasta profundidades en torno a 30 km bajo el nivel del mar (b.n.m.).

Otra zona de gran interés geológico y volcánologico es Alaska, conectada también a la subducción de la placa Pacífica. En esta región podemos encontrar un estudio de la estructura en velocidad del volcán Redoubt realizada por Kasatkina et al., (2014) en la que se invirtieron las llegadas de las ondas P y S para un total de 4.500 terremotos registrados durante 13 años. Durante el periodo considerado tuvo lugar al menos una erupción por lo que se pudo comparar la estructura en velocidad antes y después del evento eruptivo. Los resultados de este estudio mostraron la presencia de un

cuerpo de alta velocidad localizado bajo el volcán junto con anomalías para las ondas S que antes de la erupción eran muy elevadas en comparación con los valores obtenidos después. Otro volcán estudiado es el Mt. Spurr (Koulakov et al., 2013b), donde se invirtieron 512 terremotos registrados durante 4 meses. En este caso la red sísmica utilizada para registrarlos consistió en 26 sensores distribuidos en aproximadamente 900 km^2. En total se utilizaron 5.960 llegadas de ondas P y 4.973 S. Zabelina et al., (2014) realizó un nuevo estudio tomográfico en otro volcán de Alaska, el volcán Saint Elias, donde se recogieron 8 años de sismicidad registrada en 22 estaciones. La base de datos, con cerca de 8.000 terremotos se utilizó para invertir 150.000 ondas P y S y obtener la estructura en velocidad de esta zona de colisión.

Recientemente, Dawson et al., (2016) realizaron un estudio tomográfico en el volcán Mamooth Mountain en California (EE.UU). Los autores invirtieron las llegadas de las ondas P, S y calcularon los ratios Vp/Vs de un total de 2.604 terremotos. Para registrarlos, se instaló una red sísmica temporal compuesta por 11 sensores de banda ancha durante 2 años. Los resultados obtenidos muestran la presencia de un volumen bajo el volcán con valores anómalamente bajos para las P y las S, que los autores interpretan como un reservorio de CO_2 posiblemente alimentado por un sistema magmático subyacente.

La región de Java (Indonesia), ha sido ampliamente estudiada desde el punto de vista tomográfico debido a su interés geológico y volcánico. Entre otros, Nugraha et al., (2013) estudiaron el complejo volcánico Guntur invirtiendo 4.686 P y 2343 S correspondientes a 490 terremotos registrados en 20 estaciones. Los autores detectan anomalías negativas de Vp, Vs y altos valores de Vp/Vs cuyo origen interpretan como un reservorio magmático.

Uno de los volcanes más famosos del mundo, Yellowstone (EE.UU) fue el objeto de un reciente estudio (Farrel et al., 2014). Los autores recabaron la sismicidad registrada durante 26 años por la red sísmica local. En total, se invirtieron 48.622 llegadas de onda P correspondientes a 4.520 terremotos de alta calidad. En este estudio se utilizan únicamente las fases P de los terremotos y se invierte un área de 70.000 km^2 aproximadamente, en la cual, los resultados muestran un gran cuerpo de baja velocidad

localizado en torno a 15 km de profundidad. Dicho volumen es interpretado por los autores como la cámara magmática del sistema volcánico y en la que estiman entre un 5-15% de material fundido.

No todos los estudios tomográficos encuentran o pretenden encontrar una cámara magmática, sino que en muchos de ellos coincide la presencia de anomalías de alta velocidad localizadas bajo el volcán como uno de los rasgos más característicos de los edificios volcánicos. Estas anomalías generalmente se interpretan como acumulaciones de rocas plutónicas posiblemente asociadas al enfriamiento de antiguos centros eruptivos (Kasatkina et al., 2014; Lin et al., 2014a; García-Yeguas et al., 2012; Zandomeneghi et al., 2008; entre otros muchos).

Realizar una tomografía sísmica en un volcán implica tener generalmente una base de datos con suficientes terremotos para que sea fiable. De este breve resumen verificamos que en la mayoría de volcanes, para cumplir este requisito deben pasar varios meses incluso decenas de años. Esto implica, sobre todo en volcanes con actividad eruptiva frecuente, que el resultado final no sea más que el promedio de la estructura durante todo ese tiempo. De hecho, de ocurrir erupciones durante ese periodo estaríamos minimizando su aportación al resultado final. De ahí, que surja la necesidad de realizar lo que se conoce con "snapshots" o "instantáneas" que son tomografías en las que el periodo en el que se han registrado los eventos es suficientemente corto como para estimar que no se han producido cambios sustanciales en la estructura interna del volcán. Por desgracia, esta técnica requiere un gran número de terremotos en un corto periodo de tiempo, cosa que rara vez ocurre en volcanes. Sin embargo, cuando sucede se puede realizar este tipo de estudios, también conocidos como tomografía 4-D. Uno de los casos más conocidos es la erupción de 2002-03 en el volcán Mt. Etna. Dicha erupción estuvo acompañada por un intenso enjambre sísmico que permitió a los investigadores dividir la base de datos en distintos intervalos temporales para los cuáles invirtieron las llegadas de las ondas P, S y el ratio Vp/Vs (Patanè et al., 2006). Dicho estudio permitió individuar los posibles conductos magmáticos que alimentaron dicha erupción gracias a los valores anómalos del ratio Vp/Vs y su variación temporal.

1.2.2. Tomografías de velocidad utilizando sísmica activa

En los últimos 20 años el número de experimentos de sísmica activa ha ido aumentando considerablemente, así como las técnicas para generar las señales artificiales (aire comprimido, caída de masa, reacciones químicas, explosiones, etc.). La figura 1.3 representa la localización de cada uno de los volcanes a los que se va a hacer mención en los siguientes párrafos, ordenados geográficamente por zonas, y en los cuáles se ha desarrollado un experimento de sísmica activa recientemente.

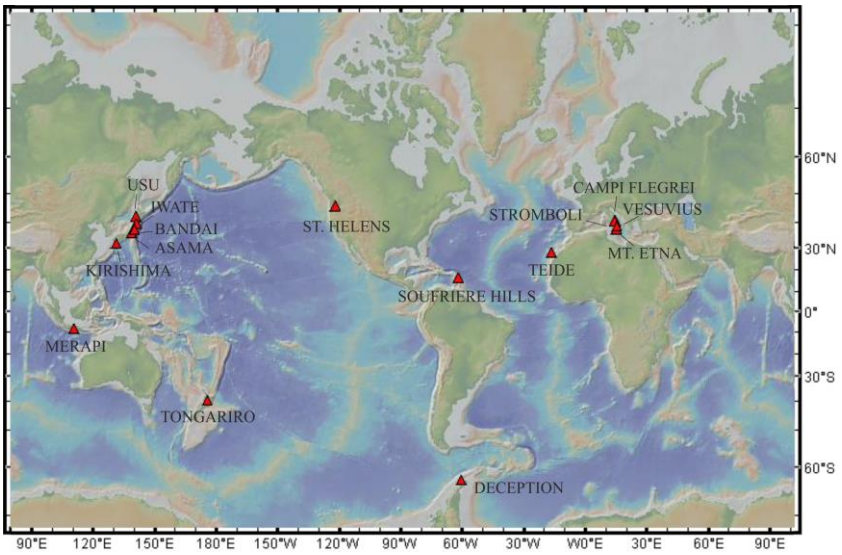

Figure 1.3. *Mapa del mundo con la localización de los volcanes dónde se han realizado experimentos de sísmica activa en los últimos 20 años.*

En 1994, Tomatsu et al., (2001) realizaron un experimento sísmico en el volcán Kirishima (Japón), obteniendo como resultado las estructuras en velocidad y atenuación de las ondas P bajo el sistema volcánico de Kirishima. Para ello realizaron 6 explosiones con una carga aproximada de 200-250 kg cada una. Dichas explosiones generaron las ondas P registradas en 163 estaciones sísmicas instaladas en torno al volcán. La selección de los tiempos de llegada de dichas ondas P se realizó de manera manual. Los principales resultados fueron la obtención de la estructura 3D en velocidad y atenuación, que

permitieron detectar una serie de estructuras superficiales bajo el volcán, a 1.5 km y 0.5 km bajo el nivel del mar (b.n.m.).

Durante ese mismo año, 1994, se realizó otro gran experimento sísmico, esta vez en el volcán Vesubio (Italia). Dicho experimento tenía como objetivo reconstruir en detalle la estructura superficial del volcán, pretendiendo incluso detectar el sistema de alimentación del mismo (Zollo et al, 1996; Gasparini, 1998). Se realizaron 3 explosiones bajo tierra, durante una primera fase, que fueron registradas por 84 sensores sísmicos alineados siguiendo un perfil a lo largo del volcán. En una segunda fase tuvieron lugar 17 explosiones de entre 250 y 800 kg de explosivo colocadas a 50 m de profundidad. Tanto las explosiones como las estaciones estaban distribuidas linealmente a lo largo de perfiles de entre 25 y 40 km de largo. Para esta segunda fase del experimento se usaron un total de 140 sismógrafos de 3 componentes. Los resultados de este experimento han permitido mejorar considerablemente el conocimiento que se tenía acerca de la estructura interna del Vesubio (e.g. Zollo et al., 1998; Di Stefano and Chiarabba, 2002; Zollo et al. 2002).

El volcán Bandai (Japón), fue el escenario de un nuevo experimento de sísmica activa en 1997 (Yamakawi et al., 2004). De nuevo se utilizaron un total de 8 explosiones como fuente sísmica, que se registraron en un total de 298 estaciones sísmicas instaladas en un área de 25 x 20 km. Como resultado principal se obtuvo la tomografía sísmica en velocidad de dicho volcán utilizando 2200 llegadas de onda P. Las estaciones utilizadas eran de corto periodo (periodo natural de 0.5 s), 6 de las explosiones se realizaron con 200-250 kg de carga explosiva detonadas alrededor del volcán, y otras 2 ("con sólo" de 100 kg) se detonaron en la parte central del volcán. En este caso, las primeras llegadas de las ondas P se seleccionaron también de manera manual.

Durante 1997-98 se realizó en el volcán Merapi (Indonesia) un nuevo experimento de sísmica activa (Zschau et al., 1998). Se instaló una red símica temporal de 75 sensores de corto periodo (periodo natural de 1 s) siguiendo 3 perfiles. En dos de los perfiles de 3 km de longitud se colocaron 30 sismómetros de 3 componentes cada uno, mientras que en el tercer perfil, de sólo 1.5 km de longitud se desplegaron los otros 15 sismómetros (Wegler et al., 1999; Wegler and Luerh, 2001). En este caso, las fuentes sísmicas utilizadas fueron cañones de aire comprimido (de 2.5 l) instalados en tanques de

agua de 4.5 m de profundidad. Los disparos de aire comprimido se realizaron cada 2 minutos con una presión de 8 MPa. Cada estación desplegadas registró entre 20 y 120 disparos que permitieron analizar la estructura interna del volcán hasta una profundidad de 300 m bajo los perfiles (Maercklin et al., 2000).

Otro experimento de sísmica activa tuvo lugar en el volcán Asama en Japón durante el año 2006. La fuente sísmica utilizada fueron 5 cargas explosivas de 250-300 kg (explosiones químicas) colocadas a 60 m de profundidad. Las ondas sísmicas provocadas por estas explosiones fueron registradas por un total de 464 estaciones sísmicas (Mark L-22D 2 Hz) (Aoki et al., 2009; Yamamoto and Sato, 2010). La geometría de despliegue se compuso de dos perfiles (N-S y E-W) cruzando el volcán. En total se generaron más de 2000 fases P, cuyo tiempo de viaje fue seleccionado de forma manual para luego ser utilizadas en la inversión tomográfica.

También en Japón, se realizó un experimento en el 2001 en el volcán Usu (Onizawa et al., 2007). Se desplegaron 288 estaciones sísmicas (1-componente, 2Hz) con una separación de 750 m entre ellas alrededor del volcán. Las fuentes sísmicas utilizadas fueron 7 cargas explosivas de 200-250 kg. A partir de los datos de las llegadas de las fases sísmicas P se realizó una tomografía sísmica que permitió obtener imágenes de la estructura interna del volcán.

El experimento SERAPIS tuvo lugar en 2001 en el golfo de Nápoles y Pozzuoli con el objetivo de estudiar en detalle el Vesubio y Campi Flegrei (Zollo et al., 2003). Para generar las señales sísmicas se utilizaron 12 cañones de aire comprimido de 16 litros montados en el buque oceanográfico NADIR (IFREMER). Se realizaron un total de 5000 disparos que se registraron en 62 estaciones sísmicas marinas (OBS) y 72 terrestres (sensores de 3 componentes) instaladas todas en el golfo de Nápoles (OBSs), Campi Flegrei, el Vesubio y las islas Ischia y Procida (Judenherc and Zollo, 2003; Vanorio et al., 2005; De Siena et al., 2010; De Siena et al., 2011). Battaglia et al., (2008b) propuso combinar los datos de sísmica activa recogidos en dicho experimento con los datos de sismicidad natural.

Desde 1998 hasta 2003 se realizó en el volcán Iwate (Japón) un complejo experimento de sísmica activa (Nishimura et al., 2000, 2005). Durante la primera parte

del experimento se detonaron 6 cargas, colocadas cerca unas de otras en un área de 30 x 10 m. Las ondas sísmicas provocadas se registraron en 8 estaciones. Durante este período tuvo lugar incluso un terremoto de magnitud 6.1, dando mayor importancia al objetivo del experimento que era estudiar posibles cambios temporales en la estructura en velocidad de la corteza. Dicho terremoto ocurrió entre la primera y la segunda explosión. El resto de explosiones se realizaron entre el año 2000 y 2003. Durante el año 2000 en la misma región, Tanaka et al., (2002) realizaron un experimento con 9 explosiones de 200-250 kg de carga e instalaron una red temporal de 330 estaciones de corto periodo de 1-componente (2 Hz de periodo natural). El área de estudio ocupó aproximadamente 1600 km^2 y los tiempos de viaje de las señales que se generaron fueron seleccionadas manualmente para obtener 2676 llegadas de onda P utilizadas posteriormente para realizar la tomografía sísmica en velocidad (Tanaka et al., 2002).

El volcán Isla Decepción en la Antártida fue el objetivo de un experimento de sísmica activa (TOMODEC) en 2005 (Barclay et al., 2009; Ben-Zvi et al. 2009; Zandomeneghi et al. 2009; García-Yeguas et al., 2011; Carmona et al., 2012; Prudencio et al., 2013a; Prudencio et al., 2015a). En este experimento se utilizó un array de 6 cañones de aire comprimido de 57 litros instalado en el Buque Oceanográfico Hespérides. Como red sísmica se instalaron 14 OBSs y 95 sensores en tierra. Se generaron más de 6600 disparos de aire comprimido obteniendo un registro final de 600.000 señales de alta calidad. Dada la geometría de la isla (forma de herradura) se realizaron disparos incluso dentro de la caldera siguiendo una malla de 0.5 km y disparando cada 120 m. En el exterior de la isla se disparó cada 170-340 m, a lo largo de tres circunferencias a distancias de 10, 15 y 20 km del centro de la isla. Además se realizaron 8 perfiles radiales de 25 km de longitud. Para la tomografía sísmica en velocidad 2-D y 3-D realizada por Ben-Zvi et al., (2009) y Zandomenghi et al., (2009) se utilizaron más de 70.000 fases sísmicas de ondas P.

En 2007 en la isla de Tenerife se llevó a cabo un nuevo experimento (Ibáñez et al., 2008; De Barros et al., 2012; García-Yeguas et al. 2012; Lodge et al., 2012; Prudencio et al., 2013b; Prudencio et al., 2015b). En este caso se volvieron a utilizar los cañones de aire comprimido montados en el Buque Oceanográfico Hespérides, siguiendo

una disposición por parejas. El array de cañones alcanzaba los 12 m de longitud y estaban separados 2.5 m entre ellos. En tierra, se desplegaron tanto estaciones de banda ancha como de corto periodo (siempre con sensores de 3 componentes). Una particularidad de este experimento fue que durante el mismo, se trasladaron un 40% de las estaciones a nuevas localizaciones con el objetivo de maximizar el área cubierta. Una vez trasladadas, se realizó una segunda tanda de disparos siguiendo el mismo recorrido que en el primer caso. En total se instalaron 137 estaciones que registraron más de 900.000 señales producidas por los 6.850 disparos de aire comprimido realizados. Todas estas señales fueron revisadas manualmente para seleccionar las llegadas de las ondas P.

El experimento SEA-CALIPSO se realizó en 2007 en la isla de Montserrat (Caribe). Como en casos anteriores se optó por producir las señales sísmicas utilizando cañones de aire comprimido montados sobre un Buque Oceanográfico (RRS James Cook). Los cañones tenían una capacidad de 42.6 litros y dispararon 4.413 veces. Se desplegó una red sísmica de 238 estaciones en tierra y 10 OBSs (Voight et al., 2014). Se registraron cerca de 115.000 señales sísmicas de alta calidad que fueron utilizadas para calcular el modelo de velocidad en 3-D bajo la isla de Monserrat Paulato et al., 2010; Shalev et al., 2010).

El volcán Tongariro en Nueva Zelanda fue objeto de un experimento sísmico en 2012 en el que se utilizó como fuente sísmica el impacto de 11 masas liberadas desde un helicóptero (Jolly et al., 2014). En este experimento se instalaron 4 estaciones sísmicas que registraron las señales producidas por los impactos a distancias cercanas a los 10 km con frecuencias de entre 3 y 12 Hz. Este experimento tenía como objetico comparar las fuentes de sísmica activa con datos de sismicidad natural y poder discriminar la evolución de actividad superficial compleja mediante nuevos métodos de correlación y localización de fuentes.

En 2006 tuvo lugar en Stromboli un experimento utilizando nuevamente cañones de aire comprimido. Para registrar las señales sísmicas se instalaron un total de 33 estaciones en tierra y 10 OBSs (Marsella et al., 2007; Castellano et al., 2008; Prudencio et al., 2015c). El Buque Oceanográfico Urania llevó incorporado un array de 4 cañones de aire comprimido que dispararon con una potencia máxima de 840 inches^3. En total se

generaron más de 1.500 fuentes sísmicas siguiendo una serie de perfiles radiales y circunferencias respecto al centro de la isla. Se disparó a intervalos de 2 minutos separando las fuentes aproximadamente 250 m entre ellas.

Uno de los volcanes más famosos, Mt. St. Helens (EE.UU), fue objeto de estudio mediante un complejo proyecto internacional involucrando fuentes pasivas, activas, estudios de magnetotelúrica, análisis geológicos y geoquímicos, etc. (Kiser et al., 2013; Levander et al., 2015). Una red sísmica de 70 estaciones de banda ancha registró la sismicidad natural desde 2014 hasta principios de 2016. Un experimento de sísmica activa iMUSH, se realizó a mediados de 2014 utilizando como fuentes sísmica explosiones químicas de 454 y 908 kg, que fueron registradas por una densa red sísmica temporal de 3.500 sensores de corto periodo. Dichos sensores se desplegaron formando arrays que fueron desplazados durante el experimento para cubrir un área mayor. Uno de los principales objetivos de este experimento, del cual no hay publicaciones disponibles en el momento de escribir esta Tesis Doctoral, es la obtención de un modelo de velocidad tomográfico que incluya eventos VT, sismicidad regional y las explosiones químicas como fuentes sísmicas.

Por último, incluso el volcán Erebus en el continente Antártico ha sido estudiado usando tomografía sísmica activa en 2008-09. Zandomeneghi et al., (2010,2013) invirtieron los datos provistos por 12 explosiones químicas registradas por 91 estaciones sísmicas desplegadas en 16 km^2 en torno al volcán. La tomografía 3-D resultante permite 'ver' la estructura interna del volcán hasta una profundidad de 600m (Zandomeneghi et al., 2013).

1.2.3. Beneficios de la tomografía sísmica

El resultado de una tomografía sísmica (pasiva o activa) no es el resultado último, sino que da pie a numerosos y no menos importantes estudios acerca de las estructuras y la dinámica volcánicas. Así, la modelo 3D en velocidad resultante permite conocer mejor a estructura interna del volcán, distinguiendo cuerpos de alta velocidad que se relacionan generalmente con cuerpos fríos, densos y/o compactos, frente a cuerpos de baja velocidad que se asocian a volúmenes más fracturados, de menor densidad y/o presencia de fluidos.

Este tipo de anomalías después se interpretan en base al conocimiento geológico y geodinámico de la región.

Además, un modelo de velocidad 3D realista que tenga en cuenta las heterogeneidades laterales es la base para realizar localizaciones de precisión. Dicho estudio es de gran utilidad a la hora de interpreta la dinámica sísmica de la región, permitiendo distinguir entre distintos mecanismos de generación de terremotos como la migración del magma o el emplazamiento del mismo.

Otros trabajos a posteriori permiten mejorar las rutinas de alerta temprana estableciendo mapas de peligrosidad y susceptibilidad en base a la interpretación de las estructuras volcánicas inferidas a través de los modelos tomográficos. Estos mapas ayudan a establecer protocolos de alerta que sirvan a la Protección Civil para mejorar los planes de emergencia volcánica del área.

1.2.4. Tomografía Sísmica en el Etna

El volcán Etna, en Sicilia (Italia), es, posiblemente el más activo de Europa y por tanto representa un caso tipo de estudio. Conocido mundialmente, se considera un volcán laboratorio debido a la gran vigilancia a la que está sometido, su accesibilidad y a su casi continua actividad. Es el volcán activo más monitorizado del mundo, incluyendo un gran número de disciplinas que van desde la geoquímica, vulcanología y petrología hasta ramas geofísicas como geodesia, gravimetría o sismología. Se caracteriza por una actividad frecuente de tipo generalmente stromboliano con coladas lávicas y algunos episodios más explosivos. En los últimos 16 años el volcán ha sufrido un aumento considerable de la frecuencia de las manifestaciones eruptivas. Algunos de los episodios más significativos durante este último siglo son las erupciones de 2001, 2002-03, 2008 y 2015.

Además, el Etna representa un caso ideal desde el punto de vista del interés y la repercusión social, ya que numerosas poblaciones se encuentran en los alrededores del edificio volcánico que permiten estudiar la ya comentada relación volcán-hombre y la adaptación del ser humano a un ambiente volcánico activo. De hecho, muchas de las erupciones pasadas han tenido ya graves repercusiones en las poblaciones adyacentes por lo que es un caso tipo para poner en práctica estrategias de predicción, prevención y

mitigación del riesgo volcánico. Otra de las grandes ventajas que presenta el estudio de un volcán como el Etna es la potencial exportación de los resultados a otras regiones volcánicas ya sean más o menos activas.

Por estos motivos, se han realizado numerosas tomografías sísmicas en el Etna, tratando de inferir la estructura interna del volcán, así como su sistema de alimentación. La sismicidad asociada a la dinámica del volcán aun siendo alta no alcanza niveles suficientes (salvo episodios concretos (Patanè et al., 2006) para realizar 'snapshots' tomográficos de un período corto de tiempo. Por lo general, las tomografías realizadas en el Etna utilizan bases de datos recogidas durante varios años con el fin de tener un número de eventos suficientemente significativo. Desde que se instalara la primera red sísmica en Etna a mediados de los 70, han sido numerosos los estudios sismológicos realizados en este volcán (Tabla 1.1). Uno de los primeros estudios cuya intención era conocer la estructura interior de Sicilia, involucrando al Etna, se hizo en 1968, cuando aún no se había descrito la tomografía como tal. Se realizaron una seria de perfiles de refracción a lo largo de toda Sicilia. Uno de esos perfiles se localizó justo al norte del volcán y permitió localizar una anomalía de baja velocidad entre 9 y 24 km bajo el mismo (Cassinis et al., 1969).

En 1977 se programó un experimento de sísmica pasiva en el que se instalaron un gran número de sensores sísmicos de 1- y 3-componentes alrededor del Etna (Colombi et al., 1979). Los datos recogidos por dichos sensores sirvieron a Sharp et al., (1980) para obtener una amplia base de datos sobre la que utilizar los tiempos de llegada de las ondas P y S producidas por eventos regionales y telesismos. Este estudio obtuvo como resultado la conocida como primera imagen tomográfica en velocidad del Etna que se caracterizó por una gran anomalía de baja velocidad localizada bajo el volcán a unos 20 km de profundidad y que fue interpretada como una cámara magmática (Figura 1.4).

Active/Passive	N.Stations	N. EQ/N. Shots	N. Phases	Area Covered	Reference
active + passive	36	14 Regional / 4 onland shots	2,200 (P&S)	60 x 50 x 27 km	(Sharp et al., 1980)
active + passive	36	160 EQ / ca 24 shots	-	10 x 20 x 10 km	(Hirn et al., 1991)
passive	25	303 EQ	3,000 (P)	45 x 45 x 20 km	(Cardaci et al., 1993)
active + passive	-	-	-	25 x 25 x 7 km	(Hirn et al., 1997)
passive	46	1249 EQ	9,564 P and 4,535 S	45 x 45 x 10 km	(De Luca et al., 1997)
passive	29	521 EQ	4,000 P	50 x 50 x 15 km	(Villasenor et al., 1998)
active	800	-	-	20 x 20 x 3 km	(Laigle et al., 1999)
passive	35	156 EQ	2,130 P and 1,189 S	25x 25 x 10 km	(Laigle et al., 2000)
passive	48	307 EQ	4,191 P and 1,189 S	40 x 40 x 18 km	(Chiarabba et al., 2000)
passive	25	286 EQ	-	20 x 20 x 3 km	(Patane et al., 2002)
passive	246	1194 EQ	8,604 P and 1,900 S	30 x 30 x 15 km	(Aloisi et al., 2002)
passive	47	488	7,062 P and 652 S	20 x 20 x 20 km	(Chiarabba et al., 2004)
passive	45	712 EQ	8,587 P and 2,293 S	30 x 30 x 5 km	(Patane et al., 2006)
passive	50	329 EQ	4,183 P and 980 S	60 x 60 x 5 km	(Monteiller et al ., 2009)
passive	37	336 EQ	5,285 P and 1,313 S	30 x 30 x 10 km	(Alparone et al., 2012)

Table 1.1 *Seismic Tomograhies performed at Mt. Etna.*

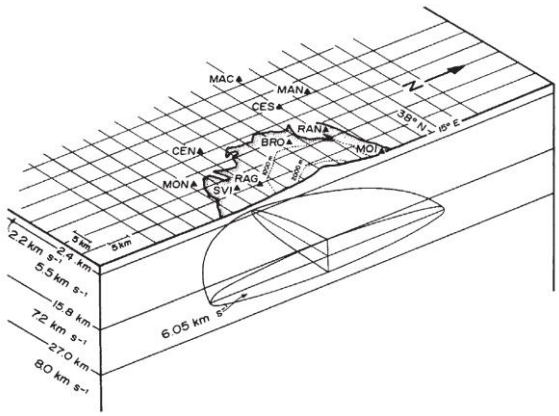

Fig. 2 Cut-away diagram of the crustal model and low velocity anomaly beneath Etna. Crustal layer velocities and depths are indicated. The ellipsoidal anomaly is shown centred beneath the volcano in the 7.2 km s^{-1} layer.

Figura 1.4. *Esquema tomográfico de la estructura en velocidad del Etna (Sharp et al., 1980)*

En 1984 tuvo lugar en Sicilia el experimento "GEOTRAVERSE EUROPEA" que consistió en una serie de disparos en tierra y mar a lo largo de 4 perfiles. A pesar de que dicho experimento no se centraba en el Etna, uno de los perfiles pasó cerca y los datos de las explosiones fueron registrados por las estaciones sísmicas del volcán y utilizados por Hirn et al., (1991) para invertir la estructura en velocidad del Etna. En total se registraron 2200 llegadas de onda P que se invirtieron para los primeros 6 km de profundidad bajo el volcán y que permitieron iluminar por primera vez un cuerpo de alta velocidad bajo el SE del Etna, conocido como "High Velocity Body" (HVB de aquí en adelante).

Pocos años más tarde Cardaci et al., (1993) utilizaron una base de datos de 303 terremotos con sus respectivas 3000 llegadas de onda P para invertir y obtener la estructura en velocidad del Etna llegando a cubrir un área de 45x45 km. Este estudio permitió confirmar la presencia del HVB junto con una anomalía de Bouguer positiva. Además, interpretan como posible cámara magmática una anomalía de baja velocidad localizada al SO del volcán a unos 10 km de profundidad.

El primer experimento de sísmica activa realizado para determinar la estructura del Etna fue el conocido como "ETNASEIS" en 1992. Éste consistió en una serie de disparos de aire comprimido en el mar que serían registrados en estaciones sísmicas instaladas alrededor del Etna. Se utilizaron 8 cañones configurados para disparar en modo

"burbuja única" con una potencia de 840 inches^3 a lo largo de 2 perfiles. En una segunda fase, una segunda nave realizó otros 3 perfiles disparando con 26 cañones y una potencia total de 3810 inches^3. Para finalizar, los últimos 2 perfiles se realizaron con un barco equipado con un array de cañones de aire comprimido de tipo industrial. Los datos obtenidos de este experimento sirvieron a Hirn et al., (1997) para mejorar la tomografía previa de Hirn et al., (1991). Sin embargo, debido a la alta atenuación provocada por la estructura del volcán y a problemas técnicos, los registros de las explosiones en mar no se registraron lo suficientemente bien para poder obtener un modelo fiable de la estructura en velocidad del volcán. Por tanto, el resultado es una pequeña mejora del modelo inicial de Hirn et al., (1991) sobre una malla de 25x 25 km llegando a una profundidad de 15 km.

Ese mismo año, De Luca et al., (1997) proponen una tomografía pasiva del Etna, utilizando 1249 terremotos con sus correspondientes 23000 llegadas de onda P y 10000 de onda S. La inversión en velocidad de dicha base de datos permitió por primera vez sumar a las evidencias ya existentes del HVB y de la anomalía positiva de Bouguer, la presencia de una anomalía con valores de ratio Vp/Vs bajos.

Villaseñor et al., (1998) invirtieron los tiempos de llegada de más de 4000 ondas P originadas por 512 terremotos registrados a lo largo de 12 años utilizando una red sísmica de 29 estaciones. Los principales resultados de dicho estudio son la descripción del ya conocido HVB y la presencia de una zona de baja velocidad con geometría vertical localizada bajo los cráteres centrales, interpretada como posibles conductos magmáticos.

Un pequeño experimento sísmico tuvo lugar en el volcán Etna, en el que se realizaron 7 explosiones en tierra alrededor del volcán. Las señales sísmicas generadas se recibieron en un array de 800 canales con el objetivo de describir y detallar el papel que juega el HVB en la dinámica volcánica. Laigle et al., (1999) interpretan dicha anomalía como un cuerpo magmático al que atribuyen emisiones de gases.

Durante el año 2000 se publicaron 3 estudios tomográficos relacionados con el Etna, cada uno de ellos independiente y con sus propios datos. En primer lugar, Laigle et al., (2000) obtuvieron una mejora de tomografías anteriores al utilizar conjuntamente ondas P y S y poder calcular así el ratio Vp/Vs. Dicho ratio presenta valores bastante

heterogéneos en el área que corresponde al HVB. Los datos fueron registrados por 35 estaciones sísmicas que conformaban la red sísmica del Etna en aquel momento. Por otro lado, Chiarabba et al., (2000) invirtieron las primeras llegadas de ondas P y S de un total de 300 eventos registrados entre 1994 y 1998 en 48 estaciones sísmicas. Ambos estudios centran su interpretación en la descripción del HVB y su importancia en la dinámica eruptiva (Figure 1.5.a). Por último, Nicolich et al., (2000) realizó una serie de perfiles de reflexión en la costa del mar Ionio analizando los datos obtenidos en el experimento ETNASEIS. Los principales resultados se refieren a un perfil de reflexión que va con dirección NE-SO a lo largo de la costa oriental de Sicilia que permiten detectar una serie de fallas principales que controlan la dinámica regional. Sin embargo, estos perfiles no llegan a vislumbrar la estructura del Etna.

Un catálogo de 1194 terremotos registrados durante 13 años sirvió a Aloisi et al., (2002) para invertir los tiempos de llegada de 8600 ondas P y 1900 ondas S. Esta inversión tomográfica pone de manifiesto nuevamente la presencia del HVB, que los autores interpretan como un cuerpo magmático muy resistente formado por un conjunto de cumulitas, diques, etc. No obstante, detectaron otra anomalía de velocidad, en este caso negativa, al sur-oeste del HVB y que se interpreta como posibles conductos magmáticos (Figure 1.5.b).

Durante los últimos 15 años la base de datos sísmica se ha incrementado drásticamente en parte debido a dos grandes erupciones laterales acompañadas de una importante sismicidad superficial (< 5 km b.s.l). Este nuevo catálogo permitió a Patanè et al., (2002) y Patanè et al., (2006) mejorar considerablemente la resolución de las tomografías precedentes en los primeros 7 kilómetros y detallando la parte más superficial del HVB. Patanè et al., (2002) utilizó para la inversión ondas P y S de 286 terremotos de gran calidad registrados durante la erupción lateral de 2001, iluminando la estructura en velocidad del volcán hasta 3 km b.n.m.. Además, por primera vez hasta el momento, se detecta una anomalía con valores bajos de ratio Vp/Vs asociada a la zona de la fractura principal de dicha erupción.

Un año después, Patanè et al., (2003) propone la presencia de un cúmulo de magma localizado a 3 km b.n.m. cerca del límite superior oeste del HVB. Para ello

interpretaron conjuntamente datos tomográficos publicados por Patanè et al., (2002) con datos gravimétricos y geodésicos. Otro avance de este trabajo es la caracterización del HVB hasta una profundidad de 18 km bajo el Valle del Bove y cómo éste se ensancha en profundidad.

Chiarabba et al., (2004) realizan un completa revisión de las tomografías publicadas hasta el momento relacionadas directamente con el volcán Etna. Proponiendo a su vez un modelo interpretativo que explica las principales características del sistema magmático que se pueden deducir de la tomografía sísmica. Estas son el HVB y una serie de cuerpos de baja velocidad alrededor del mismo.

En base a los resultados precedentes y a la importancia de obtener tomografías de un período corto de tiempo, Patanè et al., (2006) estudió las propiedades elásticas de las ondas en el tiempo para detectar intrusiones de magma rico en gas. Para ello tomó como base de datos 700 eventos registrados durante las erupciones de 2001 y 2003 (Figura 1.5.c). Invirtió las llegadas de ondas P y S en una serie de inversiones tomográficas que conforman la tomografía 4D, es decir, cómo varía la estructura en velocidad con el tiempo. Se detectó la presencia de una fuerte anomalía en el ratio Vp/Vs que incrementaba su valor durante la erupción.

En 2009, se realizó una tomografía sísmica utilizando un método preliminar basado en dobles diferencias (Monteiller et al., 2009). Estos resultados detectaron un anillo de baja velocidad alrededor del HVB que interpretaron como posible región con fusión parcial de material.

La tomografía sísmica en velocidad más reciente publicada en el Etna es la realizada por Alparone et al., (2012). Estos autores complementan la tomografía en velocidad con la atenuación sísmica y detectan la presencia de zonas con Vp (≈4.5km/s) y bajo ratio Vp/Vs (≈1.6) que se solapa con una región de bajo Qp (≈30)(atenuación de onda P). Esta región, localizada sobre el HVB se interpretó como un cuerpo magmático rico en gas (Figure 1.5.d).

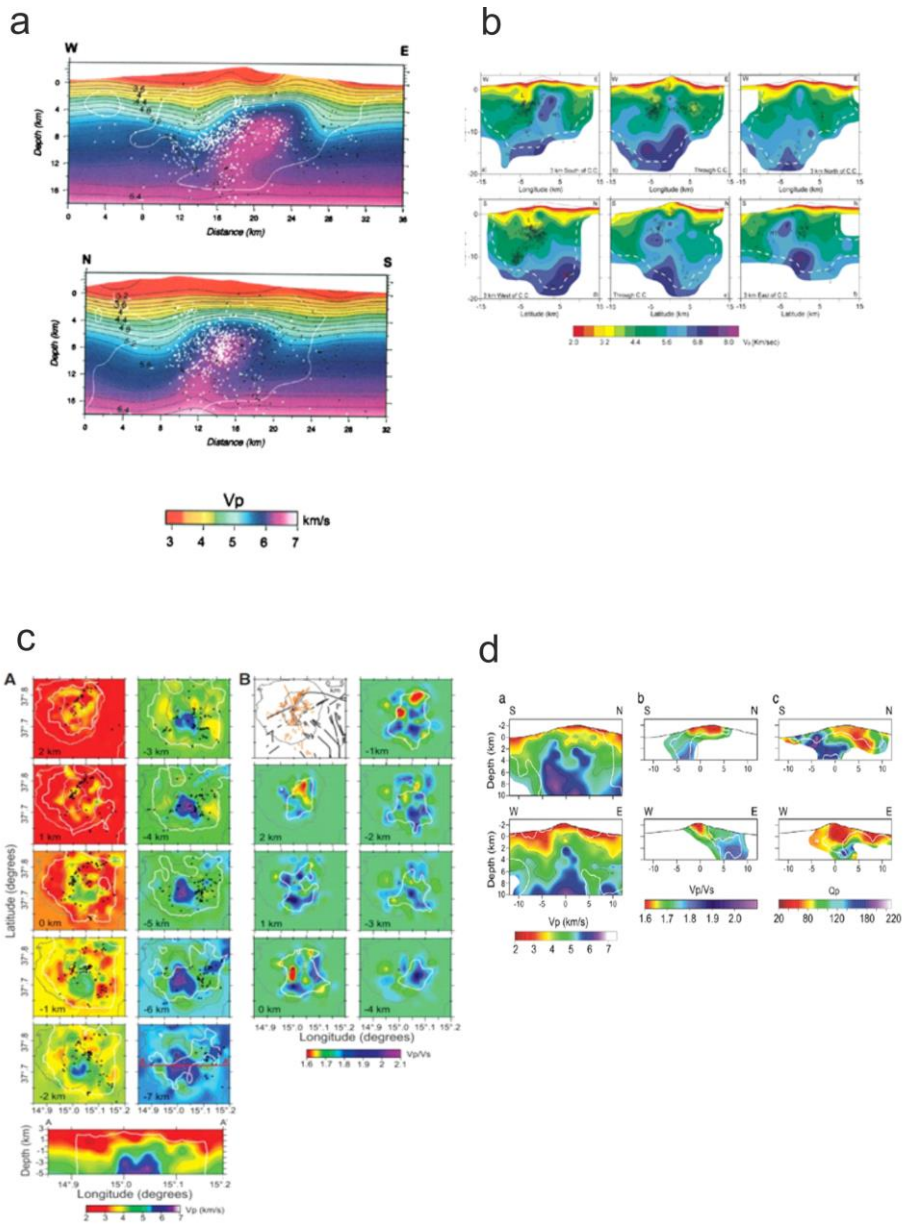

Figura 1.5. *Resultados más recientes de las tomografías realizadas en el Etna: a) de Chiarabba et al., (2000); b) de Aloisi et al., (2002); c) de Patanè et al., (2006); d) de Alparone et al., (2012).*

1.3. Experimento TOMO-ETNA

La necesidad de mejorar el conocimiento que se tiene hasta la fecha de la estructura interna de los volcanes nos ha llevado a centrarnos en los estudios tomográficos, a partir de los cuáles nos hemos dado cuenta de la importancia de tener una buena distribución de datos sísmicos de alta calidad y una red sísmica densa. Estos factores no están siempre presentes en todos los volcanes, y es a partir de dos experimentos sísmicos activos realizados en el Vesubio (Gasparini, 1998; Auger et al., 2001) y en Campi Flegrei (Zollo et al., 2003) cuando nuestro grupo de investigación comenzó a preparar experimentos similares en otros volcanes del mundo. El experimento TOMO-DEC en Isla Decepción (Archipiélago de las Shetland del Sur, Antártida) se llevó a cabo durante la campaña 2004-2005 (e.g. Barclay et al., 2009; Ben-Zvi et al., 2009; Zandomenghi et al., 2009; García-Yeguas et al., 2011). La calidad y cantidad de datos obtenida, junto con el consorcio internacional que se empezó a crear, nos permitieron afrontar un nuevo experimento sísmico, en este caso, en la isla de Tenerife (Canarias, España). La campaña TOM-TEIDEVS tuvo lugar en 2007 (e.g. Ibáñez et al., 2008; De Barros et al., 2012; García-Yeguas et al., 2012) y fue un experimento de sísmica activa realizado con el objetivo de estudiar la estructura interna del volcán Teide. Dicho volcán había tenido una reactivación sísmica en 2004 y por tanto representó una oportunidad única para estudiar dicha reactivación y su estructura interna. Ese mismo año se realizó otro experimento de características similares en la isla de Stromboli (Castellano et al., 2008; Prudencio et al., 2015c).

Los resultados obtenidos en los distintos experimentos pusieron de manifiesto la importancia de utilizar fuentes de sísmica activa para complementar la información proporcionada por los terremotos, ya que en muchos de los casos ya mencionados la tasa de sismicidad es bastante baja. Por ello, cuando se puso en marcha el proyecto europeo MED-SUV, nació la posibilidad de realizar un ambicioso experimento de sísmica activa centrado tanto en el Etna como en las regiones adyacentes y estructuralmente relacionadas (Ver Capítulo 3). Bajo este marco, se desarrolló el experimento TOMO-ETNA, con la idea de complementar el catálogo de sísmica pasiva ya existente, permitiéndonos mejorar la cobertura espacial de las tomografías previamente descritas. El

experimento se diseñó integrando actividades marinas y terrestres y realizando estudios de Sísmica de Refracción (WAS), sísmica de reflexión multi-canal (MCS), perfiles magnéticos e incluso inmersiones con un vehículo no tripulado (ROV). La complejidad de este experimento, realizado entre Junio y Septiembre de 2014, se ve reflejada en los proyectos que la financiaron (MED-SUV, EUROFLEETS2, COCSABO) y la cantidad de instituciones que colaboraron para llevarlo a cabo (Ver Anexos 1-4). Además, el experimento contó con la participación activa de varios buques: El Buque de Investigación Oceanográfica (BIO) español "Sarmiento de Gamboa"; el Buque Hidro-Oceanográfico italiano "Galatea"; y el BIO griego "AEGEO", junto al apoyo de dos naves de la Marina Italiana. En total 26 instituciones académicas y de investigación de: Italia, España, Alemania, Irlanda, EE.UU, Rusia, Francia, Grecia y México estuvieron activamente involucradas en TOMO-ETNA (Para más información acerca del experimento ver Capítulo 3 y Anexos 1-4).

1.4. Localización de Precisión y Fracturación Hidráulica

No obstante, los potenciales resultados derivados de este experimento, y de cualquier tomografía sísmica, no se quedan solo en la estructura 3D en velocidad del volcán. El siguiente paso natural es aprovechar este nuevo modelo 3D más realista para realizar una relocalización de la sismicidad registrada en la región y así definir posibles zonas sismogenéticas y su posible interpretación. En este sentido, hasta hace poco se asociaban directamente los terremotos volcánicos a la presencia de magma (Waite, 2002; Walter et al., 2007). Sin embargo, estudios recientes descritos en el capítulo 7 de esta tesis demuestran que la sismicidad volcánica puede estar también ligada a procesos de fracturación hidráulica y migración de esfuerzos (Díaz-Moreno et al., 2015). A la luz de estos resultados, se podrán explicar e reinterpretar muchos enjambres sísmicos que hasta la fecha se consideraban causados únicamente por la migración del magma.

1.5. Motivación

En esta tesis, se presenta un estudio en detalle de la estructura interna en velocidad del volcán Etna y las regiones circundantes, incluyendo otro complejo volcánico de gran importancia como son las Islas Eolias. Para ello se ha realizado el que probablemente sea uno de los experimentos de sísmica activa en volcanes más complejo,

costoso y completo del mundo. Dicho experimento nos permitió obtener una gran base de datos de señales sísmicas de alta calidad que han sido procesadas utilizando uno de los más novedosos y robustos algoritmos de análisis de llegadas de ondas sísmicas basado en el análisis espectral de las señales. El tiempo de llegada de las ondas P detectadas tanto de las fuentes activas como de los terremotos, han sido invertidas conjuntamente en un nuevo software desarrollado ad-hoc para la inversión tomográfica conjunta de datos de sísmica pasiva y activa. Por último, esta tesis no muestra la obtención de la tomografía sísmica como un resultado finalista, sino que proponemos una serie de estudios posteriores de relocalización sísmica y análisis de curvas de difusividad que permiten mejorar el conocimiento de la dinámica sísmica en regiones volcánica. Para ello, se muestra un caso de estudio en la Isla de El Hierro, aprovechando la crisis sismo-volcánica que tuvo lugar entre 2011 y 2013. Se ha elegido esta región debido a la alta concentración de enjambres sísmicos en un corto periodo de tiempo. Así, realizar un trabajo similar para el Etna, sería objeto de una nueva tesis doctorado debido a la cantidad de enjambres sísmicos ocurridos en los últimos años y que deben ser analizados independientemente y en profundidad. Aun así hemos llevado a cabo una primera aproximación de dicho análisis utilizando datos correspondientes a un enjambre sísmico de 2002-03. Una correcta interpretación de los resultados permitiría relacionar los enjambres sísmicos con la migración de magma o con la migración de estrés debido a la inyección de fluidos.

1.6. Objetivos

Los objetivos de esta Tesis Doctoral se basan en dos pilares fundamentales:

i) *Obtención de un modelo de velocidad realista y tridimensional de la región que comprende el volcán Mt. Etna, el archipiélago de las Islas Eolias y las áreas circundantes, a partir de la inversión conjunta de datos de sísmica activa y pasiva*: Para la obtención del modelo tomográfico conjunto se han utilizado los datos obtenidos mediante un complejo experimento de sísmica activa y pasiva llamado TOMO-ETNA. Los datos han sido posteriormente analizados y procesados utilizando novedosos algoritmos de procesado de señales (AMPA). Una vez analizados los datos sísmicos se procesan mediante un nuevo

software tomográfico desarrollado ad-hoc para esta Tesis Doctoral. Dicho código se llama Passive Active Ray Tomography Software (PARTOS), y permite la inversión conjunta y simultánea de datos de sísmica activa y pasiva.

ii) ii) *Aplicaciones avanzadas de los modelos de velocidad para el estudio de los mecanismos físicos que controlan la sismicidad en volcanes*: Se resalta un estudio avanzado basado en el cálculo del parámetro *b*, en la localización precisa de terremotos, y en el cálculo de curvas de difusividad para la serie sismo-volcánica de El Hierro 2011-13, a partir de un modelo de velocidad tomográfico tridimensional que permite interpretar de manera novedosa la distribución y evolución de la sismicidad volcánica.

2. Geophysical, Geodinamic and Volcanological framework of Mt. Etna volcano, Eolian Islands and surrounding region

2.1. Mt. Etna volcano

Considered as one of the most active volcanoes in the world, Mt. Etna stands on the eastern coast of Sicily (Italy). It reaches 3,330 m high and has a basal perimeter of about 140 km (Chester et al., 1985) (Figure 2.1a, b, c).

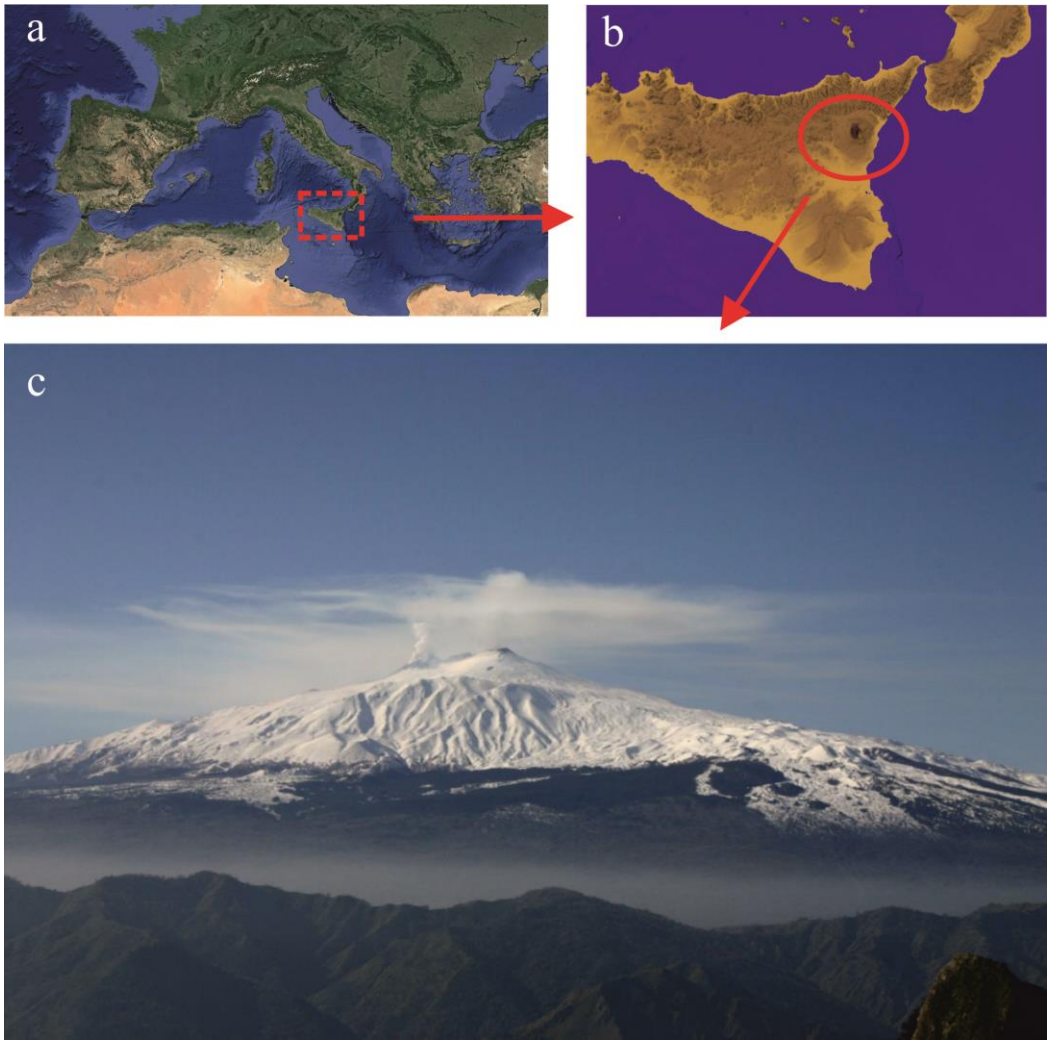

Figure 2.1 *a) Location of Sicily within the European framework; b) Location of Mt. Etna volcano in Sicily (Italy); c) View of Mt. Etna.*

Mt. Etna is a complex strato-volcano that presents several active summit craters. Currently there are 5 main active craters known as Voragine, Bocca Nuova, North East Crater, South East Crater and New South East Crater (hereafter referred to as VOR, BN,

NEC, SEC and NSEC, respectively; Figure 2.2b). Eruptive activity is almost continuous from all this craters, characterized by volatile degassing, explosions, lava fountains and lava flows. Recent lava flows are placed in one of the most important features of the volcano known as "Valle del Bove" (Figure 2.2b). It is a wide depression located on the eastern flank of the volcano (Doglioni et al., 2001). Moreover, additional eruptive fractures are located on the flanks of the volcano and have been the site of very important lateral eruptions (among these, 1991-1993; 2001, 2002-2003 eruption).

The present activity can be defined into two main types:

1) Quasi-continuous degassing activity with occasional strombolian activity. It is related to the summit craters (Cristofolini et al., 1988).

2) Flank eruptions. Effusive type eruptions along great fissures (Cristofolini et al., 1988).

The first type can combine at the same time volatile degassing with hydromagmatic and strombolian eruptions, together with lava fountains and flows. On the other hand, the flank eruptions are always characterized by lava flows and lava fountains. Though, some explosive episodes had also been recorded (Behncke and Neri, 2003a; Andronico et al., 2005).

During the last 50-60 years eruptive frequency at Mt. Etna is very high. It comprises periods of strong but short in time explosive episodes together with longer effusive flank eruptions as defined by Behncke and Neri, (2003b). These authors individuated ca. 200 eruptive episodes since 1970.

On the other hand, magma origin has also varied since the beginning of the 20th Century, ranging from mantle-plume source to island-arc source (Schiano et al. 2001). This change explains the increase of the explosive activity.

Several authors consider lava flows propagation the main volcanic hazard in the Etna area (e.g., Crisci et al., 2004). However, few times lava flows have threatened populations around Mt. Etna, last time was in 1991-93 when the lava flows stopped near the Village of Zafferana Etnea (ZE) (Barberi et al., 1993; Calvari et al., 1994; Calvari and Pinkerton, 1998) (Figure 2.2b). More recent paroxysms (2001 and 2002-03) destroyed tourist facilities at Rifugio Sapienza (RS) and Piano Provenzana (PP) (Figure 2.2b). On

the other hand, phreatomagmatic events, lava fountaining and strombolian activity as expressions of explosive activity should be taken into account as a volcanic risk for the Etna local populations, as suggested by many authors (Dellino and Kyriakopoulos, 2003; Andronico et al., 2005; Scollo et al., 2007). Explosive events, (also present during 2001 and 2002-03 flank eruptions and many other episodes) have historically caused an unusual ash-fall in the surrounding populated areas that affected directly the local population, economy and air traffic (Barnard, 2004; Andronico et al., 2005).

Due to the mentioned persistent activity, this volcano is considered as a "natural laboratory", allowing researchers from all over the world to study the volcanic dynamics from many different points of view (geological, geophysical, geochemical, petrological, etc.). This thesis represents a multidisciplinary study to contribute to the knowledge of the volcanic processes and the crustal structure of the area, including volcano internal structures such as dikes, magmatic reservoirs, etc.

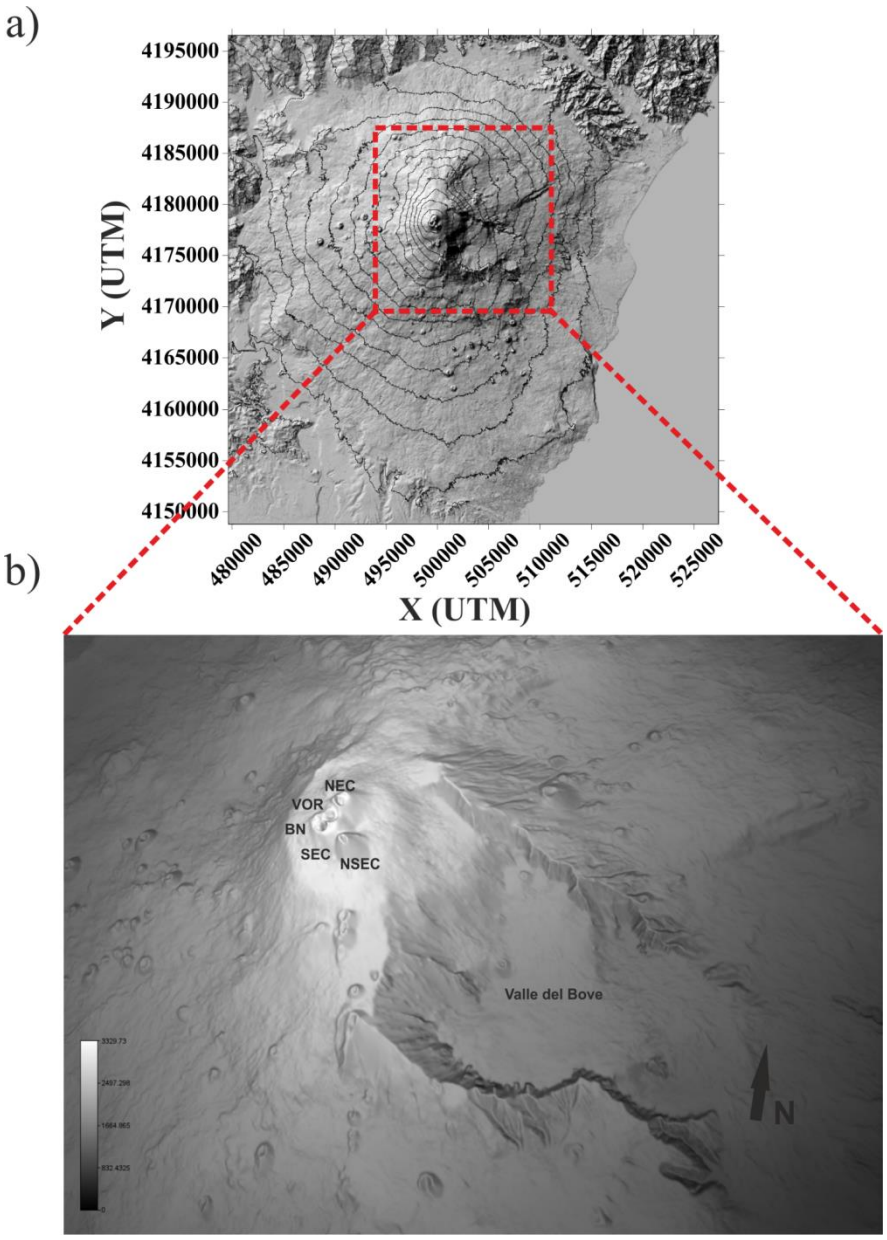

Figure 2.2 a) *Digital Elevation Model (DEM) of Etna area. The squared area (dashed red line) is detailed in b) and reports the location of ZE, PP, RS, NEC, VOR, BN, SEC, NSEC and Valle del Bove (see text).*

2.2. Mt. Etna in the regional framework

The volcano structure is surrounded by 3 main regional structures: i) to the north and westwards we find the Apenninic-Maghrebian Chain; ii) southwards appears the Hyblean Foreland that belongs to the African plate (Lentini et al., 2006); iii) finally to the East stands the Ionian basin, which is an extensional basin originated during middle-late Mesozoic (Catalano et al., 2001) (Figure 2.3). This collisional limit induces a regional N-S compression that is combined with an E-W extension, related to the Malta Escarpment System (Bousquet and Lanzafame, 2004). This extensional regime is located in the eastern part of the volcano. On the other hand, the western part is dominated by the regional compressive regime related to the regional Eurasia-Africa plate collision (Monaco et al., 2005). The Moho appears to vary considerably from 30 km underneath the Hyblean Plateau to 18 km below the Ionian basin (Nicolich et al., 2000, and reference therein). According to this regional description, Mt. Etna's location fits neither typical arc magmatism nor a back-arc spreading region associated with the Apennines subduction (Doglioni et al., 2001, Patanè et al., 2011).

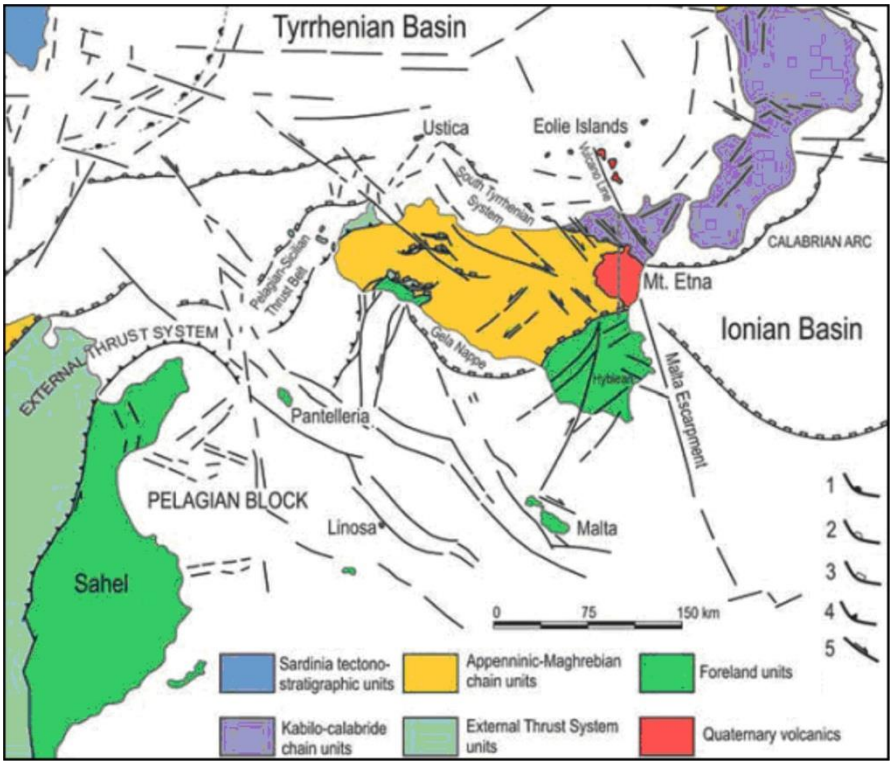

Figure 2.3 *Structural setting of central Mediterranean Sea and location of Mt Etna: 1) Regional overthrust of the Sardinia-Corsica block upon Calabride units; 2) Regional overthrust of the Kabilo-Calabride units upon the Apenninic-Maghrebian chain; 3) External front of the Apenninic-Maghrebian chain upon the Foreland units and the External Thrust System; 4) Thrust front of the External Thrust System; 5) Main normal and strike-slip faults. (Modified from Branca et al., 2011).*

2.3. Geologic Evolution

Recent studies by Branca et al., (2004, 2008, 2011) shed light into the spatial and temporal evolution of Etna volcanic system. These authors describe 4 main volcanic phases according to stratigraphic and geochronological studies (De Beni et al., 2011; Gillot et al., 1994) (Figure 2.4).

The first phase is a period of discontinuous and scattered eruptive activity composed by tholeiitic basalts. It is known as Basal Tholeiitic and took place 500 ka. ago (Corsaro and Pompilio, 2004a; Tanguy et al., 1997) (Figure 2.4a). Subalkaline pillow

lavas, shallow tholeiitic intrusions and hyaloclastic breccias form the geological unit (Branca et al., 2004). The initial sub-aerial stages began around 330 ka. ago and mainly consisted on fissure eruptions forming a thin lava plateau (Branca et al., 2008; De Beni et al., 2011).

The second phase, known as Timpe phase, began around 200 ka. ka. ago. Its activity consisted mostly of fissure eruptions on the Ionian Sea (Figure 2.4b*)*. This volcanism ended up forming a preliminary volcano structure. Its composition changed from a sub-alkaline type of the Basal Tholeiitic phase to an alkaline-Na composition during the Timpe phase (Corsaro and Pompilio, 2004b; Tanguy et al., 1997). Then, the main eruptive mechanism changed from fissure-type to central-type eruptions. This new type of eruptions formed the base of the SW and SE flanks of Etna main structure (Branca & Ferrara, 2013). Valle del Bove phase is the third stage of Mt. Etna's origin (Figure 2.4c). During this stage (about 100 ka.ago) most volcanic vents appeared in the Eastern flank on Etna, which is known as Valle del Bove. De Beni et al., (2011) describe in detail the formation and evolution of several polygenic volcanoes associated with this phase. Lava composition during Valle del Bove stage is mainly hawaiitic to benmoreitic (Guest et al., 1984, Corsaro et Pompilio, 2004a). The main stratovolcano structure of actual Mt. Etna volcano was formed during this phase (Branca et al., 2011; De Beni et al., 2011). The last period is known as Ellittico Crater (Coltelli et al., 2000). It took place ca. 60 ka. ago and finished 15 ka.ago. During this stage the actual structure of Etna was modulated. The main feeding system shifted northwards and westwards (Figure 2.4d). The eruptive processes that took place varied from effusive to explosive activity from both summit craters and flank lateral eruptions. Wide areas of lava flows were formed covering Mt. Etna flanks (Branca and Ferrara, 2013). The end of this stage was characterized by an explosive period (at least 4 plinian-type eruptions). This episode provokes the collapse of the summit craters leading to the formation of the Ellittico caldera.

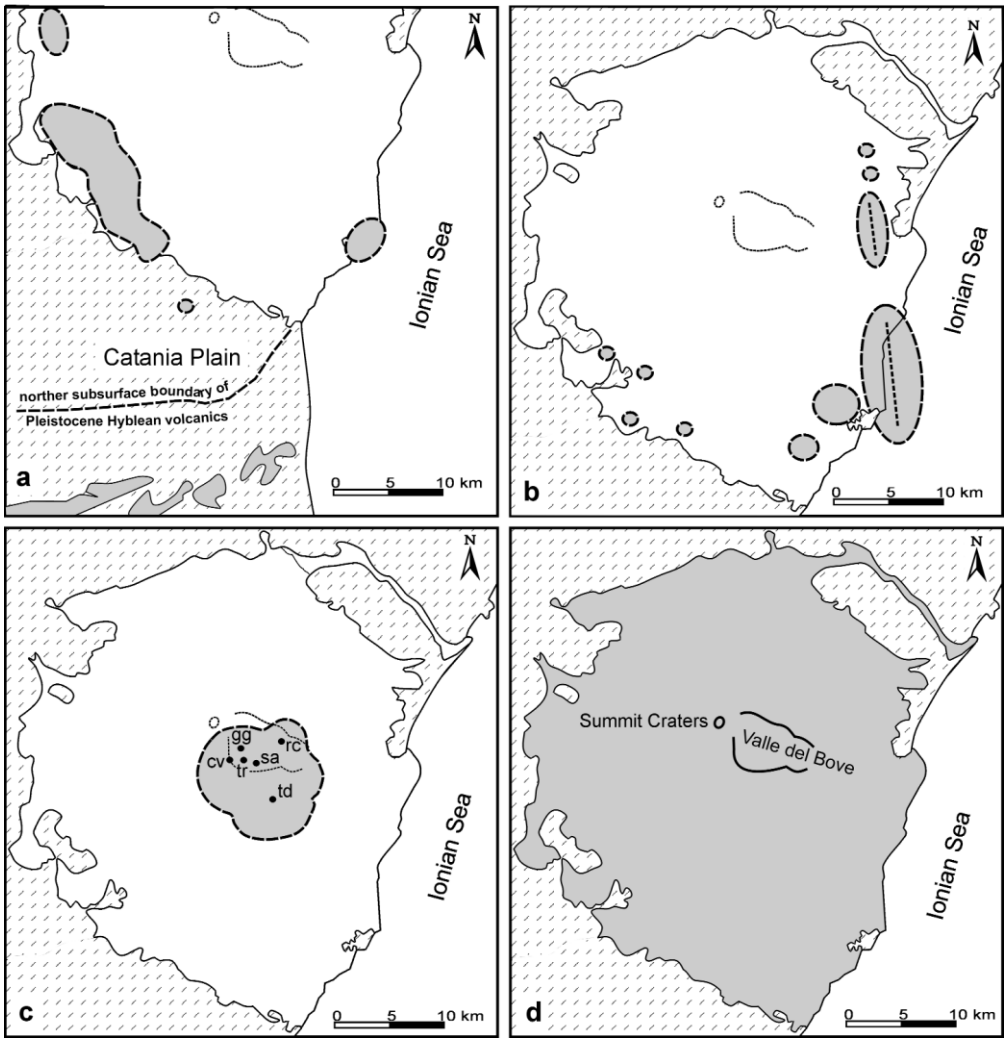

Figure 2.4. *Schematic representation of Etna volcano evolutionary phases: a) Basal Tholeiitic phase; b) Timpe phase; c) Valle del Bove phase; d) Stratovolcano phase. Grey areas indicate the location of the volcanoes. (From Branca et al., 2004).*

This caldera was filled during the following 15 ka. by uncountable effusive eruptions. This area is currently known as Piano del Lago Unit (Calvari et al., 1994). Meanwhile, lateral effusive eruptions continue taking place. The commented effusive activity is responsible of the principal morphological structure of Mt. Etna.

One of the most important settings of the current Etna edifice is Valle del Bove, located in the eastern flank of the volcano. This caldera was formed due to a flank

collapse 10 ka. ago. The collapse involved a part of the main edifice of Etna named Mongibello volcano (Calvari et al., 2004). Mongibello volcano played a major role in the current morphology of Etna. A series of dramatic explosions of this volcano led to the present Cratere del Piano. This occurred during Holocene period (Branca et al., 2011). Nevertheless, the caldera was filled again during a series of effusive eruptions that took place 2 ka. ago. The mentioned activity was responsible of building the main summit cones. That eruptive period had mostly a quite primitive hawaiite composition (Cristofolini et al., 1991). It is also the responsible of building up the present summit craters.

2.4. Major structural features

It is widely thought that fault systems play a major role previous and during volcanic eruptions (Monaco et al., 2005; Neri et al., 2004; Wicks et al., 2011). In the case of Etna, a variety of fault systems are found all around the volcano and reported in the new volcano-tectonic map Azzaro et al., (2012a) (Figure 2.5).

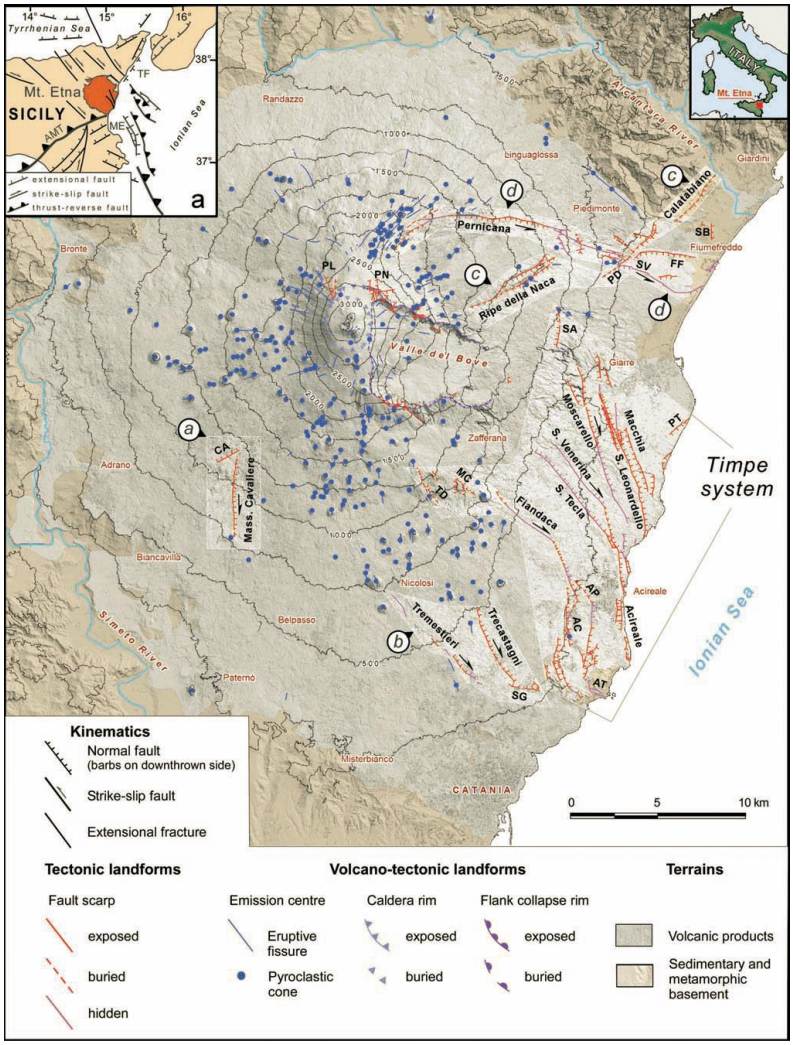

Figure 2.5 *Volcano-tectonic map of Mt. Etna. Fault abbreviations: a, Ragalna system; b, Tremestieri-Trecastagni-S. Gregorio system; c, Ripe della Naca-Piedimonte-Calatabiano system; d, Pernicana system; AC, Acicatena; AP, Aciplatani; AT, Acitrezza; CA, Calcerana; FF, Fiumefreddo; MC, Mt. Cicirello; PD, Piedimonte; PL, Punta Lucia; PN, Pizzi Deneri; PT, Praiola-Torre Archirafi; SA, S. Alfio; SB, Serra S. Biagio; SG, S. Gregorio; SV, S. Venera; TD, Tardaria. Inset map (a) illustrates the major regional tectonic structures (simplified from Lentini et al., 2006; Argnani et al., 2009): AMT, front of the Appennine-Maghrebian thrust belt; ME, Malta Escarpment; TF, supposed Taormina fault (From Azzaro et al., 2012a).*

The following is a description of the main structural system in Etna area according to Monaco et al., (2010) and Azzaro et al., (2012a).

- Ragalna fault system. It is mainly formed by 5 km of N-S normal striking faults generating shallow seismicity up to 2 km b.s.l. (Azzaro et al, 2012a).
- Tremestieri – Trecastagni - S. Gregorio fault system. It is characterized by strike-slip motion accompanied by shallow (1-2 km depth) seismicity (Lo Giudice and Rasà, 1992; Azzaro et al, 2012a). It is located on the south-eastern flank of the volcano and trends NNW-SSE. The largest fault reaches 5 km long.
- Ripe della Naca – Piedimonte - Calatabiano system (Azzaro et al, 2012a). It is a set of 15 km ENE-WSW striking faults. Located on the north-eastern flank of the volcanic edifice, it is thought to form part of a larger system. The northern limit may arrive to the Calabria peninsula, while the south limit may interact with other fault systems near the Valle del Bove region.
- Provenzana – Pernicana fault system (PPFS). It is located in the north-eastern flank of Mt. Etna and it is considered the most active fault system in the area and. This structural system is almost 18 km long and up to 2 cm/y sinistral movements has been measured (Neri et al., 2004; Bonforte et al., 2011). This major fault system is composed of several minor E-W left strike faults.
- Timpe fault system. It is composed of normal faults that dip toward Ionian Sea. It is a 20 km-long belt located on the Eastern lower flank of Mt. Etna. The fault trend changes from SSW.NNE on the northern part to a NNW-SSE on the southern part (Monaco et al., 1995, 1997; Lanzafame et al., 1996; Azzaro, 1999; Azzaro et al., 2012b). This belt is thought to play a major role in the regional dynamics as it is the northern onshore expression of the Malta Escarpment System.
- NE Rift. It is a complex of subparallel fissures striking NE- SW reaching 5 km long (Branca et al., 2003). It is located on the NN-E of the volcanic edifice and it has been involved in many recent eruptive periods.

- N-S fissure system. Placed on the southern flank of the volcano, these fissures that are 2 km long, trend N-S down to Nicolosi village. Along these fractures many monogenetic cones can be observed (Monaco et al., 2005).

The existence of instability phenomena and in particular eastward sliding movements in the eastern flank of Etna is evidenced by a great variety of studies (Gresta et al., 1990, 1997, Bonforte et al., 2009; Solaro et al., 2010, among others). Actually, although the existence of these phenomena is overt, clear information about the presence and location in depth of 'dècollement' surfaces is still lacking. This instable region (Figure 2.6) is limited to the north by the E–W-trending Provenzana – Pernicana Fault System ((b) in figure 2.5) with left-lateral to normal motion (Alparone et al 2013) and, to the SW by the NS Ragalna Fault system with dextral to normal movement ((a) in figure 2.5; Neri et al., 2007). Eastward this area is divided by several NW–SE trending faults (Solaro et al., 2010). Moreover, eruptive activity and flank deformation appear strictly related. On the one hand, magma intrusions may accelerate flank instability (Bonforte and Puglisi, 2003; Neri et al., 2004; Puglisi and Bonforte, 2004), on the other hand the extensional regime due to flank instability is able to facilitate shallow intrusion in the volcano (Neri and Acocella, 2006).

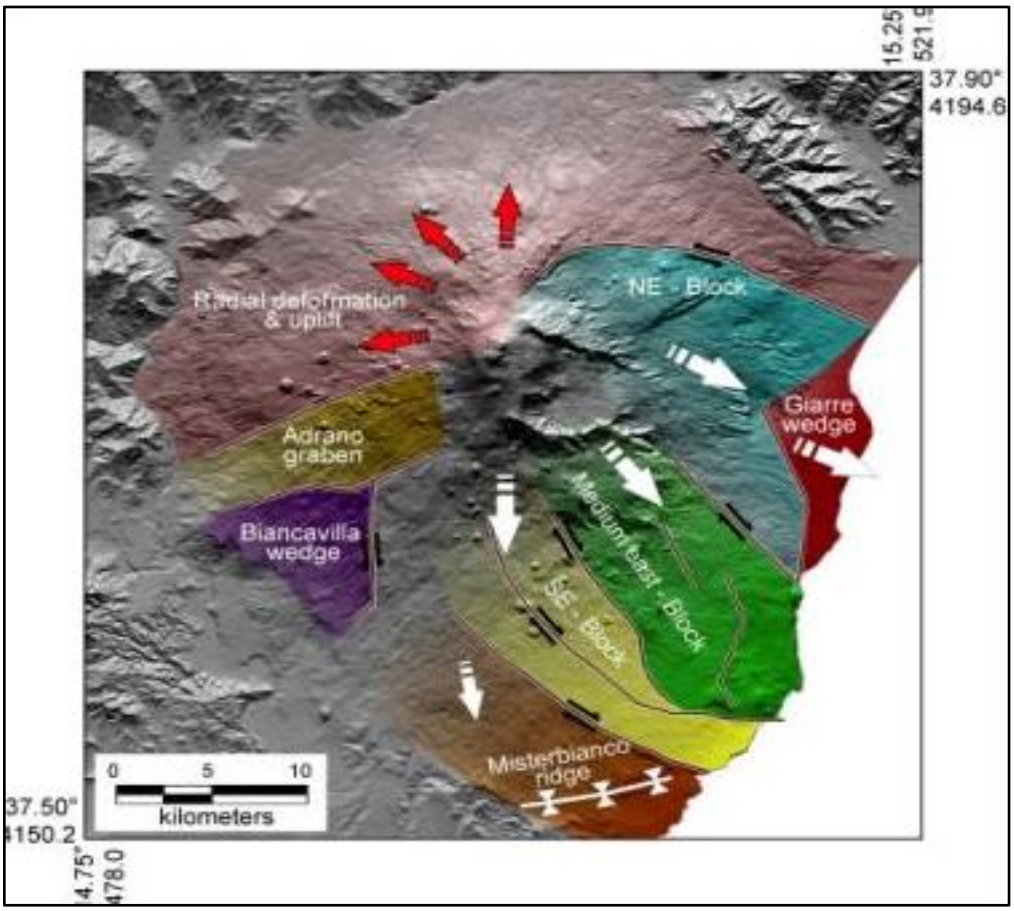

Figure 2.6 *Main kinematic domains of Etna volcano. (From Bonforte et al., 2011).*

2.5. Multidisciplinary monitoring of Mt. Etna volcano

Active volcanoes are very complex geological systems. Therefore, a multidisciplinary approach is mandatory to improve the knowledge of volcano dynamics. Mt. Etna is one of the highly monitored volcanoes in the world. This monitoring includes multidisciplinary networks that range from geochemical to geodetic, gravimetric and seismic among others.

2.5.1 Volcanological Monitoring

Volcanological monitoring at Mt. Etna is performed '24-7' by researchers from Osservatorio Etneo – Sezione di Catania dell'INGV (INGV-OE hereafter). Images from

remote thermal cameras and seismic signals are recovered in real-time to analyse the level of seismicity and volcanic activity, providing the researchers a 'quick view' of the state of the volcano (Figure 2.7). Additionally, periodic 'in-situ' observations are carried out by researchers from INGV-OE to take samples of gases and eventual volcanic products (ashes, bombs, rocks, etc.) at the central craters. These samples are then analysed by Geochemical and Petrology researchers.

Figure 2.7 *Control room managed by INGV-OE for Mt. Etna 24-7 monitoring. (Courtesy of G. Risica).*

2.5.1.1. Geochemistry

Permanent network:

Volcanic gasses are commonly emitted in a volcano either through fumaroles or diffusively along the whole edifice. Sampling techniques can vary from direct sampling at fumaroles or remote sampling comparing the gas composition of the atmosphere with the ash clouds. The gases monitored by the INGV.OE are H_2O, SO_2, CO_2, He and HCL, using a set of 10 geochemistry instruments deployed all around the volcano (Figure 2.8):

a) COSPEC: spectrometer that measures SO2 directly from the ash cloud.

b) UV Scanner and Camera: SO2 flux is measured stablishing evolution models of the gas emissions.

c) FTIR: spectroscopy that uses the infrared signal to analyse the gas composition.

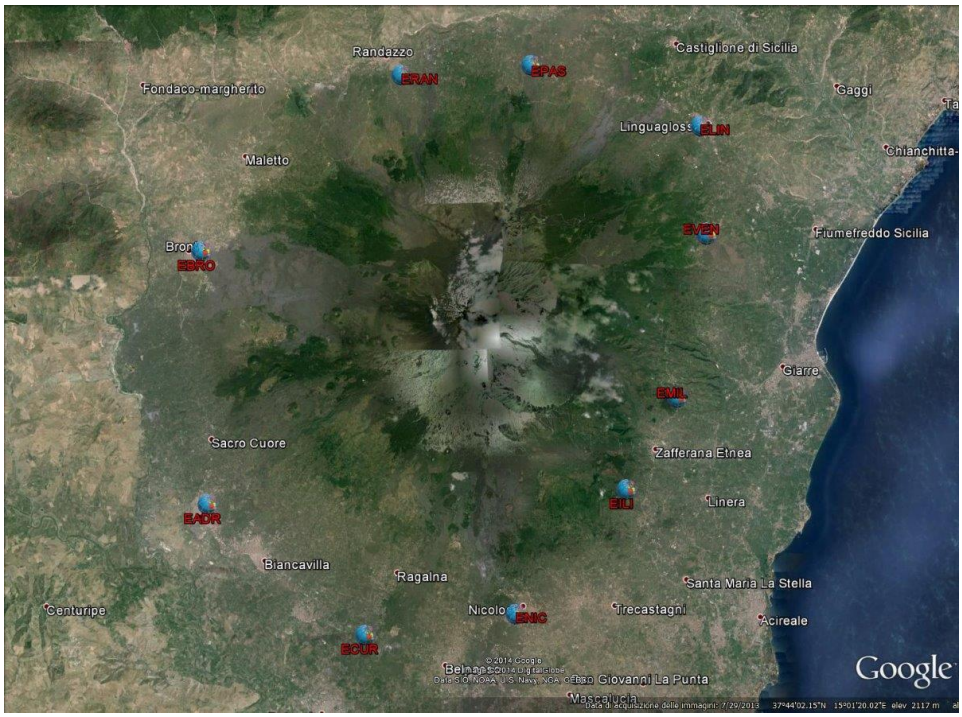

Figure 2.8*. Geochemical Network deployed at Mt. Etna.*

Data analysis and results:

Analysis of the gas emissions gives clues on the magma composition and its origin. Usually, absolute measures may not be as useful as ratios between different gases or isotopes of the same gas (eg. CO_2/SO_2, He^3/He^4) (Padrón et al., 2013). H_2O/CO_2 and the CO_2/SO_2 ratios of the gas emission at Mt. Etna have shown a great variability on the gas composition indicating possible magma mixing (Shinoara et al., 2008). Caracausi et al., (2003a) recently relate the quantity and composition of the He/Ne and He/CO2 emissions with the pressure of the magma storage at Mt. Etna. Some authors have characterized even the potential dimension of the magma chamber basing on the He^3/He^4

ratios arguing that the obtained values reflect also a shallow storage of the magma (Caracausi et al., 2003b).

2.5.1.2. Petrology

On the other hand, petrologic studies do not play a major role on the volcanic 'real-time' monitoring. However, the analysis of volcanic products composition can give important clues about the origin of the magma. Indeed, the mineral composition of a volcanic rock is a key to understand the source of the magma. Different mineral distribution on a rock may tell us different conditions of magma formation. Several theories have been proposed of the magma origin at Mt. Etna (Hoffmann 1988; Armentieri et al 1989, Marty et al 1994; Schiano et al 2001; Tonarini et al 2001) and are summarized in Corsaro & Pompilio (2004). Although technical differences, all the authors hypothesized that should be a main depleted mantle source (Ocean Island Basalts) with some type of lithospheric "contamination". This lithospheric enrichment could be caused by the nearby subduction contribution.

The composition of the etnean lavas have varied in Mt. Etna history from tholeiitic (400 ka) ago to more alkaline rocks (Branca et al 2004, Corsaro & Pompilio 2004c). More recently, from 1970s the chemical composition on Etnean lavas has changed again dramatically showing enrichment on K. Alkaline-Na have changed to alkaline-K composition (Corsaro et al 2009). These changes have been studied by many authors and two main hypotheses have been described: i) Contribution of two or more mantle sources (Cristofolini & Romano 1982, Chester et al 1985, Joron et al 1984,); ii) single mantle source with different rates of partial melting (Tanguy 1978, 1980, Tanguy et al 1997, Busa et al 2002). Heterogeneous mantle ith peridotite veins could be responsible of this change (Tanguy et al 1997).

Eruptions of primary magmas in the volcano are seldom, the most important ones have been 1974, 2001 and 2002-03. These lavas show volatile-rich mafic compositions that are supposed to be formed at depths of around 10 km b.s.l. (Figure 2.9). This primary magma has very high buoyancy and ascends very quickly with high explosivity rates due to its volatile-rich content (Corsaro & Pompilio, 2004c, Spillaert et a.,l 2006; Corsaro et al., 2009).

Moreover, another magmatic reservoir has been inferred due to lava composition. It should be placed at depths of 4-5 km b.s.l. and is responsible of most of the latest eruptions (Figure 2.9). It is a more evolved magma that has been stored for longer time with eventual mixing with the primary magma (Spillaert et al., 2006, Corsaro et al., 2009b; Corsaro et al., 2013). Bubble forming processes takes place in this storage, being the main cause of the eruptive dynamics as the saturation in bubbles of the magma reaches enough pressure to ascend violently.

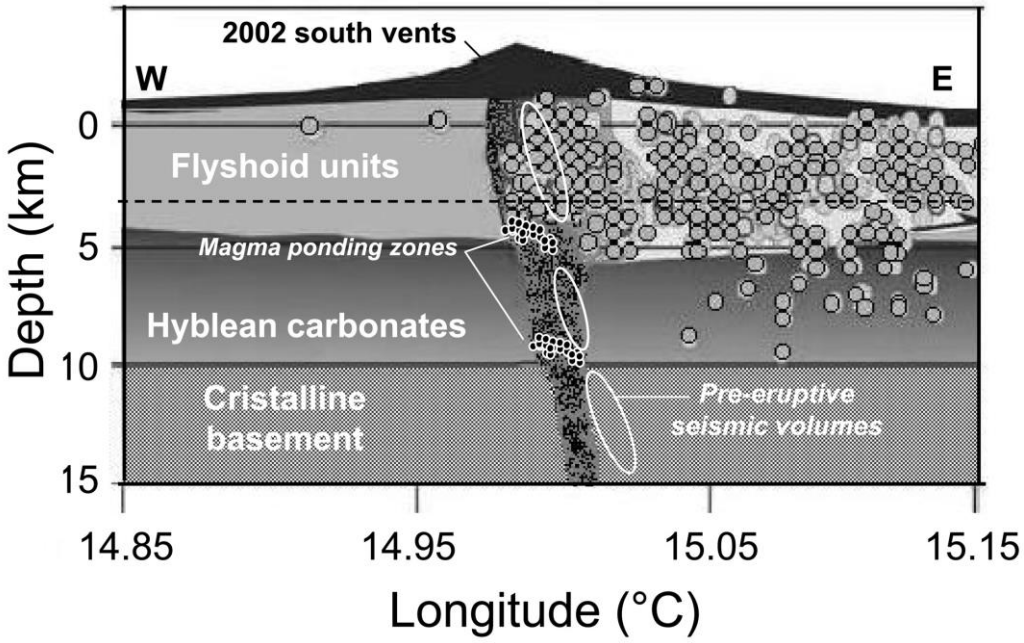

Figure 2.9 *Schematic model of the main magmatic reservoirs described and inferred from a petrographic point of view. (From Spilliaert et al., 2006).*

These disciplines give us information about the composition and origin of the magma. Along the next section we summarize the characteristic of the main and geophysical networks installed on Etna area, the data analysis technique and the most recent results, which are the base of knowledge of the internal structure of the volcano. Merging all these advances we will be able to obtain a general structural and geodynamic model of the volcano.

2.5.2 Geophysical Monitoring

2.5.2.1 Magnetism

The signal registered in a magnetic station is the sum of three main magnetic fields: i) the principal ii) the external and iii) the local field. The principal magnetic field is that originated from the Earth core, while the external field is the one that arrives from the sun. The magnetic local field, the most useful for volcanic monitoring, depends on the local geology and structures. The main variations of this field on a volcano are caused by termomagnetic, piezomagnetic, and electrokinetic anomalies. Termomagnetic anomalies are caused by changes in the temperature of the rocks. Demagnetization appears as the temperature of the rock is increased up to the Temperature of Curie (TC), when it loses its magnetization. Therefore, it remains "invisible" for the magnetic sensors. Remagnetization, on the other hand, occurs when the temperature decrease and the minerals reach temperatures below the TC and getting magnetized. This type of anomaly is very useful when a dyke intrusion takes place as the magnetic anomaly gets larger as it coolest. However, the intrusion itself does not generate a termomagnetic anomaly but a piezomagnetic one, caused by a sudden change in the stress field. Earthquakes, fractures or dyke intrusion may lead to a magnetic anomaly of this type. Therefore, if an ongoing eruption is accompanied by an earthquake swarm, the magnetic anomaly it could be detected. Nonetheless, if the magma rise by an open conduit without fracturing the host rock, no magnetic anomaly is registered until the magma coolest.

Magnetic permanent network:

The magnetic permanent network comprises 16 stations deployed following a N-S profile along the summit craters (Figure 2.10):

1. Scalar (proton) magnetic sensors: measure the intensity of the magnetic field. Usually used for the local campaigns.
2. Vectorial magnetic sensors: measure the intensity and the components of the magnetic field.
3. Magnetotelluric sensors: only one, at the moment it does not work due to technical issues.
4. Geoelectric sensors. Permit the study of the electrocinetic anomalies.

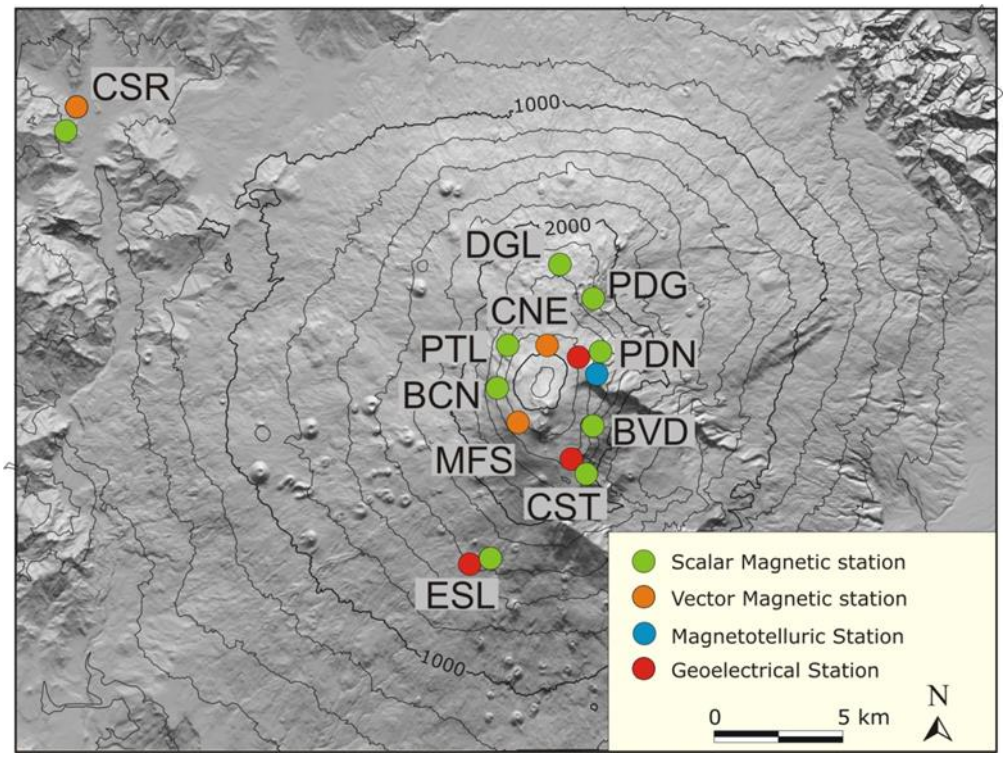

Figure 2.10. *Location map of the magnetic permanent network. Courtesy of R. Napoli.*

Data analysis and results:

Depending on the scope of the analysis we can divide magnetic techniques into: i) aeromagnetism; ii) volcano monitoring; and iii) local research campaigns. Aeromagnetism campaigns are used to obtain the magnetic anomalies on a regional scale (Caracciolo et al., 2014; Nicolosi et al., 2014). This technique allows to deepen more but with lower resolution. Nicolosi et al., (2014) performed an aeromagnetic experiment on Mt. Etna on 2012, succeeding to individuate the volcanic deposits and their limit with the sedimentary basin. The authors interpreted a clay-rich landslide deposit at the base of Mt. Etna, which still moves towards the east. Moreover, Caracciolo et al., (2014) using the same aeromagnetic survey, described the presence of two main trending lineaments (−35°N and 0°N), which they interpreted as the main magnetic anomaly caused by the

regional tectonic stress and contact between the highly magnetized volcanic rocks and the sedimentary basin beneath the volcano. They found that the magnetic signature is not correlated with the topographic structure and at least 3 main magnetic anomalies can be found within the volcanic edifice (Figure 2.11). Indeed, the magnetic NW-SE anomalies they obtained have the same orientation as some major structural features such as the Malta Escarpment.

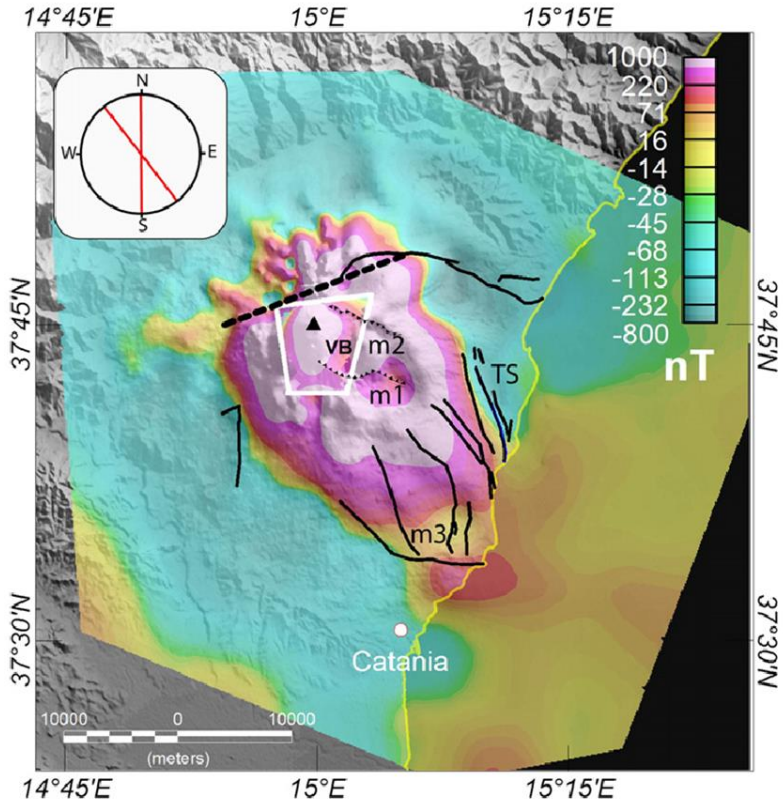

Figure 2.11. *Reduction to the Magnetic Pole (RTP) magnetic anomaly map of Etna province. Black triangle lines define the Valle del Bove (VB) scars; the area enclosed by the white box contains survey B; the black dashed line separates the two different magnetic domains; upper left sketch shows detected Fry analysis structural lineaments; black lines: main tectonic lineaments; TS= Timpe Fault System; m1, m2 and m3: magnetic anomaly areas. (From Caracciolo et al., 2014).*

Volcano monitoring techniques are carried out in real time by the INGV-OE with data sampled every 5s. The permanent stations register the magnetic field including the principal, external and local field. In addition to the stations deployed along the volcanic edifice, one frame station has been installed 20 km away from the volcanic edifice. This station is used to correct the principal and external magnetic fields from the recorded signal in the rest of the stations. In the end, only the local magnetic field registered on the permanent network is analysed. The permanent network installed on the volcano registered some magnetic anomalies during the 2002-03 flank eruption. The anomalies were first visible at PDN station and later registered by the PDG station. Del Negro et al., (2004) analysed these piezomagnetic anomalies and modelled the possible sources. As the anomaly propagated towards the north-east, a series of NE-SW dike intrusions were interpreted.

Magnetic modelling allowed Napoli et al., (2008) to "image" a magmatic intrusion during the 2008 eruption. Piezomagnetic anomalies were registered at different stations of the permanent network during the onset of this eruption. Seismic activity and deformation rates helped to constrain the source that resulted in a NW-SE magmatic intrusion located north-westward from the summit craters (Figure 2.12).

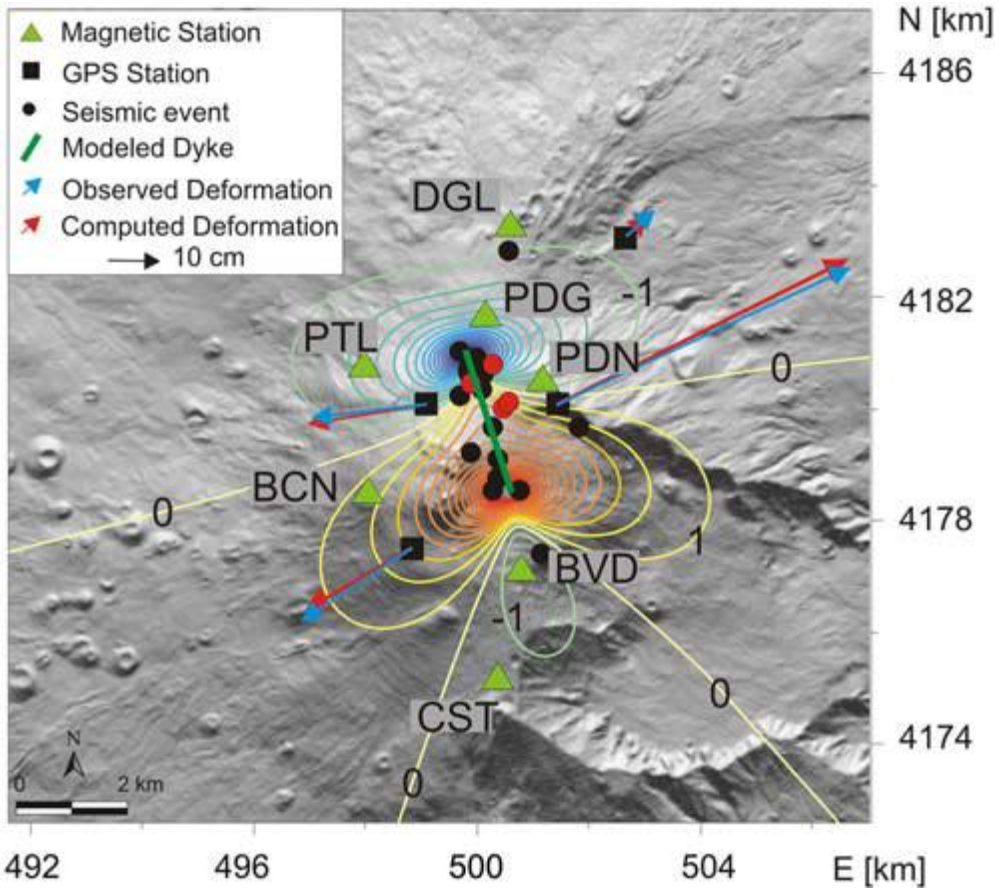

Figure 2.12. *Piezomagnetic anomaly (contour lines at 1 nT) generated by the intrusive dike. Observed (after Puglisi et al., 2008) and computed deformation at the summit permanent GPS stations are also reported. The epicentres of the most energetic seismic events are shown with circles (after Patanè et al., 2008). The red circles are the seismic events in correspondence of the step-like magnetic changes. (From Napoli et al., 2008).*

Local magnetic campaigns are usually carried by INGV-OE and involved small shallow (up to 1 km depth) areas where high resolution is necessary (as shallow dike structures activated during the eruptions (Del Negro et al., 2004). In this case, proton magnetometers are used to register the local magnetic field. Several local experiments have been performed in Etna volcanic edifice (Del Negro & Napoli, 2002; Del Negro et

al., 2002). Del Negro & Napoli, (2002) carried out a magnetic experiment that covered the eastern flank of the volcano, including an offshore area. This study defines a wide volcanoclastic deposit on the eastern flank (Chiancone deposit), interpreted as due to a catastrophic event occurred in the past. Additionally, Del Negro et al., (2002) studied the same region, and observed some highly magnetized materials interpreted as volcanic lavas. These lavas are deposit following a NW-SE orientation, which results to be coherent with Timpe fault system which is considered the onshore expression of the Ibleo-Maltese Escarpment. Indeed, the authors interpret that the Malta Escarpment is the responsible of a highly fractured crust area that has been used by the magma as a preferential path. These volcanic bodies are located offshore and are related to the Hyblean Plateau.

On the other hand, regular magnetic campaigns work on local scale and reach a depth of no more than 1 km. After 1989 eruption an important experiment took place during two years to study and analyse the magnetic signature of an open fracture located on the south-eastern flank. This fracture appeared during the 1989 eruption but no lava emerged from. Nonetheless, two years of magnetic profiles on the same fracture detected an increasing magnetic anomaly that has been interpreted as an aborted dyke (Del Negro, C., & Ferrucci, F., 1998).

2.5.2.2 Gravimetry

Gravity permanent network:

Distributed along two major profiles (W-E and N-S), the gravity network is composed by 71 benchmark for relative measurements and 13 absolute gravimeters (Figure 2.13), distributed in several arrays (Carbone et al., 2003, Greco et al., 2010): i) Main Network deployed as a ring around the summit; ii) Summit Profile deployed following a NE-SW direction crossing the central craters; iii) E-W Profile located slightly southern from the central craters; and iv) Reference network located outside the volcanic edifice. The network is design to obtain both discrete and continuous measurements of the gravimetric field.

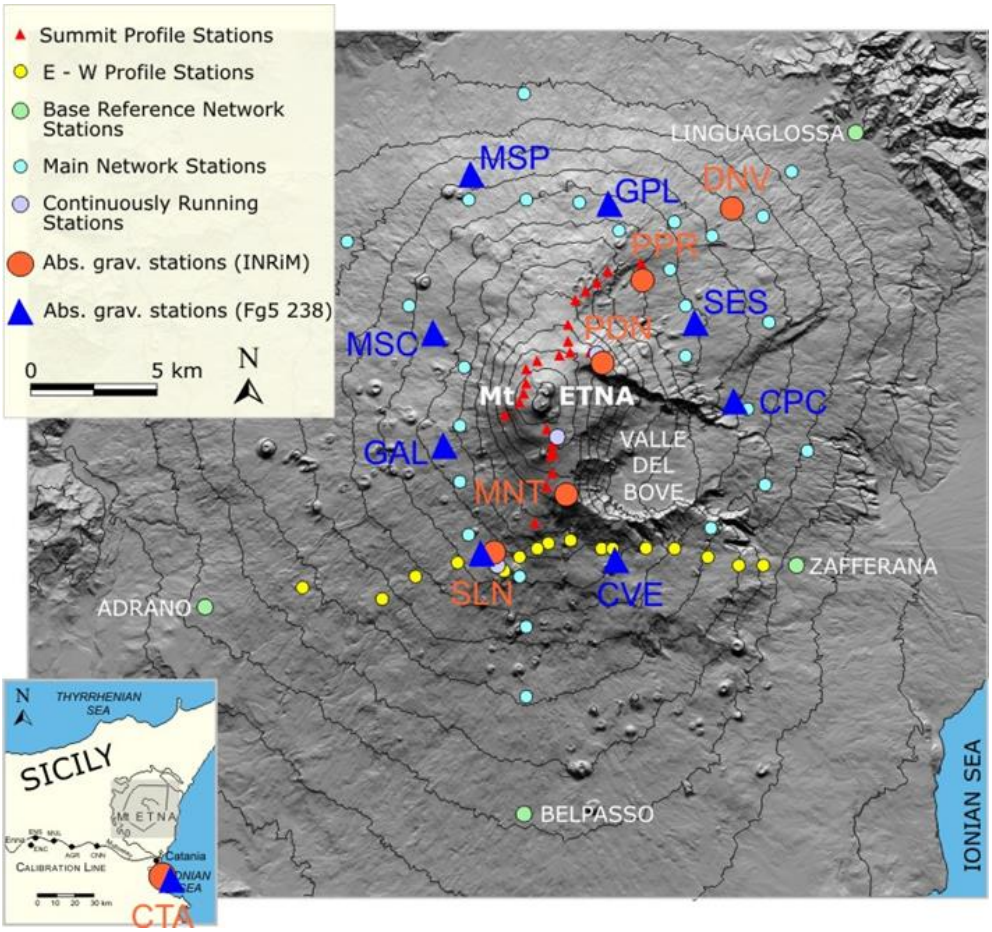

Figure 2.13. *Gravity Network Map. (From Greco et al., 2010).*

-Data analysis and results:

The analysis of the microgravimetric data (±1mGal) is based on the anomalies of the gravimetric values from a theoretical model. Nonetheless, several cases of microgravity changes without any significant deformation have been detected. Many authors have hypothesized the processes responsible of that behaviour (Carbone et al., 2014; Currenti & Williams, 2014). A magma intrusion into void spaces could be one of them (Johnson et al., 2010), but also significant changes on the density of magma bodies could be responsible of the same effect (Battaglia et al., 2008a). Currenti & Williams, (2014) propose and study the role of magma compressibility and source geometry effects

in the microgravity and deformation relationship. On the other hand, Carbone et al., (2014) suggest that microgravity changes without ground deformation could be related with changes in the fracturing rate of the medium. This increase of fracturing may lead to a new magma path.

Usually, both deformation and gravity data are analysed together, as they are in many cases related. Bonaccorso et al., (2011) combined gravimetric and geodetic measurements to analyse a seven-year period before the 2001 eruption. This analysis enlightens a period of intense magmatic recharge characterized by a positive gravimetric anomaly and an overall inflation of the volcanic edifice. An increase in the microgravity values is related to a mass increase underneath the volcano, and is usually interpreted for the case of Mt. Etna as a new magma intrusion or a recharge of the magmatic reservoir. Moreover, gravity and seismology are also complementary techniques as postulated by Carbone et al., (2009), who analysed together gravity and seismic data to model the long term behaviour of the volcano.

2.5.2.3 Geodesy

Geodesy permanent network:

Geodetic Network aims to monitor the deformations on the volcano edifice as well as some important structural systems (among these PPFS, Tremestieri – Trecastagni - S. Gregorio fault system and Timpe fault system) whose activity is considered strictly related to volcano dynamics. This network detects small changes on the surface of the edifice using: i) levelling; ii) clinometry; iii) global positioning system (GPS) and; iv) interferometric synthetic aperture radar (InSAR) techniques (Puglisi et al., 2004).

The deformation network on Mt. Etna exists since the 1980s and during time, it has gradually improved its coverage. From 1980 to 1988 it was composed of a series of EDM stations that were distributed in three areas around the volcano. Since the early 1990s GPS sensors were installed improving dramatically the quantity and quality of the data. Currently ca. 40 GPS stations, together with 13 biaxial electronic tiltmeters and 4 dilatometers are deployed all around the volcano (Figure 2.14). Additionally 80 GPS benchmarks are available to perform local short-term experiments. GPS sensors measure the spatial variations of the benchmark using satellites information sampling every 30 s.

Among other contributions, this daily sampling of the GPS data allows measuring the average site velocity (Palano et al., 2010). The permanent tilt network at Etna is installed in shallow boreholes (Bonaccorso et al., 1999). Precision of the tilt network is around 0.2-0.5 μrad (for shallow sensors) and 0.05 μrad (for depth sensors), including temperature and thermoelastic effects (Bonaccorso et al., 1999). For the tilt network the sampling rate varies from 1 to 10 min. Data is recorded using static, quick-static or kinematic measures. On the other side dilatometers are deployed in boreholes at 300 m depth and measure the ground dilatation.

Currently, the stations are deployed following a series of frame network and subnetworks that allow the study both the whole edifice and small structures (Puglisi et al., 2004):

a- Frame network: a series of stations installed on the surrounding areas of Mt. Etna that form part of a larger regional network. This network registers in static mode.

b- Principal inner network: It is composed by around 18 station covering the edifice from 600 to 2900 m above sea level (a.s.l.). It is connected both to the frame and the gravimetric networks and it is mainly used to monitor the deformation of the whole edifice.

c- East-West Kinematic Profile: ca. 15 stations located along an E-W profile from 600 to 2000 m a.s.l.. Kinematic measures are performed with these sensors.

d- North-South Kinematic Profile: The network is composed by ca. 25 stations located mostly at 2000 m a.s.l.. It monitors the volcanic activity as well as many fractures located on the NE rift (see section 3).

e- "Ionica" Network: Almost 25 geodetic stations deployed all along the Ionian coast of Sicily. The main aim of the network is to monitor the Eastern-flank instability and quantify its movement.

f- "Rocca Campana" Network: A set of 6 sensors are aimed to register movements along the PPFS. This subnetwork is connected to the "Ionica" one, as both the PPFS and the Eastern-flank dynamics are strongly connected.

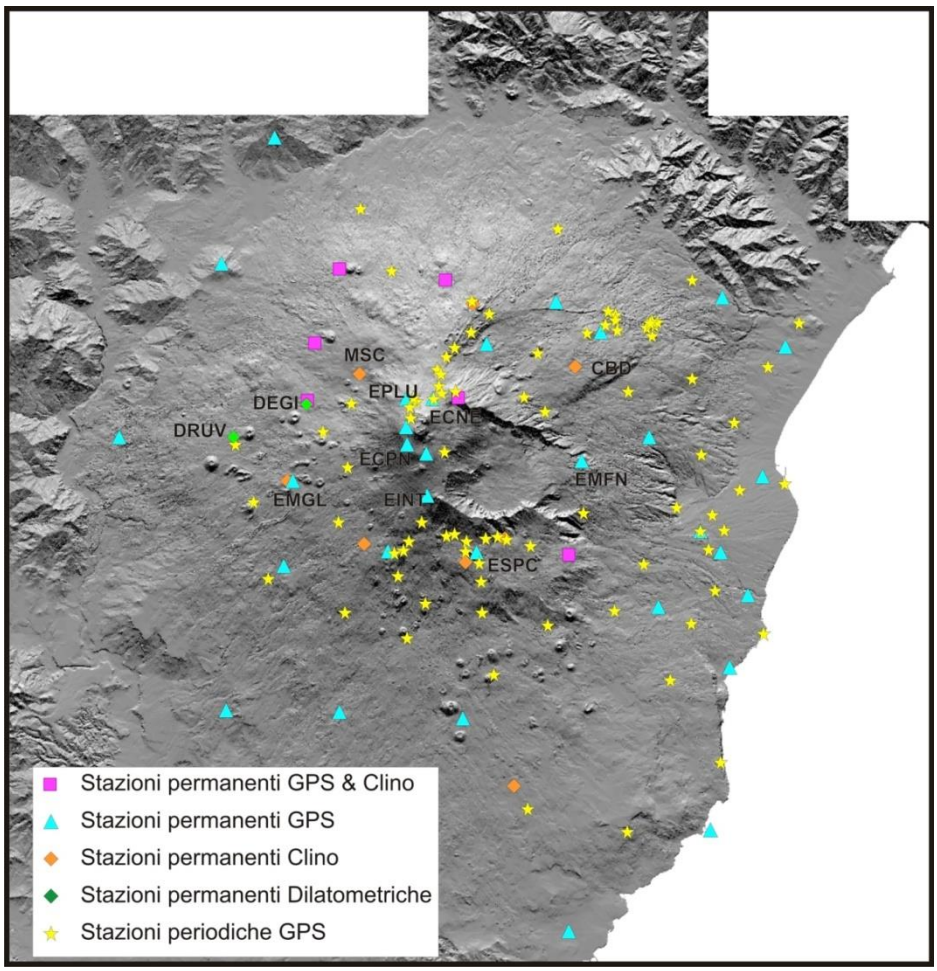

***Figure 2.14**. Geodetic Network Map.*

Data analysis and results:

The main aim of the geodetic analysis is to model the source of the deformation observed. As for other geophysical fields (seismology, magnetism, etc.) this represents solving the inverse problem. This means we know the position of the stations, the observed deformation values and a simple structural model; using these input data the source needs to be imaged. At the present times, the deformation sources can be solved using 3 main simple-geometric models: i) the spherical Mogi model; ii) the spheroidal model; and iii) the Translation model. These models allow to "image" different sources

underneath the volcano in response to the deformation values observed. Geodetic analysis is usually carried out using software packages (eg. AMIT/GLOBK, Herring et al., 2006). The analysis of the deformation parameters registered since 1990s, show periods of inflation and deflation of the volcanic edifice usually interpreted as phases of charge and discharge of the magmatic reservoir (Figure 2.15).

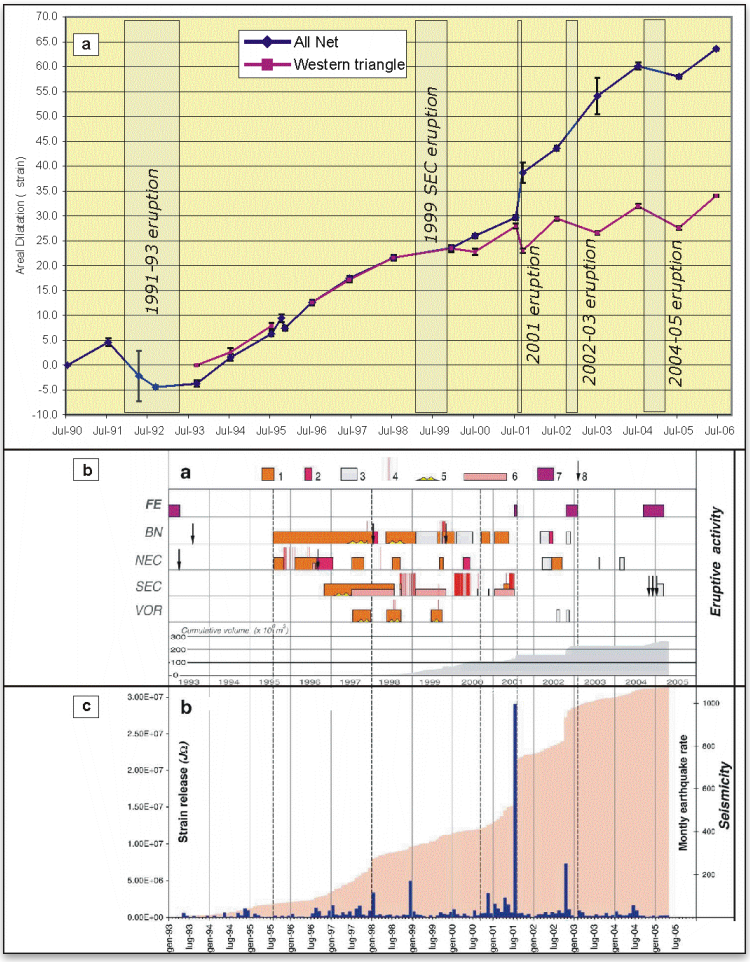

Figure 2.15. *(a) Cumulative areal dilatation measured since 1990, by the GPS network. (b) Correlation of the eruptive activity at the different summit craters and flank eruptions (FE). Lower part of b shows the cumulative eruptive volume. (c) Histogram with the number of earthquakes per month (vertical bars) and cumulative strain release (shaded area). (from Bonforte et al., 2008).*

A series of shallow magmatic bodies such as dykes have been defined by using GPS analysis (Puglisi et al., 2004). The definition of these dykes comprises also their orientation which results crucial in order to assess the risk. Major differences are observed between the North and West flanks and the East and South flanks. These differences include a compressional regime of the North and West flanks and an extensional behaviour in the East and South flanks (Bonforte & Puglisi, 2006). Moreover, a movement toward E-SE of the Eastern flank is well characterized by the GPS data analysis. Quantitative measures of these displacements have been carried out reaching almost 30 mm/year of sinistral displacement on the PPFS (Palano et al., 2008, 2010). This complex deformation framework leads to a multisource modelling that includes a spherical source located at around 3-5 km depth, together with a series of spheroidal shallow sources (from 1km b.s.l. to 2 km a.s.l.) as the volcanic sources (Bonforte et al., 2009, 2013). Tectonic sources are related to the eastern and southern flank instability and are modelled as 2 translational sources located at 0.5 km depth for the eastern flank and 2-3 km depth to the southern flank. Bonaccorso et al., (2013) proposed a series of volcanic and tectonic sources modelled using geodetic data to explain the relationship between the eruptive active and the Eastern Flank instability at MT. Etna (Figure 2.16).

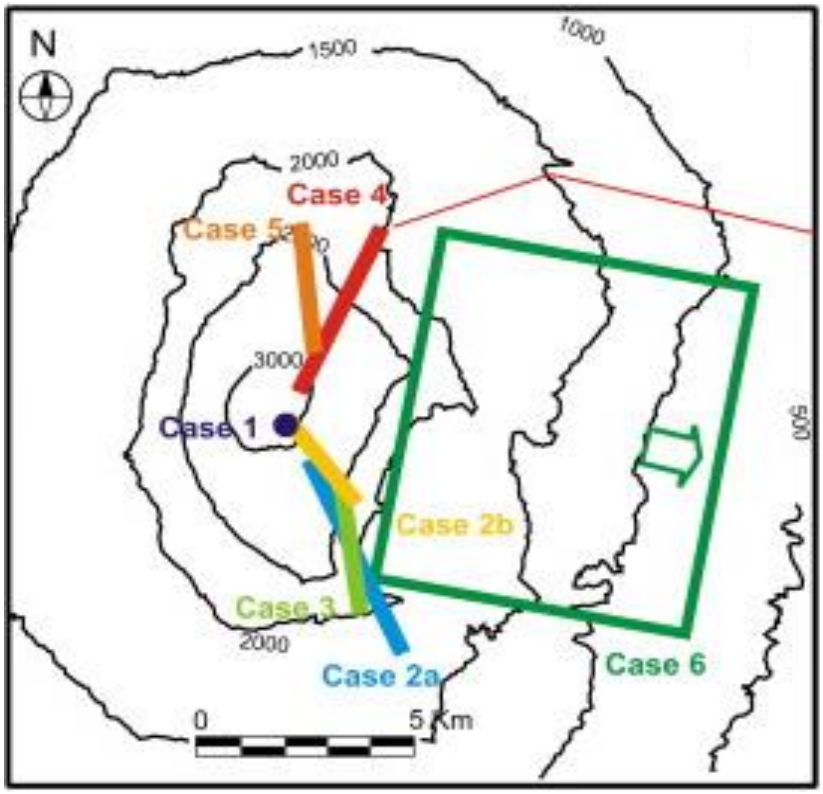

***Figure 2.16**. Sources Modelled to describe volcanic-tectonic relationship at Mt. Etna from 1980 to 2010. Cases 1to 5 are related to volcanic activity and case 6 is related to the tectonic flank instability (From Bonaccorso et al., 2013).*

Many recent studies put together several disciplines as geodesy, seismology and gravimetry. These geophysical data are related and often common patterns can be described. Especially microgravimetry and ground deformation are usually related, with some exceptions (see gravimetry section).

When seismology and deformation are combined, interesting results come out. Gonzalez et al., (2013) studied the relationship of a clear change in the deformation pattern and a seismic swarm occurred in April 2001. They interpreted that the stress released by a seismic swarm may provoke a drastic reduction of the inflation pattern.

2.5.2.4. Seismology

Seismic Permanent Network:

For the purpose of this work, the most interesting monitoring network is the seismic one, which will be described in the following paragraphs.

The seismic permanent network managed by INGV-OE currently consists of 93 stations located in an area between the Aeolian Archipelago and Hyblean Plateau (Figure 2.17) including the Etna area where the 50% of them are installed. On Etna area 13 broadband stations are placed near the summit craters, equipped with 3 component Nanometrics Trillium sensors. They register with a sample frequency of 100 Hz by a Nanometrics Trident Digital System. The seismic network has been enhanced since 2003 and its present configuration is described on several papers (e.g., Patanè et al., 1999; Patanè et al., 2004). This network transmits the data via satellite or radio to the INGV-OE headquarter (Figure 2.7).

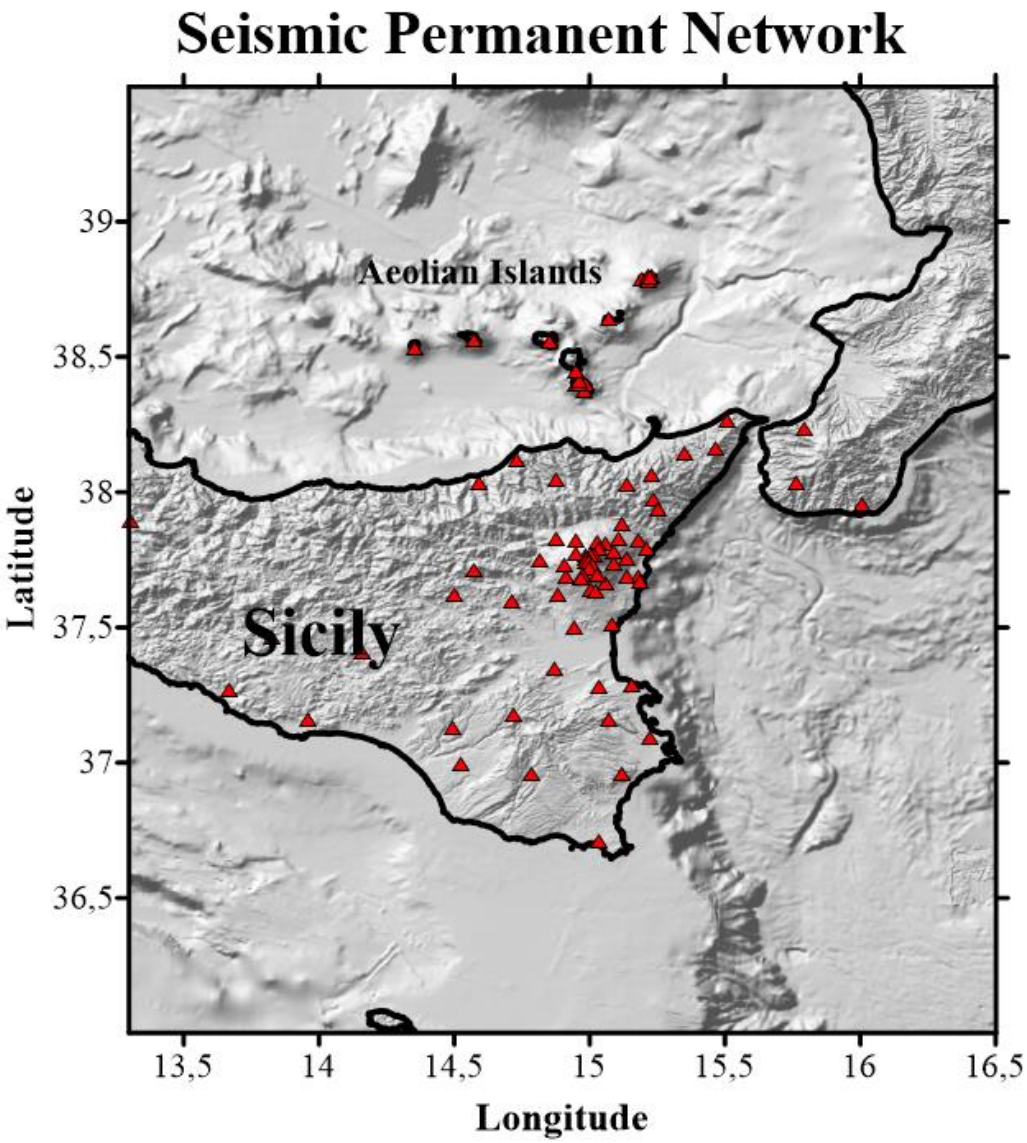

Figure 2.17. *Location of the permanent seismic stations operated by the INGV-OE in Etna area during 2014 (red triangles).*

Seismicity description:

It is widely known that seismology is one of the most important geophysical tools to enlighten and characterize geological and volcanic structures such as fault and dyke systems. Seismicity at Mt. Etna has been recorded and analysed since 1978. Patanè et al

(2004, 2011) describe the seismic events recorded since the first station was installed, and classify them as:

a- Volcano-Tectonic events (VT): Also called A-type earthquakes, VTs are characterized by an impulsive arrival, an exponential decay, and frequency range that vary from 2 to 20 Hz, similar to the regular tectonic earthquakes. These events can be caused by several processes as the regional or the local tectonic stress, gravitational loading, pore pressure effects and hydraulic fracturing, thermal and volumetric forces associated with magma intrusion, withdrawal, cooling or some combinations of any or all of these (McNutt, 2005). The VT events occur in swarms rather than isolated events, being this fact the main difference with the pure tectonic events (McNutt, 2002). In Mt. Etna, we can find deep (15-30 km) and intermediate (5-15 km) VTs, which are high frequency earthquakes (>5 Hz). However, shallow VT events (<5 km) have a more emergent arrival with lower frequencies content (around 4 Hz) (Figure 2.18). The presence of these events is often related to the open of new fractures in response to the magma migration process. In this sense, the pattern of VT earthquakes is usually used to "image" the magma migration (Roman et al., 2006, Bell et al., 2012). However, other authors suggest that in some cases, these seismic swarms could be response of the stress propagation instead of magma migration (Diaz-Moreno et al., 2015).

b- Fluid-related events: These seismic signals are originated by the presence of fluids and its interaction with the volcanic edifice. Low frequencies are predominant in this group. Among these events we find (Figure 2.18):

i. Long- Period events (LP)
ii. Volcanic Tremor
iii. Explosion Quakes
iv. Very-long-period Events (VLP)

LP events (often called low frequency (LF) or B-type earthquakes) present a frequency range that varies from 0.5 to 5 Hz, and are characterised by emergent P-waves. No S-waves arrivals are observed. They suppose an important eruption precursor as they often appear before the onset of an eruption. Its origin, still under debate, could be interpreted as the resonance of magmatic conduits due to the ascent of fluids, and with the

conditions of pressurization of the fluid systems (either magmatic or hydrothermal) (Chouet, 1996a, 2003; Chouet et al., 2008, 2010; Neuberg et al., 2000, 2006) (Figure 2.18).

Another important signal related to fluids interaction (both magmatic and hydrothermal) is the volcanic tremor (McNutt, 1992, Chouet, 2003) (Figure 2.18). Frequency range for this signal varies from 0.1 to 10 Hz. The tremor spectra often present some sharp peaks that some authors relate to source effects (Almendros et al., 1997; Hagerty et al., 2000). On the other hand, harmonic (banded) tremor is characterized by regular increases of amplitude (Powell & Neuberg, 2003; Cannata et al., 2010). It is usually associated with hydrothermal processes (McNutt, 1992). The origin of the volcanic tremor, as well as LP, is thought to be related to the resonance of the magma ascent within the conduits. Especially, a complex interaction between the fluids and the magmatic conduits has been described by (Chouet, 1996b). Routine analysis on the spatial-temporal distribution of the tremor source is used to follow the evolution of the source. Although both LP and tremor events share similar characteristics and origin, they differ on the time duration: LP duration usually takes no more than few seconds, while volcanic tremor may have durations that range from minutes to months (Chouet, 1992). The changes in the amplitude, frequency content and source location of the tremor are used as a precursor of an eruptive episode (Saccorotti et al., 2004, Patanè et al 2011). Therefore, monitoring and analysing the volcanic tremor is mandatory from surveillance point of view (Balmforth et al., 2005).

Explosion-quakes or volcanic explosions are seismic signals characterized by a frequency between 1-5 Hz and non-distinguishable phase arrivals (Del Pezzo et al., 1992). The presence of acoustic waves merged within the seismic signal derives in the necessity of using infrasonic sensors to register and analyse them. One of the most important features of these signals is the infrasonic component remain unchanged during the propagation. Therefore, high quality source dynamic location and analysis can be performed. The origin of this explosive signal can be described by: i) the acoustic resonance of magma and gas within the conduit, (Buckingham and Garces, 1996; Garces and McNutt, 1997; Hagerty et al., 2000), ii) bubble coalescence (Vergniolle et al., 2004),

or iii) strombolian bubble vibration (Vergniolle and Brandeis, 1994, 1996; Vergniolle et al., 1996, 2004). Explosion quakes are events that occurred at very shallow depths and can be related to the degasification processes of the magma and the dilatation and contraction of the magmatic conduit.

Very long period events have a dominant period of 2-100s (Ohminato et al., 1998) (Figure 2.18). Although several theories have been proposed, the origin of these signals is thought to be related to the elastic response of the magmatic system to transient volumetric changes. Fluid transit or bubble gas decompressions are some of phenomena that could lead to this type of seismic signal (Uhira and Takeo, 1994; Kaneshima et al., 1996; Chouet, 1996b; Zuccarello et al., 2013). Chouet et al., (2003) hypothesized that VLP signals analysis could, indeed, enlighten both geometry of the shallow plumbing systems and temporal variations of magma physical properties. Changes on the amplitude, frequency and waveform of the VLP events are thought to be related to pressure variation inside the magmatic conduits (Saccorotti et al., 2007; Patané et al., 2008; Cannata et al., 2009; Chouet et al., 2010; Patanè et al., 2013; Zuccarello et al., 2013).

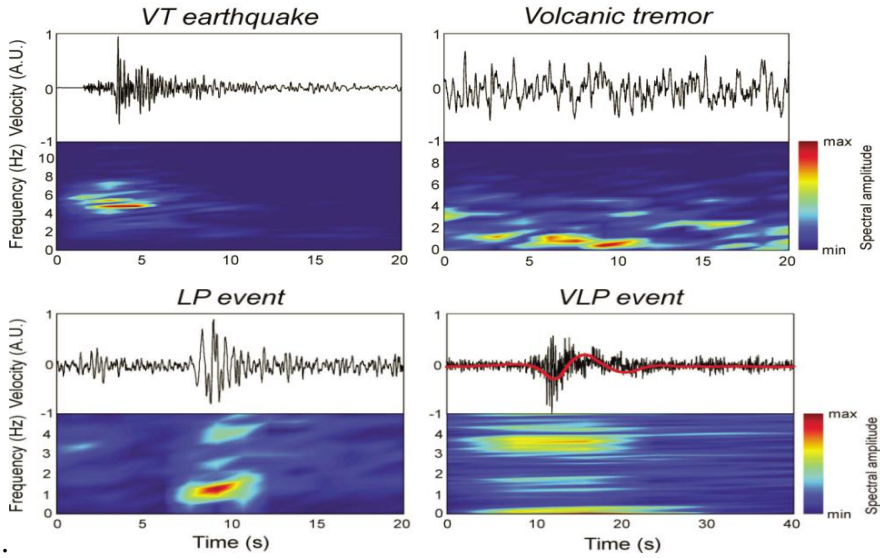

Figure 2.18*. Waveform and spectrogram of different seismic signals. Red line shows the signal filtered below 0.15 Hz. Redrawn from Patanè et al (2011).*

Data analysis and results:

The analysis and study of these seismic signals leads to a better knowledge of the volcano's interior. However, the procedures vary depending on the type of signal to study.

The analysis of the VT events usually begins with a 1D location of the seismic signal. It is often performed in real time by automatic algorithms using a 1D generic velocity model. This gives us a quick idea of where the hypocentre is. In order to perform further more detailed analysis, 3D relocation is needed. A wide range of algorithms are currently available: i) double-difference relative relocation (HypoDD, Waldhauser & Ellsworth., 2000); ii) Probabilistic non-linear relocation (NLLoc, Lomax et al., 2000). A precise relocation with a proper velocity model is essential to address further analysis (Musumeci, 2002, Musumeci et al., 2004). Especially in volcanic areas where many lateral heterogeneities are present.

B-value analysis of the seismicity is used when a large catalogue is available and it leads to a characterization of the seismicity. High values of *b* are usually related to volcanic processes, while lower values correspond to tectonic origins. Murru et al., (1999) performed a *b*-value mapping of the Etna region finding two main high-b-value anomalies that the authors interpreted as magma storages.

Velocity and attenuation tomography, as described in the introduction section, allows us to obtain the distribution of the P and S wave velocities and the attenuation parameters underneath the volcano (Martínez-Arévalo, 2005). These models lead to enlighten major deep structures such as high velocity bodies or large fractured zones (Patanè et al., 2011). Other studies regard attenuation techniques is that carried out by De Gori et al., (2011), who analysed the body wave attenuation for incoming eruptions.

Other advanced studies may be the shear wave splitting analysis carried out by Bianco et al., (2006), who enlightened some changes on the time delays and polarization of the shallowest earthquakes on Mt. Etna just before the onset of an eruption. Moreover, many studies have focused on the focal mechanism and stress and strain tensors calculations of the VT seismic activity (Cocina et al., 1997, 1998; Barberi et al., 2000, 2004; Patanè and Privitera, 2001). Barberi et al., (2000) found a marked E-W

compression in the upper part of the crust (up to 10 km depth) (Bonanno et al., 2011). The stress field changes dramatically in the deepest part of the crust (below 10 km depth) to an N-S compression. The deep stress field is interpreted to be related to the Eurasia-Africa plate convergence while the upper part is controlled by hydraulic pressure caused by magma intrusions (Figure 2.19).

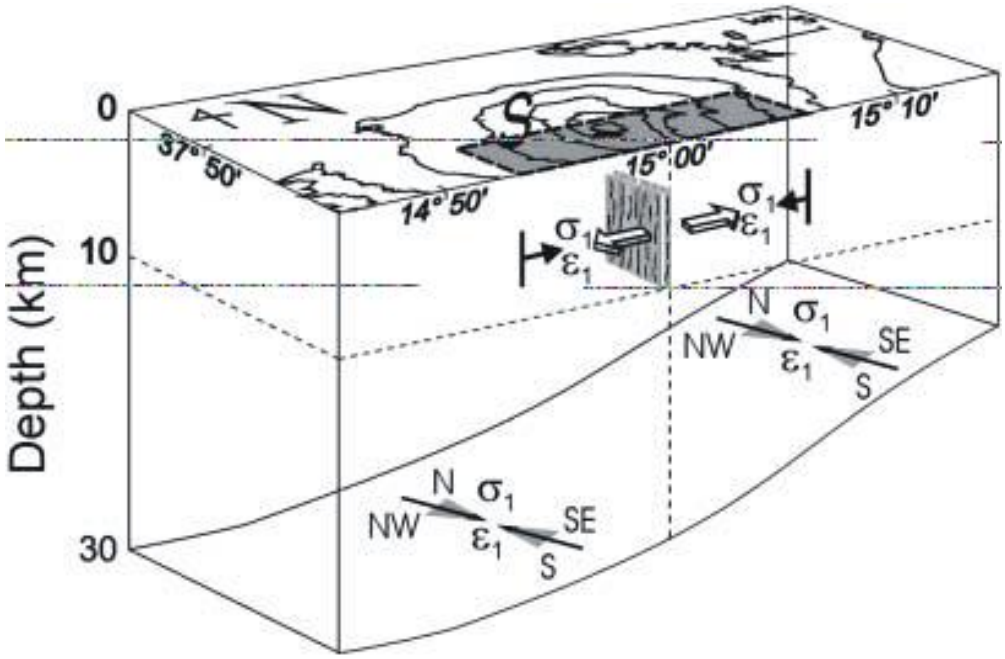

Figure 2.19. Sketch model *representing the stress and strain field beneath Mt. Etna. (From Barberi et al., 2000).*

VT seismicity located at Mt. Etna volcanic system and surrounding areas is not homogenously distributed. Several seismogenic areas can be individuated (Figure 2.20):

1) NW sector: Located near the towns of Maletto and Bronte, this area of the volcano edifice, is the deepest seismogenic zone (20-30 km depth). Nonetheless this seismicity has been usually interpreted as regional tectonic related many authors discuss the possible relation with the volcanic (Patanè et al., 2013). VTs are registered within this area.

2) PPFS: The seismicity located in this area is very shallow (up to 3 km b.s.l.) (Azzaro et al., 1998; Alparone et al., 2013). Events that occur here are VT and present mainly transcurrent sinistral focal mechanism following the fault kinematic observed on the field. The role of the PPFS within the volcanic dynamic is still under debate. Some authors suggest that the tectonic activity of the fault system leads to a decompression of the volcanic system that allows magma to rise up. On the contrary, other authors state that is the pressure of the rising magma that activates the tectonic of the PPFS.

3) Rift S-Parmentelli area: South western of the central craters we find a seismogenic area between 12-16 km b.s.l. where many seismic swarms took place. This seismogenic zone was particularly active after to 2001. Therefore, some authors interpret these swarms as magma related events during recharging phases (Cocina et al., 2010).

4) Summit craters: Below the central crater mostly LP, VLP and some VT events are registered. This seismicity is very shallow, not more than 5 km depth (Patanè et al 2004).

5) Valle del Bove area: A great part of the seismicity registered is located within this seismogenic area. Earthquakes in Valle del Bove are located up to 7 km depth and are VT events (Calvari et al., 2004).

6) Western sector: The seismicity located on the western sector of the volcano (red ellipse, figure 2.20.) was mainly registered between 1988-2001. Several seismic swarms took place, especially during the ongoing tremor and inflation processes accompanying eruptions. (Bonaccorso et al., 2004; Mattia et al., 2007) interpret them as a fragile response of the medium due to a magmatic intrusion. After 2001 eruption only few events have been located within this area.

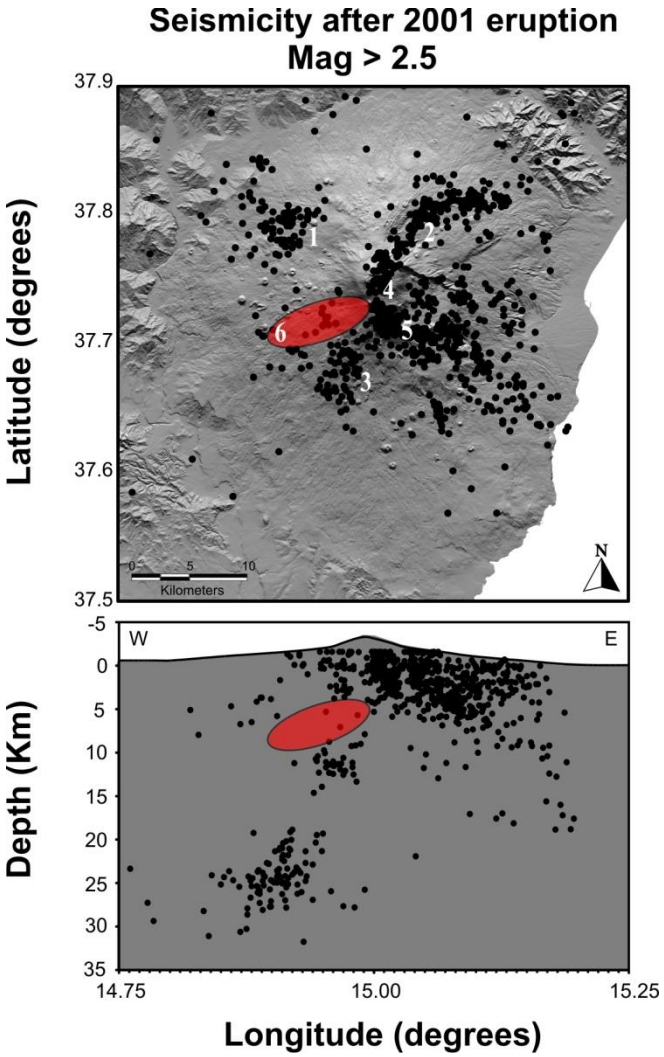

Figure 2.20*. Epicentral map and E-W vertical section of the M>= 2.5 seismicity (black circles) recorded during 2001- 2010 (INGV-OE Researchers). Red area indicates the seismogenic volume active before the 2001 eruption and associated to some recharging phase of the volcano (Bonaccorso & Patanè 2001). The numbers are referred to the seismogenic zones described in the text.*

A key point on the information provided by seismic events is that those at low frequency (Tremor, Lp, VLP, explosion quakes) allow us study the shallower part of the volcanic edifice (up to 2 km depth). On the other hand, high frequency events (VT), due to their location enlighten deeper structures of the volcano (more than 2 km depth), while

their resolution on the shallower layers is poorer. The analysis of the low frequency events (LPs, VLPs) is mainly focused on the location of the source and it dimension. Accurate location is mandatory to develop moment tensor inversions that may shed light into the source process. As no impulsive P-wave arrival is present, tremor location using standard procedures is not possible. Therefore, tremor quantitative analysis is carried out by applying new location methods based on the space distribution of the signal amplitude, and using modern seismic arrays techniques (Battaglia and Aki, 2003; Di Grazia et al., 2006; Di Lieto et al, 2006; Carbone et al., 2008). Many techniques are currently available to assess the LP and VLP location and analysis (Zuccarello, 2015): i) semblance method (Patanè et al., 2008), ii) seismic array techniques with frequency-slowness analysis (Metaxian et al., 2002), iii) amplitude decay (Battaglia et al., 2003), iv) coupled inversion for location and moment tensor (Kumagai et al., 2002), (v) travel time inversion with improved pick readings achieved through stacking similar events (Saccorotti et al., 2007), vi) absolute and cross-correlation location (De Barros et al., 2009). These methodologies may lead to a better knowledge of the plumbing system (Falsaperla et al., 2002; Aiuppa et al., 2010). Infrasonic events are also studied using advanced techniques that include spectral analysis, clustering and classification methods, location with semblance method, etc. (Cannata et al., 2011; Cannata et al., 2013a). Classify the different types of infrasound events in different families is essential to distinguish different sources and it can be carried out using SVM method (Langer et al., 2009). After characterising each type of infrasonic events location methods are used to "image" the source (Cannata et al., 2013b).

2.6. General model of Mt. Etna

The analysis of more than 30 years of geophysical and volcanological data has leaded to a better understanding of the internal (shallow and deep) structure of Mt. Etna. There are many ways of getting to know the internal structure of a volcano as discussed in the Introduction Chapter and along this Chapter. The next paragraphs try to summarize and clarify a structural and dynamic model of Mt. Etna.

Seismology plays a major role in studying the internal deep structure of a volcano and due to its relevance to this study we will focus on it. The study of seismic activity

can be performed using a large variety of techniques (i.e. b-value estimations, seismic velocity tomography, seismic attenuation tomography, etc.), among which, we find seismic tomography. Tomographic studies on Mt. Etna have been widely described in the Introduction Chapter. These tomographies reveal the presence of an aseismic high velocity body inferred to be an old cooled magma body. Other studies of interest are the b-value estimations proposed by Murru et al., (1999). These authors find two high b-value anomalies and interpreted them as magma bodies. These magma patches were placed one below Valle del Bove at around 10 km depth and the other at 3 km depth underneath the western flank of the volcano. Additionally, Gresta et al., (1998) described an aseismic body situated south-eastern of the volcano between 5 and 25 km depth. This volume is interpreted as magma conduits that feed Mt. Etna directly from the upper-mantle (Gresta et al., 1998). Probably, the most important and better constraint feature is the presence of a high velocity body (HVB) south-eastern from the summit craters, mainly enlighten by the seismic tomographic analysis. On the other hand, Allard et al., (2006) using volcanological, geophysical and geochemical observations describe the presence of a small magma storage located at 5 km depth, above the HVB. Geochemical studies infer the presence of a main magmatic conduit from where an important gas plume rise. This gas plume is responsible of the intense degasification processes visible on the central craters.

Additionally, petrologic researchers infer several magma sources:

i) Deep source: located at ca. 10 km depth is responsible of the magma from 1974, 2001 and the beginning of 2002-03 flank eruptions. Characterized by a high explosivity, the magma rises rapidly following structural weaknesses. Parent magma is richer in volatiles. It enters in this area and initiates to differentiate. Magma ascent is controlled by buoyancy rather than tectonics (Corsaro & Pompilio 2004)

ii) Intermediate source: located at around 4-5 km depth, formation of bubbles. The magma from this zone fed the 2002-03 eruption. Defined by several authors (Spilliaert et al 2006; Corsaro et al 2013a) this intermediate storage system is characterized by a long term mixing of the deep ascending magma with the more evolved magmas.

iii) Shallow source: described as a series of dykes and small stationary reservoir, is located at depths < 5 km b.s.l depth (Corsaro et al 2013). Forming part of the intermediate storage, very local short-term magmatic processes occur.

To explain the complex dynamic of Mt. Etna we find at least five models:

1. Tectonic plays a major role through three fault systems (ENE, NNW and WNW) that intersect. This conjunction of faults produces a weakness zone that allows magma to rise up (Ritmann, 1973; Cristofolini et al., 1979; Lo Giudice et al., 1982) (Figure 2.21a).

2. Upwelling of the asthenosphere due to an extensive melting of a mantle diaper. This model describes the emplacement of tholeiitic magma along the Moho discontinuity. This magma evolves with time to an alkaline basaltic magma that feeds Mt. Etna eruptions (Tanguy et al., 1997) (Figure 2.21b).

3. Great volume of magma originated in the asthenospheric part of the subducted African plate (Gvirtzman and Nur, 1999) (Figure 2.21c). Doglioni et al., (2001) postulated a similar model in which a transtensional "window" appears between the Sicilian and Ionian parts of the Apennines plate.

4. Magma ascent is highly conditioned by extensional stress features. These structures are related to a series of normal crustal faults placed along the Ionian coast of Sicily (Monaco et al., 1997, 2005) (Figure 2.21d).

5. The eastern flank to Mt. Etna plays a major role. Geodetic (i.e. GPS and SAR) analyses have shown sliding movements of this flank towards the shore (Froger et al., 2001; Lundgren et al., 2003). This area is confined to the north by the Pernicana fault system and to the south by the NE rift and the Ragalna fault system. It includes the whole Valle del Bove valley. Some authors postulate that this instability causes a decompression of the volcano's interior that allows magma to rise up (Branca et al, 2003; Neri et al., 2004, Neri and Acocella, 2006). On the other hand, other authors infer that magma uprising is the cause of this sliding motion and therefore the cause of the instability (Bonforte and Puglisi, 2003; Neri et al., 2004; Puglisi and Bonforte, 2004; Neri et al., 2009, (Figure 2.21e). However, the origin of this instability is still under discussion. Some authors state that there is a shallow slip plane placed at 1 km a.s.l., which is in

agree with the shallow seismicity (Lo Giudice and Rasà, 1992). Other authors, however, associate this motion to a detachment located at 5 km depth within ductile sediments of Gela-Catania Foredeep (Borgia et al., (1992); Rust and Neri, 1996). On the contrary, Bousquet and Lanzafame, (2001) describe a shallow (1-2 km a.s.l.) decollement of the volcanic pile and the sedimentary lower deposits. Finally, Tibaldi and Groppelli, (2002) propose two detachment planes (shallow and deep). These weakness surfaces provoke the slip motion of the eastern flank.

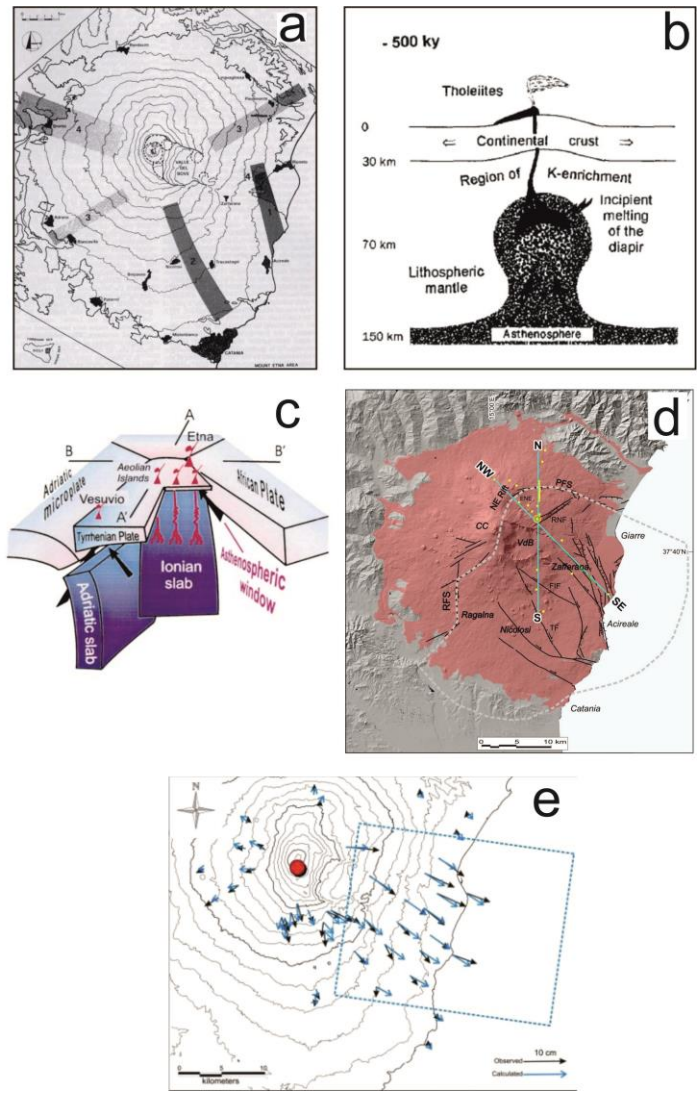

Figure 2.21 (a) Main sheaves of tectonic linear elements in the Etnean area (Lo Giudice et al., 1982). (b) Schematic representation of Mt. Etna in Tanguy et al. (1997). (c) Three dimensional sketch of the south Tyrrhenian subduction zone (Gvirtzman and Nur, 1999). Red lines represent magma rising. Black arrows represent local patterns of mantle flow driven by slab motion. (d) Cartoon showing the kinematic interpretation of major structures of Mt. Etna (redrawn after Neri et al., 2005). (e) Ground velocity map of the Mt. Etna region (Bonaccorso et al., 2006).

2.7. Aeolian Island Archipelago

The Aeolian Arc is a volcanic structure, about 200 km long, located on the internal margin of the Calabrian-Peloritan forearc region, a Hercynian belt affected by Late Quaternary extensional tectonics and uplift (Figure 2.3). The Calabro-Peloritan basement runs from northern Calabria to eastern Sicily, and connects the southern Apennine and the Sicily-Maghrebian chains. It is bounded by the Sangineto tectonic line, in the north, and the Tindari-Letojanni-Malta line, in the south. The structure of the Calabro-Peloritano belt consists of a stack of various nappes composed of pre-Alpine metamorphic and granitoid rocks, often with Alpine metamorphic overprint, Mesozoic to Tertiary sedimentary rocks, ophiolitic sequences, and Quaternary sediments.

The Aeolian Arc is formed by seven subaerial volcanic edifices (Alicudi, Filicudi, Salina, Lipari, Vulcano, Panarea and Stromboli), emplaced on a 15 to 20 km thick continental crust, and their products, which ages between 1.3 Ma and the present, belong to the calc-alkaline, high-K calc-alkaline, shoshonitic and alkaline potassic associations. The geochemical affinity of these rocks and the occurrence of deep seismicity (up to 550 km; Milano et al., 1994) below the Southern Tyrrhenian Sea led to interpret the Aeolian Islands as a volcanic arc related to the active subduction beneath the Calabrian Arc (e.g. Beccaluva et al., 1985; Mantovani et al., 1996).

Structural trends and volcanic activity in the area are strongly controlled by the regional stress fields and bring to identify three distinct sectors:

- Western sector (Alicudi and Filicudi islands), dominated by NW-SE-oriented tectonic lineaments;

- Central sector (Salina, Lipari and Vulcano islands), aligned along the important regional transcurrent fault joining the Aeolian Islands to the Malta Escarpment with a NNW-SSE-oriented trend; on Salina and Lipari subordinate E-W-oriented trends are also present;

- Eastern sector (Panarea and Stromboli islands), characterized by prevailing NE-SW-oriented tectonic lineaments;

The Aeolian Arc structure has been recently investigated (Chiarabba et al., 2008; Di Stefano et al., 2009) through high resolution Vp,Vp/Vs and Qp passive tomography

performed on the base of 15 years of earthquake recordings by the Italy's National Seismic Network. Tomography results show two arc-shaped low- and high Vp bands, located respectively at 25 and 100 km depth. Between 100 and 300 km two high Vp zones lie beneath Neapolitan and South Tyrrhenian regions, separated by unperturbed high Vp mantle. Intermediate depth seismicity is interpreted by the same authors as associated with the subduction of a thin oceanic crust, suggesting the occurrence of vigorous metamorphism. The high Vp/Vs and low Qp anomalies in the overlying mantle is probably associated with melting, this last related to dehydration induced by metamorphism.

2.8. Surrounding Areas

The tectonic configuration of this area originates by the occurrence of major tectonic processes which started after a stage of plate convergence, consuming a subducting Mesozoic ocean from Gibraltar to Liguria, and were likely induced since the Oligocene by the slab retreat (Figure 2.3). This new tectonic regime, through a segmentation and reorganization of the convergent plate boundaries, has led to the formation of highly arcuate orogenic belts encircling young back-arc oceanic basins, i.e., Liguro-Provençal, Algerian, Alboran, and Tyrrhenian basins (see Malinverno and Ryan, 1986; Jolivet and Faccenna, 2000; Faccenna et al., 2014).

Mt. Etna stands out astride different domains represented by the Sicilian/Calabrian sectors of the collisional/subduction belt and the foreland which form its basement. In particular, to the south, the Pelagian block and the Ionian Sea, separated by a Mesozoic lithospheric boundary, the NNW–SSE-striking Hyblean–Maltese-Escarpment fault system (e.g. Doglioni et al., 2001), represent the continental and oceanic foreland of the underthrusting Nubia plate (the African plate west of the East African Rift), respectively (Roure et al., 1990; Ben-Avraham and Grasso, 1991). The orogenic zone develops by the Sicilian-Maghrebian Chain and the Calabro-Peloritan Arc; the former is a S-to-SE verging thrust belt considered as the eastern prolongation of the North African Chain, the latter extends from the southern Calabria to the northeastern part of Sicily (in overthrusting with the Maghrebian domain) and includes the innermost geological units originate from the deformation of the European margin domains (e.g.,

Bouillin et al., 1986). Current tectonic setting of the Arc, which connects the NW–SE trending southern Apennines with the WSW-striking Maghrebian thrust zones, has been closely related to the opening of the Tyrrhenian Sea, coming with the rollback of the Ionian slab and the resulting ESE-ward drift of the Calabro-Peloritan massif (Malinverno and Ryan, 1986; Billi et al., 2011). Indeed, tomographic images (Chiarabba et al., 2008; Neri et al., 2009; Scarfì et al., 2016) and the occurrence of intermediate and deep earthquakes (between 50 and 400 km) point out the existence of a NW dipping and sinking slab beneath the Calabrian Arc and the southern Tyrrhenian Sea, which can be considered the residual of the older slab extending over more than a thousand kilometers from northern Italy to the Maghrebides (e.g., Spakman and Wortel, 2004).

Northward, the back-arc Tyrrhenian oceanic basin is characterised by the active volcanism of the Aeolian Archipelago. It is a volcanic arc made up of seven major islands and a wider seamount system, as a result of the Ionian lithosphere subduction beneath the Calabrian Arc (e.g., Caputo et al., 1972; Barberi et al., 1994; Mantovani et al., 1996) and of a postsubduction extensional deformation (Beccaluva et al., 1985; Westaway, 1993; Ventura et al., 1999; De Astis et al., 2003).

Although there is a general agreement about the fact that a NW-SE trending lithospheric-scale tear-zone through the Aeolian Islands, northeastern Sicily and the Ionian Seas represents the current southern edge of the Ionian subduction system, recent studies (e.g. Gutscher et al., 2015; Polonia et al., 2016; Scarfì et al., 2016) showed the structural complexity of the crustal boundaries in this area which develop by NW-SE regional transtensional fault systems. They appear to have a primary role driving the geodynamics of the central Mediterranean and likely influencing the evolution and activity of the Etna volcano.

3. TOMO-ETNA experiment. Joint marine and on land seismic active survey

3.1. The importance of an active seismic tomography in Etna volcano

Mt. Etna is one of the most fascinating natural laboratories for studying the deep structure of an active volcano using seismic tomography techniques. As described in Chapter 2, Mt. Etna's eruptive dynamics are the result of a complex interaction between magma in its plumbing system, the regional (deep crust) tectonic regime, and local (shallow crust; volcanic edifice) structures, partially controlled by flank instability. Magma ascent driving conditions (e.g., structural setting, tectonic forces) are not yet completely understood. One of the main limitations in understanding the volcano's eruptive dynamics is the insufficient knowledge of its intermediate and deep crust. As indicated in Ibáñez et al. (2016a) in the last 25 years, several seismic and tomographic experiments have been focused on the study of Mt. Etna's structure using different techniques and data sets. As most volcanoes, natural seismicity's rate at Mt. Etna is not very large, therefore, tomographic studies can only be performed with long time periods of data.

The TOMO-ETNA experiment is an international and multi-institutional joint effort focused on providing answers to some of the open questions associated to the structure and dynamic of Mt. Etna (Ibáñez et al., 2016a, 2016b, Coltelli et al., 2016). This experiment takes the advantage of the use of both active and passive seismic sources and the combination of information of other seismic and geophysics measurements such as marine seismic reflection (Coltelli et al., 2016; Firetto-Carlino et al., 2016), or magnetic profiles (Cavallaro et al., 2016). Additional studies regarding TOMO-ETNA experiment were focused on seismic array modelling (Zuccarello et al., 2016), seismic attenuation (Zieger et al., 2016), and even monitoring the Cetacean activity during the marine activities (Monaco et al., 2016).

A tomography image involves a great amount of seismic data (Lees, 2007) recorded by a dense seismic network, a requisite often difficult to achieve in a reasonable time interval due to an absence of seismicity or the lack of stable and dense seismic networks (e.g Chouet, 1996, 2003; Chouet and Matoza, 2013; MacNutt, 2002, 2005; Wassermann, 2002; Zobin, 2011). This problem can be solved by planning active seismic experiments such as we will summarize in this section. Following Koulakov and Shapiro

(2015), it is possible to use different seismic sources divided into three categories: human-made sources, earthquakes, and ambient seismic noise. Fully controlled artificial sources are expected to provide the highest accuracy of tomographic images. At the same time, their implementation on volcanoes is very sophisticated and expensive. Another shortcoming of artificial sources is that they cannot be produced at depth. In regions with well-distributed volcanic or local tectonic seismicity, earthquakes may give a distribution of sources plausible for high-resolution seismic tomography. However, many volcanoes do not generate sustained seismicity. Human-made seismic sources include explosions, vibrators, air-gun shots, and weight (or mass) drops and are usually called active sources. There are some onshore experiments which use chemical explosions of sufficiently large magnitude to generate seismic signal propagating to the distances of dozens kilometers and depths of a few kilometers. The problem of such explosions is that they are fairly expensive and thus their number is strongly limited. Furthermore, chemical explosions are not ecologically friendly and they are prohibited in most volcanic areas (Koulakov and Shapiro, 2015). An alternative method of active-source onshore generation might be using vibrators which are more ecologically safe compared to explosions. However, for the purposes of volcano tomography, the vibrators should be sufficiently powerful and heavy to enable the required propagation of seismic rays. In reality, the transportation of powerful vibrators appears to be not possible in most volcanic areas; therefore, they are not widely used in practice. In case a volcano is located close to the seashore, it is possible to use underwater air-guns as sources of seismic signal. The advantage is that air-gun shots are rather cheap and sufficiently powerful. They can be frequently generated along the ship cruise that gives a huge data base with a clear technology of processing. The main issue is that these sources are limited by the shore line and not suitable for most volcanoes. The major advantage of the active sources is that their parameters are known. The problem is that they are located close to the surface, and seismic signal propagate along the nearly horizontal ray paths. Another difficulty, which is mostly observed for the air-gun shots, is that they generate very weak S waves that cannot be picked and used for tomography studies (Koulakov and Shaphiro, 2015).

In the last 20 years the number of dedicated experiments using active seismic sources is increasing. In order to give a real dimension of the nature of the TOMO-ETNA experiment, we summarize some of the most important experiment carried out in active volcanoes around the word in Table 3.1. In figure 3.1 we plot the position of the volcanoes described below. An important remark regarding the data analysis of the listed experiments is that for all of them, first arrival picking has been performed manually. This fact implies an enormous amount of work in order to produce quality P- and S-wave travel times and will be discussed in detail along chapter 4.

Coming back to Mt. Etna volcano, Chiarabba et al., (2004) presented a complete description of the previous active seismic experiments performed in this incredible scenario. According to these authors, one of the first active seismic studies was done in 1968 to study the seismic refraction structure of Sicily and with only one profile to the north near Mt. Etna (Cassinis et al., 1969). The first deep seismic sounding focused on Mt. Etna's structure was done in 1977 (Colombi et al., 1979). Further, in 1992 an active seismic experiment was performed with the project ETNASEIS (Hirn et al., 1997; Nicolich et al., 2000). This experiment consisted on offshore shots aiming to study the structure of Mt. Etna together with additional profiles to study the Ionian marine basin. Active seismic signals were generated by 8 air-guns with a power of 840 in^3 of volume shooting along 2 profiles. These shots were carried out with the oceanographic research vessel N/O LE NADIR of IFREMER (France). Additional shots were

Region		Active Source	N. Sources	N. Stations	Station type	Year	P-Phases	Area	Reference
Japan	Kirishima	Chemical Explosions	6 (200-250 kg)	163		1994			Tomatsu et al., (2001).
	Bandai	Chemical Explosions	8 (200-250 kg)	298	1-component short-period seimometers	1997	2,200	25×20 km	Yamakawi et al., (2004).
	Asama	Chemical Explosions	5 (200-300 kg)	464	1-component 2 Hz Mark L-22D seismometer	2006	>2,000		Aoki et al., (2009); Yamamoto and Sato, (2010).
	Usu	Chemical Explosions	7 (200-250 kg)	288	1-component 2 Hz seismometer	2001			Onizawa et al., (2007).
	Iwate	Chemical Explosions	6 (200-250 kg)	330	1-component 2 Hz seismometer	1998 -2003	2,676	30 m × 10 m	Nishimura et al., (2000, 2005); Tanaka et al., (2002)
Italy	Vesuvius and Campi Flegrei	Chemical Explosions	20 (200-800 kg)	140	Most 3-component digital seismometers	1994		25 to 40 km long profiles. Only at Vesuvius.	Zollo et al., (1996, 1998, 2002); Gasparini, (1998); Di Stefano and Chiarabba, (2002).
		Air-gun	5,000	134	OBSs and 3-	2001		Vesuvius an	Zollo et al., (2003); Judenherc and Zollo,

			shots		component digital seismometers			Campi Flegrei Caldera	(2004); Vanorio et al., (2005); Battaglia et al., (2008); De Siena et al., (2010); De Siena et al., (2011).
	Stromboli	Air-gun	>1,500 shots	43	OBSs and 3-component digital seismometers	2006			Marsella et al., (2007); Castellano et al., (2008); Prudencio et al., (2015c)
	Mt. Etna	Chemical Explosions				1968			Cassinis et al., (1969).
		Chemical Explosions				1977			Colombi et al., (1979)
		Air-gun				1992			Hirn et al., (1997); Nicolich et al., (2000)

Indonesia	Merapi	Air-gun	1 shot every 2 minutes	75	Short-period seismometers	1997-98	>2,500	3 seismic profiles with a total of 4.6 km long	Zschau and Westerhaus (1998); Wegler et al., (1999); Wegler and Luerh, (2001); Maercklin et al., (2000).
Antartica	Deception Island	Air-gun	>6,600 shots	109	OBSs and 3-component digital seismometers	2005		25 km x 25 km	Barclay et al., (2009); Ben-Zvi et al. (2009); Zandomeneghi et al. (2009); García-Yeguas et al., (2011); Carmona et al., (2012); Prudencio et al., (2013a); Prudencio et al., (2015a).
	Mt. Erebus	Chemical Explosions	12	91	seismometers	2008-09		4 km x 4 km	Zandomeneghi et al., (2010, 2013).
Canary Islands	Tenerife Island	Air-gun	6,850 shots	137	3-component digital seismometers	2007	>120,000		Ibáñez et a., (2008); De Barros et al., (2012); García-Yeguas et al. (2012); Lodge et al., (2012); Prudencio et al., (2013b); Prudencio et al., (2015b).

Caribbean Sea	Monserrat Island	Air-gun	4,413 shots	248	OBSs and 3-component digital seismometers	2007	115,000		Paulato et al., (2010); Shalev et al., (2010);Voight et al., (2014).
New Zealand	Tongariro	Drop of masses	11 masses	4	seismometers	2012			Jolly et al., (2014).
USA	Mt.St. Helens	Chemical Explosions	35 (454 or 908 kg)	3,500	Short-period seismometers	2014		80 km x 80 km	Kiser et al., (2013); Levandier et al., (2015).

Table 3.1. *Brief summary of the most important active seismic experiment performed over the world during the las 20 years.*

carried out by N/O OGS-EXPLORA vessel along 3 profiles. They shot with 26 guns of a total volume of 3,810 in^3. Finally, 2 last profiles were performed using EXPLORA with an industrial-type air-gun array. Hirn et al (1997) analyzed ETNASEIS data to improve their original tomography (Hirn, 1991). Unfortunately, due to Etna's heterogeneity structure together with some instrumental issues, a convincing velocity model of the volcano edifice was not obtained.

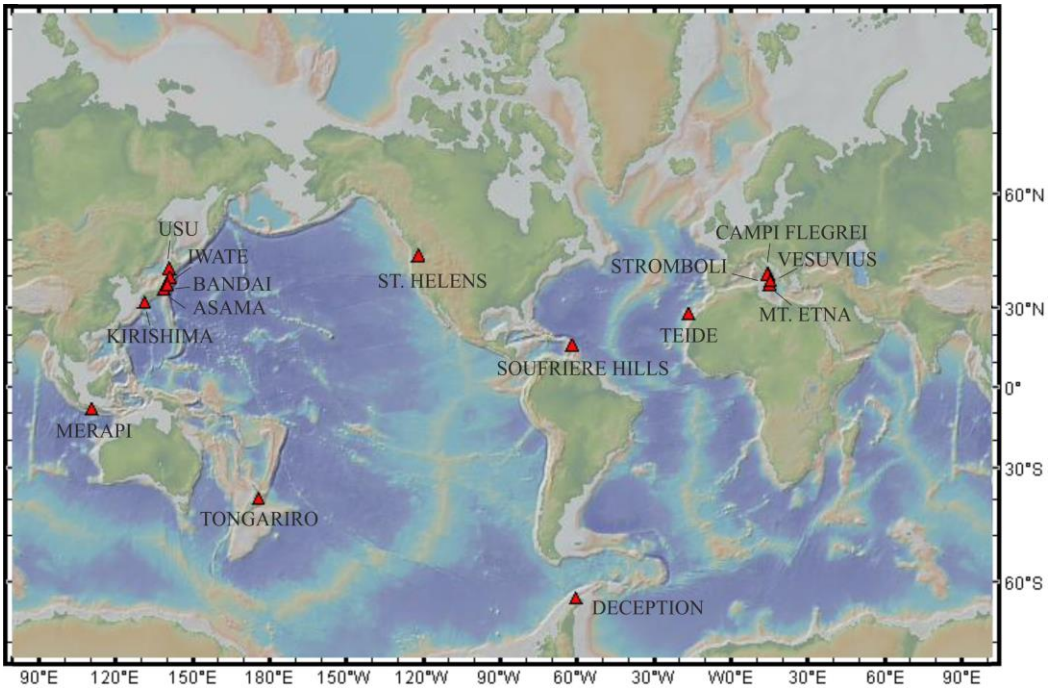

Figure 3.1*. Map with the location of the volcanoes where active seismic experiments have been performed (Table 3.1).*

The TOMO-ETNA active seismic experiment is probably, as it will be described below, one of the most complex experiment performed in an active volcano to obtain a seismic tomography. Ibáñez et al., (2016a) provide a large description of the objectives, plans and involved research projects associated to this experiment. In order to solve some of the problems associated to the exclusive use of active sources this experiment was designed using both active and passive seismic sources. Passive sources (earthquakes) were selected for the period in which the active experiment was performed (June-October, 2014) in order to produce a real snapshot of the Mt. Etna structure and to avoid potential influences of structural evolution with time following the observations done previously by Patané et al. (2006). In the present chapter we describe all activities

developed to carry out the necessary activities to work on land, from the search of sites to the recovery of equipment and data.

3.2. Seismic instruments and networks

A dense temporary seismic network was deployed during the TOMO-ETNA experiment in order to complement the permanent network and to cover a larger area. The joint network (including temporary and permanent stations) was composed of around 267 seismic stations including OBSs, Short Period and Broadband seismometers, which will be described along the next paragraphs.

3.2.1. On-land portable short period seismic stations

On-land portable seismic stations were provided by the Geophysical Instrument Pool Potsdam (GIPP), Germany (Ibáñez et al., 2016b). They are composed of a DATA-CUBE3 recorder and triaxial seismometers PE-6/B 4.5 Hz or Mark L-4C-3D. In figure 3.2 we show pictures of these types of seismic stations. The data logger is a three-channel recorder (Figure 3.2a) with a sample rate value of 100 samples per second. Its main characteristics are a selectable gain x1 to x32 full scale input of 4.1 Vpp and gain 1 and sample rate up to 400 sps (3 channels), and an effective resolution typically of 21.5 bit (theoretical resolution of 24 bits) and 100sps. Tables 3.2 and 3.3 show some important parameters of the acquisition systems and the seismic sensors such as the sensitivity and clip values. The GPS of the station is integrated on the top of the Cube data logger and has an accuracy of <10ms over 20 days without processing or < 0.01ms with processing. These stations were powered with 2D cells batteries with an average duration of 14 days. The sensor is composed of one vertical with an input impedance component SM-6/U-B 4.5 Hz geophone and two horizontal component SM-6/H-B 4.5Hz geophones (Figure. 3.2b). The flat response of the sensor ranges from 4.5 Hz to > 150 Hz with a damping of 0.56. Additionally, some Mark L-4C-3D sensors were deployed with the CUBE recorders (Figure 3.2c). These geophones are three-component and have a response from 1 Hz to >100 Hz with a damping of 0.7.

Further information about the data logger and the geophone can be found in GFZ Potsdam web-page:

(http://www.gfz-potsdam.de/en/section/geophysical-deep-sounding/servicesinfrastructure/geophysical-instrument-pool-potsdam-gipp/instruments/seismic-pool/).

For TOMO-ETNA Experiment we deployed 80 Cube stations with 78 3-D PE-6/B Geophones and 2 Mark L-4C-3D Geophones, some of them were transferred from one location to another during the experiment in order to maximize the network coverage.

Figure 3.2*. Pictures of the short-period seismic stations deployed on-land during the experiment and belonging to the GIPP (Germany).* ***a)*** *DATA-CUBE3 recorder,* ***b)*** *3-D PE-6/B Geophone,* ***c)*** *Mark L4C sensors.*

3.2.2 On-land broadband portable seismic stations

On-land Broadband (BB) portable seismic stations were provided by the GIPP, Germany (Ibáñez et al., 2016b). They are composed of an EarthData PR6-24 recorder and Nanometrics Trillium Compact seismometer (Figure 3.3a, b, Table 3.3). The PR6-24 is a data logger for stand-alone use with three-channel digitizer with a 140dB dynamic range at 100 sps of sampling rate. The seismometer is a Trillium Compact, a broadband three-component sensor with a flat response that ranges from 120 sec. to 100 Hz. Its three symmetric triaxial sensors are resonance-free up 200 Hz. These stations were powered with solar panels connected to a 75Ah 12 V batteries.

Further information about the broadband stations can be found in GIPP, GFZ Potsdam web-page:

(http://www.gfz-potsdam.de/en/section/geophysical-deep-sounding/servicesinfrastructure/geophysical-instrument-pool-potsdam-gipp/instruments/seismic-pool/)

For TOMO-ETNA Experiment we deployed 17 Broadband Stations that operated from June 20th to October 28th, 2014. They registered not only the air-gun shots from the active experiment but natural seismicity occurred during the 4-month period, allowing us to increase and enhance the passive database (Barberi et al., 2016).

In figure 3.3c we plot the response curve for the Trillium Compact (+EarthData), the Mark L-4C (+Cube) and the PE6/B (+Cube) seismometers.

c

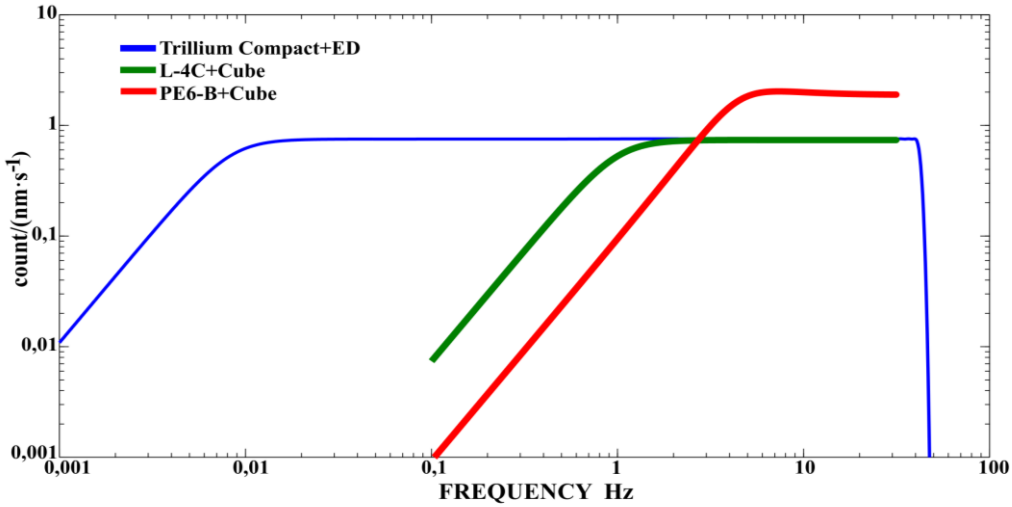

Figure 3.3. *Pictures of the Broadband portable seismic stations deployed during the experiment.* ***a)*** *EarthData PR6-24 three-channel recorder, and* ***b)*** *Trillium Compact broadband three-component sensor.* ***c)*** *Response curve for the Trillium Compact (+EarthData), the Mark L-4C (+Cube) and the PE6/B (+Cube) seismometers. Curves have been calculated using the information described in the text.*

Device	**Gain**	**LSB**	**Sensitivity (Counts/Volt)**	**Clip (pp)**
CUBE3	1	244 nV	$4.0984 \cdot 10^6$	4.1 V
	16	15.3 nV	$6.5574 \cdot 10^7$	0.26 V
EDL	1	1 µV	$1 \cdot 10^6$	16V

Table 3.2. *Main characteristic of the different acquisition systems used. LSB represents the least significant bit that denotes the resolution equivalent in Volts of one sample.*

Device	**Frequency**	**Generator Constant (V·s/m)**	**Damping**
PE-6/B	4.5 Hz	28.8	0.56
MARK L-4C	1 Hz	180	0.7
Trillium Compact	120 s	750	0.7

Table 3.3. *Main characteristic of the seismic sensors used.*

3.2.3 Ocean Bottom Seismometers (OBSs)

3.2.3.1 Spanish OBSs

The Unidad Tecnológica Marina (CSIC-UTM, Barcelona, Spain) provided 15 Ocean Bottom seismic stations (OBSs). Their technical name is LC SP 4×4 IGPP-SIO-UCSD OBS, and includes a HighTech HTI-90-U hydrophone. The geophone is a short-period Sercel L28 model, with natural frequency of 4.5 Hz and a sample rate of 200 sps. Data logger and electronics are BART ORE Offshore software (Figure 3.4). The OBSs clock are Seascan TCXO (0.02-0.05 ppm), which must be synchronized with high-precision on-board GPS before deployment and recovery phases, in order to correct time shifts during the recording period. Usual time drift of this clock for 20 days is around 10 msec. These stations were powered with 12 V batteries with autonomy of 2 months.

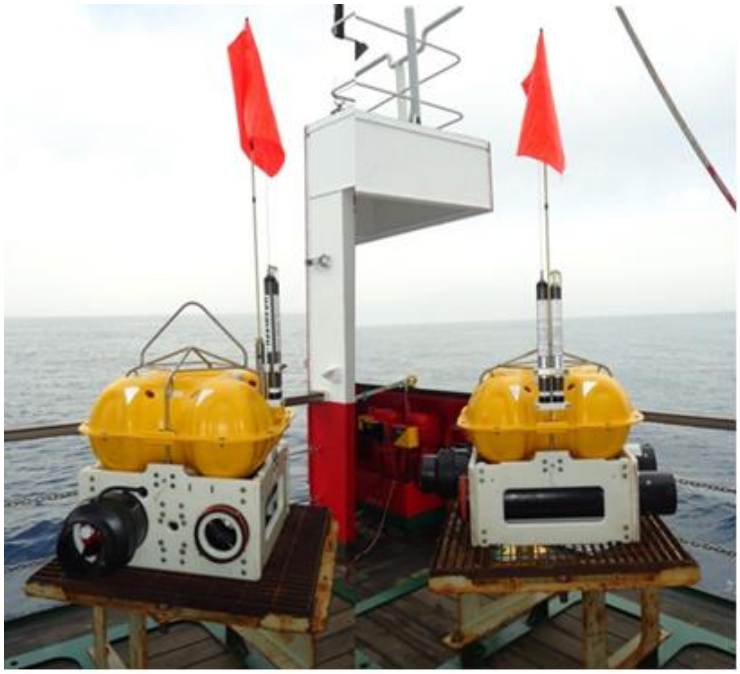

Figure 3.4*. A picture showing Spanish's OBS.*

2.3.2 Italian OBSs

The INGV "Osservatorio de Gibilmanna", Palermo, Italy, provided two types of OBS stations to be deployed: i) Short-period SM/6 Geophone registering within a frequency range of 4.5-140 Hz and with 250 sps; and ii) Broad-Band Güralp CMG40T-OBS sensors that registered between 60s and 100 Hz with a sample rate of 100 sps. In figure 3.5 we show a picture of one of this OBS station. A total of 10 short-period OBSs

and 2 Broad-Band OBSs were used in this experiment. All seismic stations were powered with 12 V batteries with autonomy of 1 month for the short period and 6 months for the BB.

Figure 3.5. *A picture showing Italian's OBS.*

2.4. Array Pozzo Pitarrone

Two broad band seismic stations of the permanent monitoring network are installed at Pozzo Pitarrone (Zuccarello et al., 2016), one at surface (EPIT) and one at the well bottom, at depth of about 130 meters (EPIP). These two stations formed part of a temporary seismic array deployed in the area around Pozzo Pitarrone between May and October 2014. The array consisted of 8 three component broad-band stations arranged in two roughly concentric rings of radii 100 m and 200 m centered at EPIT station. The seismometers used for the array were Guralp CMG-40T 60 s [http://www.guralp.com] and Nanometrics Trillium 120 s compact [http://www.nanometrics.ca], and signals were acquired by Nanometrics Taurus data loggers recording at 200 sps, with 24 bits dynamic range.

2.5. Permanent network

We have used also the data recorded by the INGV permanent network (Figure 3.6). Seismic stations of this network deployed related to the Mt. Etna volcanic edifice are broadband seismometers composed by three-component Nanometrics Trillium sensors. These sensors have a period of 40s, a frequency response of 0.025 Hz and a sensitivity of 1553 V/M/S. They register with a sample frequency of 100 Hz using a Nanometrics Trident Digital System (24 bits). For TOMO-ETNA Experiment we used the data registered in 71 seismic stations from this permanent network. The data is provided by the INGV in DMX format, which is a simplified type of SUDS format. In this case, careful data processing is needed to transform DMX to a SAC format.

a)

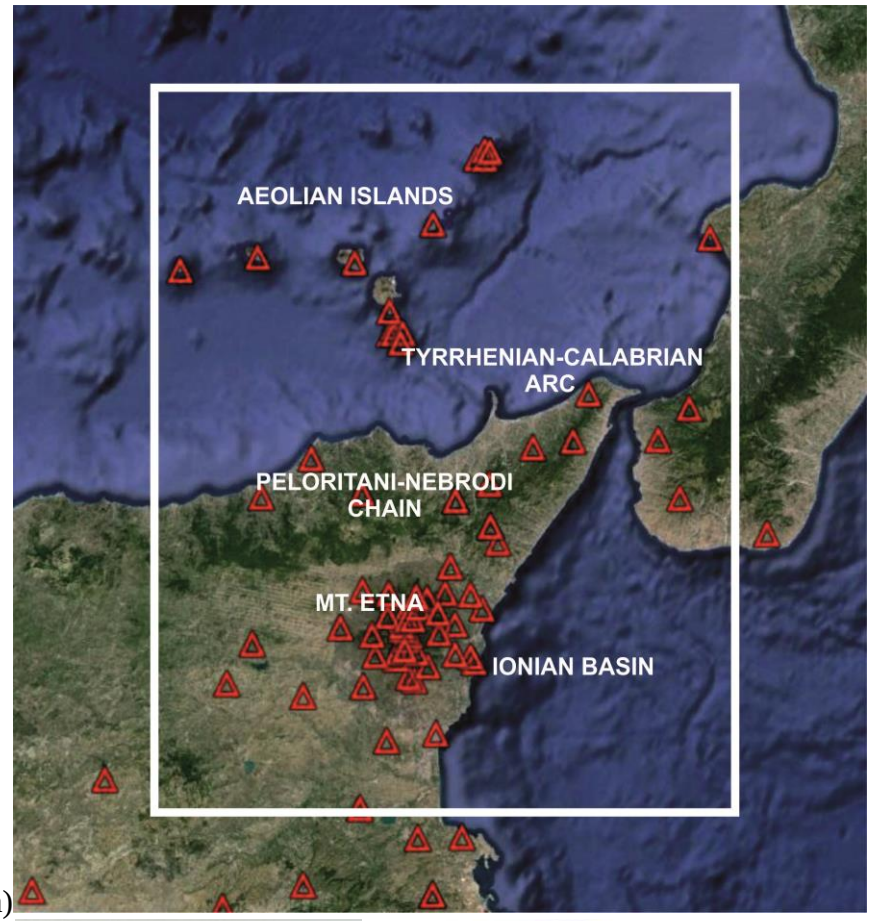

b)

c)

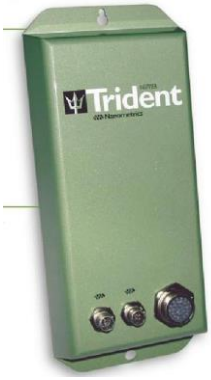

Figure 3.6. a) *Map of the location of the seismic stations of the permanent seismic network of the INGV, Italy, used in the TOMO-ETNA experiment .**b)*** *Three-component Nanometrics Trillium sensors. **c)** Nanometrics Trident Digital System (24 bits).*

3.3. Seismic sources

3.3.1 Air-gun signals

The active source were provided by the Spanish oceanographic vessel 'Sarmiento de Gamboa' and consisted on an array of 16 air-guns deployed forming a 2-lines array 10 m below sea level (Figure 3.7). The volume of the guns was of: 520 x 4, 380 x4, 250 x 4, 150 x 4 cu.in.; having a total volume of 5200 cu.in. They were spaced 1m from each other, within the line, and 9 m between the lines. For TOMO-ETNA refraction experiment the air-guns shot every 90s, while for the reflection experiment was of 30 s with a 3900 cu.in. of total volume.

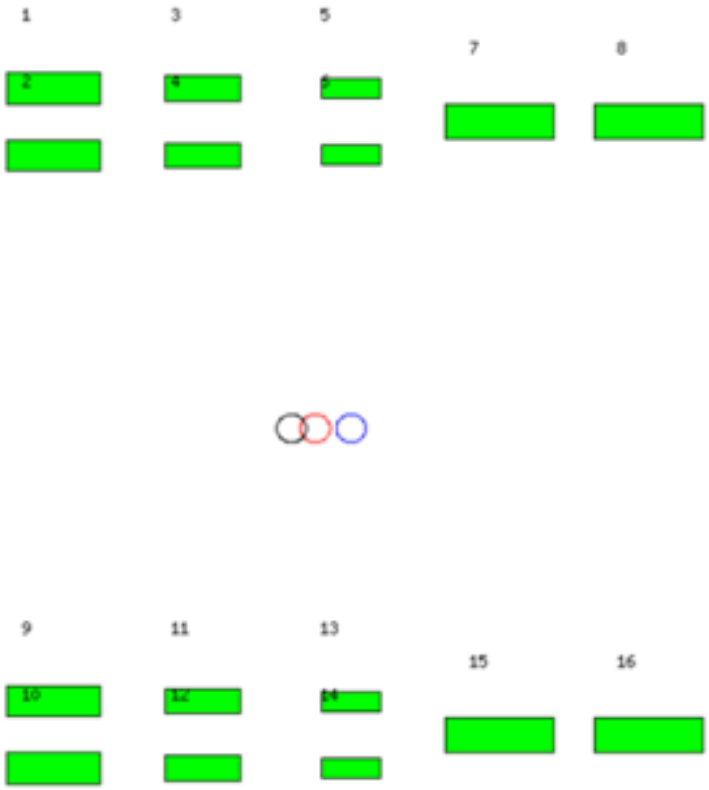

Figure 3.7. *Spatial configuration of the air-guns array mounted in the vessel "Sarmiento de Gamboa" used in the generation of the active seismic signal. Circles represent the theoretical position of the highest energy bubble obtained with this array of air-guns.*

The signal responsible of this bubble is simulated using a software package named “GUNDALF” (Figure 3.8). Previous to the onset of the experiment, many tests were performed by the Unidad Técnológica Marina to obtain the most efficient distribution and power of the guns. The test carried out permitted to adjust several parameters leading to an optimal configuration of the guns that lead to the most efficient output signature. The chosen signature has a dominant frequency of 20 Hz and a total acoustic energy of 479,939.9 J. and an acoustic efficiency of 40.8% (Figure 3.8). In figure 3.9 we show a picture of the real bubble generated by the air-guns mounted in the “Sarmiento de Gamboa” Spanish vessel.

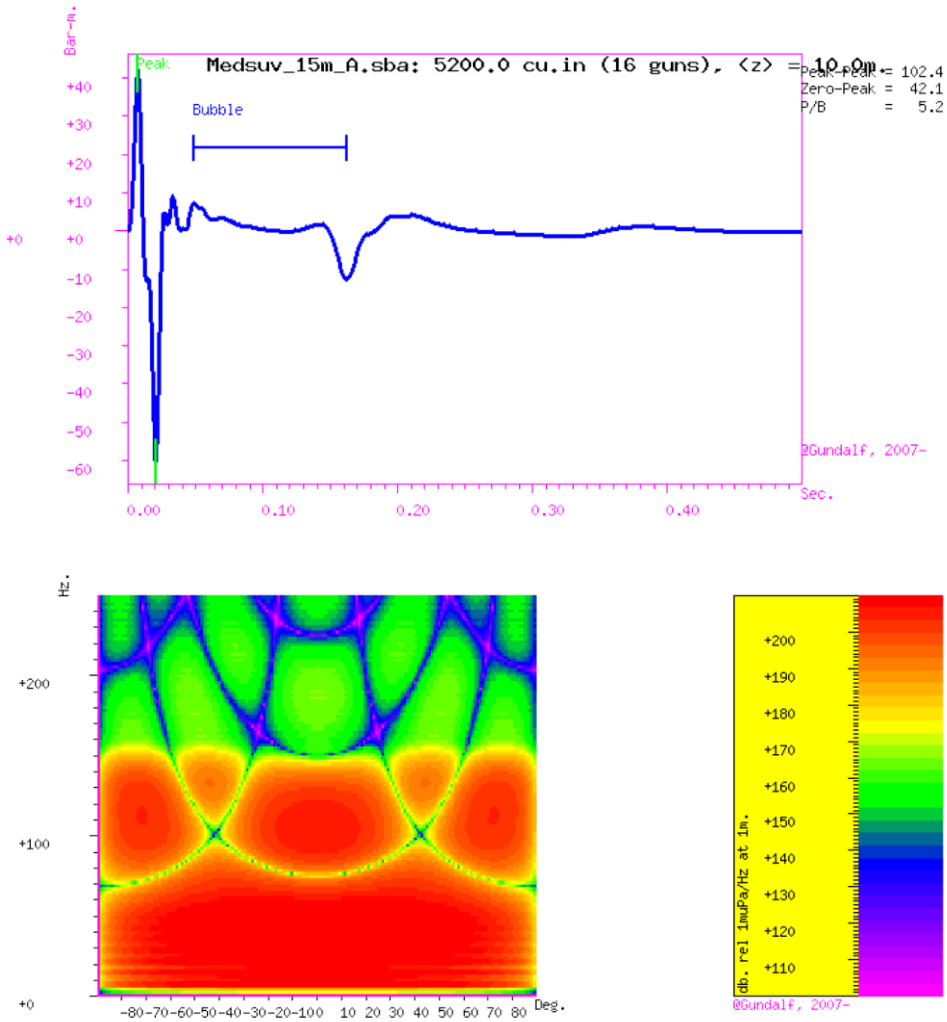

Figure 3.8. a) Theoretical pulse of the active source performed in the time and the spatial domain. **b)** Bubble directivity simulation.

Figure 3.9. *A picture of the real bubble generated by the air-guns mounted in the Vessel "Sarmiento* de Gamboa".

3.3.2 Earthquakes

A total of 452 earthquakes were selected from the INGV data base for the period June 1st to November 30th, 2014. The preliminary selection was done using these criteria: i) it must be recorded in at least three seismic stations from the permanent INGV seismic network, and ii) inside of the region selected for this study. In figure 3.10 we plot the epicenters of this carefully chosen seismicity. The local magnitude of these events ranged from 0.3 to 3.8, and the focal depth ranged from 1.5 km above sea level (Etna edifice) to 215 km below sea level (subduction structure below Eolian Islands). The selected period of time was chosen in order to produce a seismic tomography as a snapshot of the structure of the region. Patané et al. (2006) evidenced how the continuous magmatic dynamic of the volcanic structure produce significant changes in the physical properties of the volcanic region, and therefore changes in the velocity patterns. If a larger time interval for the earthquakes were selected, we may introduce a bias in the final picture of the structure due to potential changes of the velocity values, mainly in the Mt. Etna edifice and roots. Barberi et al., (2016) prepared an exhaustive description of the seismic and volcanic activity of the region and in Mt. Etna during the period of the experiment.

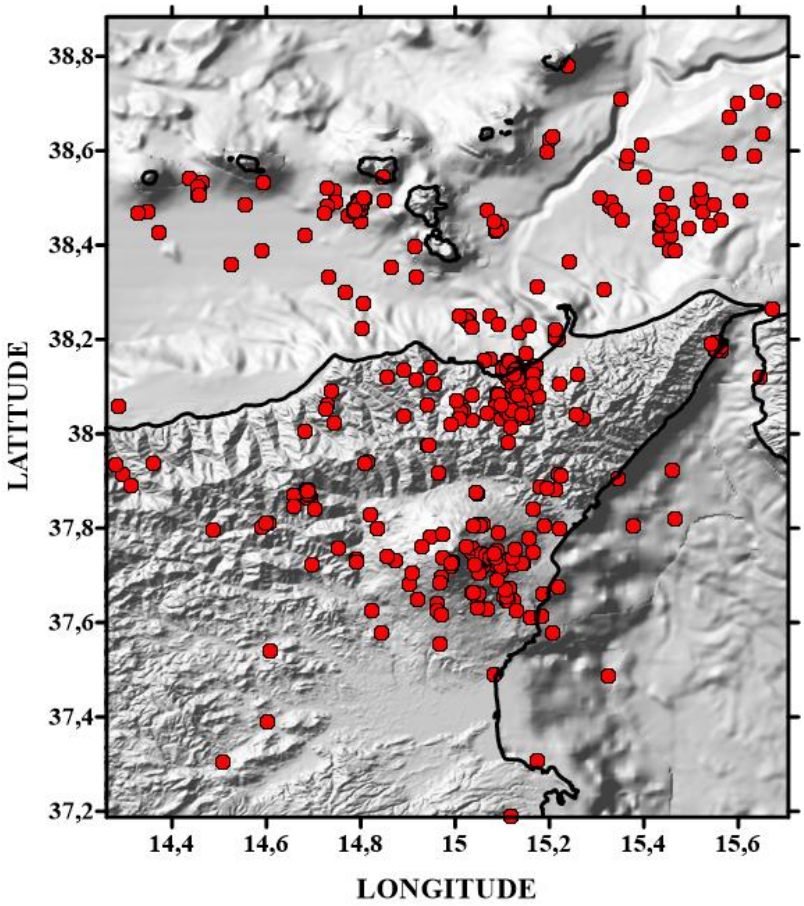

Figure 3.10. *Map with the 452 earthquakes used in the TOMO-ETNA experiment, occurred between June and October 2014.*

3.4. Land operation

3.4.1 Search of sites

The on-land phase started with the search of the potential places to locate the portable seismic stations. This is a very important and sensitive step since a careful selection of the site will permit to deploy efficiently and safety the seismometers. This search was done imposing a series of quality criteria to place a seismic sensor:

a) Low ambient/cultural/volcanic noise level.

b) Protected and safety sites.

c) Easy to arrive and maintain.

d) Consolidated host rock.

Initially, an area of 5,500 km^2 was selected as the region to deploy the stations. The size was estimated taking into account the main objective of the project: to produce a

seismic tomography of Mt. Etna volcano and surrounding areas in order to place this volcano in a regional framework. This zone comprises the Eastern coast of Sicily and Mt. Etna volcanic edifice (see Figure 1 of Ibáñez et al., 2016a). Although the area under interest comprises part of Sicily Island, the Eolian Islands and part of the South of the Italian Peninsula (Calabria), since in both Eolian Islands and Calabria the permanent INGV seismic network has several stations, we centered our effort exclusively in Sicily Island. The first step was to place on a map a set of 200 theoretical locations for the portable seismic stations according to the above quality requirements. Once this preliminary map was defined, from the beginning of April to end of May 2014 a team led by A. Díaz-Moreno from the UGR and O. Cocina from INGV-Catania, with the support of several researchers of the INGV-Catania, visited each of these locations, in some cases more than once. Finally, 150 potential locations were selected covering almost homogeneously the region under interest. The work of this team included to stablish contact with the private owners or the public authorities responsible of the sites and ask for permission to the temporal deployment of the seismic stations. Official documents were provided by the INGV in order to have an additional support in this negotiation. Preferentially the team selected public properties such as Cemeteries, Parks or Schools (the planned shooting period was during a non-teaching season). If no public properties were identified, then private areas with the possibility of restricted access were selected such as golf resorts, rural hotels, farms, among others. In the Mt. Etna structure, the special protected area due to the Natural Park declaration facilitates this search and location of sites. This Natural Park characteristic was also used for several stations placed in the Peloritani Mountains. In several times they had to convince both authorities and private owners of the importance of the stations and the experiment. Many private owners were concerned about possible health issues regarding the installation of the stations (the most repeated question done for many owners was if the seismic stations had any level of radioactivity or how noisy they could be). The search teams were always composed by at least one Italian researcher from the INGV due to of the importance of having a local and institutional representative.

The BB stations needed additional requirements such as a place to install solar panels and consolidate and cover basement since they will be operating for longer time. Furthermore, the objective was to record natural seismicity generated by Mt. Etna volcano, and therefore they must be located close to the volcano edifice. Therefore, most

of the selected places for the portable BB stations were sites already used for the allocation of other geophysical or geochemical instruments.

From all potential locations described in the book, we selected the best 100 places following the above-mentioned criteria and following a geometrical point of view. Indeed, we tried to deploy a geometric seismic network following a dense regular grid structure. In the end, mostly of the selected places were public sites. As curiosity we can mention that more than 25 cemeteries were used to install seismic stations. Indeed, no robbery or damage of any instruments had been reported during the experiment. At the end of the experiment the only risk that the seismic stations were exposed were forest-fires and the actions of farm animals. In any case we were lucky and no damages were reported. As an example, near the village of Catenanuova a fire was declared. Flames stopped just few meters from the station as illustrated in figure 3.11.

Figure 3.11. *Picture showing the rests of a fire near the location of a seismic station. Red star marks the station position. It is noteworthy that the fire covered a big area all around the station but no damage has been reported.*

In total around 10,000 km were driven by the different search teams during this search period. Once a site was identified as suitable, the search team prepared a document containing information on the location, details about driving instructions, owners contact, photos, etc. In figure 3.12 we report an example of this type of document. All these documents were compiled in an electronic and printed format under the coordination of A. Díaz-Moreno and with the collaboration of Italian and Spanish researchers. From all potential locations described in the book, we selected the best 100 places following the

above-mentioned criteria and following a geometrical point of view. Indeed, we tried to deploy a geometric seismic network following a dense regular grid structure. The aim of this book was to allow to the deployment teams to arrive promptly to the locations. Taking into account that many of the researchers involved had never visited the place, the information was very accurate and detailed. It is noteworthy that this information was a complete success since all the researchers were able to reach the locations without major problems, leading to a much more efficient work. At the present it is planned to print the complete information (more than 250 pages of data) in a type of open file report in order to be accessible to the rest of the scientific community working in Mt. Etna volcano.

Due to the large extension of the region under study, once the best sites were identified the whole region was divided in four sectors with an almost same number of seismic stations contained in each one. In each sector a city or village was selected and placed to accommodate the researchers responsible of the deployment, maintenance and recovery of the seismic stations. The four sub-teams were located in the city of Catania and in the villages of Randazzo, Milo and Villafranca.

Figure 3.12. *Information slides of one location. In this case is the Cemetery of Regalbuto town.*

3.4.2 Deployment

In June 16th, 2014 the active seismic experiment TOMO-ETNA, officially started the preparation of the seismometers to be deployed in the Etna volcano and surrounding area. Once the seismic stations provided by the GIPP-GFZ institute arrived (80 short period and 20 broad band stations), a detailed revision of the equipment was carried out, and then stored in the in the INGV headquarter in Nicolosi. It was necessary to transport a large amount of material from Catania to this place. In Figure 3.13 we illustrate this process of transportation and storage of the equipment.

Figure 3.13. *Four pictures illustrating the transport and storage of the seismic sensor of the portable seismic network previous to their deployment.*

On June 17th a training session of the use of the equipment was programmed for a selected group of Italian and Spanish researchers (deployment team leaders) that will be responsible for a process of further training to the other researchers. This first training was performed by Prof. B. Lühr from the GFZ of Potsdam (Germany). In figure 3.14 we illustrate this process. On June 18th and 19th this team of leaders deployed some of the seismic stations in some places near of the Etna volcano under the supervision of Prof.

Lühr. The aim was to check the right operation procedure and to test potential mistakes, faults or other minor problems. On July 20th the whole TOMO-ETNA team (a great part of the non-Italian researchers arrived on June 19th) participates in a new training session in Nicolosi and received the seismic stations that each sub-team must to deploy. As part of the training process each team received the information of the pre-selected sites to deploy the seismic stations. This information was presented in the document described above.

Figure 3.14. *Pictures of the first training lessons on the use of the seismic stations provided by Prof. B. Lühr from the GFZ of Potsdam (Germany).*

For each seismic station we require the compilation of a file with technical information associated to the instruments and deployment procedure. In figure 3.15 we show an example of this sheet.

Each of the four working groups was equipped with:

- A station wagon and a van.
- A smartphone with Italian card, including internet connection and a GPS application.
- Four halogen headlamps with batteries.
- A toolbox with various kinds of screwdrivers, pliers, wrench, scissors, electrical duct tape, duct tape, gloves, compass, level and a tester.
- Two Picks, two shovel and two hoes.
- A fluorescent jacket for each person with identification of the project, INGV and UGR.
- Two back-packs of 50 liters of capacity to transport sensors and batteries.

- Their correspondent number of data logger, seismometers and batteries, including batteries of replacement for the data logger.
- A folder with the information of their respective stations (instruction of use, replacement and maintenance), sites and routes to arrive to them.
- A clear identification sheet for the car and people in it, as they belonged to the INGV-Catania, to the MED-SUV project and TOMO-ETNA experiment.

Additionally, we were supported by different INGV technicians from Catania, Rome, Naples and Bologna. These technicians were in charge of the deployment of the BB stations.

TOMO-ETNA STATION CODE: E_ _ _

Instrument Serial Number		
Sensor (Geophone) Serial Number		
Hard Disk Serial Number (for BB)		
Installation person/people		
Place of installation (+ coordinates**)**		
Date (day-hour)of installation		
Type of batteries (Solar panel, batteries, etc.**)**		
Charge		
Photos	**Yes**	**No**
Commentaries/Problems/Suggestions		

Figure 3.15. *An example of the technical sheet for each seismic station.*

In June 23rd the deployment started. The working-plan for the deployment was conceived in order to optimize the different assigned routes and to install the seismic stations as fast and as safety as possible. In figure 3.16 we plot the stations location distributed according the different working teams, moreover, we have marked, as an example the different routes followed by the different teams in one day of work.

Additionally, in figure 3.17 we illustrate some moments of the installation process. Summary of the number of seismic stations deployed:

a) Villafranca Group: 14 short period seismic stations.

b) Randazzo Group: 18 short period seismic stations.

c) Milo (Etna) Group: 12 short period seismic stations.

d) INGV-GPS technicians: 8 Broad Band seismic stations.

e) INGV-Seismiological technicians: 6 Broad Band seismic stations.

f) Catania Group: 4 Broad Band and 36 short period seismic stations.

In June 26th the 95% of the seismic station had been deployed in their different sites according with the pre-establish selection. The final map with the sites of the whole seismic network deployed for the TOMO-ETNA experiment, including the permanent seismic network of the INGV is presented in figure 3.16.

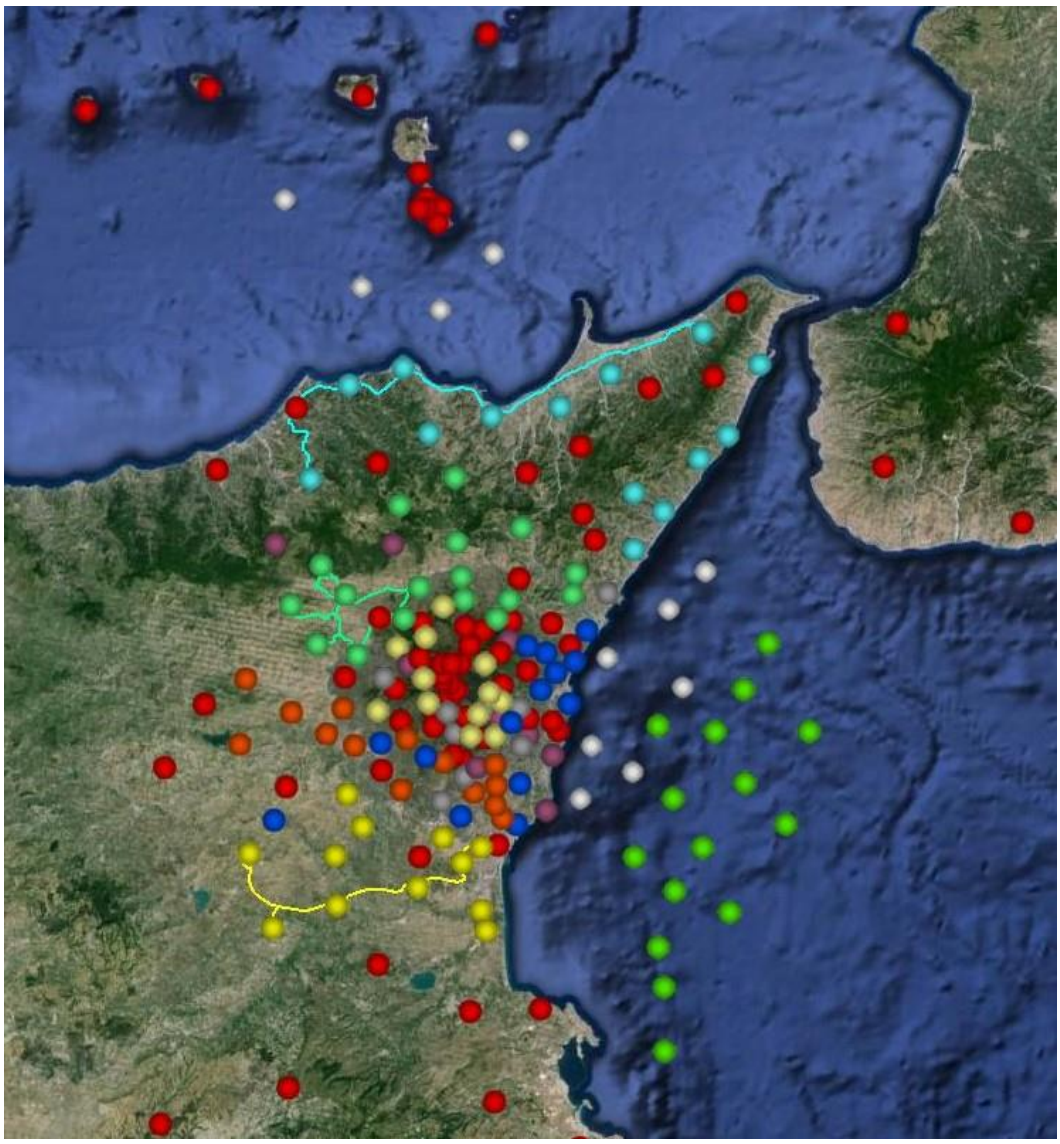

Figure 3.16 *Final map of the deployed stations. Different colours represent the different deployment teams that were in charge of them. Red dots are the stations from the permanent network of the INGV. Yellow dots shows stations deployed by the South-Catania team; dark-blue dots represents stations installed by for the East-Catania team, orange dots symbolize the West-Catania team; light yellow dots belong to the Etna-team stations; grey and purple dots represent INGV-technicians team; light green dots characterize the Randazzo team; light blue show Villafranca team; green dots are the Spanish OBSs; and white dots denote the Italian OBSs; Coloured-lines show some examples of daily team routes (>200 km each).*

Figure 3.17. *Snapshots of different moment of the deployment of the seismic stations process.*

3.4.3 Maintenance

After the phase of installation of the seismic stations, each group developed activities of maintenance and control. These activities were focused mainly in the controlling of the proper operation of the seismic stations and the change of the batteries. The change of the batteries was done every 7 days to ensure a proper operation of the data acquisition. To avoid potential vandalism on the seismic stations, every site was visited at least once every 2 or 3 days.

As routine procedure, every day the operation coordinator, Dr. J. Prudencio, contacted with each headquarter to indicate the activities of the day, potential changes, recovery information and potential problems, including potential help of the other teams to every site.

During the second stage of the shooting process, after July 10th, some of the short period seismic stations were moved from their original planned sites to new one in order to cover additional sites and improved the distribution of stations. In total 23 short period stations were moved. In this case the initial planned 98 portable stations sites were increased to 121 sites.

3.4.4 Recovery

On July 24th, 2014 the seismic active phase of the experiment TOMO-ETNA finalized. At this date the whole portable short period seismic network was recovered. The Broad Band seismic network remained operative until October, 28th 2014. At the same time the Oceanographic Vessel "Sarmiento de Gamboa" arrived to the Catania harbor after the recovery of 25 short period OBSs, leaving operative other 2 Broad Band OBSs. They were recovered by the RV "Aegaeo" in November 25th, 2014. The recovery process of all seismic stations was a success and all the deployed instruments were recovered operating and with no damages. In total, more than 25.000 km were driven during the experiment. In figure 3.16 we show the final position of the whole stations used in the TOMO-ETNA experiment.

3.5. Seismic signals

3.5.1 Seismic data bases

The TOMO-ETNA dataset comprises 26,364 air-gun shots (9,705 refraction shots and 16,659 reflection shots) registered in 80 short-period, 17 broadband, 27 ocean bottom stations (OBS) (15 provided by the Spanish team and 12 Italian team) and 71 broadband-short-period (INGV permanent network) stations, summing 5,140,980 seismic signals. In figure 3.18 we illustrate the route followed by the RV "Sarmiento de Gamboa" during the

whole shooting process. For additional information of the marine activities see Coltelli et al., (2016). For the refraction experiment we have a database of 1,892,475 seismic signals (including all stations). Additionally, we recorded a total of 452 earthquakes in a dense seismic network. When the magnitude of the earthquake was larger than 3.0 it was recorded in more than 50 seismic stations. In figure 3.19 we show an example of a regional earthquake recorded in this network. Red dots indicate the estimate P-wave onset determined by using an automatic algorithm described by Alvarez et al. (2013) and García et al. (2016).

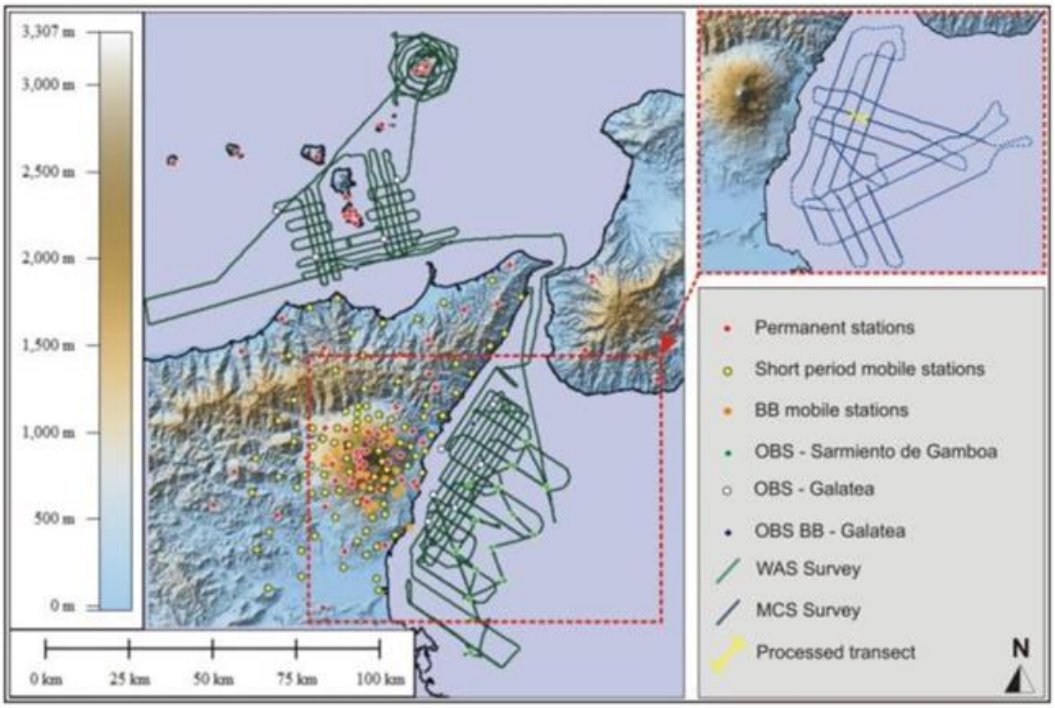

Figure 3.18. *The route followed by the RV "Sarmiento de Gamboa" during the shooting period.*

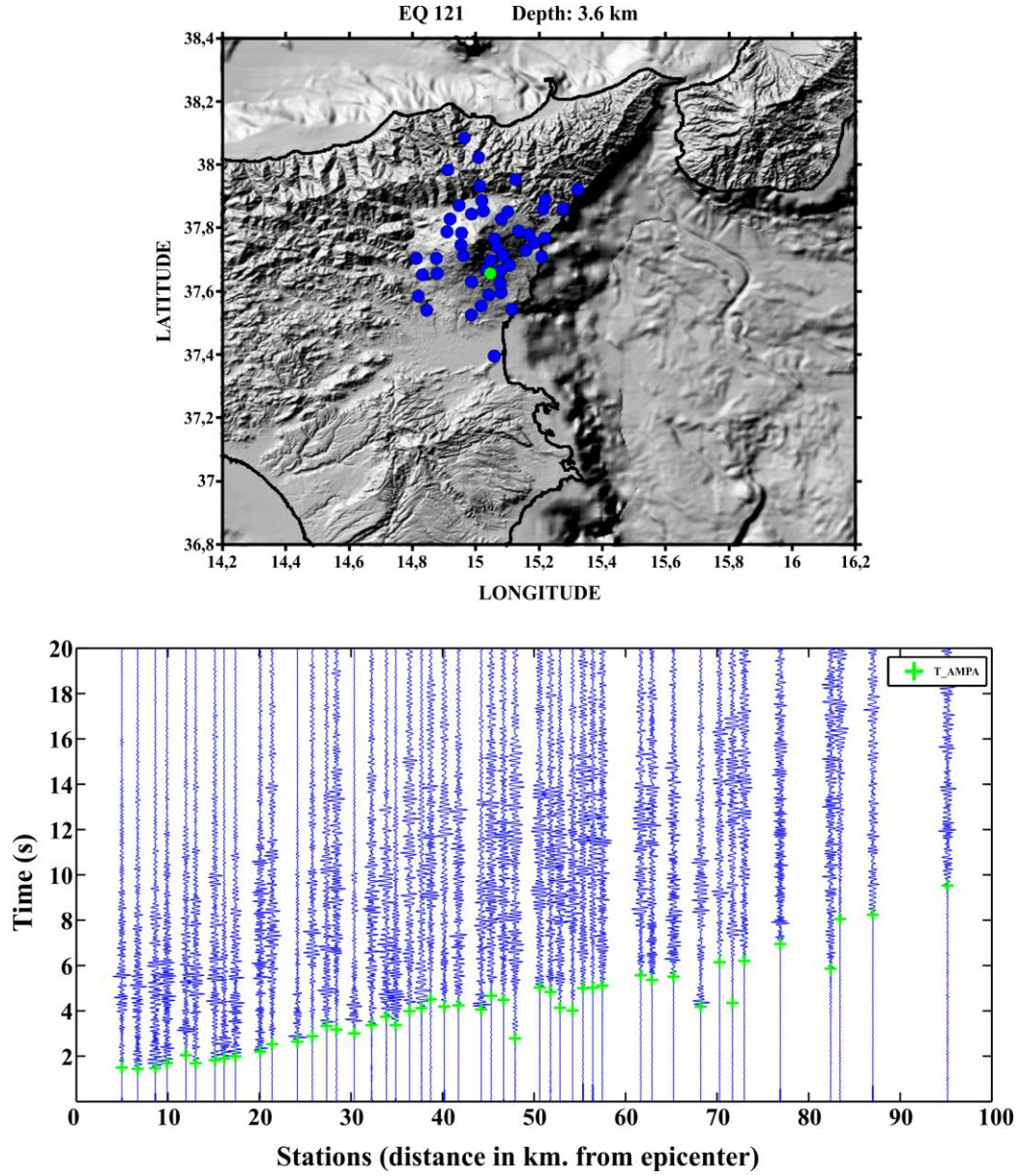

Figure 3.19. *Example of a volcano tectonic earthquake recorded in several portable seismic stations of the TOMO-ETNA experiment.*

In general, the quality of the signals is high. Due to the large area covered in this experiment, it was not possible to record the air-gun shots in the whole seismic network. In average the maximum distance shoot-station to have good quality was of around 50 km. In figure 3.20 we plot an example of 3 hours of shooting period recorded in a single station. Red starts indicate, as in the case of the earthquakes, the estimated P-waves onset

of every explosion calculated automatically. In order to show the quality of the recorded signals we plot an example of a single shot recorded in four types of seismometer (short period, Broad Band, Permanent and OBSs) at different distances (Figure 3.21). It is remarkable how the signal has been filtered and attenuated by the medium. As indicated in the characteristics of the active source, the theoretical source spectra are wide, ranges frequencies from 4 to 40 Hz. However, the spectrograms of the recorded signals show a maximum peak of amplitude between 6 to 12 Hz. This observation was used to select a filter between 4 and 12 Hz for the signal analysis in the tomographic inversion (Díaz-Moreno et al., 2016).

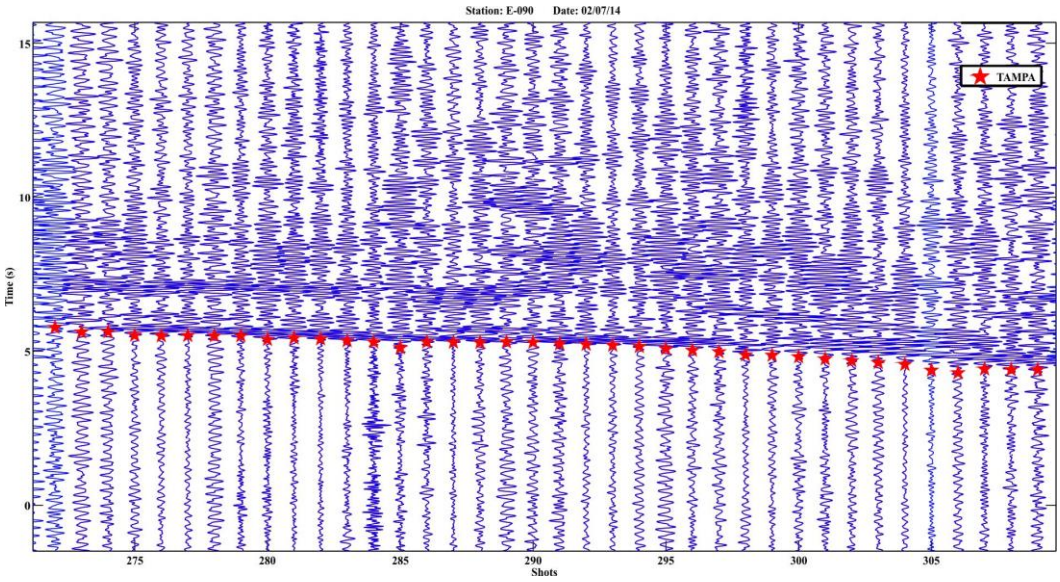

Figure 3.20. *An example of different correlative shots recorded in a single short-period portable station.*

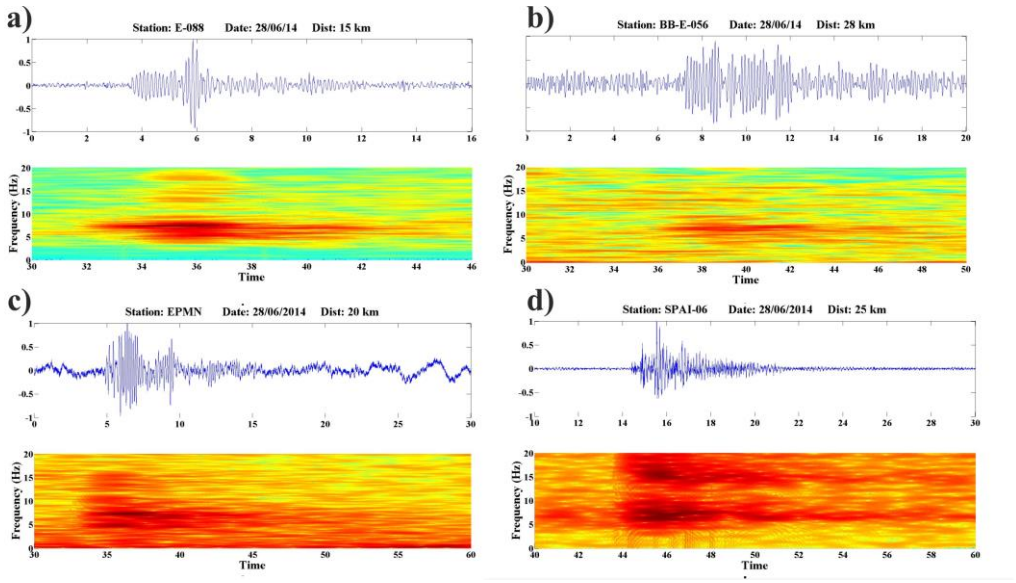

Figure 3.21. *Examples of a shot recorded in different seismic stations: a) Short Period; b) Broad Ban; c) OBSs and; d) permanent station of the INGV.*

3.6. Final remarks.

As reported in the present chapter and compared to previous campaigns, probably the TOMO-ETNA experiment is the most complex experiment focused to obtain information on the inner structure of an active volcano and surrounding areas using both active and passive seismic sources. The efficiency and co-ordination in the performed work has allowed deploying in a shortly time a large number of seismic stations. All of them were operative along the scheduled time, recovery safety, and even if the island of Sicily is a very populated region, no seismic stations were damaged. The first step in the success of this deployment was based on an efficient search of potential sites a few months before the arrival of the working team, including complete and detailed information on the characteristics of the sites, owners, contacts and easy indications of how to arrive to them. The final document generated in this search is very valuable information that could be used in the future in new experiments. The second factor contributing the success was the division of the deployment and maintenance teams in different groups distributed in different sectors covering the whole region under study. These teams were autonomous and following the indications of the provided documents were able to design an efficient daily working program, coordinated by a single person

who was responsible for any final decision. It is remarkable the high quality, portability and feasibility of the used seismic stations. The cube short period seismic stations are ideal to be used in this kind of experiments. The quality of the recorded data predicts final results that could have a high impact in the scientific community. The analysis of these data and the results obtained are described in the next chapters.

4. Advances on the automatic estimation of the P-wave onset time

4.1 Seismic Waves Picking (An Approach)

P- and S-wave arrival determination and travel time calculation are the first stage and the base in most seismic studies. The picking of the seismic wave arrival can be defined as the detection of the instant of time when the first energy of the fastest phase arrives at a station. Such arrival is often identified by a change in energy, amplitude, frequency contents or wave polarization higher than the background noise. This time onset, when registered in several stations, is used to calculate the hypocentre and time origin of the seismic source. Historically, these estimations have been determined manually, which is optimal for few data, but requires a seismological expertise to carry it out. However, when large datasets must be picked, the task becomes very time consuming and human-made errors can occur, especially when the expertise changes. Indeed, manual picking often lacks of objectivity, as each expertise may detect the onset following slightly different criteria (i.e zero crossing, higher than a certain threshold, etc.). During the last decades, providing an automatic picking algorithm has become a key point in many seismic laboratories in order to assess large datasets and to diminish potential human mistakes. Several methods have been proposed that fit well for certain datasets but sometimes they are not exportable to other regions (Benítez et al., 2007, Cortés et al., 2014). Along the following paragraphs we summarize some of the latest and more relevant procedures proposed for automatic picking based on different parameters analyses. We want to remark that this is not a detailed review of all the existing techniques but a state of the art of the most important ones, regarding the frequency domain analysis.

Many approaches for automatic picking have been proposed in time and frequency domains like: the pioneer classical picker of Allen (1978) based on STA/LTA, improved by Baer and Kradolfer (1987); approaches based on higher order statistics like kurtosis or skewness (Saragiotis, 2002; Küperkock et al., 2010, Langet, 2014); picking based on the waveforms predominant period (Hildyard et al., 2008); or wavelet analysis (Zhang et al., 2003); and multiband frequency analysis (Álvarez et al., 2013) as examples in the frequency domain. Autoregressive techniques based on the Akaike Information Criterion (AIC) like Takanami and Kitagawa (1988), pattern recognition systems like

ANN (Gentili and Michelini, 2006) and polarization analysis have also been successfully implemented (Reading et al., 2011; Ross et al., 2014; Kurzon et al., 2014).

Latest tendencies in automatic picking opt for combinations of several of the referred techniques, selected according to specific needs and available data. Iterative, tandem or parallel approaches like Nippress et al., (2010), Küperkoch et al., (2012), Álvarez et al., (2013) or Ross et al., (2014), are jointly applied to combine complementary strengthens.

The automatic procedure is needed because, besides the demand of capacity to process the massive dataset produced, signals will have diverse signal to noise ratio (SNR) due to the seismic noise generated in their path towards the seismometers and the low density of the materials they have to travel across. Automatic real-time signal processing and noise reduction permits outperforming human analysis in terms of precision and consistency of the travel time estimations.

In this work, we have applied the P-phase picking procedure described by Álvarez et al., (2013) and García et al., (2016). Along this chapter we will describe this algorithm used to determine the P-wave arrivals for both active and passive data. The dataset used is that recorded during the TOMO-ETNA experiment, and detailed in the previous chapter. It includes more than 3 million raw seismic signals that must be analysed. For such a large database, manual picking is discarded as it would need several months to carry it out. Unifying the different signal formats recorded is the first stage and it is detailed in the following paragraphs.

4.2. Signal pre-processing

The first step is to unify the data formats. Initially, all the seismic data is recorded in a different format depending on the station (short-period, broadband, OBS, etc.). This procedure is not as easy as it may seem, since it is a very sensitive procedure. In the following paragraphs the different original formats and they conversion are detailed. Our preferred format to work with is .mat (matlab) so that we can process the data in a less time-consuming way.

We analysed separately both earthquake and shots data. For the shot database we started with the CUBE stations. These stations save the data in binary daily files that

should be then converted to an appropriate format. The GFZ Potsdam institute provides useful algorithms to convert Cube format to MiniSeed format. During the recorded period, many of the 90 stations deployed lost the GPS signal sometimes, leading to more than one daily file. The binary output format is transformed to a more accessible MiniSeed format. We found out that the registered data had some gaps, meaning that for certain periods of time the station did not register. The most probable cause of this is the loss of GPS signal. Fortunately, MiniSeed files are written with an absolute scale of time, thus, allowing us to identified and exclude these gaps. Another step we performed was to convert MiniSeed to SAC in order to be able to choose the more suitable type file to work with. On the other hand SAC files have the time information not in absolute values but in a single time vector from 1 to the end of samples. Therefore, gaps could not be well identified using this type of files. For this reason we decided to work directly with the MiniSeed data. To reduce computation time we transform the data to .mat format taking only the pieces of signal we needed. Indeed, we cut the signal 30s before that data and 60s after each shot. When we find a gap in the registration, the shots occurred in that period are not taken into account for that station.

Once the Cube database is organized in the new format, we plotted all shots registered in one station during one day using matlab tools. This way of representation allows us view the movement of the vessel and to estimate the acoustic wave (1.5 km/s) registered on the stations near the coast. Indeed, controlling the arrival time of the acoustic wave is a simple and very effective procedure to check that the GPS data times are correct, and that there is synchrony between the GPS data time of the airguns and the stations (See chapter 6).

The data extracted from the broadband stations are in MiniSeed format; therefore, not further conversion is needed, only to .mat files. In this case we followed the same procedure as for the Cubes, we took the time data of each explosion to cut the MiniSeed file 30s before it and 60s after it and save it in Matlab files. The only problem we address in this step was that the coordinates of the broadband stations were daily calculated and differ from one day to another in some decimals. In order to have a final station coordinates we calculated the mean of all these daily GPS coordinates.

The INGV permanent stations provide data formatted in .DMX files, which result to be a compressed type of .SUDS files. This type of file is organized in a completely different way as the previously mentioned MiniSeed or SAC. They save registration of 1min for each station. In this case, the INGV research team provided the necessary tools to convert them to a friendlier SAC format. In any case we may address the same problems as with the Cube data; if any gaps are present we will not be able to detect them with the SAC format. Nonetheless, we converted them to .mat files following the previously discussed procedure and fortunately, we found no gaps for the registration of these stations.

The Spanish OBS data is provided in RAW binary format. The tools for conversion permit to obtain an output format known as PascalSegy. This data files were, then, organized in the common .mat files for their analysis.

The Italian OBS data available at the time of this Thesis are only those recorded by the Broadband OBSs. These data are saved in SAC files and therefore easy to handle. Procedure was the same as for the rest of data, using .mal files as the final format.

Once the four different formats of raw data corresponding to the four types of stations are converted into a unique readable format, missing data, registers with lack of GPS signal, and extremely bad SNRs abrupt offset in amplitude, are detected and discarded. Secondly, continuous registers are segmented into windows of analysis around the expected arrival times based on the catalogue of shooting times for the active database, and the earthquake catalogue for the passive data. Thirdly, band-pass filtering in the band of interest is done. All the stations used in this experiment allow recording of the three components as described in the previous chapter. Figure 4.1 shows signal associated to the three components recorded by the CUBE station (E-108) on the 10th July 2014. The movement of the vessel and the locations of the stations and Etna volcano are depicted with a blue line, a red spot and a black spot, respectively. The upper panel shows the seismogram registered 40 seconds after the air-gun shot number 70 (i.e. the zero time corresponds to the time when the shot took place). The lower panel presents the spectrograms associated to each component. The P-wave onset corresponds to a packet of energy in the frequency range of [6-8] Hz. According to the Fermat's principle and as can

be observed in this figure, the vertical component is the one providing the best information of the wave arrival. Following this criterion, the signals registered in the vertical component (Z) have been used in this work for estimating the wave arrival associated to the shot.

Most of the signals registered in the different stations used in the experiment have a low SNR (i.e. they are affected by strong background noise and /or non-stationary noise processes). For example, the three components in figure 4.1a, present low SNR, with a strong noisy artefact centred at about 18 Hz at around 20 seconds of time. Taking into account the band of activity of the events we want to pick and in order to emphasizes only P-wave arrivals, for both air-gun shots and earthquakes, all the Z-components have been filtered using a band-pass linear phase filter in the band [4-12] Hz. The group delay was compensated accordingly. This type of filter was opportunely chosen, based on the previous simulations on which zero-phase filters demonstrated a worse behaviour in the presence of an impulsive arrival. The left panel of figure 4.1b shows the recording of the vertical component in the same site and date than figure 4.1a, for the first 80 shots. The right panel shows the signals after filtering. The improvement in terms of SNR is obvious. P-wave arrivals are difficult to identify in unfiltered signals while they are clearly observed in the ones filtered.

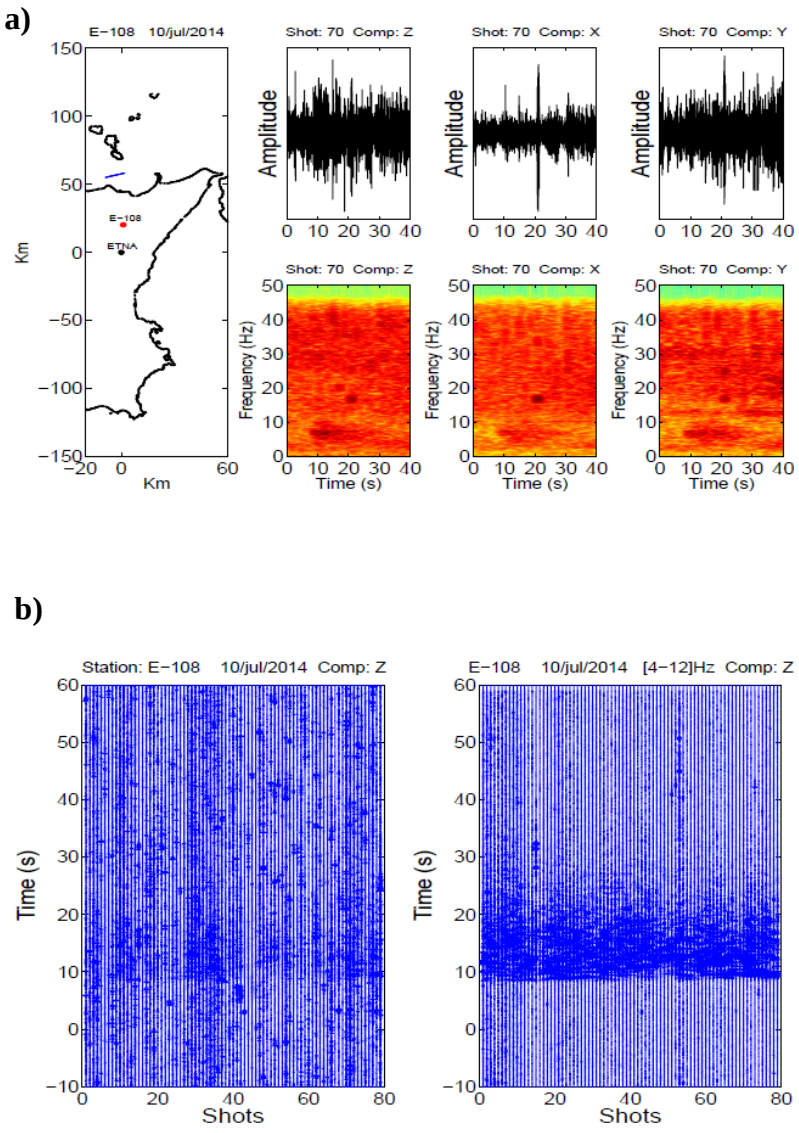

Figure 4.1 a) *Example of a non-filtered signal in the three components in time and frequency domains from station E-108 (red dot).* ***b)*** *Comparison of a series of shots (blue line) registered in the same station (E-108) before (left panel) and after (right panel) filtering.*

4.3. Advanced Multiband Picking Algorithm (AMPA)

The automatic P-Phase picking algorithm used to calculate the travel times of the TOMO-ETNA database, named AMPA, is fully detailed in (Álvarez et al., 2013). In such work, the finest picking is obtained with AMPA working in tandem with the autorregresive techniques applied by Takanami and Kitagawa (1988). Due to the ineffective computational cost of this tandem approach, for the TOMO-ETNA database, plain AMPA has been used. The picking algorithm is also available in an open-source toolkit with a user-friendly windows environment and downloadable in Romero et al., (2016). AMPA, standing for Adaptive Multiband Picking Algorithm, is a picking strategy focused on determining P arrival times for signals strongly affected by a low SNR or processes involving non-stationary noises. In order to do so, AMPA performs two steps with the signal to be picked:

i) Multiband envelope detection and noise reduction, eliminating contributions below band-dependent envelope thresholds.

ii) Enhancement of signal envelopes and durations corresponding to P-phase arrivals.

Given the need of reliability for certain picking applications like high-resolution tomographies, the travel times determined by AMPA have quality assessment to permit different trade-offs between high detection rates and quality of the picking depending on the specific needs of the application.

Figure 4.2a pictures the paths for step i) of the AMPA process, denoting sv(n) the filtered window of signal., on which a P-phase arrival is expected. For each band, the signal subband envelope is detected (refered as xi, i=1,…,k for each of k bands), and a threshold quantization is applied to it. Right panel of figure 4.2a shows an example on which six subband envelopes (z1,…,z6) are plotted after threshold quantization. Envelope samples with amplitude smaller than a certain threshold are quantized to value 1. The final signal of this first AMPA step, named lztot, is the sum of all the bands de-noised envelopes depicted in the lowest graph of right pannel in figure 4.2a.

Figure 4.2a shows the step of detection and enhancement of P-phase arrivals. The sum of all subband denoised envelopes (lztot) is passed through a set of enhancing filters

designed following the principled of Communication Theory for an optimum detector. Its impulse response should be the time reversal of the expected signal (see panel a in figure 4.3). In order to increase response is supplemented with a portion of negative response, resulting in the final impulse response hb(n) depicted in panel b of figure 4.3. Envelopes with a sharp rise of energy and slow decay corresponding to phase arrivals will be enhanced, while other envelope patterns will be minimized. The length of the window of the enhancement filter, L, is an important design parameter as the filter will enhance events with duration in the order of L. The duration of the event-related phase will be related to many factors like its magnitude, the signal propagation attenuation, the type of seismic source, etc. In order to preserve the detection of arrivals with different durations, different lengths are used in parallel (with a subsequent half-way rectifier to eliminate resulting negative amplitudes), defining the final Characteristic Function (CF hereafter) as the product of the analysis performed on each of them.

CF, the resulting output after denoising the multiband envelopes and enhancing impulsive arrivals with soft decays for lengths similar to the ones expected, will be used to find the picking time. Figure 4.3 shows three different CF outputs (d, f and h) for an example earthquake (c), an emerging noise (e) and an impulsive noise (g). Impulsive and emerging noises are eliminated thanks to the optimum detector. Finally, the P-phase arrival time will be detected as the instant of time when CF takes the maximum amplitude.

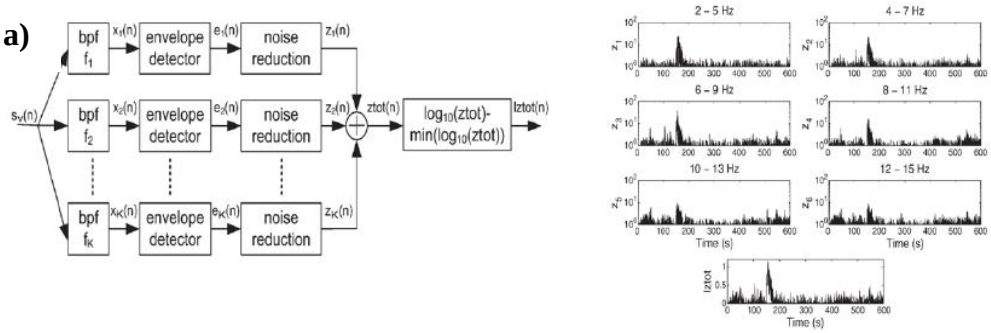

Figure 4.2 *Block diagram explaining AMPA picking algorithm.* ***a)*** *Multiband denoising phase of AMPA.* ***b)*** *P-arrival enhancement phase of AMPA procedure.*

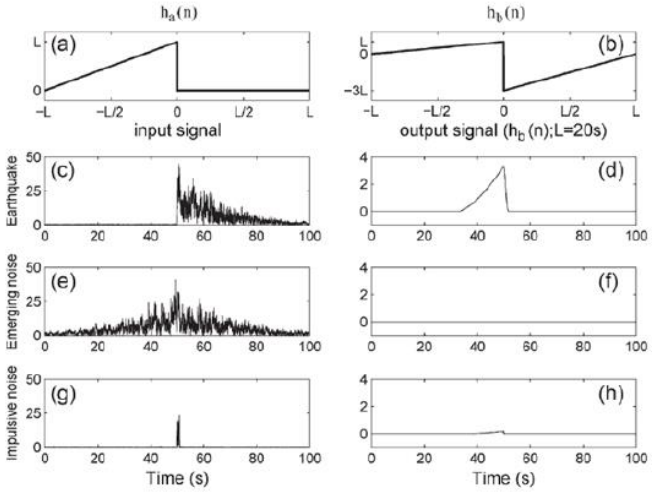

Figure 4.3 a) *Theoretical impulse response of an optimum detector for inputs with a sharp start and a smooth decay.* ***b)****Impulse response of the optimum detector referred in (a), increasing its penalty for smooth starts.* ***d)****,* ***f)****, and* ***h)*** *represent the Characteristic functions (CF) obtained respectively for the example inputs of:* ***c)*** *earthquake;* ***e)*** *emerging noise; and* ***g)*** *impulsive noise.*

4.4. Calibration of AMPA

Several parameters of the algorithm must be calibrated depending on the events to be picked. The lower and upper frequencies of the band of analysis and the number of subbands (referred as 'k' along this section) need to be set. In the case of TOMO-ETNA, the band [4-12] Hz, used also in the pre-filtering stage, has been used for both active and passive data. Also, the number of optimum filters and their length should be set depending on the lengths of the expected events. For this experiment 3 filters with respective 200, 100 and 50 samples (for sampling frequency of 100 Hz) were used after experimental calibration.

4.5. Quality assessments

When arrival times are required for high-resolution tomography, the number of erroneous picks has to be as small as possible since residuals of outliers in the post-picking detection must be of the same order than residuals due to velocity anomalies (Nippress et al., 2010). AMPA makes 2 automatic quality assessments of the picking to define a range of reliability of the results needed depending on the specific application. Firstly, the amplitude of the CF defined (named Zmax) will give assessment of similarity to a reference impulsive arrival with a slow decay and a defined length. Secondly, an SNR in the surroundings of the arrival time picked is also calculated. Figure 4.4 shows the P-phase picking for an earthquake artificially contaminated with Additive White Gaussian Noise with different SNRs. ON each panel, CF is plotted below the event. Picking time (T_{AMPA}) corresponds to the maximum Zmax in the figure. It can be observed that parameter Zmax decreases slightly as the SNR decreases in subsequent subfigures, while a robust behaviour against noise is perceived in all of them.

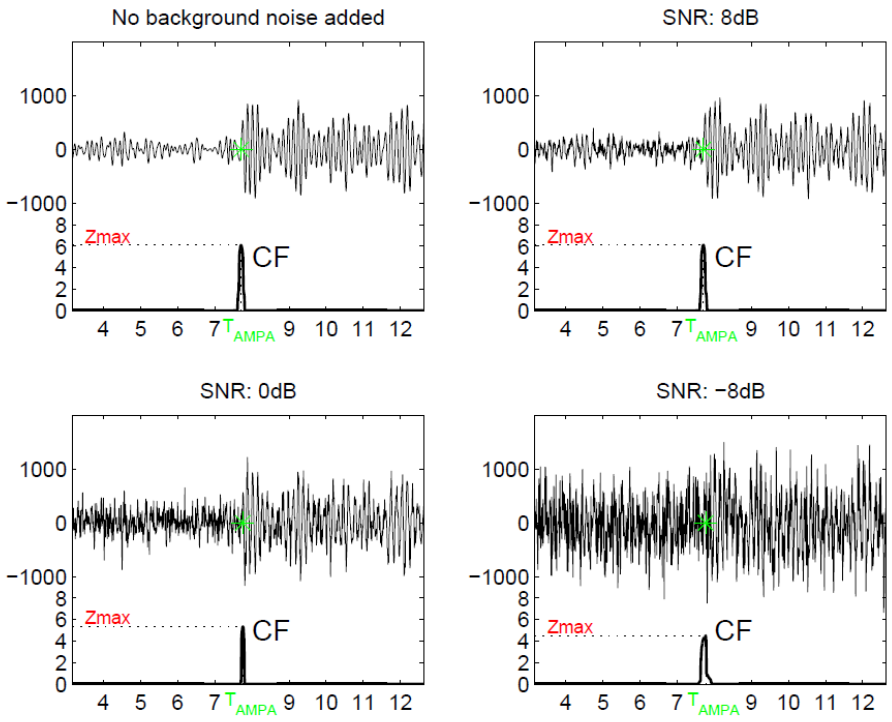

Figure 4.4 *Examples of P-phase picking for an earthquake artificially contaminated with different levels of noise. AMPA sets the arrival time at the instant when CF gets its maximum amplitude. The effect of noise can be seen as Zmax amplitude decreases two points comparing the clean signal (upper left panel) to the most challenging scenario with SNR=-8 dB (lowest right panel).From García et al., (2016).*

In order to enhance and optimize the AMPA algorithm with TOMO-ETNA data, we performed an iterative procedure for P-phase picking. It is based on the fact that the shots were registered every 90 s and therefore, the hypocentral distance between shot and station nearly changed. Indeed, the travel times between consecutive shots must be quite similar. This means that time difference between the P-phase onset on and *i*- signal and the onset time of the *i-1* signal (Δtime hereafter) should be small. The algorithm compares the picking time with the previous and following register on a selected station

searching for the CF maximum value comprehended between both times. This iterative searching is preformed several times until a minimum value is achieved.

4.6. TOMO-ETNA Database

For the case of TOMO-ETNA database, after several tests including manual revision of the picking, we selected the quality thresholds for the final dataset. We considered three different quality parameters: i) Zmax; ii) SNR; and iii) Δtime. We defined a minimum Zmax value of 6 (the higher the value the better is). The SNR minimum value defined was of 2 and a Δtime of < 0.5 s. Table 4.1 shows three examples of how restrictive the thresholds are. Indeed, we only select high-quality data in order to ensure a completely trustful tomographic result. The reduction of the initial register signals to the final dataset is dramatic and this fact is caused by several conditions: i) high ambient noise rate; ii) volcanic tremor that masks the signals; iii) high attenuation of the P waves for the furthest stations, etc.

Station-date	**Number of shots registered**	**Zmax**	**Zmax + SNR**	**Zmax + SNR + Δtime**
Broadband (EMFO)-	701	96	280	182
Short-Period (E-90)	862	66	342	260
Broadband (e6014)	862	05	76	35

Table 4.1 *Number of shots selected for the register of one station in one day (28-06-2014), after applying the different quality threshold: Zmax>6; SNR>2 and Δtime<0.5 s.*

Figure 4.5 shows the active seismic signals of several hours of shooting registered in a certain station. Additionally, in the figure we plot the theoretical water wave arrival, which gives us an idea of the movement of the vessel.

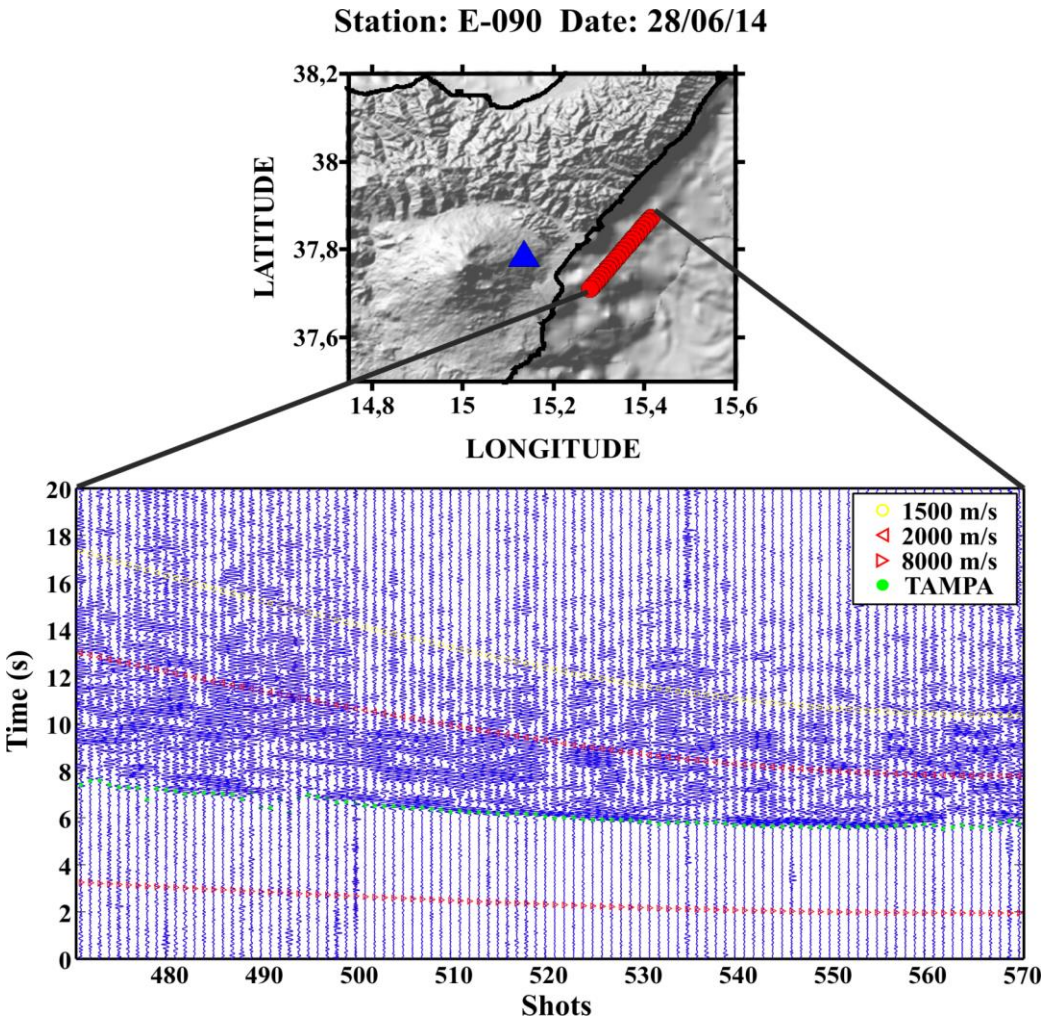

Figure 4.5 *Seismic Signals and P-phase picking of 100 shots registered in one short-period seismic station (E-090). The upper panel shows the position of the station (blue triangle) and the position of the shots (red circles). Lower panel shows the seismic recording of these shots. Red triangles mark the upper and lower limits of seismic velocity used to constrain the P-phase picking. Yellow triangles mark the theoretical water wave arrival using a P-wave velocity of 1.5 km/s. Green dots represent the P-phase arrival detected by AMPA using the iterative procedure.*

Another quality assessment is to visualize how the seismic signals are register following a 1-D profile moving away from the shot location and evaluate the quality of

the automatic picking. This test is illustrated in figure 4.6 for the active sources where we plot a series of 10 seismic stations including short-period, broadband and OBSs from the temporary network and stations from the permanent INGV network. We selected a 10-station E-W profile crossing Mt. Etna edifice to test the quality of the seismic signals and the accuracy of the picking (Figure 4.6a). As evidenced in figure 4.6b, we recorded high quality seismic signals up to 50 km from the seismic source and we were able to detect automatically the P-phase onset for these distances. Note that for the register of the shots in the OBS station, the water wave is so energetic that can mask the actual P-wave arrival. In this case, an analysis in the frequency domain, like AMPA procedure, permits distinguishing the real P-wave arrival from other slower arrivals (Figure 4.6c).

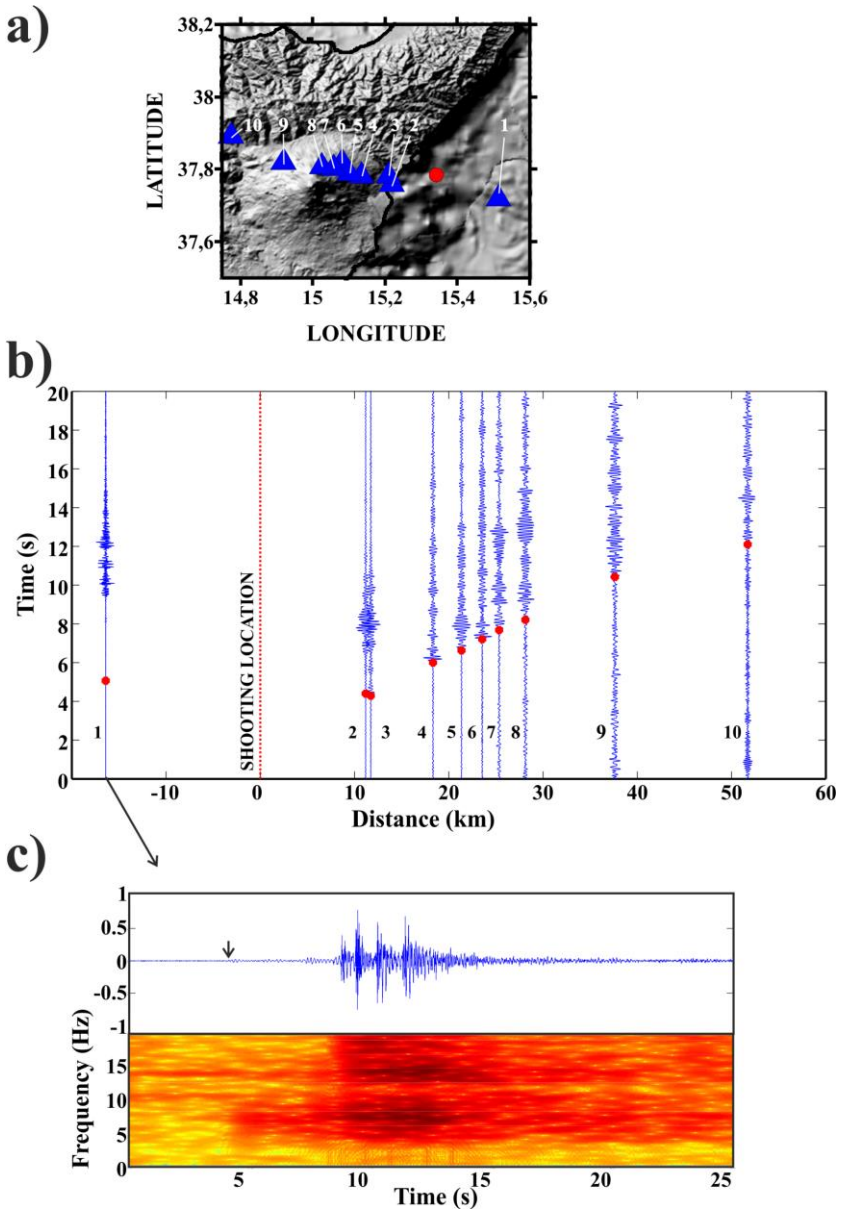

Figure 4.6 a) *location of the selected seismic station profile (Blue triangles represent the station) and the shot position (red circle).* ***b)*** *Seismic signal registered in each station represented in terms of the epicentral distance to the shot.* ***c)*** *Seismic signal and spectrogram of the shot register in an OBS station. Black arrow marks the P-phase arrival.*

On the other hand, the passive sources were registered often in more than 50 stations satisfying the set quality thresholds (Figure 4.7). It is remarkable that as well as for the active sources, the earthquakes were registered even at large epicentral distances. Indeed, figure 4.7 shows an example of an event registered with high quality at distances of more than 90 km from the epicentre.

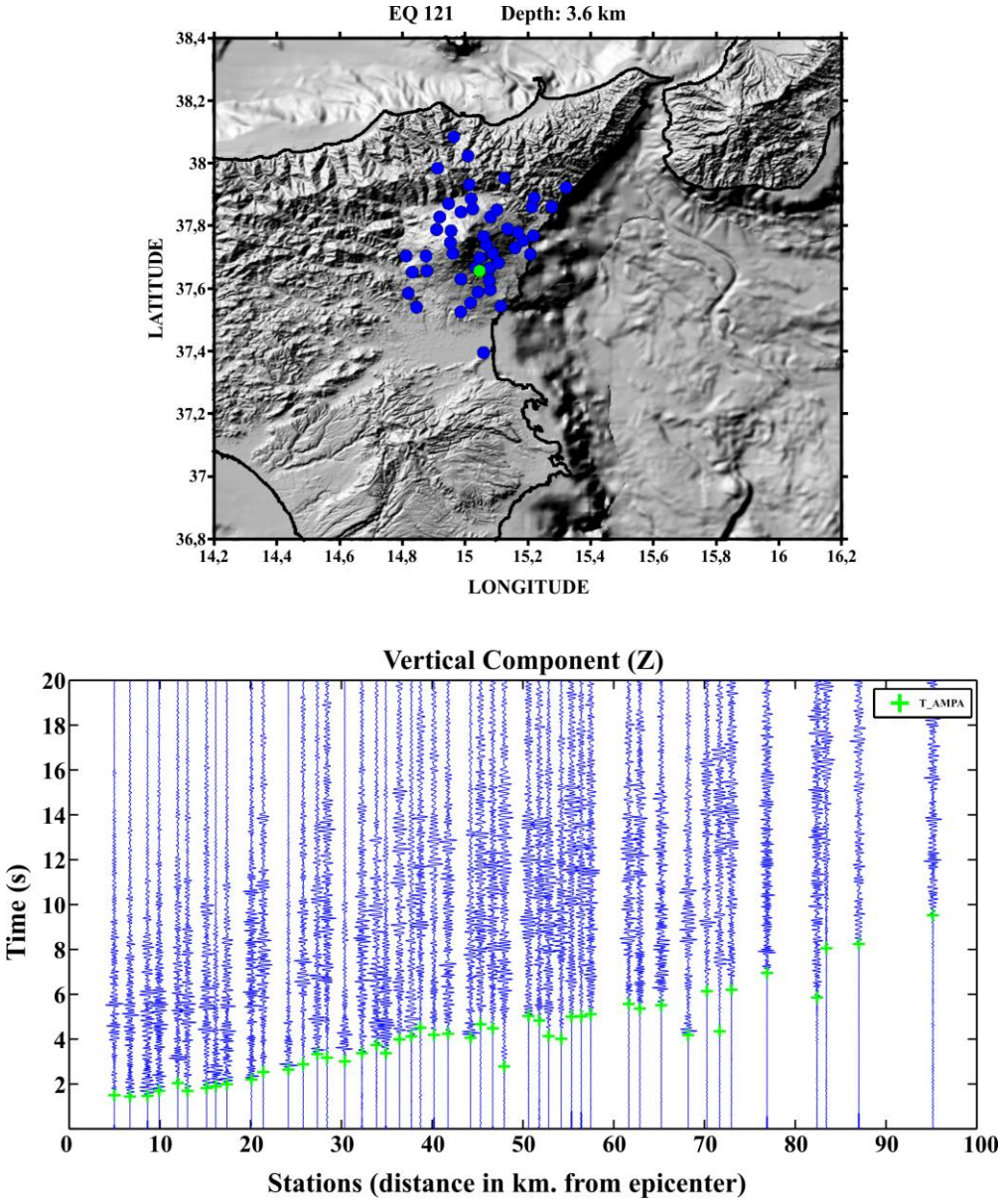

Figure 4.7 a) *location of the selected earthquake (green dot) and the stations that registered it with enough quality (blue dots).* ***b)*** *Seismic signal registered in each station represented in terms of the epicentral distance to the earthquake. Green cross represent the P-wave onset detected by AMPA.*

4.7. Final Dataset and Remarks:

At the end of the picking process, we obtained a final dataset of 184,797 P-phase travel times for the active sources and 11,802 P-phase travel times for the passive sources. This picking has been performed using the 267-station network operative during the TOMO-ETNA experiment, which includes short-period, broadband and OBS stations. Once the final high-quality dataset is set, the seismic velocity tomography can be carried out. In this work we invert for the first time active and passive seismic data simultaneously, by developing a new software described by Díaz-Moreno et al., (2016). This tomographic code will be described in detail along the next chapter of this thesis. Additionally, a user-guide of the software is provided in Appendix 5.

5. Joint Passive Active Ray Tomographic Software (PARTOS)

...

5.1 Tomographic Software State of the Art

The TOMO-ETNA experiment described in chapter 3 (Ibáñez et al., 2016a) provided a large high-resolution seismic dataset, aiming to enlighten the complex internal structure of Mt. Etna and surrounding areas. This database includes active and passive data recorded during 2014 (Barberi et al., 2016; Ibáñez et al., 2016b). In this work we take advantage of this large high-quality dataset to perform for the first time at Mt. Etna volcano a simultaneous joint inversion of active and passive sources by applying a new tomographic code developed ad-hoc (Díaz-Moreno et al., 2016). This software named PARTOS (Passive Active Ray TOmography Software) will be described along this chapter and a User Manual of it is provided in Appendix 5.

Seismic tomography methods appeared in the early 1970s and from their first application these techniques have been widely used in different scales and environments. Their theoretical and mathematical bases are well known by the scientific community, but still new algorithms and approached are being developed. Implementation procedures on a tomographic code may vary depending on the scope of the study (global, regional or local) and the data available (Koulakov 2012, Koulakov and Shapiro 2015). At present, several tomographic algorithms can be easily found among the international community. Some of these codes were developed for a specific region and later adapted to other regions. For example the code developed by Toomey et al., (1994) was initially applied in the Pacific Rift and later adapted to other regions such as Deception Island in Antarctica (Zandomeneghi et al., 2009). On the other hand, many codes have been developed to be used in a wide range of areas. Some of the most relevant and well known codes are: SIMULPS (Thurber 1983; Eberhart-Phillips 1993) applied in Vesuvius (Lomax et al., 2001) and Mt. Etna (Patanè et al., 2006) among others; FAST (Zelt & Barton 1998) applied in India by Rao et al., (2015); TOMODD (Zhang & Thurber 2003; applied for example by Kato et al., (2010) in Wakayama, Japan; or Alparone et al., (2012) in Mt. Etna, Italy); or LOTOS (Koulakov et al., 2009a). Each of these codes is different in some procedures such as ray tracing, grid parameterization or matrix inversion among others. When only passive seismic signals (earthquakes) are used, its application is mainly limited to regions with high seismicity.

LOTOS software (Koulakov, 2009a) has become one of the most widely used codes for tomographic inversion of passive data. LOTOS code is a friendly widely used tomographic code that permits study from small regions using local events to regional inversions using teleseismic events (Jakovlev et al., 2013). The robustness of the algorithms implemented and the capacity to handle different scales studies (regional or local), together with its friendly use makes of this code one of the most popular and used software among the scientific community. Robustness of the code has been highly proved by the numerous of published works applying this software in a large variety of regions (Table 1). These studies vary from active volcanic areas, dormant volcanoes and non-volcanic areas, and demonstrate the versatility of the code. Passive seismic data comes from local, regional and teleseismic earthquakes. These data are generated within a wide range of depths and therefore give usually a better ray coverage in depth of the studied region. However, number of earthquakes depends on the region. Earthquake location coordinates and origin time are unknown and must be calculated by using the available information: arrival of the seismic waves to the different seismic stations. Local and regional seismicity usually produces clear P- and S-waves that are, then, inverted for obtaining plausible velocity models and source parameters.

The limitation of lack of seismicity is partially solved with the use of active sources. These seismic data comes from human-made seismic sources and there is a wide range of methods: chemical reactions, drop of a mass, airgun shots, explosions, etc. (Koulakov, 2012, Koulakov and Shapiro, 2015). At present, active source tomography has been implemented in few codes such as FAST and ATOM-3D (Koulakov 2009b).The main characteristic of these codes is that the take into account the water table when computing the ray-tracing, which is a very sensible step when studying sea-related environments such as volcanic islands.

ATOM-3D code follows the same structure as LOTOS, but for active datasets. In this case, no relocation of the events is performed, as location and origin time of the active source is a priori known, and it is taken as a fixed parameter. This algorithm has been successfully tested in some active seismic studies such as Tenerife (García-Yeguas et al. 2012) and Eastern Greece (Shahrukh et al. 2012). The main advantage of the use of

active sources is that they permit to register seismic waves in whatever region. Nonetheless, it is very expensive and therefore not always available (Koulakov & Shapiro 2015). Commonly, active sources give very detailed information of the shallower layers of the crust. However, resolution in depth is poor due to the fact that they can only be produced near the surface. The main characteristic of the active sources that make them useful for seismic tomography is that we certainly know the exact time origin and location of both source and receiver, and therefore we only have the ray tracing variable. Clear P-wave arrival can be registered from active sources while S-wave arrivals are not always available.

Recently, some efforts have been focused on the use of both seismic sources to obtain a joint seismic tomographic image. For example, a few algorithms merge both active and passive data (eg. Battaglia et al 2008b; Rawlinson & Urvoy 2006; Wagner et al. 2007). The major complexity of these new joint procedures is that active and passive seismic data have different characteristics such as its source location; therefore, it is important to take into account these differences in order to better adapt the algorithms for each case. The combination of these two types of sources permits to diminish their lack of information and enhances their valuable information. Active sources can cover areas where no natural seismicity is located. On the other hand, earthquakes may give important information of the deep layers of the crust and of S-wave properties. By merging active and passive data we obtain better ray coverage in both shallow and deep layers, leading to a higher resolution of seismic tomography models.

Along this chapter, we describe PARTOS, a new tomographic code developed for joint inversion of active and passive datasets. This code was born to solve the above mentioned necessities.

Region		Type	N. EQ	N. Stations	Period	Area	P-S wave	Reference
Kamchatka Peninsula	Kluchevskoy volcanic group	Active volcanoes	>5,000	17	1 year	4,984 km^2 Grid 3 km	33,428 P 33,865 S	Koulakov et al. (2011)
			80,000	17	10 years (1-year interval) 4D tomography	2,250 km^2 Grid 0.5 km	50,000 to 80,00 phases per interval	Koulakov et al. (2013a)
	Kluchevskoy-Kizimen	Volcano group	100,000	23	10 years	3,520,000 km^2	>1,000,000 P and S	Koulakov et al. 2016
Alaska	Mt. Spurr	Active volcano	512	26	4 months	918 km^2 Grid 1 km	5,960 P 4,973 S	Koulakov et al. (2013b)
	Mt. Redoubt	Active volcano	4,500	19	13 years	1,225 km^2 Grid 1 km	N/A	Kasatkina et al. (2014)
	Saint Elias	Collision zone	8,000	22	4 years	158,720 km^2	150,000 P and S	Zabelina et al. (2014)
Indonesia	Krakatau	Active	700	14	1 year	1,485 km^2	3,128 P	Jaxybulatov

		volcano				Grid 3 km	2,050 S	et al. (2011)
	Toba Caldera	Supervolcano	1,500	30	4 months	6,250 km^2	3,377 P 2,462 S	Koulakov et al. (2009b)
México	Popocatepetl	Active volcano	504	22	2 years	260 km^2 Grid 1 km	2,830 P 3,259 S	Kuznetsov & Koulakov (2014)
Canary Islands	El Hierro	Active volcano	13,040	9	1.5 year	300 km^2 Grid 2 km	89,583 P 95,339 S	García-Yeguas et al. (2014)
Saudi Arabia	Harrat Lunayyir	Basaltic field	1,879	8	< 1 year	1,050 km^2 Grid X km	8,904 P 10,579 S	Koulakov et al. (2014)
Chile	Villarica	Active volcano	50		1 year			Thorwart et al 2014
Colombia	Galeras	Active volcano	14,150	58	>25 years	425 km^2 Grid 1 km	N/A	Vargas & Torres (2015)
Costa Rica	Central Costa	Active	2,000	73	2 years	N/A	31,912 P	Dinc et al.

	Rica	Tectonic Region					9,298 S	(2010)

Table 1Recent most relevant tomographic studies performed using LOTOS code (Díaz-Moreno et al., 2016).

5.2 Description of the code

PARTOS code has been developed for the simultaneous tomographic inversion of active and passive seismic data. The workflow of the algorithm and general data structures are shown in Figure 5.1.

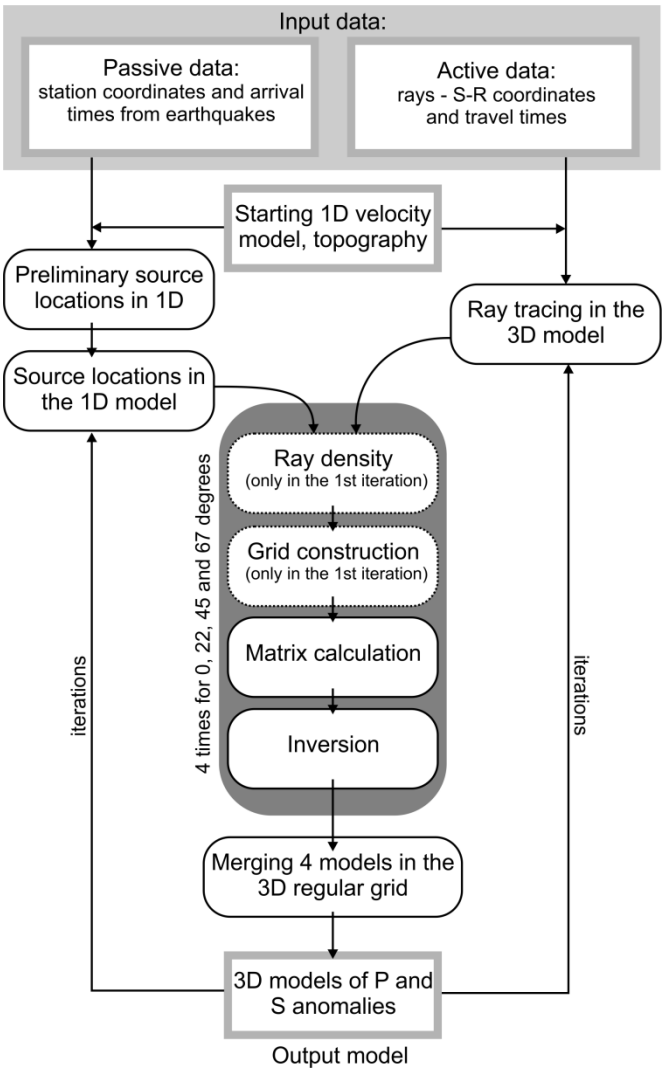

Figure 5.1. *Schematic PARTOS workflow for active and passive data. Rectangles represent the data files and rounded blocks depict the steps of the program. Steps with*

dotted lines are performed only once in the first iteration (From Díaz-Moreno et al., 2016).

5.2.1 Input data:

The input data for the calculations include the data groups related to active and passive seismic experiments, as well as the starting 1D velocity model and other parameters for calculations. The passive source data include two files: one with geographical coordinates of stations and another one with arrival times of P- and S waves from earthquakes to the stations. The information on the source coordinates and origin times is not strictly required. In case of its absence, the sources can be placed to the center of the network or beneath the station with minimum arrival time. If the locations of events are available a priori, they can be included to the initial data file that may facilitate the calculations.

For the active source data, there is only one file. Each line in this file corresponds to one ray containing geographical coordinates of the source and the receiver and travel time of seismic wave. The first three lines should correspond to the gathers for which the data were picked. In the cases of offshore surveys with the use of air-guns, the gathers are usually the stations, whereas in the cases of using a few explosions and numerous receivers, the gathers are the sources.

The initial data files may contain the two-dimensional map of topography (in case of absence, the flat topography is predefined at zero depth). It is especially important in cases of offshore experiments, when the travel time in the water layer between air-guns and sea bottom should be taken into account.

The file with the 1D model of the P and S wave velocities should be defined. The velocity values are set at some depth levels; between these levels, the velocity is linearly interpolated. The values of the initial S-velocities are often determined from the P-velocities based on constant Vp/Vs ratio.

In addition, a file with a set of different parameters used for calculations should be defined. This file includes, among others, the grid spacing, parameters for ray tracing and source locations, weights for the active and passive data, damping parameters for

inversion, and visualization settings. Defining these parameters is mostly based on several trials of performing the inversions for real and synthetic datasets.

5.2.2 Source locations and ray tracing

For the passive data, the location of sources is conducted in a same way as in the LOTOS code (Koulakov, 2009a). For the preliminary locations, there are two options providing simplified algorithms for computing travel times of seismic rays: i) the first option presume computing a table of reference times in the starting 1D model for all combinations of source depths and epicentral distances. In this step, analytical formulas for ray tracing in the 1D model from Nolet (1981) are used. Then the travel times of rays are calculated by linear interpolations of values from this table; ii) for some areas where the depths of events are compatible with the lateral dimensions, another option with computing travel times along straight ray paths appears to be more efficient. Using these approximations makes possible conducting voluminous calculations of source coordinates using the grid search method, which is described in Koulakov and Sobolev (2006c).

The second step localizes the sources in the 3D P and S velocity models using the gradient descending method (Alinaghi et al., 2007). In this case, the calculation of the travel times is performed using the bending method of the ray tracing based on the principle of time minimization proposed by Um and Thurber (1987). This algorithm permits any parameterization of the velocity distribution. The only necessary step is to define one positive velocity value at any position of the study area. For each iteration, this step is performed for an updated 3D velocity model derived from the previous iteration. Figure 5.2 shows a schematic illustration of the bending method. This example is set using a checkerboard with anomaly contrasts of ±30% (Koulakov 2009a).

The minimum travel time is calculated in several stages. The initial raypath is a straigh lines between source and receiver, which are considered fixed (1 and 2 in Figure 5.2a). Bending is calculated during the first step by perpendicularly deforming the ray from its center (point A). Bending of the ray is performed in and across its plane. Shift values for the new path depend linearly on the distance between A and the end of the new segment. For the second step (Figure 5.2b), three fixed point are present (points 1, 2 and 3) and bending is calculated for 2 segments. Further steps follow the same procedure

(Figure 5.2c). In this example, the final ray is composed by 8 different segments tending to travel through positive anomalies and avoiding low velocity anomalies (Figure 5.2d). Note that this scheme is illustrated in 2-D, while the implemented algorithm computes 3-D velocity distributions.

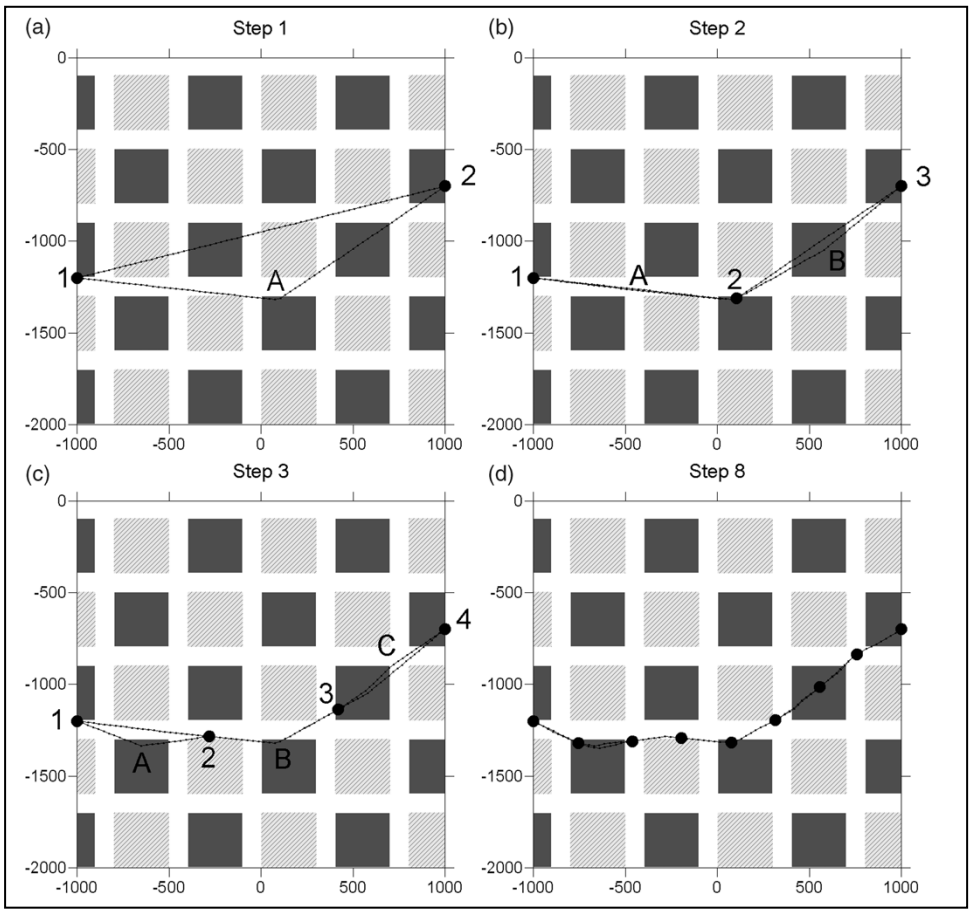

Figure 5.2. *Bending method scheme. Ray construction is illustrated for an exagerated velocity distribution. 1D velocites vary from 2.5 to 9 km/s in 2km depth. Grey squares represent negative anomalies of -30%; black squares represent positive anomalies of +30%. (From Koulakov 2009a).*

The same algorithm of ray tracing is used for the active-source data. In the case of the offshore shooting using air-guns on the sea surface, the ray is computed for the entire paths including the parts in the water layer, where velocity is presumed constant

and equal to 1.44 km/s. The calculations are performed using the regular 3D bending ray tracer between the source on the sea surface and the station.

5.2.3. Grid construction

To parameterize the 3D velocity distribution, we construct the mesh with nodes distributed in the study volume according to the ray density. Between the nodes, the velocity anomalies are continuously approximated using a linear interpolation. Because of significant disproportion in the amount of passive and active data, the ray density is computed using different weights for the P and S data. The nodes are placed only in areas with sufficient ray coverage (typically, with the ray density of 0.1 of the average value). In the map view, the nodes are installed regularly with a fixed grid spacing. In the vertical direction, the grid spacing depends on the ray density; this is, the higher the ray density is the finer the grid spacing can be. In well covered areas, the spacing is equal to the minimum predefined value; and it becomes larger where the ray density is lower.

Usually, the grid spacing is set smaller than the expected resolution so that every restored anomaly was based on several nodes. This helps to avoid the dependency of the results on the grid configurations. To further reduce this effect, we perform the inversion for several grids with different basic orientations (typically, four grids with orientations of 0, 22, 45 and 67 degrees). After computing results for all grids, they are averaged in one 3D model using a regular mesh. The grid is constructed only one time in the first iteration. In the following iterations, the velocity anomalies are updated in the same nodes.

5.2.4. Matrix calculation and inversion

To perform the tomography inversion, we compute one matrix which includes the pairs of the active and passive data. The matrix elements responsible for the velocity distributions are the first derivatives A_{ij} representing time deviation along the j-th ray due to the unit velocity variations in the i-th node (eq.1).

$$A_{ij} = \int_{\gamma} \Delta g_j(\gamma) dS / \Delta \sigma_j \quad (1)$$

Where Δg_j represents the slowness perturbation at the point of the ray caused by slowness anomaly $\Delta \sigma_j$, at the j-th node (Koulakov & Sobolev, 2006b). Their values are

computed by numerical integration along the ray paths derived after the steps of locations (for the passive data) and ray tracing (for the active data). For the passive data, each row of the matrix contains also four elements responsible for source parameters (Px, Py, Pz and 1) and one unit element responsible for the station correction (P or S). For the active source data, there is only one additional element responsible for the gather correction (usually, stations, for the air-gun surveys and sources, in cases of explosions on land). The data vector contains the time residuals computed for the current velocity model.

The inversion is damped by using two additional matrix blocks. The first block, which is responsible for amplitude damping, is a diagonal matrix containing only one non-zero element in each row and zero data vectors. Increasing weight of this block decreases the amplitude of the solution. The second damping block controls the flattening of the solution. Each row of this block contains two nonzero elements with equal values, but opposite signs, corresponding to all combinations of neighboring nodes in the parameterization mesh. Increasing the weight of this block decreases velocity gradients in the resulting models.

The inversion of the large sparse matrix is performed using the LSQR algorithm (Page and Saunders, 1982; Nolet, 1981). The most important parameters controlling the inversion with the values optimized for a specific case of the TOMO-ETNA experiment are presented in Appendix 5. The values of these parameters are determined after several trials with synthetic and observed data.

5.2.5. Combining the velocity models and iterating

The models computed for several differently oriented parameterization meshes are averaged and combined in one model defined on a regular grid. This model is used in the next iteration for performing the ray tracing (for active data) and source re-location (for the passive data). Number of iterations is usually fixed at a predefined value as a compromise between the calculation time and accuracy of the solution. To stablish the number of iterations, we use a threshold parameter that represents the time residuals (Koulakov, 2009a). This threshold is usually set at 0.5 and we consider the solution as stable once it decreases slowly down the threshold (usually after 5-6 iterations). In this case, tuning of the solution properties is conducted using the damping parameters. A

regular inversion running in a ‘core i7’ personal computer takes approximately 2 hours to perform 5 iterations.

5.2.6. Synthetic modeling

Synthetic modeling is an important element of the tomography workflow that allows not only assessing the resolution, but also estimating the optimal values of the parameters for calculations. The synthetic modeling should, as adequately as possible, represent the realistic procedure of tomography inversion. The synthetic model is defined as a sum of the 1D reference model (might be different of the starting model used for reconstruction) and synthetic anomalies. The code gives several possibilities of defining seismic anomalies with the use of checkerboard or free-shaped polygonal prisms in horizontal or vertical sections. The calculation of the synthetic data is conducted for the same ray paths as in the case of observed data. The ray tracing is performed using the 3D ray tracer based on the bending algorithm. The synthetic travel times are perturbed with random synthetic noise having similar statistical distribution as the residuals after inversion in the case of observed data. The amplitude of the noise is defined to achieve similar variance reduction during the inversion as during inversion of the experimental data. After computing the synthetic travel times, for the passive data we randomly shift the coordinates and origin times.

The reconstruction of the synthetic model contains same calculation steps as in the case of observed data analysis including the stage of initial source location for the passive data. During the synthetic inversion, we try different values of free parameters to achieve the best correspondence of the reconstructed anomalies with the original model. These parameters are then used to invert the experimental data.

A large set of synthetic tests have been carried out in order to test the stability of the algorithms and the quality of the dataset used. These tests include horizontal and vertical checkerboards, free anomaly tests and Jackknifing tests for three different data subsets (Fig. 5.3). Along the next chapter we plot and discuss the tomographic inversion results obtained applying PARTOS to the TOMO-ETNA dataset; and the already mentioned synthetic modelling tests. In order to prevent very large chapters, we moved many of the resolution figures to Appendix 6.

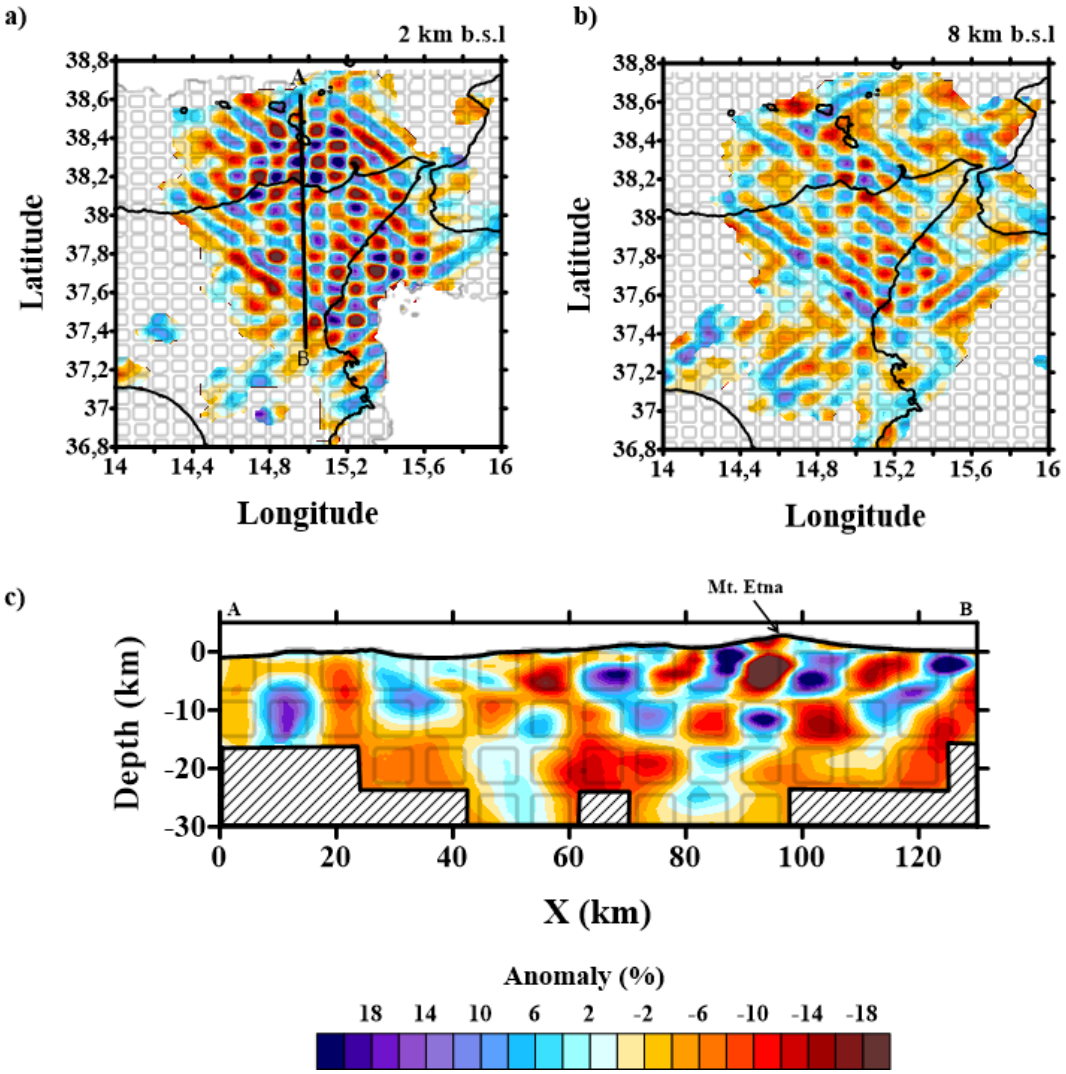

Figure 5.3. *Synthetic modelling of TOMO-ETNA experiment region: a) 8-km-cells horizontal checkerboard at 2 km b.s.l.; b) 8-km-cells horizontal checkerboard at 8 km b.s.l.; c) 8-km-cells Vertical Checkerboard through a N-S profile across Mt. Etna.*

5.3. Final remarks

As final remarks we can state that PARTOS is a friendly tomography code born from the necessity of combining active and passive seismic data during a tomographic inversion. The robustness of the algorithms used is widely proved as most of the algorithms applied were adapted from previous versions of LOTOS and ATOM-3D codes, which are widely used among the scientific community during the last decade. New features have been implemented to enhance the robustness and completeness of the calculations, making the software fast and adaptive to different kind of datasets.

6. Joint active and passive P-wave seismic tomography of Mt. Etna volcano, Aeolian Islands and related geodynamic region

6.1. Joint Seismic Tomography: Database and Study Area.

The joint seismic tomography of Mt. Etna, Aeolian Islands Archipelago and surrounding areas is presented in this chapter.

For that purpose we used the active and passive seismic data recorded during the TOMOETNA experiment detailed in chapter 3. This database has been already pre-processed using advanced P-wave detection algorithms described in chapter 4. Throughout the mentioned data processing we obtained a final dataset of 184,797 P-phase travel times for the active sources and 11,802 P-phase travel times for the passive sources. The seismic network consisted on 267 stations including short-period and broad-band sensors and OBSs. The final dataset has been inverted using a Joint Active Passive Ray Tomography Software called PARTOS, which is explained in chapter 5.

The first step of the joint tomographic inversion is the selection of the starting 1D velocity model that will be used during the rest of the procedure. Then we discuss the grid dimensions and the reliability of the results throughout the synthetic test carried out. Further information regarding the ray tracing and ray density of the solution is presented to prove the quality and robustness of the solutions. Finally, main results both in absolute velocity and anomaly are presented using horizontal and vertical section to better illustrate a series of anomalies that will be further discuss along this chapter.

In order to have a clearer sight of the resulting structures, we focused our tomographic inversion in three different regions as follows (Figure 6.1):

i) Region 1: TOMO-ETNA experiment area

ii) Region 2: Aeolian Island Archipelago

iii) Region 3: Mt. Etna volcanic edifice

Along this chapter we present the results preceded by the synthetic tests and ray density maps for each of these regions separately, in order to give each of them their own importance.

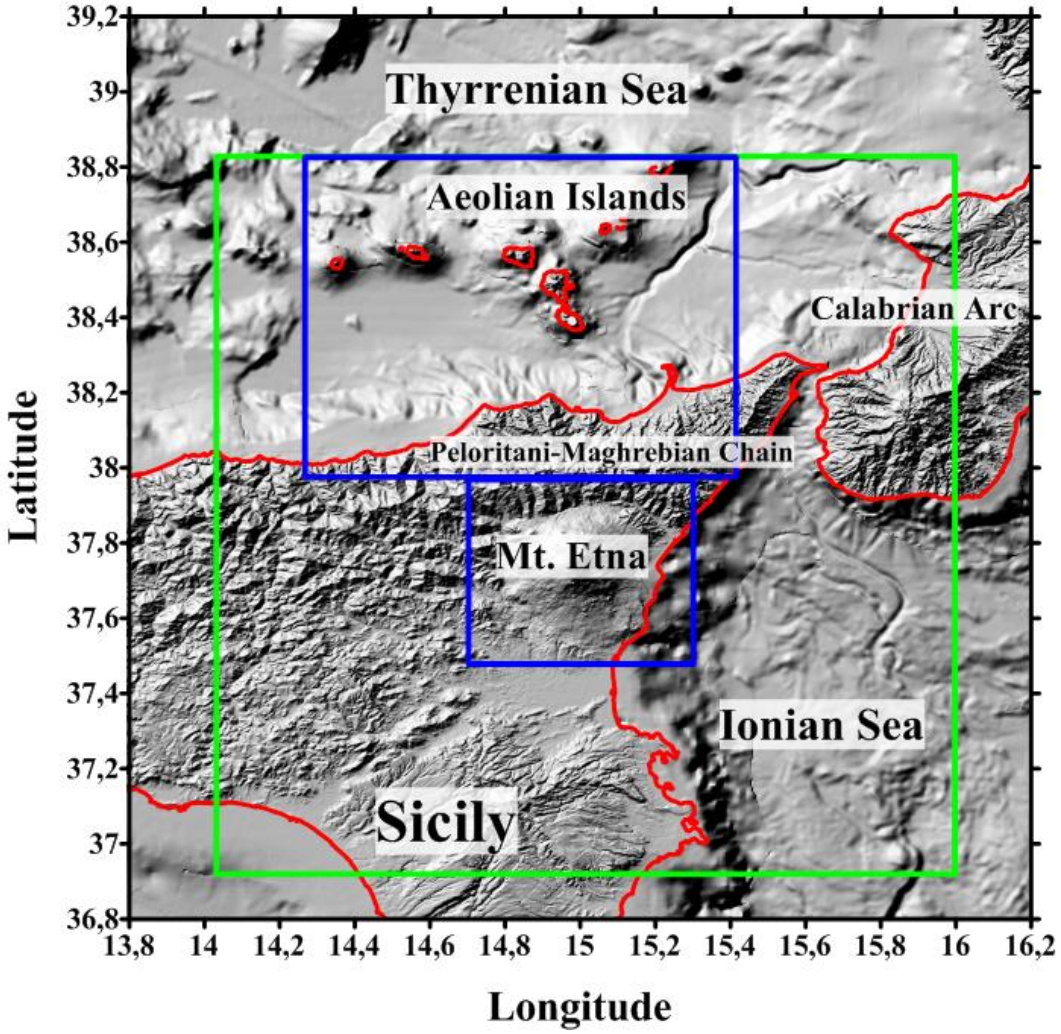

Figure 6.1. *Map of the study area marking the three different regions individuated for the joint inversion: i) Region 1: TOMO-ETNA experiment area (Green square); ii) Region 2: Aeolian Island Archipelago (blue square); Region 3: Mt. Etna volcanic edifice (Blue square).*

6.2. Initial Velocity Model

Establishing the initial 1D velocity model is a crucial step of the tomographic procedure, indeed, slightly different 1D velocity models may lead to different solutions. Therefore it is important to know the geological framework of the region and try to reflect as much a priori information as possible. On the other side, it is convenient to define the initial velocity model with few layers, allowing the tomographic algorithm to freely search the optimal velocity for each node.

First step was reviewing pre-existing velocity models of the region, finding great differences between those calculated for the large-eastern-Sicily region and Mt. Etna volcanic edifice. Mt. Etna's velocity model is described with lower velocities associated to the shallower layers, while the larger region presents higher velocities for the same layers. This difference can be easily explained by comparing the geology of both regions, as volcanic deposits of Mt. Etna are related with lower velocities. On the other hand, the large region averages these lower volcanic velocities with the higher velocities associated to the metamorphic Maghrebian-Peloritanian Chain.

Many 1D velocity models are extracted directly from the dromochrone of the dataset, which is very useful in tectonic, structurally simple regions. Nonetheless, the dromochrone of the TOMO-ETNA database reflects the high complexity of the region under study, and remarks the differences mentioned above (Figure 6.2). Different patterns can be individualized from the original cloud, noting faster and slower regions, remarking the importance of obtaining three-dimensional velocity models that reflect lateral heterogeneities. Therefore, we must take into account that a unique 1D velocity model obtained directly from the dromochrone may not be accurate for the three regions under study; indeed, we searched for an ad-hoc velocity model for each region under study. As an example, table 6.1, shows the initial 1D velocity model we used for the large region (Region 1), for Aeolian Island Archipelago (Region 2), and for the Mt. Etna volcanic edifice (Region 3). We established the same velocity models for Region 1 and 2 after reviewing several tests.

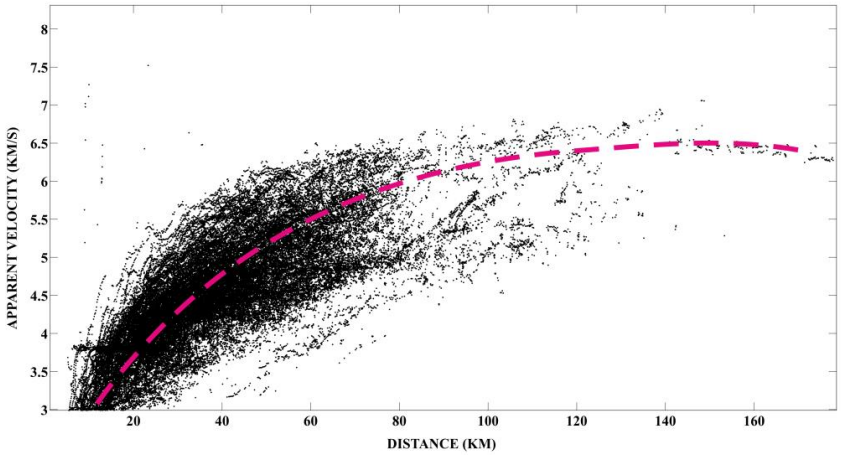

Figure 6.2. *Dromochrone from TOMO-ETNA active seismic final dataset.*

Depth (km)	**P-wave Velocity (km/s) Regions 1 and 2**	**Depth (km)**	**P-wave Velocity (km/s) Region 3**
-4	5.10	-2	2.02
0	5.28	0	3.39
6	5.79	1	3.78
12	6.27	2	4.12
18	6.44	4	4.77
24	6.45	6	5.22
30	7.86	10	5.78
45	8.00	14	6.13
100	8.10	20	6.62
300	8.10	25	6.97
		30	7.80
		50	8.30

Table 6.1. *1D velocity models defined for the tomographic inversion of the whole TOMO-ETNA experiment area (Region 1), for the Aeolian Island Archipelago (Region 2), and for the Mt. Etna volcanic edifice (Region 3). Note that negative depths are considered above sea level.*

6.3. Joint Seismic Tomography Inversion. Region 1

Along the following sections we present the main results of the joint tomographic inversions carried out in the above mentioned regions. For each of them we present the main velocity anomaly images and the absolute velocity maps related. We discuss in detail some of the most important features enlighten in each region, including high and low velocity anomalies related to both tectonic and volcanic structures.

Region 1 is an area that covers 300x300 km comprising eastern Sicily, Mt. Etna volcano, Ionian and Thyrrenian Seas and Aeolian Islands Archipelago (Figure 6.1). Firstly, we present the results of some of the synthetic tests performed in order to constrain grid dimensions and to estimate the reliable area based on our dataset. Then we describe the ray density calculated and finally we show the tomographic images and discuss the main anomalies observed.

6.3.1. Synthetic tests

For the tomographic inversion of this region we selected a grid with a step of 6 km in horizontal and 2 km in vertical, reaching to 30 km in depth. These final grid dimensions were selected after several synthetic tests that vary from horizontal and vertical checkerboards, jackknifing tests and free anomaly synthetic tests. In order to make this chapter easy to read we only present few of the mentioned tests. For more information, go to Appendix 6.

6.3.1.1. Checkerboards

In order to determine the optimal spatial resolution and the smearing effect we carried out a series of checkerboard tests starting with a coarse area comprising the whole TOMO-ETNA study region. Figure 6.3, shows the results of the horizontal and vertical checkerboards inverted for this region. For the horizontal board we inverted a 300x300 km area, using different grid spacing ranging from 12 to 4 km. The horizontal configuration that better resolves the compromise between anomaly size and solution accuracy is a 6km-spacing anomalies. Checkerboard is computed by inverting a pattern of ±10% anomalies periodically placed with opposite polarity and separated 3 km from each other. For this resolution, the model solves convincingly the anomaly pattern in a

horizontal region of around 180·120 km (Figure 6.3a, b) and up to 30 km in depth beneath Mt. Etna (Figure 6c).

6.3.1.2. Free Anomaly test

Inverting a synthetic test using a predefined anomaly permits to determine whether our resulting anomalies can be trusted or not. Following this premise, we have designed 2 anomalies, one of them similar in size and shape to those expected with the real inversions in order to check the capacity of the model to solve them. Positive and negative free anomalies have been set for the larger area (Figure 6.4.a, c). These anomalies are designed to be larger than the grid spacing in order to avoid 1-node anomalies. Figures 6.4.b, and d, show results of these synthetic tests, denoting the optimal reconstruction of both anomalies for 2 different horizontal layers.

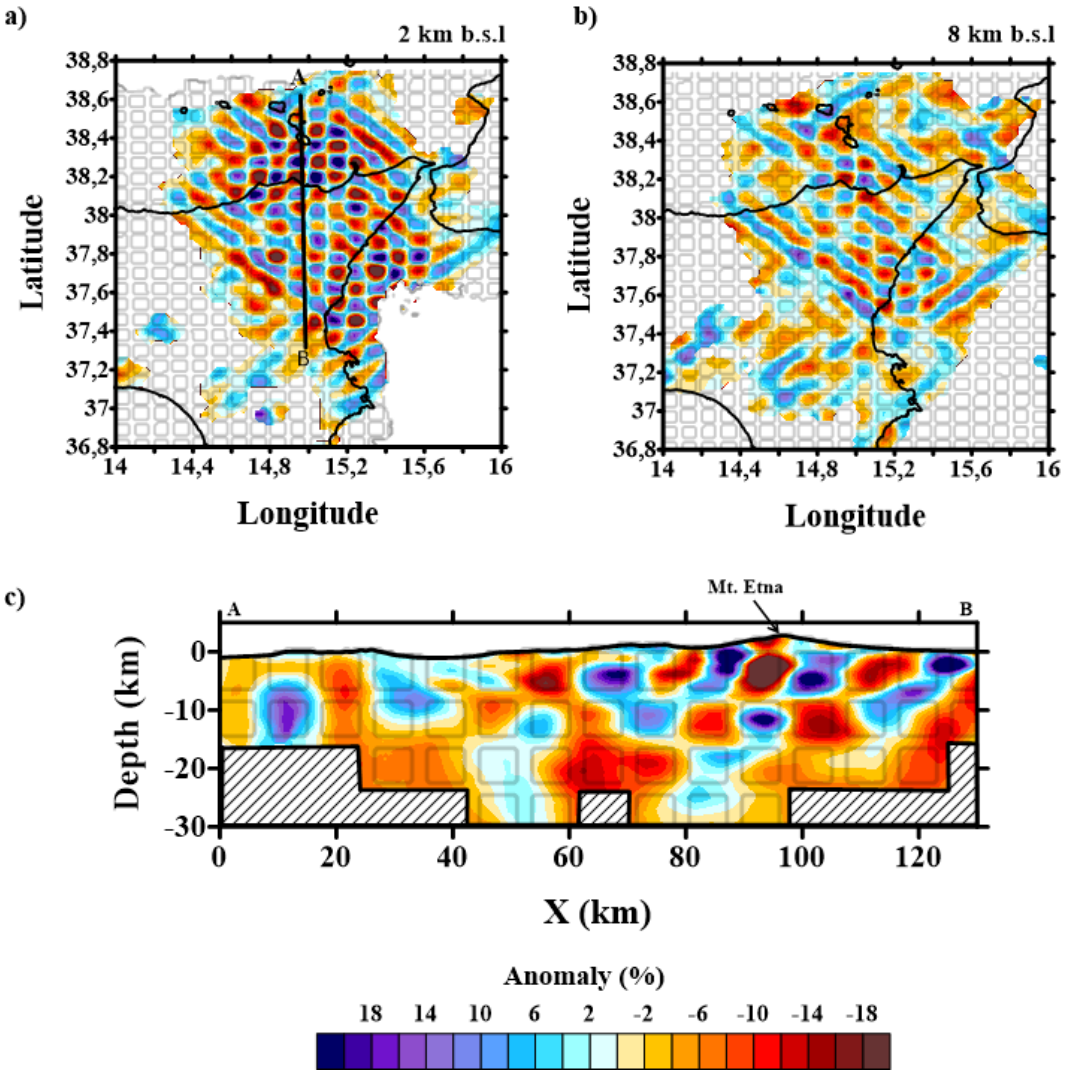

Figure 6.3. *Synthetic modelling of TOMO-ETNA experiment region: a) 8-km-cells horizontal checkerboard at 2 km b.s.l.; b) 8-km-cells horizontal checkerboard at 8 km b.s.l.; c) 8-km-cells Vertical Checkerboard through a N-S profile across Mt. Etna.*

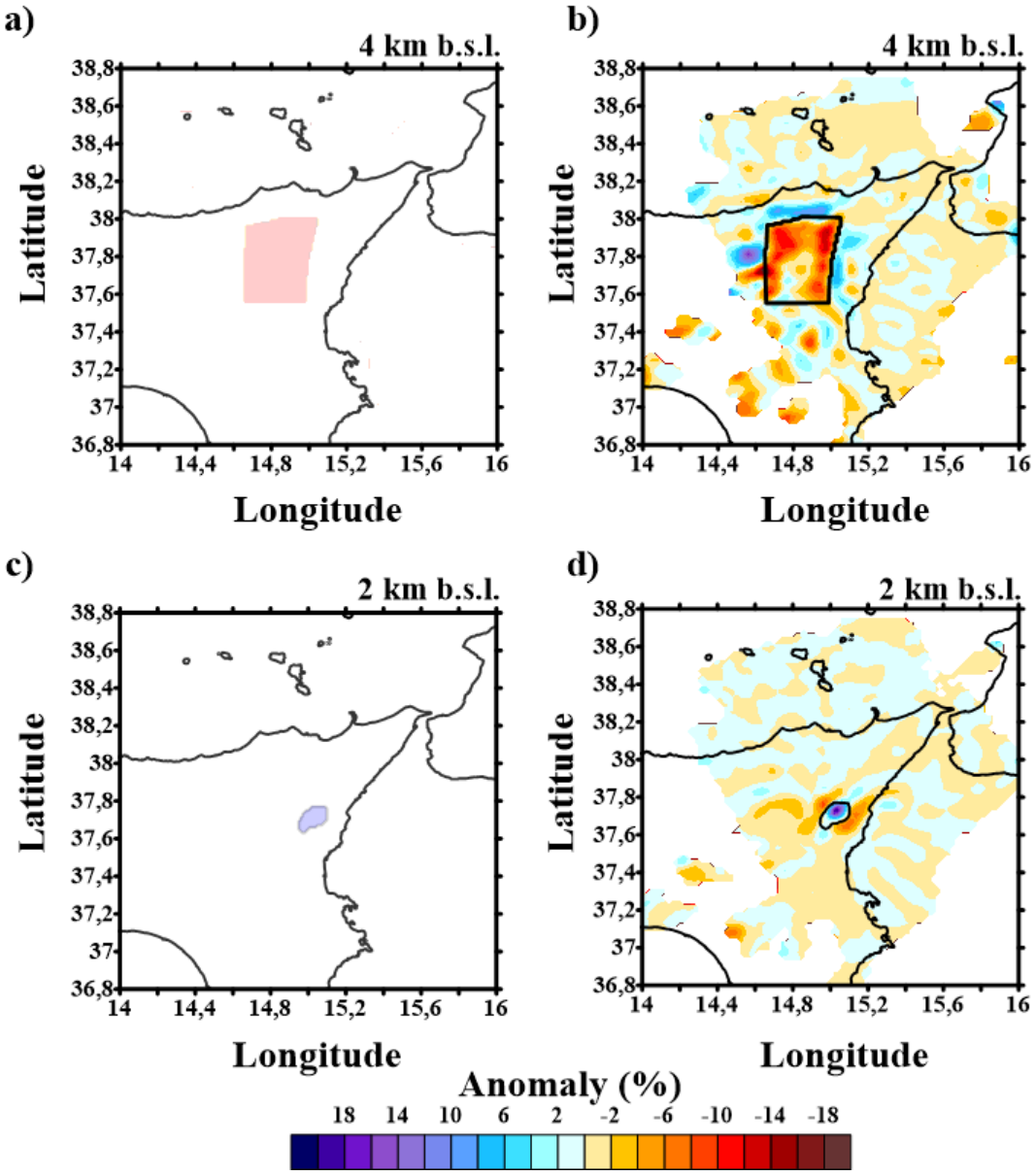

Figure 6.4. *Free anomaly tests for Region 1. a) Free anomaly 1; b) inversion result for free anomaly 1; c) Free anomaly 2; d) inversion result for free anomaly 2.*

6.3.1.3. Jackknifing Test

Noise detection and reduction is an important step during the complete tomographic procedure. Noise reduction is performed during the preprocessing and picking of the data. Additionally, determining the contribution of remnant noise to the final results can be done by performing jackknifing test. This synthetic approach is based on inverting random subsets of data and comparing the final results. Important noise disturbance will modify dramatically the results from different subsets while stable results with low noise should not be modified when reducing the inverted dataset. Some authors as Garcia-Yeguas et al., (2014) take as random subsets the odd and even travel times of the complete dataset. For the TOMO-ETNA dataset we carried out this test by choosing the 50% and 33% of the travel times. The result is the inversion of a reduced dataset that will give us a clear idea of the stability of the results and the possible noise disturbance. Final images of the jackknifing test are presented in figure 6.5 for the whole area, where we compare the full dataset inversion with the 50% and 33% subsets for a single layer (2 km b.s.l.); This figure clearly demonstrate the low noise disturbance to the final results, providing the definitive clue to the quality and reliability of our tomographic results.

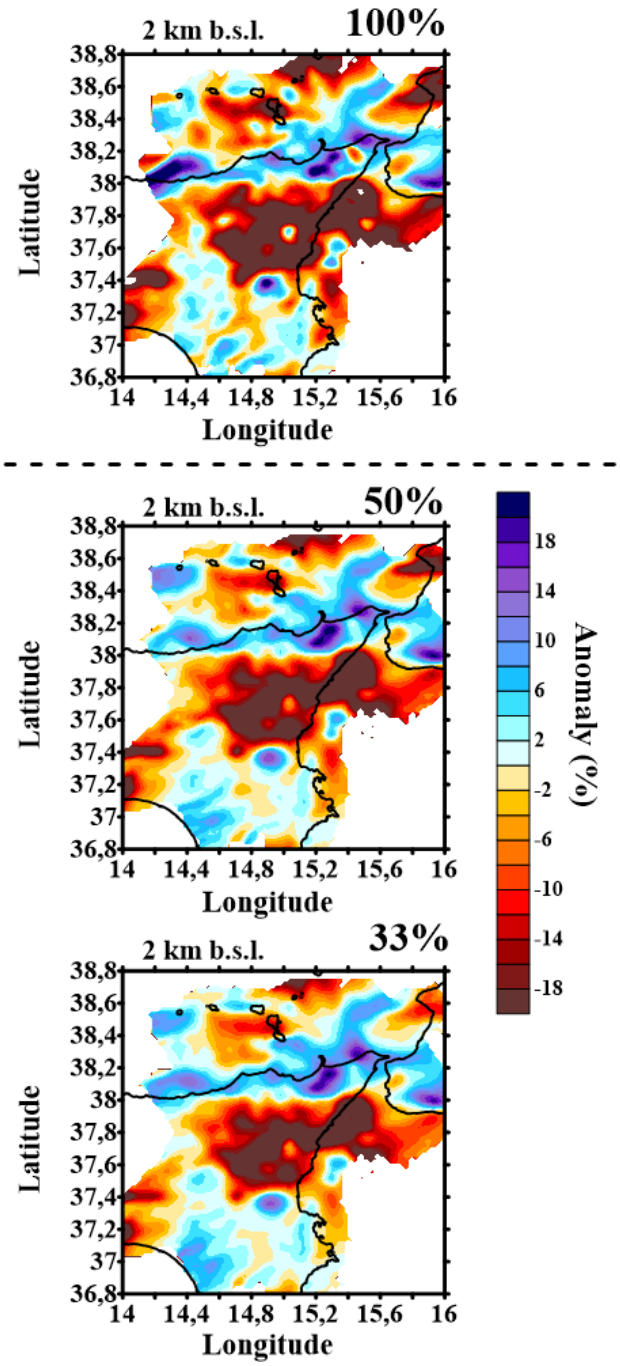

Figure 6.5. *Jackknifing test for Region 1: a) complete dataset inversion; b) 50% of the dataset inverted; c) 33% of the dataset inverted.*

6.3.2. Ray Density

The ray density of the final solution gives us a clear view of the resolution of the model as we see the ray coverage of the whole area. Therefore the areas with a higher ray density are those, whose results are more reliable in confront with those poorly covered. Figure 6.6 shows the ray density for Region 1 separated in different horizontal layers. These results are in agree with the previous synthetic tests, proving the well resolved area is pretty much the same in both checkerboard and ray-density maps.

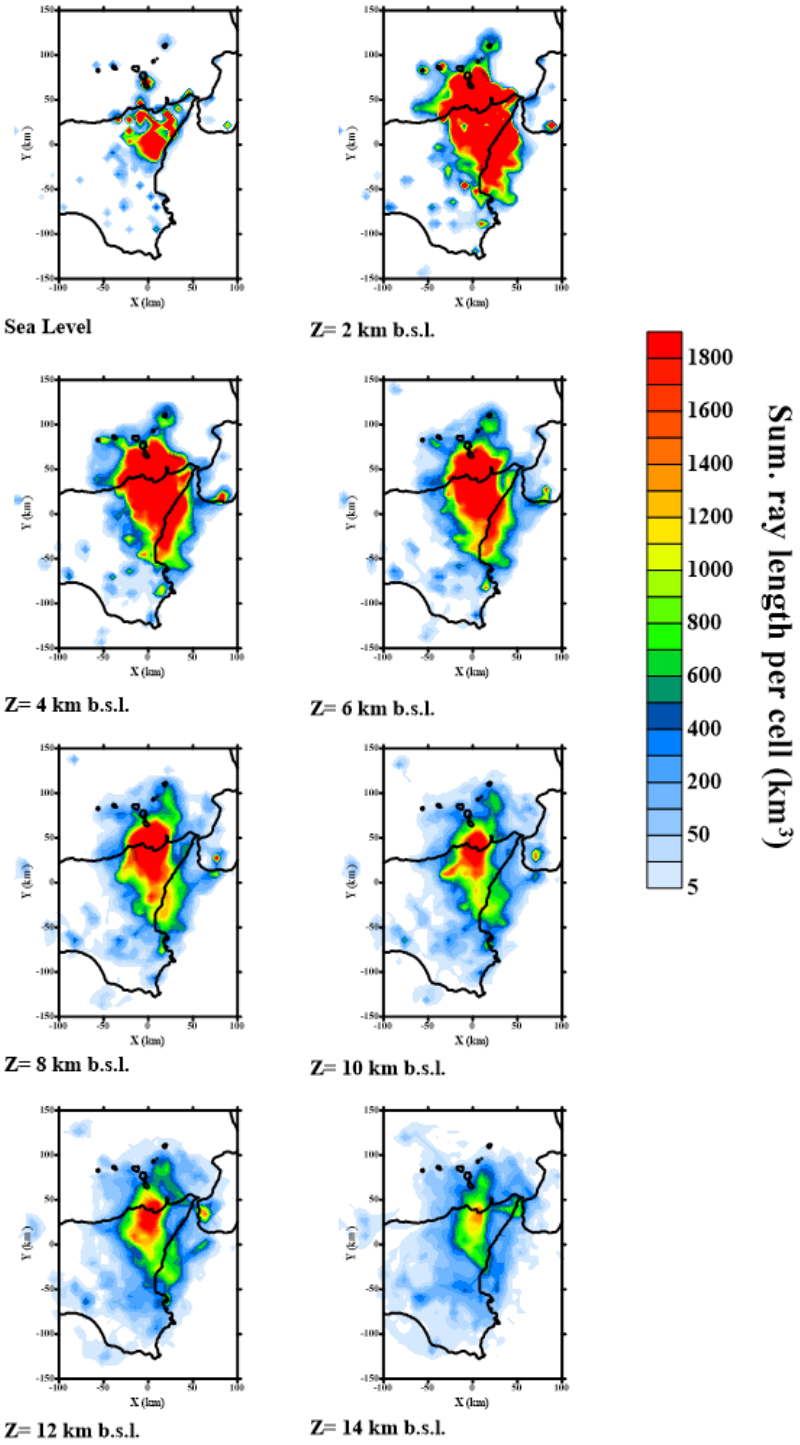

Figure 6.6 *Ray Density for Region 1 for different horizontal layers.*

6.3.3. Joint Tomography Results. Region 1

Along the following paragraphs we illustrate the main horizontal and vertical tomographic images obtained inverting the TOMOETNA final dataset for Region 1. We provide additional discussion of the main observed anomalies based on regional structure interpretations from previous authors. To provide a clear view of the results, we plot first a set of horizontal layers in both absolute velocities (Figure 6.7) and velocity anomalies (Figure 6.8). Then, some relevant vertical sections are presented (Figure 6.9). Finally, we enlarge some of the most relevant horizontal layers (Figures 6.10, 6.11, 6.12 and 6.13), and vertical sections (Figure 6.14) in order to better discuss the main structural anomalies.

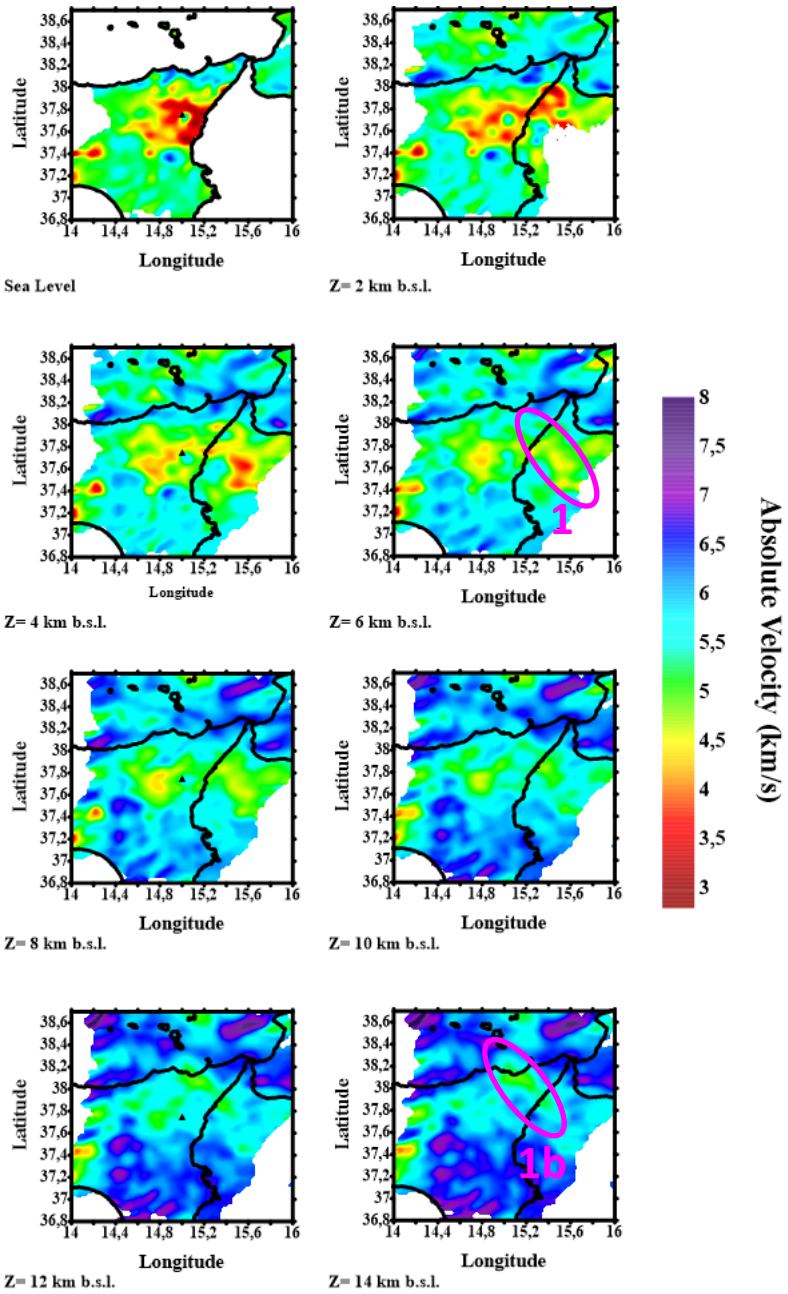

Figure 6.7. *P-wave absolute velocity maps for region 1 at different depth layers. Pink ellipses mark the main structures to be discussed in the text. 1) NW-SE low velocity anomaly velocity (up to 8-10 km depth). 1b) NW-SE low velocity anomaly velocity (10-14 km depth). Black triangle represents Mt. Etna.*

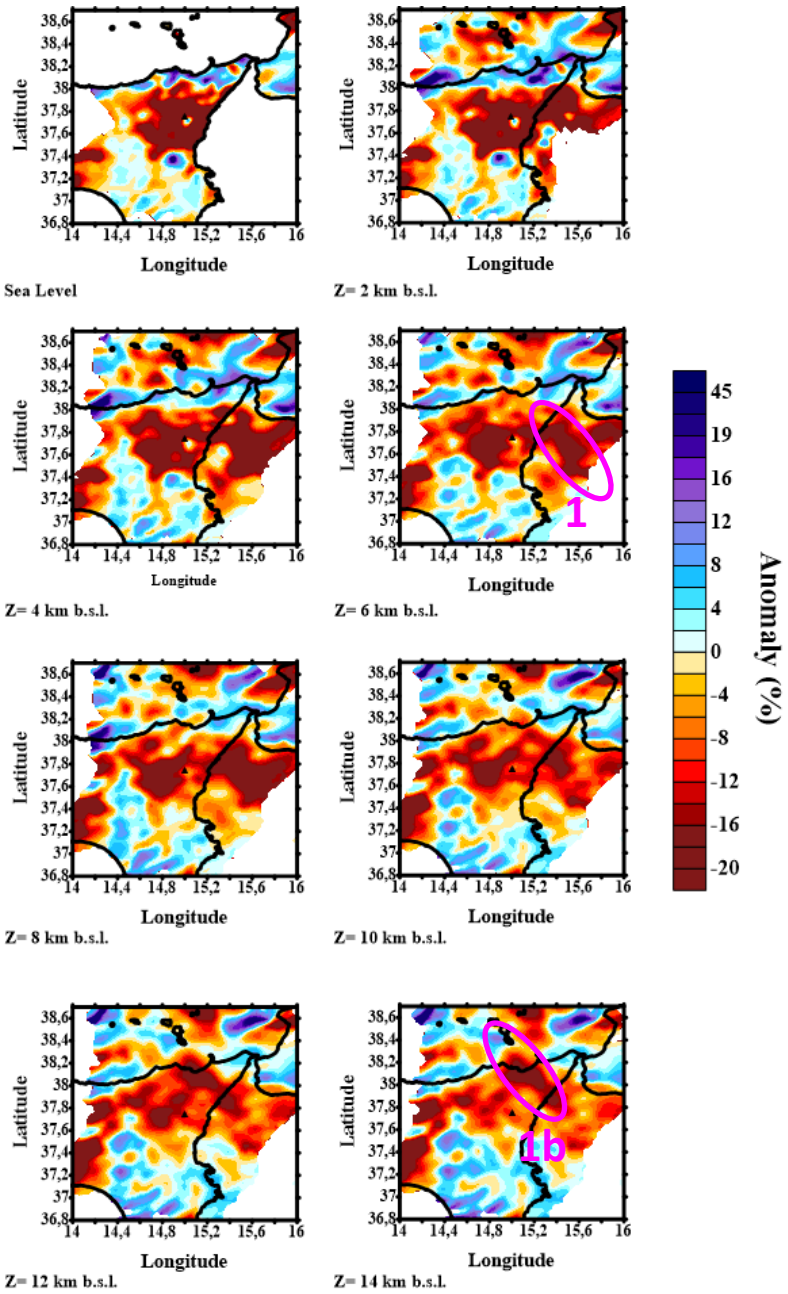

Figure 6.8. *P-wave velocity anomaly maps for region 1 at different depth layers. Pink ellipses mark the main structures to be discussed in the text. 1) NW-SE low velocity anomaly velocity (up to 8-10 km depth). 1b) NW-SE low velocity anomaly velocity (10-14 km depth). Black triangle represents Mt. Etna.*

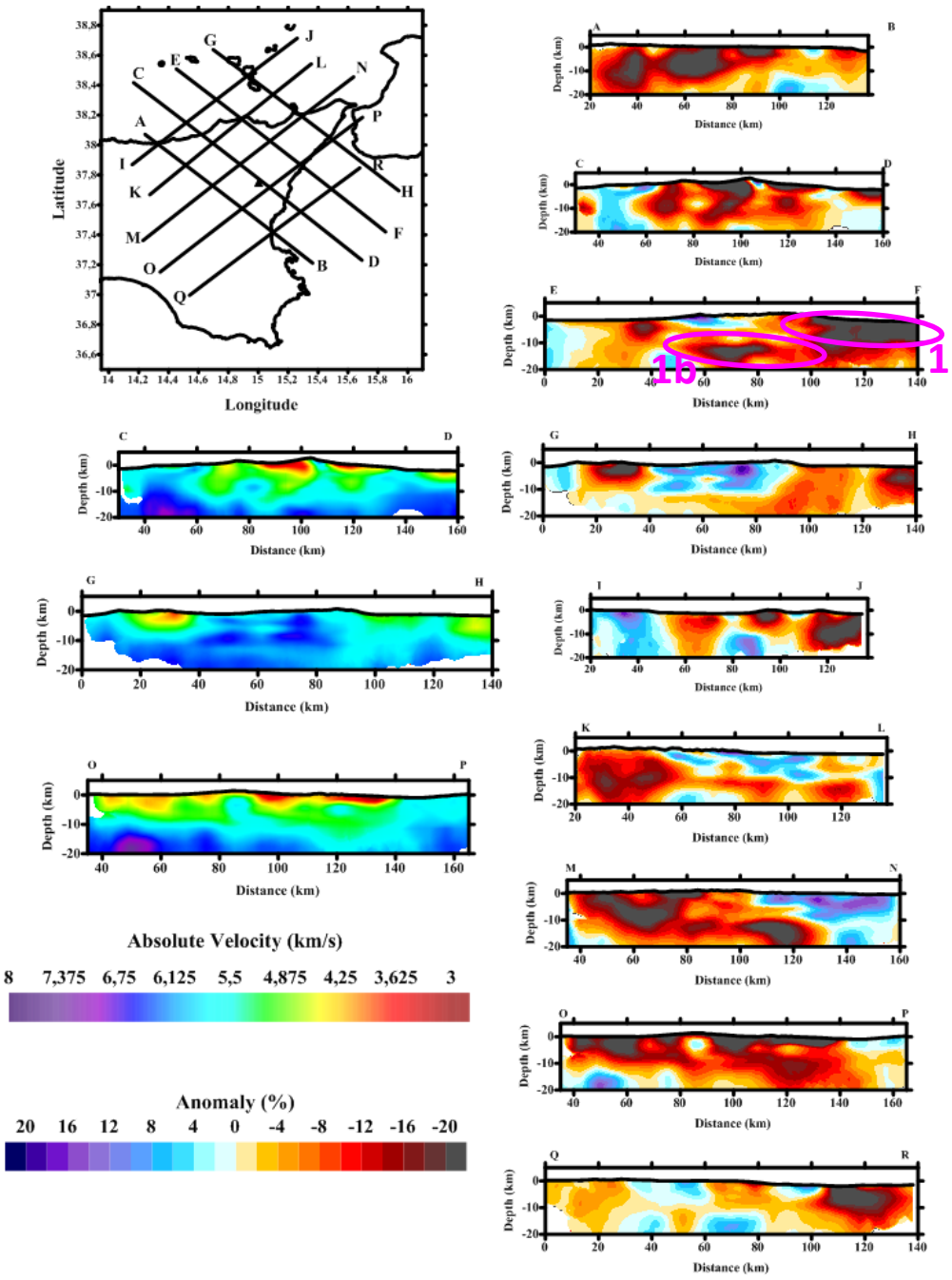

Figure 6.9. *P-wave absolute velocity and velocity anomaly vertical sections maps for Region 1. Black triangle represents Mt. Etna.*

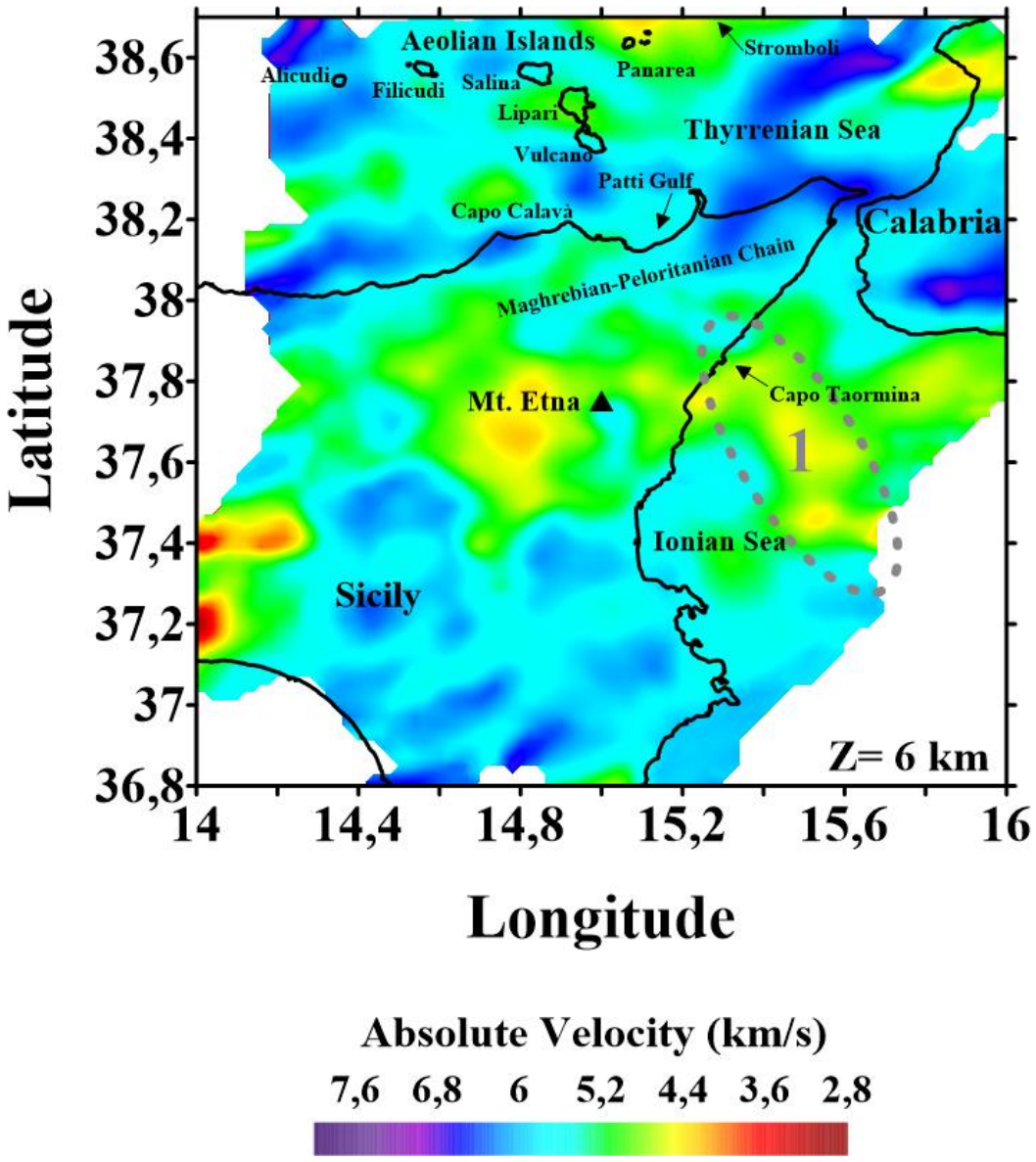

Figure 6.10. *P-wave absolute velocity map for region 1 at 6km depth. Grey ellipses mark the main structures to be discussed in the text. 1) NW-SE low velocity anomaly velocity (up to 8-10 km depth). 1b) NW-SE low velocity anomaly velocity (10-14 km depth). Black triangle represents Mt. Etna.*

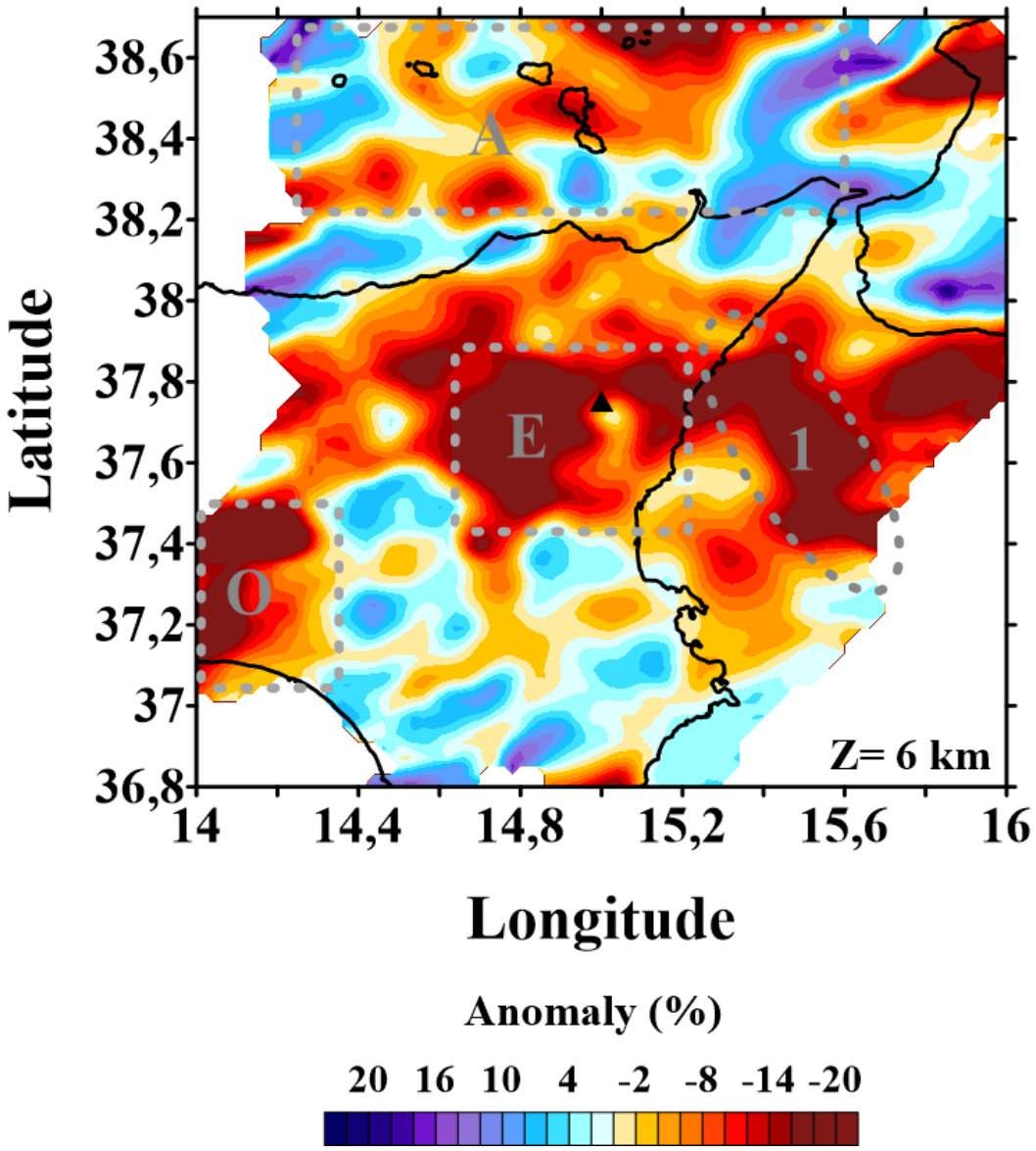

Figure 6.11. *P-wave velocity anomaly map for region 1 at 6km depth. Grey ellipses mark the main structures to be discussed in the text. 1) NW-SE low velocity anomaly velocity (up to 8-10 km depth). Black triangle represents Mt. Etna; A) Aeolian Island Archipelago (Region 2); E) Mt. Etna Volcanic system (Region 3); O)Border- effect Anomaly not interpreted in the text.*

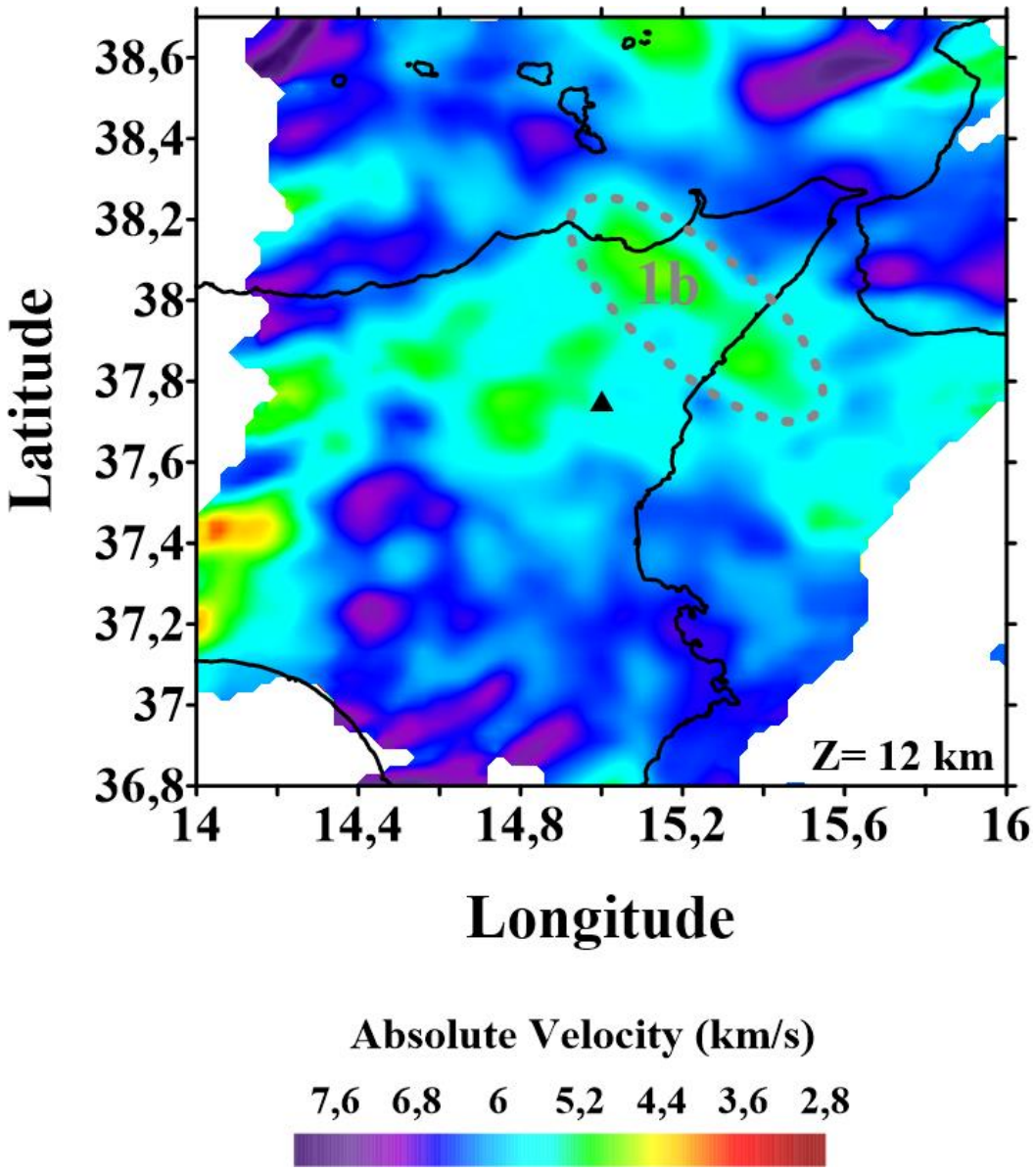

Figure 6.12. *P-wave absolute velocity map for region 1 at 12km depth. Grey ellipses mark the main structures to be discussed in the text. 1b) NW-SE low velocity anomaly velocity (10-14 km depth). Black triangle represents Mt. Etna.*

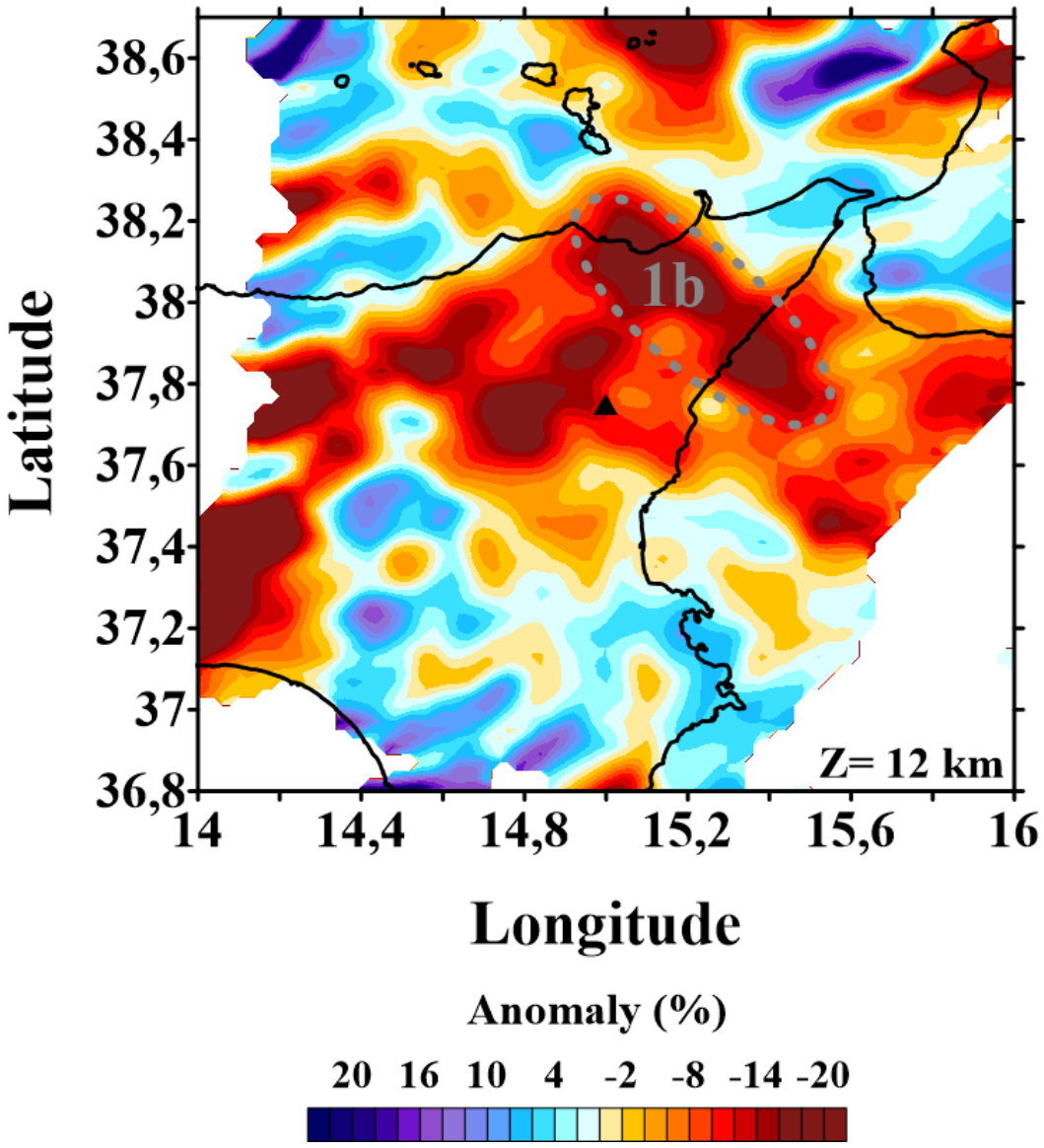

Figure 6.13. *P-wave velocity anomaly map for region 1 at 12km depth. Grey ellipses mark the main structures to be discussed in the text. 1b) NW-SE low velocity anomaly velocity (10-14 km depth). Black triangle represents Mt. Etna.*

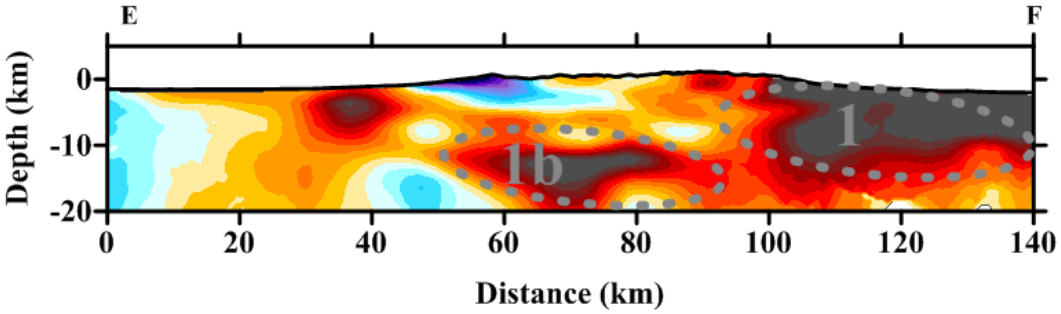

Figure 6.14. *P-wave velocity anomaly vertical section E-F of Region 1. Grey ellipses mark the main structures to be discussed in the text. 1b) NW-SE low velocity anomaly velocity (10-14 km depth).*

At a first glance on figure 6.11, it is possible to define as *anomaly E* the volcanic edifice/system, due to its important low velocity anomaly in confront to the higher velocities of the methapmorhic Maghrebian-Peloritanian Chain of northern Sicily. It reaches more than 30% of anomaly, marking the strong difference with the surrounding area. This region will be further analysed as an individual study area (Region 3). Moreover, The Aeolian Island Archipelago, denoted as "A" in figure 6.11, is studied as a separated region (Region 2). We want also to remark the presence of an important low velocity anomaly located in the southwestern margin of the map on figure 6.11 (denoted as "O"), which has never been interpreted before. We consider it a border-effect due, as it has no convincing structural interpretation and it is located at the edge of the map, with very poor resolution (See ray density map on figure 6.6).

The main remarkable anomalies regarding this inversion are:

-*Anomaly 1*: NW-SE velocity contrast that extends from Capo Taormina toward SE in the Ionian Sea for about 60 km (*anomaly 1 in figures 6.10, 6.11 and 6.14)*. This low velocity anomaly is clearly visible from Sea Level and up to 8-10 km. It presents absolute velocity values of 4.4 km/s that contrast with values of around 5.2 km/s of the surrounding area (Figure 6.10). Additionally, it represents a 20% anomaly from the starting velocity model (Figure 6.11).

-*Anomaly 1b*: Continuation of previous anomaly 1 in depth toward NW (where it is visible up to 14 km depth reaching the coast of Vulcano Island. In this case, the absolute velocity contrasts range from 5.5 km/s for the anomaly and more than 6 km/s on the surrounding area (Figure 6.12). In anomaly, the values reach again more than 20% (Figure 6.13). Figure 6.14 shows a vertical section that allows us to image the geometry in depth of this anomaly.

According to Billi et al., (2006) and Barreca et al. (2014), anomalies 1 and 1b correspond to the denominated "Aeolian-Tindari-Letojanni Fault System" (ATLFS hereafter). Scarfì et al., (2016) reviewed some of the main hypothesis regarding this structure. These hypothesis ranges from a crustal expression of the Subduction Tear Edge Propagator Fault (STEP fault hereafter), proposed by Billi et al., (2006) among others; to a continuation of the Hyblean-Maltese Fault System (HMFS hereafter),(Lanzafame & Bousquet, 1997). In the end, these authors, as well as Barreca et al., (2014) and Polonia et al., (2016) consider this fault system a brittle deformation zone that acts as dextral transfer zone separating a compressional regime, present on the western part of the Aeolian Archipelago, from an extensional regime to the northeast of the Archipelago.

6.4. Joint Seismic Tomography Inversion. Region 2

The tomographic inversion of the Aeolian Island Archipelago (Region 2, figure 6.1.) was set in an area of 126x126 km and a grid spacing of 3 km in horizontal and 2 km in vertical up to 24 km in depth. As in the previous section, we firstly present the results of some of the synthetic tests performed in order to constrain grid dimensions and to estimate the reliable area based on our dataset. Then we describe the ray density calculated and finally we show the tomographic images and discuss the main anomalies observed.

6.4.1. Synthetic tests.

Along the next paragraphs we present a set of synthetic analyses carried out to ensure the resolution, reliability and quality of our solution for Region 2. These tests follow the same scheme described for Region 1.

6.4.1.1. Checkerboards

Checkerboard test for region 2 have been carried out using different grid spacing reaching to a final grid spacing of 3 km in horizontal and 2 km in vertical (Figure 6.15). Nonetheless the results of these checkerboards are poor in confront with the previous ones, the robustness of the final solutions is backed by the rest of the synthetic tests and ray coverage. Figure 6.15., presents the results of the related checkerboard using 3 km anomalies periodically sited with positive and negative values of 20% of anomaly.

6.4.1.2. Free Anomaly test

For the inversion of the Aeolian Islands the free anomalies designed are represented in figure 6.16.a, c. Positive and negative anomalies are both convincingly resolved as noted in figure 6.16.b,d. Designed anomalies have similar geometry as the real ones, thus, the robustness and reliability of the results is confirmed.

6.4.1.3. Jackknifing Test

On the other hand, figure 6.17 shows the same Jackknifing test for Etnean (left column) and Aeolian Islands (right column) regions. When compared with the complete dataset inversion (see upper panels) no dramatic changes can be noticed and therefore the stability of the resulting model is assessed.

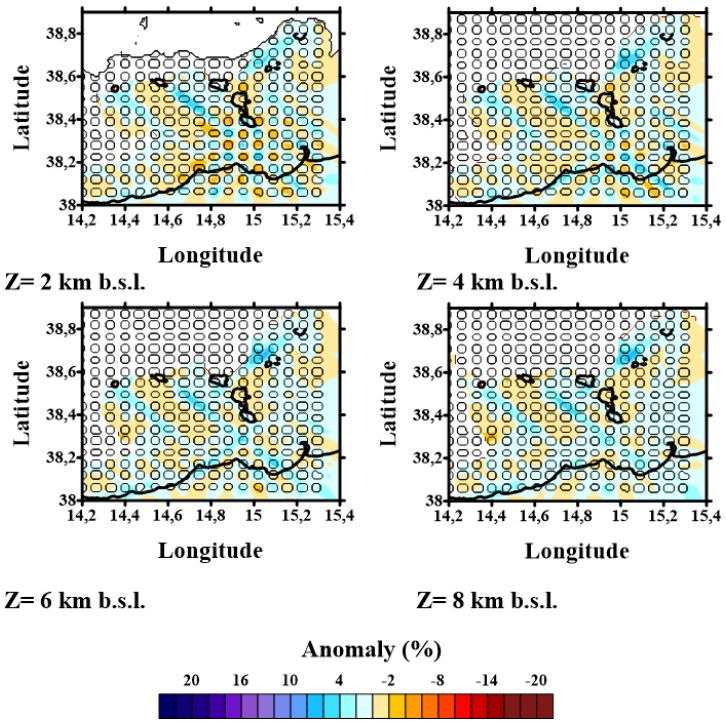

Figure 6.15. *Horizontal Checkerboard for Region 2.*

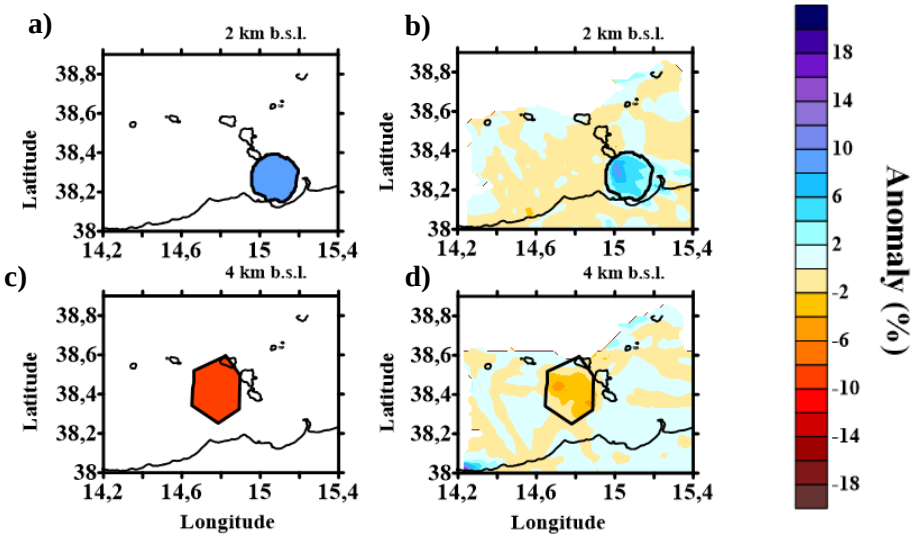

Figure 6.16. *Free anomaly tests for Region 2. a) Free anomaly 1; b) inversion result for free anomaly 1; c) Free anomaly 2; d) inversion result for free anomaly 2.*

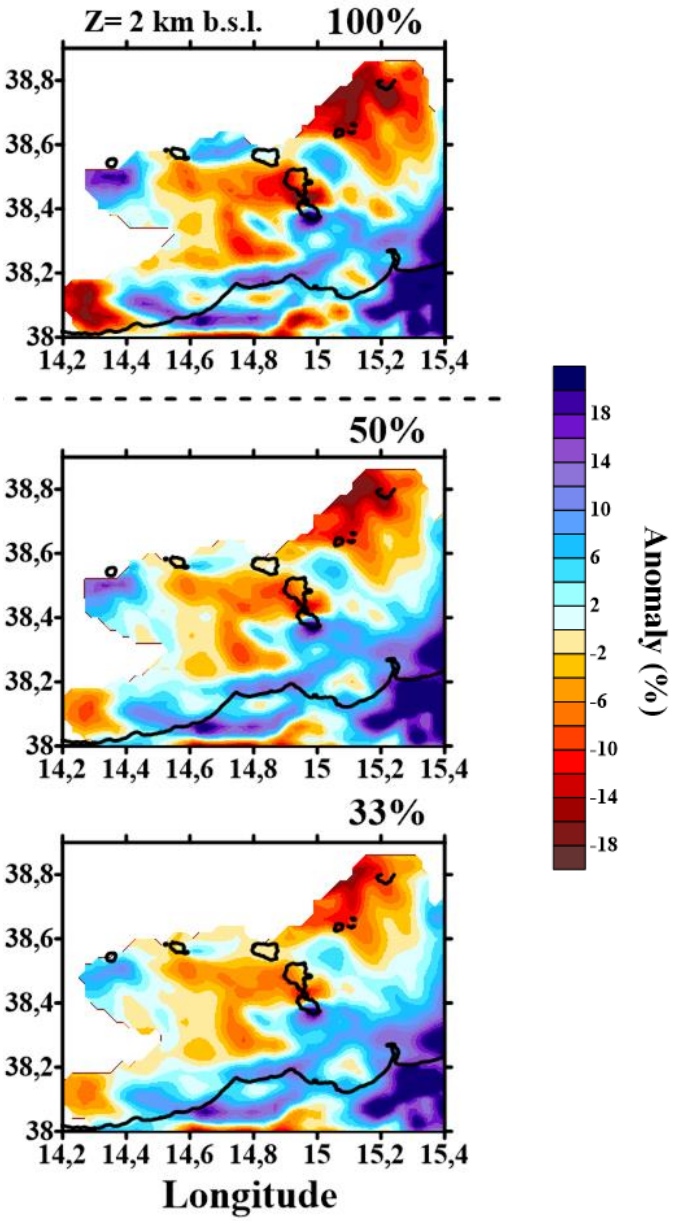

Figure 6.17. *Jackknifing test for Region 2: a) complete dataset inversion; b) 50% of the dataset inverted; c) 33% of the dataset inverted.*

6.4.2. Ray Density

Ray density of the inversion of Region 2 is shown in figure 6.18. The ray distribution in this region allows us to confirm the quality of the results and the reliability of the solutions as the study area is well covered by the rays, especially in the first 12 km. Deeper than 12 km results are not 100% reliable since the number of rays crossing each cell is too low.

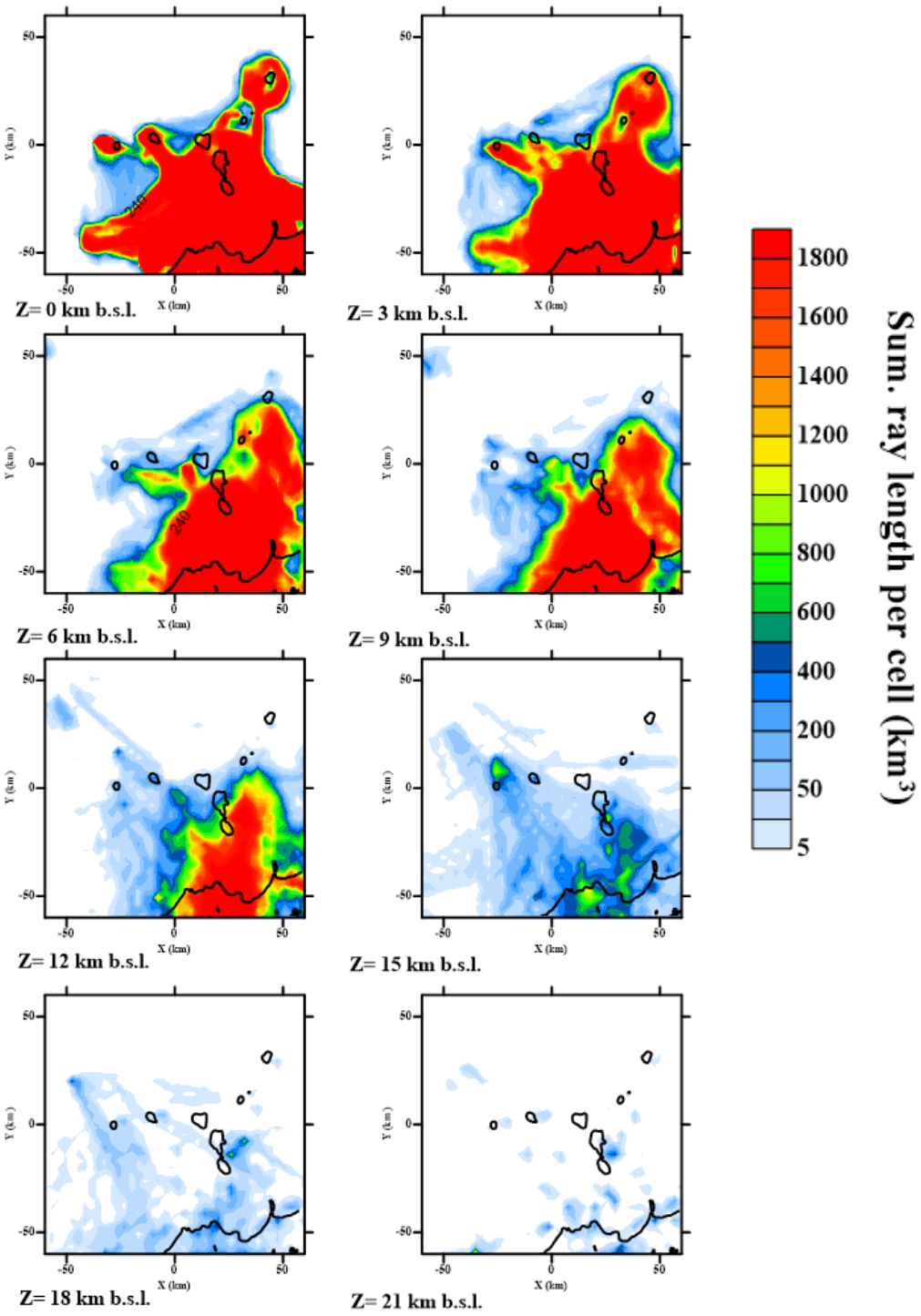

Figure 6.18 *Ray Density for Region 2 for different horizontal layers.*

6.4.3. Joint Tomography Results. Region 2

As for Region 1, along the following paragraphs we illustrate the main horizontal and vertical tomographic images obtained inverting the TOMOETNA final dataset, in this case for Region 2. We provide additional discussion of the main observed anomalies based on regional structure interpretations from previous authors. To provide a clear view of the results, we plot first a set of horizontal layers in both absolute velocities (Figure 6.19) and velocity anomalies (Figure 6.20). Then, some relevant vertical sections are presented (Figure 6.21). Finally, we enlarge some of the most relevant horizontal layers (Figures 6.22, and 6.23), and vertical sections (Figure 6.24), in order to better discuss the main structural anomalies.

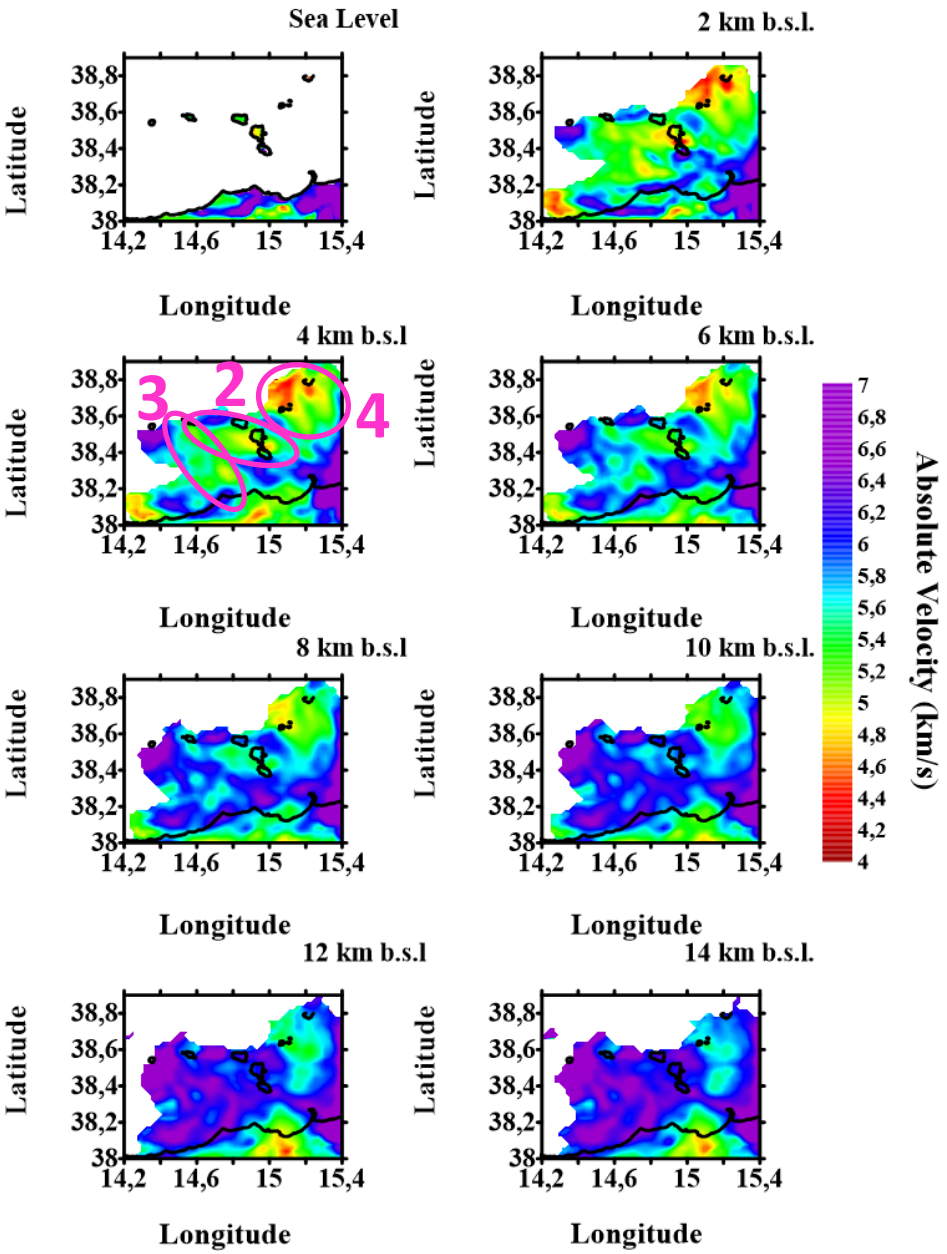

Figure 6.19. *P-wave absolute velocity maps for region 2 at different depth layers. Pink ellipses mark the main structures to be discussed in the text. 2) WNW-ESE low velocity anomaly velocity (2-14 km depth). 3) NW-SE low velocity anomaly velocity (2-8 km depth). 4) Circular low velocity anomaly below Stromboli-Panarea Region (2-14 km depth).*

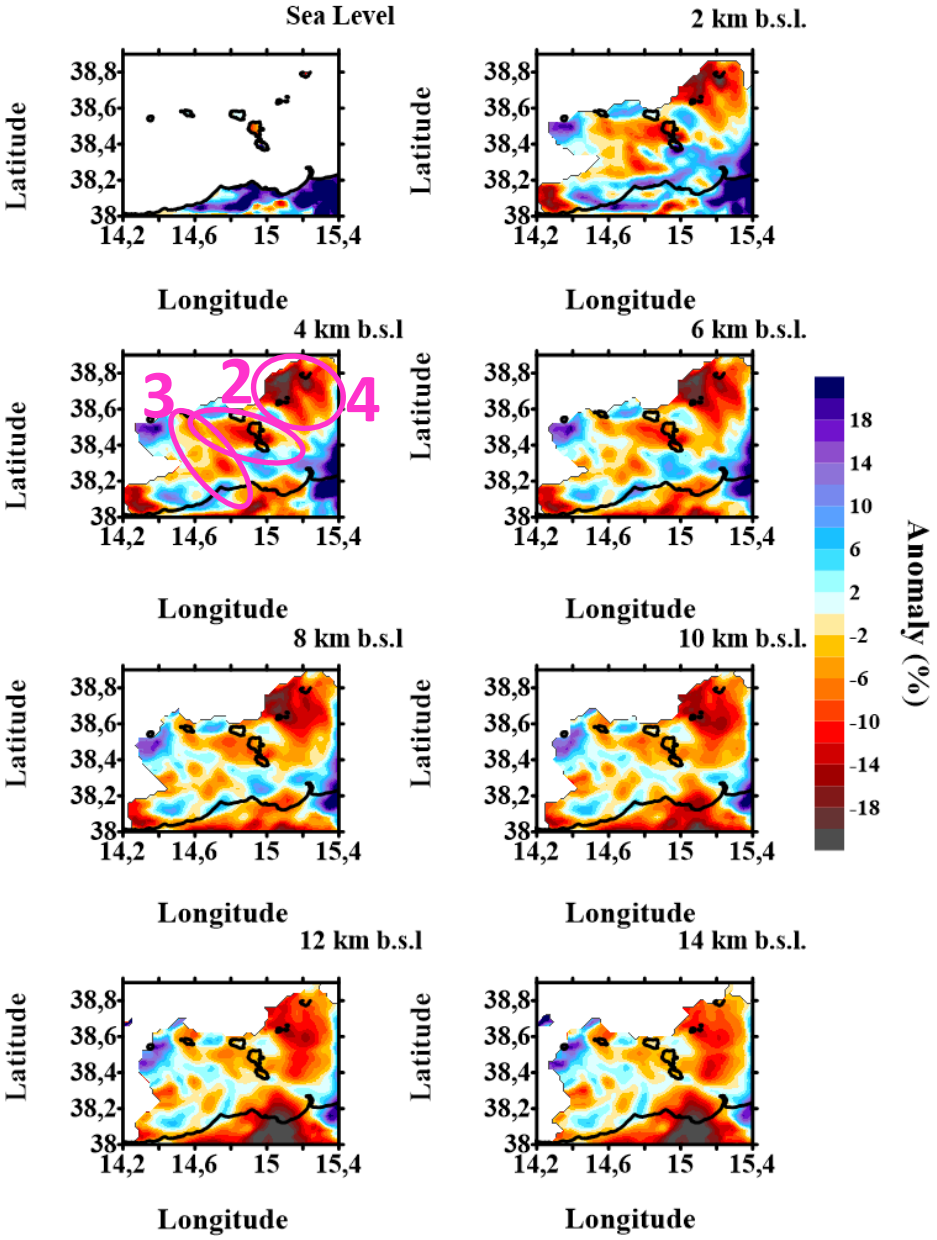

Figure 6.20. *P-wave absolute velocity maps for region 2 at different depth layers. Pink ellipses mark the main structures to be discussed in the text. 2) WNW-ESE low velocity anomaly velocity (2-14 km depth). 3) NW-SE low velocity anomaly velocity (2-8 km depth). 4) Circular low velocity anomaly below Stromboli-Panarea Region (2-14 km depth).*

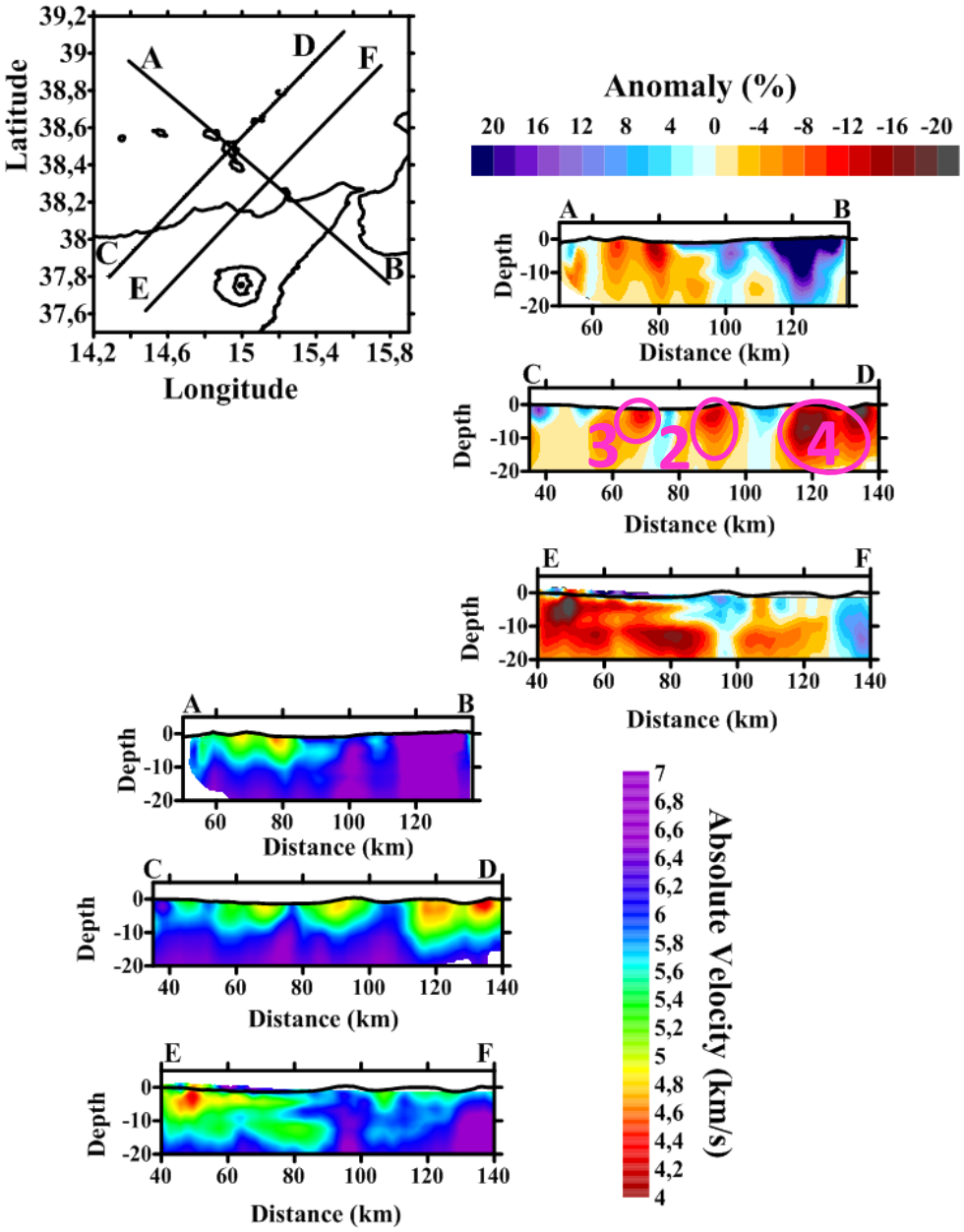

Figure 6.21. *P-wave absolute velocity and velocity anomaly vertical sections maps for Region 2.*

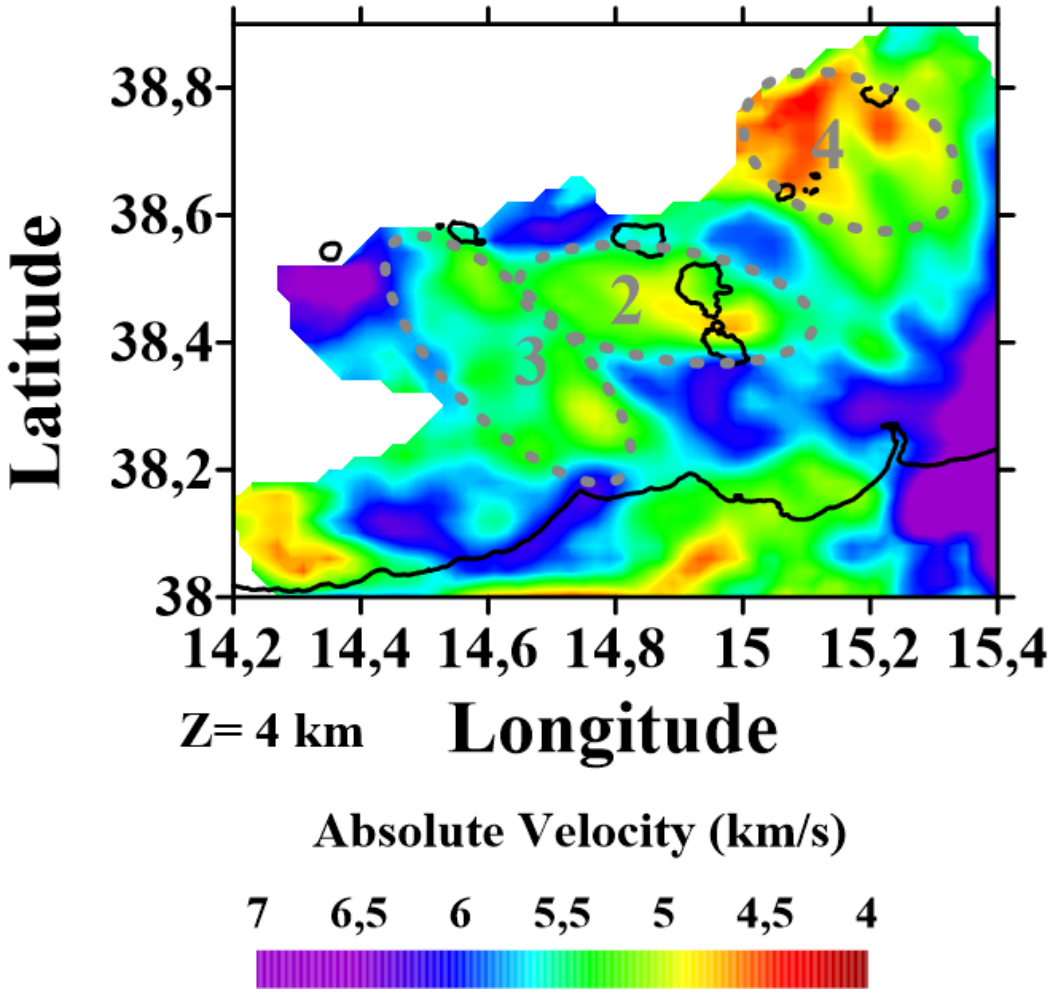

Figure 6.22. *P-wave absolute velocity map for region 2 at 4km depth. Grey ellipses mark the main structures to be discussed in the text. 2) WNW-ESE low velocity anomaly velocity (2-14 km depth). 3) NW-SE low velocity anomaly velocity (2-8 km depth). 4) Circular low velocity anomaly below Stromboli-Panarea Region (2-14 km depth).*

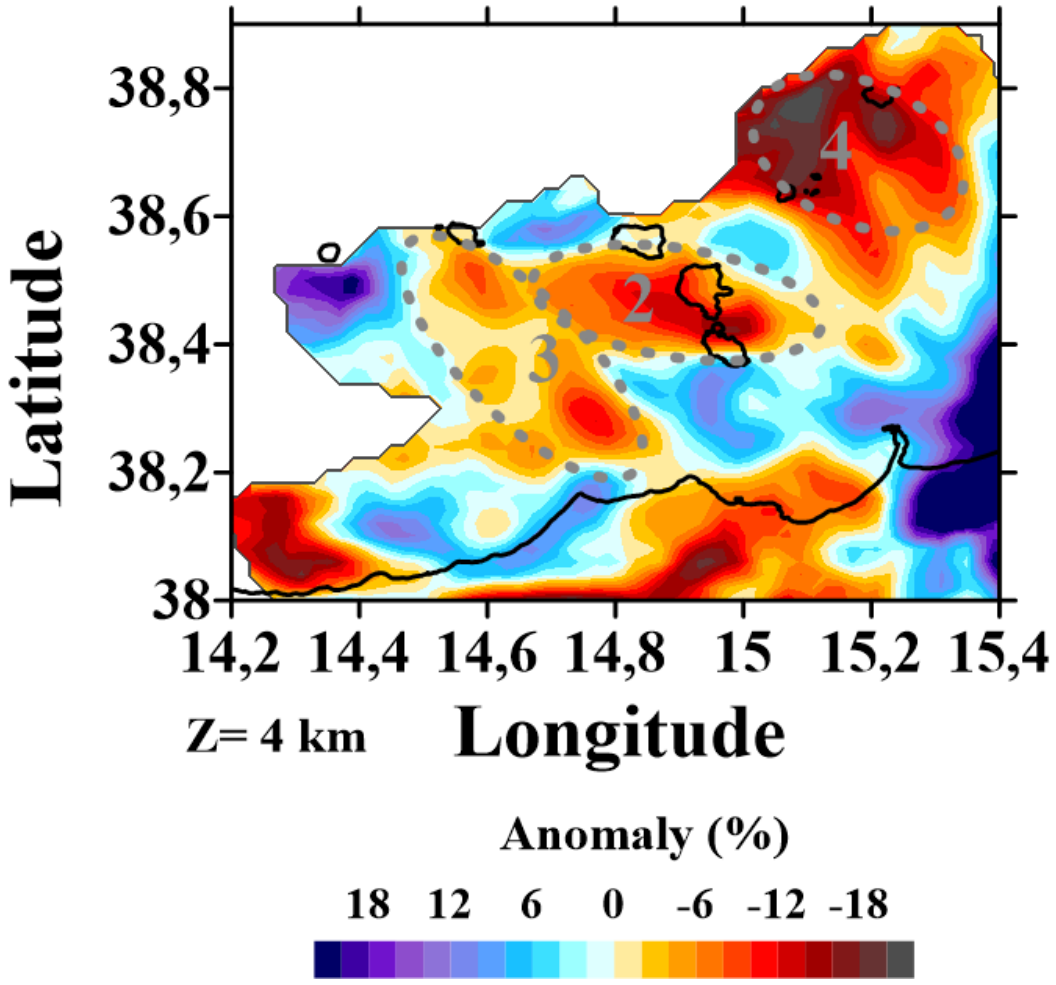

Figure 6.23. *P-wave absolute velocity map for region 2 at 4km depth. Grey ellipses mark the main structures to be discussed in the text. 2) WNW-ESE low velocity anomaly velocity (2-14 km depth). 3) NW-SE low velocity anomaly velocity (2-8 km depth). 4) Circular low velocity anomaly below Stromboli-Panarea Region (2-14 km depth).*

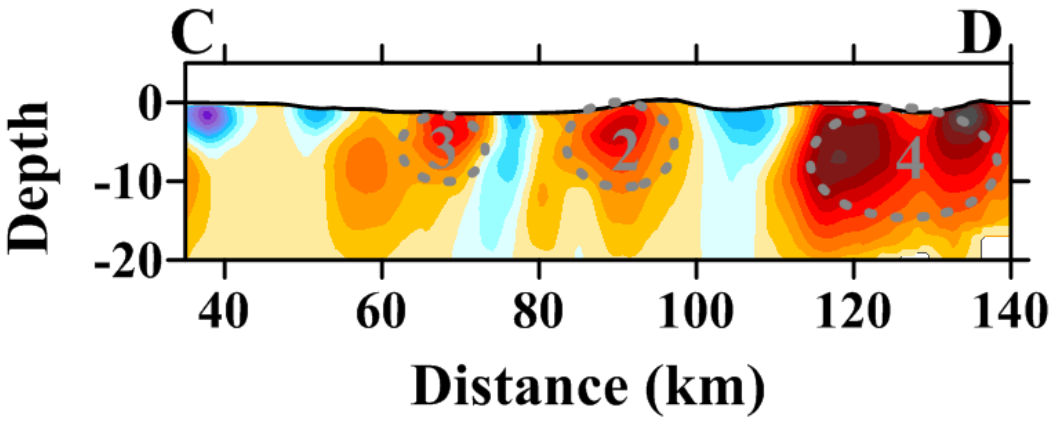

Figure 6.24. *P-wave velocity anomaly vertical section C-D of Region 2. Grey ellipses mark the main structures to be discussed in the text. 2) WNW-ESE low velocity anomaly velocity. 3) NW-SE low velocity anomaly velocity. 4) Circular low velocity anomaly below Stromboli-Panarea Region.*

The inversion of this region, allows us to better define some major features that were highlighted in Region 1 and enlighten new relevant structures:

- *Anomaly 2:* In the area of the Aeolian Archipelago, together with previous anomalies 1 and 1b, another low anomaly is highlighted. It presents absolute velocities of 4.5 km/s at 4 km depth, which are quite lower than the average Thyrenian Sea velocities at the same depth (Figures 6.22, 6.23 and 6.24).On the other hand the anomaly values reach 15% of the starting velocity model. This structure, striking about WNW-ESE and extending between Filicudi and the Vulcano-Lipari complex is known as “Sisifo-Alicudi Fault System” (SAFS hereafter) (Barreca et al., 2014). SAFS is a dextral strike-slip motion fault system that accommodates the compression of the westernmost part of the Aeolian Archipelago. The eastern limit of this belt juxtaposes with the ATLFS near the Island of Vulcano; the westernmost limit coincides with the compressional W-E belt.

-*Anomaly 3*: at 4-8 km of depth, another velocity discontinuity (low/high anomaly contrast) with NW-SE direction is revealed in the Capo Calavà offshore (Figures 6.22, 6.23 and 6.24). The Patti Gulf-Capo Taormina-Ionian Sea alignment along a roughly

NW-SE to NNW-SSE direction is recognized to be a discontinuity that marks the current southern termination of the Ionian subducting lithosphere, in the sense of a STEP fault (Govers and Wortel, 2005); i.e. it is a lithospheric tear fault decoupling the subducting lithosphere from the non-subducting one. Its activity in northeastern Sicily and Ionian Sea has been recognized at sub-crustal depth by tomographic images, seismic events distribution and focal mechanism kinematics (see e.g. Scarfì et al., 2016; Polonia et al., 2016). At shallower levels, the possible lack of a clear NW-SE velocity discontinuity has to be interpreted as the shallow expression of that main lithospheric-scale tear fault, characterised by a transtensional complex with NW-SE and NE-SW fault systems and topography uplift (see Faccenna et al., 2011; Scarfì et al., 2016 and references therein).

-*Anomaly 4*: low anomaly below the Stromboli area. A low Vp anomaly (>20%) in a large and volume between Stromboli and Panarea (Figures 6.22, 6.23 and 6.24). The location at the edge of the well-resolved area makes the reliability of this finding questionable; however, there is a broad agreement with the results found by various authors (Piromallo and Morelli, 2003; Montuori et al., 2007; Chiarabba et al., 2008; Calò et al., 2009; Scarfì et al., 2016), who argue for the accumulation of significant amounts of partial mantle melting, feeding the present-day activity of the Tyrrhenian volcanoes.

6.5. Joint Seismic Tomography Inversion. Region 3

The area inverted for the Mt. Etna volcanic region extended 60x60 km in horizontal and up to 24 km in depth (Region 3, figure 6.1). The grid spacing set was of 2 km in both horizontal and vertical directions.

6.5.1. Synthetic tests.

6.5.1.1. Checkerboards

The checkerboard related to this inversion is shown in figure 6.25. In this case the anomaly pattern set was of ±20% anomaly with 2km size separated 5 km from each other. Results show good horizontal resolution for a 60·60 km region (Figure 6.25.a, b) and resolves anomalies of 2 km size up to 10-12 km depth beneath Mt. Etna (Figure 6.25.c).

6.5.1.2. Free Anomaly test

Similar procedure as for regions 1 and 2, we performed the free anomaly test for Region 3. The configuration inverted for the region of Mt. Etna volcano is shown in figure 6.26.a, and c. Again, the designed anomalies are sized taking into account the grid spacing in order to try to reproduce realistic anomalies. Results of this test shown in figure 6.26.b, and d, denote the high quality of the inversion. Moreover, this test supports that similar anomalies in size and shape for real inversions can ben trustfully interpreted. The free anomaly tests carried out for the three regions show in all of them very promising reconstruction of the anomalies, proving that our obtained anomalies are suitable to be solved by the inversion using the set parameters and model. Moreover, it proves the robustness of the inversion code for modelling synthetic anomalies of whatever geometry.

6.5.1.3. Jackknifing Test

On the other hand, figure 6.27 shows the Jackknifing test for Etnean region. When compared with the complete dataset inversion (see upper panels) no dramatic changes can be noticed and therefore the stability of the resulting model is assessed. The Jackknifing test performed to all 3 regions confirms the very high quality of the data selected for the inversion, as even using 33% of them the resultant images are quite similar to the full dataset ones. Therefore we can ensure that our results are not biased by noise effects from the data.

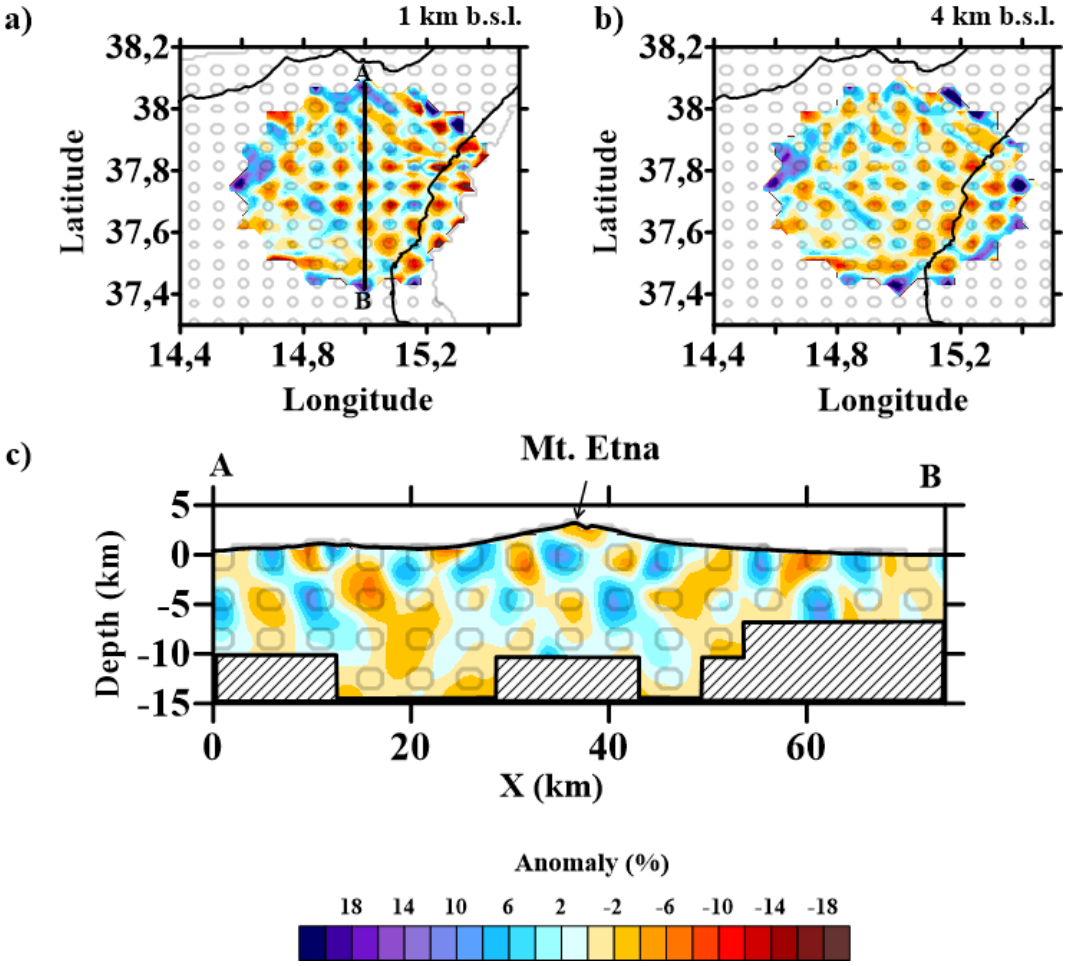

Figure 6.25. *Horizontal Checkerboard for Region 3.*

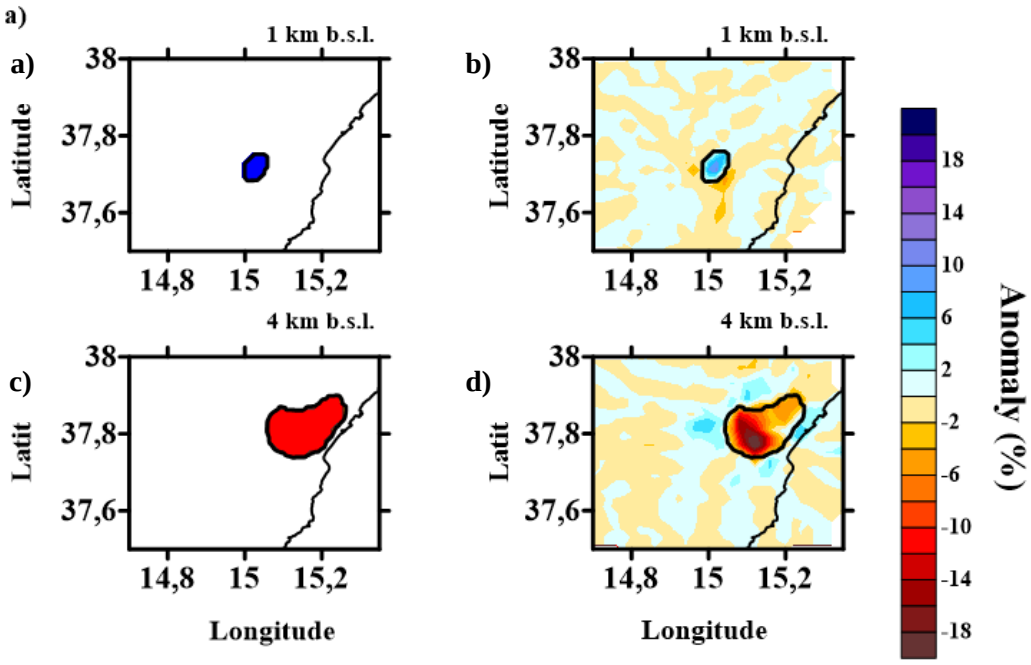

Figure 6.26. *Free anomaly tests for Region 3. a) Free anomaly 1; b) inversion result for free anomaly 1; c) Free anomaly 2; d) inversion result for free anomaly 2.*

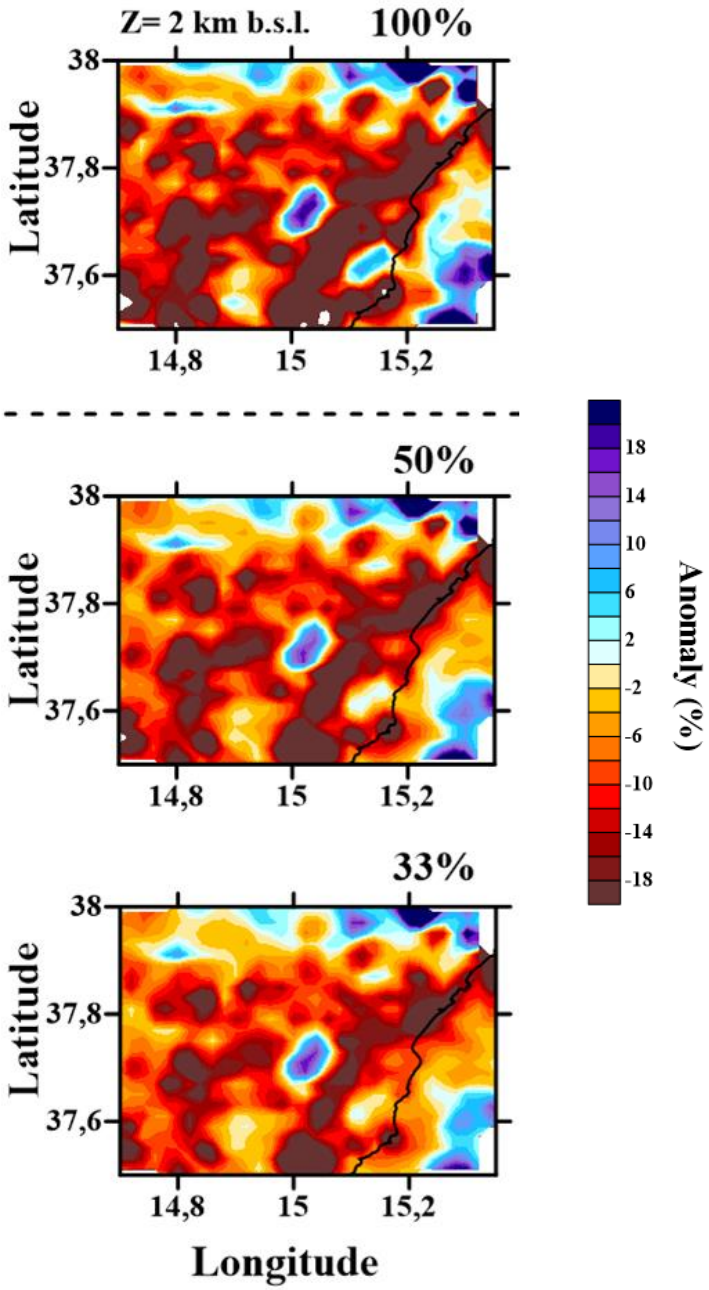

Figure 6.27. *Jackknifing test for Region 3: a) complete dataset inversion; b) 50% of the dataset inverted; c) 33% of the dataset inverted.*

6.5.2. Ray Density

The ray distribution in Mt. Etna volcanic edifice allows us to confirm the high quality of the results and the reliability of the solutions as the study area is well covered by the rays, especially in the eastern flank of the volcano. Ray density of the inversion of Region 3 is shown in figure 6.28. Although the western flank of the edifice is less covered, the density of rays crossing each horizontal layer is more than enough to trust the solution. The low ray coverage on the western flank is indeed a remarkable result; as it delimitates a region where the rays are highly attenuated and we hypothesized due to the presences of magmatic fluids.

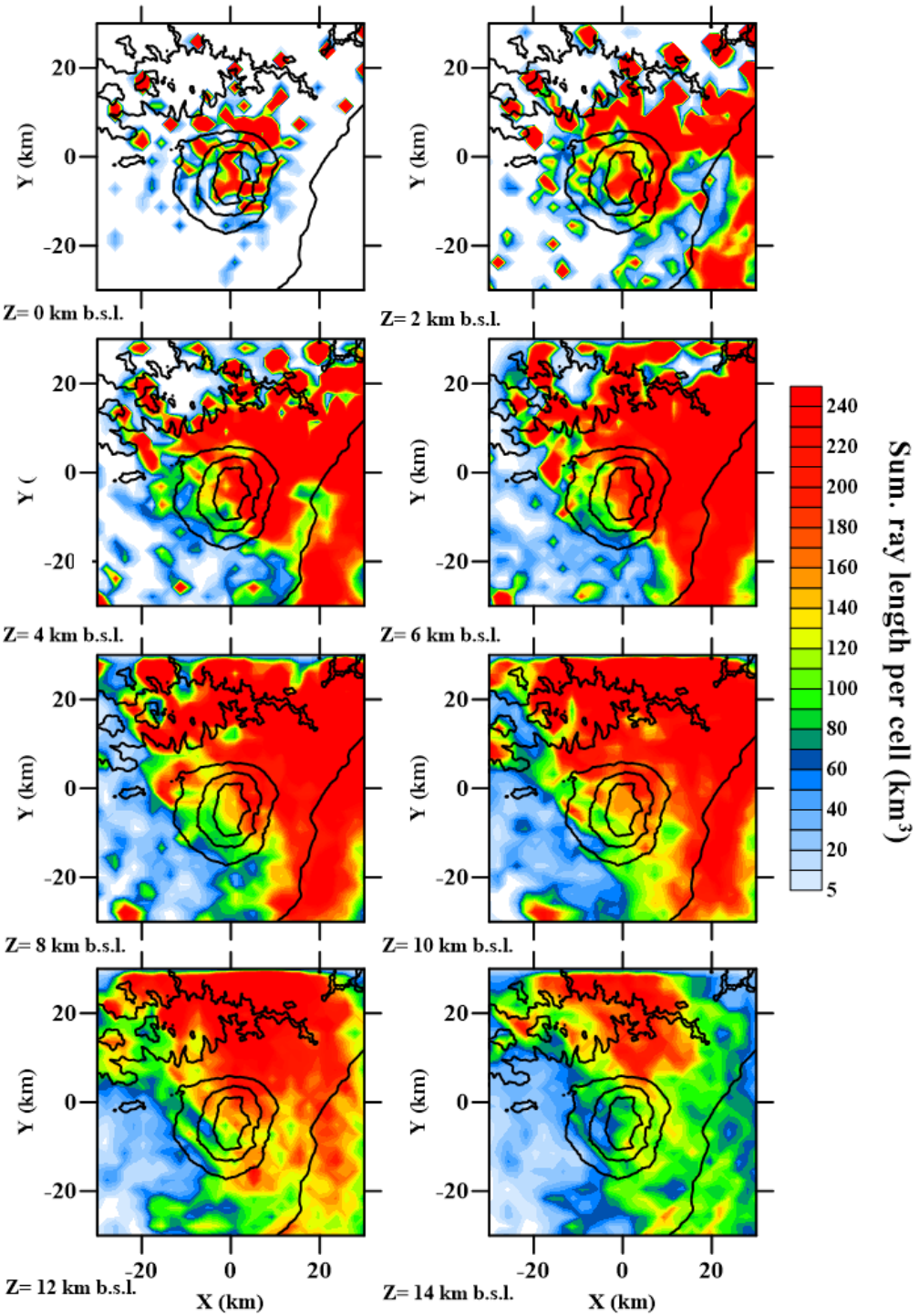

Figure 6.28. *Ray Density for Region 3 for different horizontal layers.*

6.5.3. Joint Tomography Results. Region 3

As for previous regions, along the following paragraphs we illustrate the main horizontal and vertical tomographic images obtained inverting the TOMOETNA final dataset, in this case for Region 3. We provide additional discussion of the main observed anomalies based on regional structure interpretations from previous authors. To provide a clear view of the results, we plot first a set of horizontal layers in both absolute velocities (Figure 6.29) and velocity anomalies (Figure 6.30). Then, some relevant vertical sections are presented (Figure 6.31. Finally, we enlarge some of the most relevant horizontal layers (Figures 6.32, and 6.33), and vertical sections (Figure 6.34), in order to better discuss the main structural anomalies.

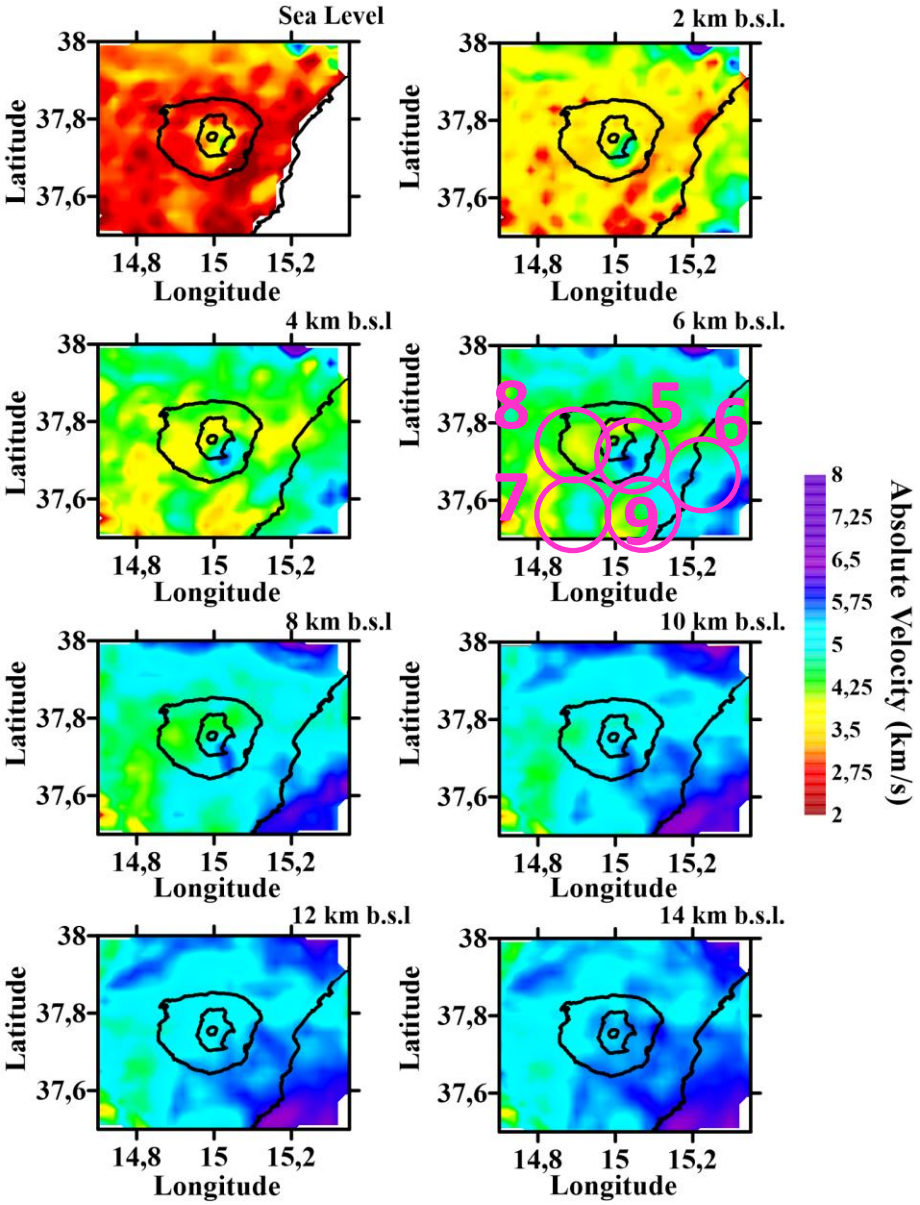

Figure 6.29. *P-wave absolute velocity maps for region 3 at different depth layers. Pink ellipses mark the main structures to be discussed in the text. 5) Round high velocity anomaly slightly SE from central craters. 6) Round high velocity anomaly located on the coast; 7) Round high velocity anomaly located SW from central craters; 8) Round low velocity anomaly located W from central craters; 9) Round low velocity anomaly located S from central craters.*

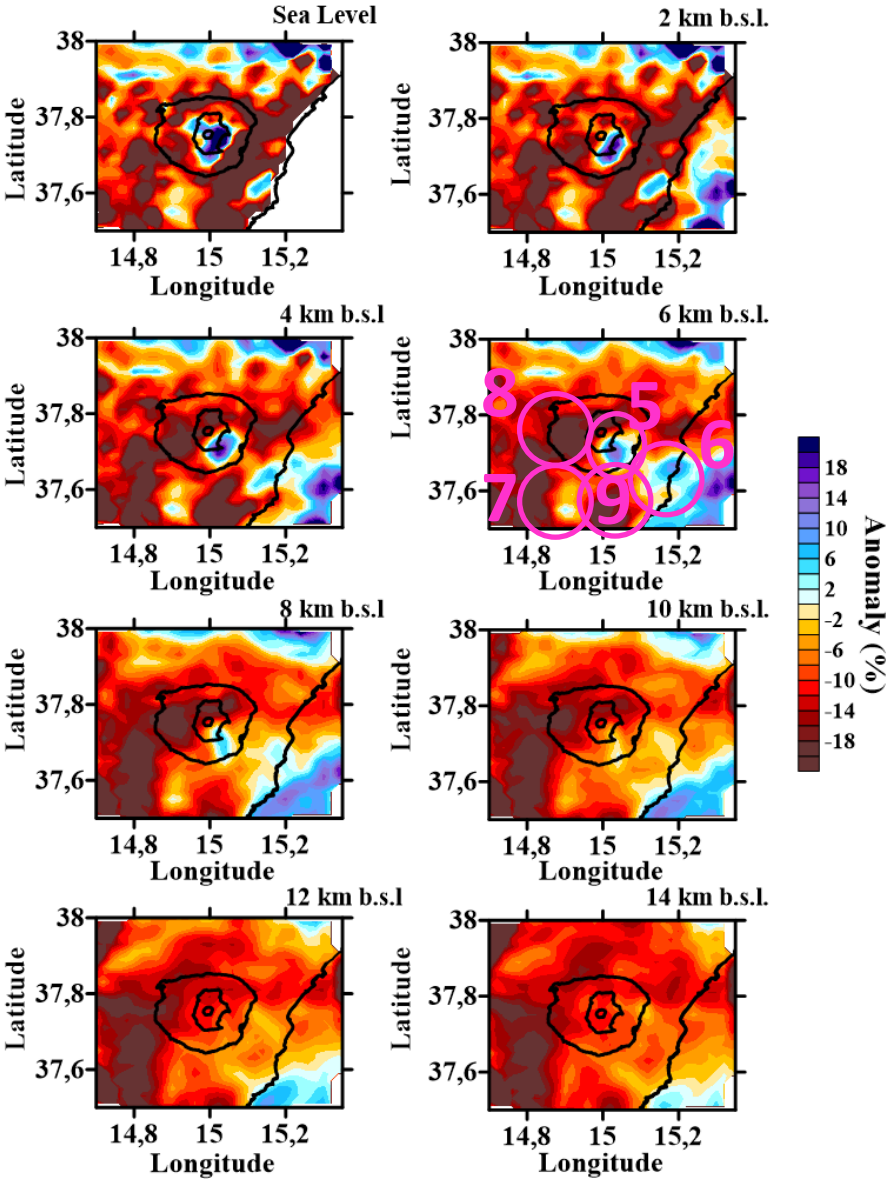

Figure 6.30. *P-wave velocity anomaly maps for region 3 at different depth layers. Pink ellipses mark the main structures to be discussed in the text. 5) Round high velocity anomaly slightly SE from central craters. 6) Round high velocity anomaly located on the coast; 7) Round high velocity anomaly located SW from central craters; 8) Round low velocity anomaly located W from central craters; 9) Round low velocity anomaly located S from central craters.*

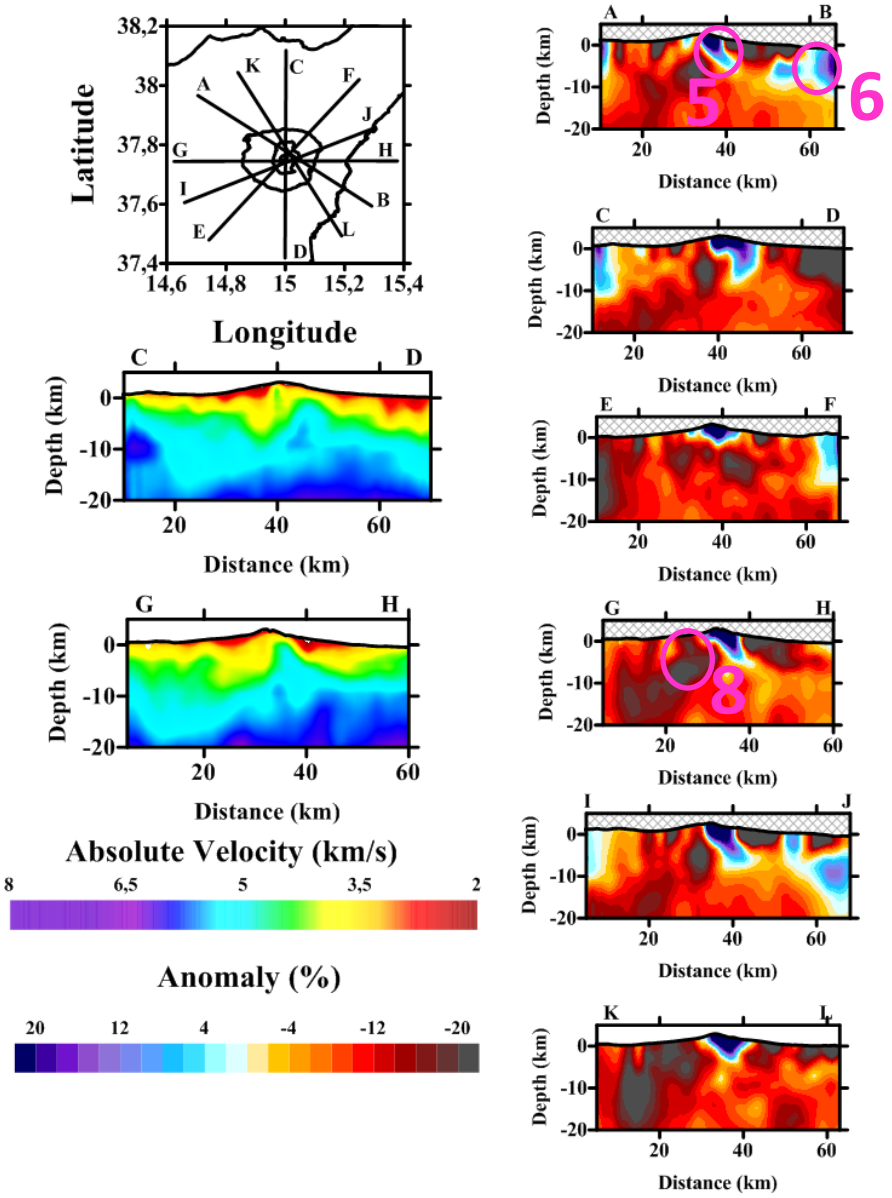

Figure 6.31. *P-wave absolute velocity and velocity anomaly vertical sections maps for Region 3. Pink ellipses mark the main structures to be discussed in the text. 5) Round high velocity anomaly slightly SE from central craters. 6) Round high velocity anomaly located on the coast; 8) Round low velocity anomaly located W from central craters.*

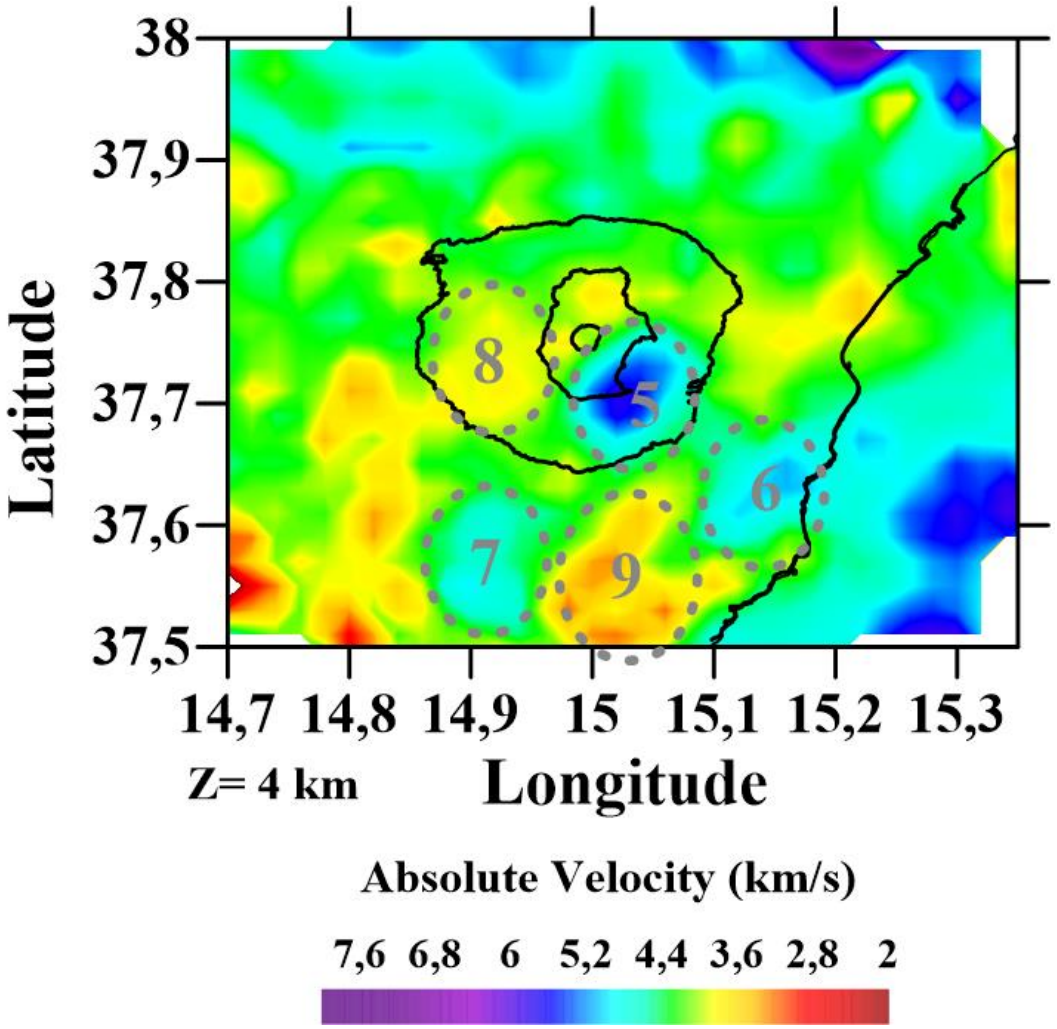

Figure 6.32. *P-wave absolute velocity maps for region 3 at 4km depth. Grey ellipses mark the main structures to be discussed in the text. 5) Round high velocity anomaly slightly SE from central craters. 6) Round high velocity anomaly located on the coast; 7) Round high velocity anomaly located SW from central craters; 8) Round low velocity anomaly located W from central craters; 9) Round low velocity anomaly located S from central craters.*

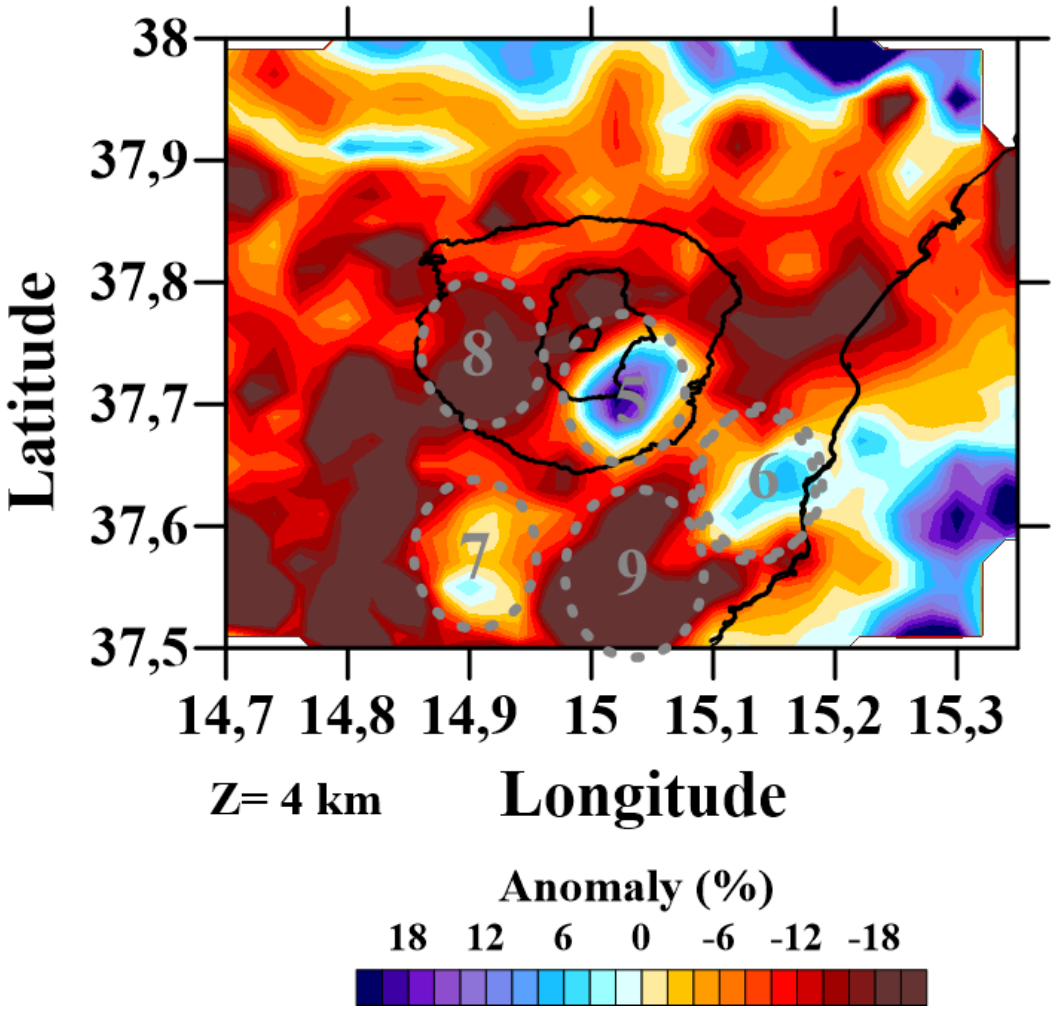

Figure 6.33. *P-wave velocity anomaly maps for region 3 at 4km depth. Grey ellipses mark the main structures to be discussed in the text. 5) Round high velocity anomaly slightly SE from central craters. 6) Round high velocity anomaly located on the coast; 7) Round high velocity anomaly located SW from central craters; 8) Round low velocity anomaly located W from central craters; 9) Round low velocity anomaly located S from central craters.*

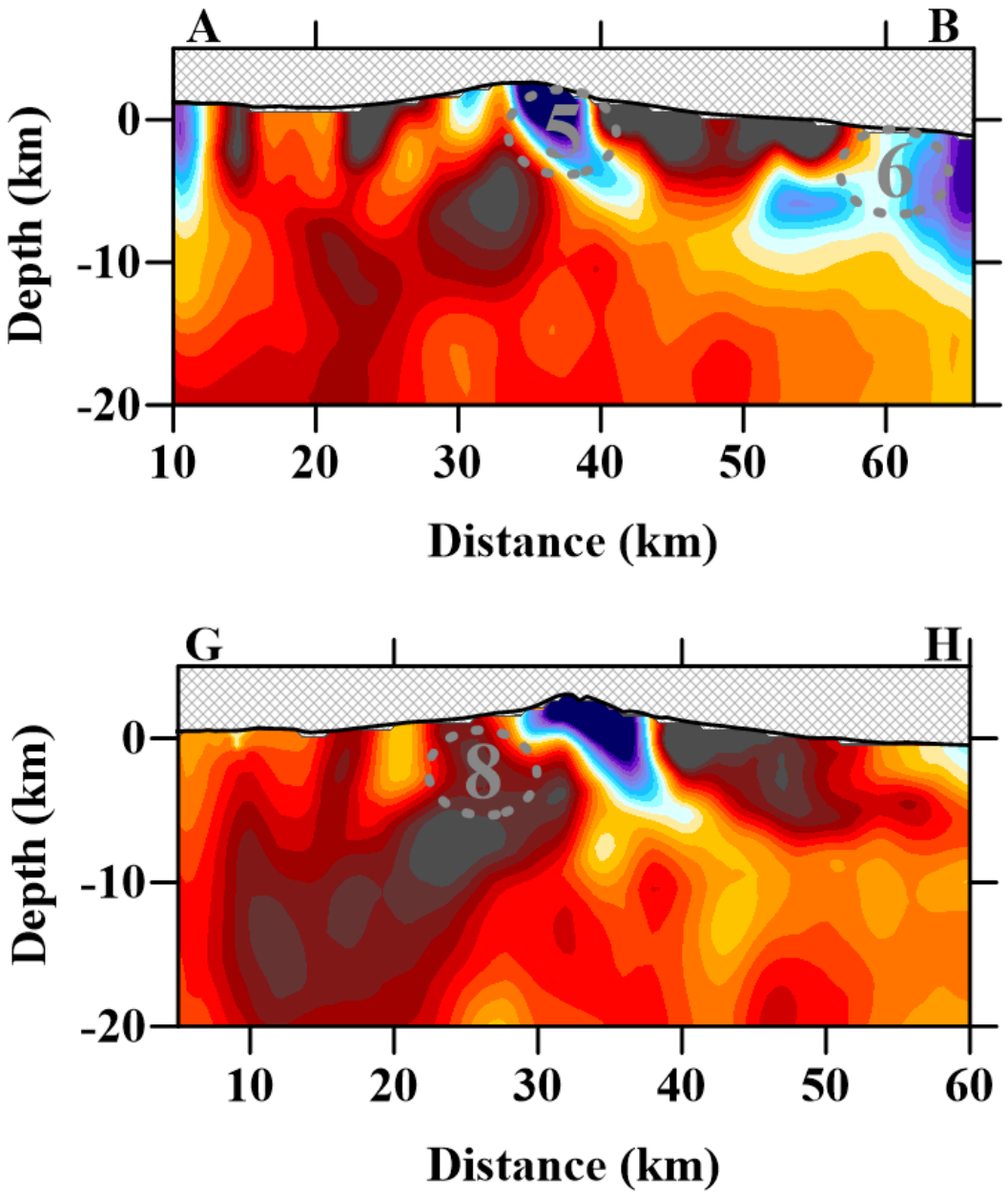

Figure 6.34. *P-wave velocity anomaly vertical sections (A-B and G-H) of Region 3. Grey ellipses mark the main structures to be discussed in the text. 5) Round high velocity anomaly slightly SE from central craters. 6) Round high velocity anomaly located on the coast; 8) Round low velocity anomaly located W from central craters.*

From this tomographic inversion results, we highlight the presence of many high and low velocity anomalies (Figures 6.32, 6.33 and 6.34). Some of them are connected in depth (anomalies 5 and 6) (Figure 6.34) and some isolated (anomalies 7 and 8). These four anomalies will be further described an interpreted in the following paragraphs:

-*Anomaly 5*: Located slightly southeastern underneath the central craters, this high-velocity anomaly is widely known as High Velocity Body (see chapter 2). This feature appears in all the previous tomographic analysis being located up to 18 km depth. The dimensions of this volume may slightly differ from one author to another, averaging ca 600 km3 (e.g., Chiarabba et al., 2004). Falsaperla et al., (2013) also presented different tomographic cross sections, which better define the shape of the HVB up to 7 km b.s.l., and the results are clearly in agree with our observations. Moreover, this volume is inferred to be composed of high strength mafic rocks such as cumulites or dykes (see chapter 2). Its origin is interpreted as old magmatic deposits. Detailed studies of its composition have been carried out by Corsaro et al., (2014). These authors analyzed the composition of several xenoliths that may have the same origin of the HVB. Analyses reveal an intrusive gabbroic rock composition of the volume, indeed, involving a slow solidification process of a quite mafic magma.

-*Anomaly 6*: High Velocity anomaly located on the southeastern sector of Etna area, close to the coast. This volume is clearly resolved between 4km and 14 km depth where it seems to disappear or collide with a larger high velocity anomaly eastern offshore. We are investigating on the relationships between this HV volume and the presence of the Moho discontinuity upwelling, observed by Nicolich et al. (2000) in the Ionian margin of Sicily up to 17 km b.s.l.. Moreover, we are also analyzing the probably connection between the HVB (anomaly 5) and this volume (anomaly 6) at 4-8 km depth approximately (see vertical sections A-B and I-J. Figures 6.31 and 6.34).

-*Anomaly 7*: High Velocity anomaly located southwestern of the volcanic edifice. Due to the poor spatial resolution in this sector, as shown in the ray density distribution in Figure 6.25, we do not furnish any interpretation of this anomaly. However, this high velocity volume may be correlated up to 6 km b.s.l., with a high density anomaly, revealed by preliminary gravimetric analyses (J. Fernández, personal communication). -

Anomaly 8: Low Velocity anomaly western from the central craters A low velocity volume in this sector of the volcano have been highlighted by Aloisi et al. (2002), which was associated with the presence of magmatic reservoir and correlated with the anomalous b volume revealed by Murru et al., (1999).

-*Anomaly 9:* Low Velocity anomaly southern from Mt. Etna. This 20% negative anomaly presents absolute velocity values of around 3.6 km/s at 4 km depth. This volume has never been interpreted and therefore must be further investigated.

6.6 Final Remarks

It is important to note that the presented results correspond to a joint active passive tomographic inversion of a very short in time dataset. Indeed, we consider our results as a snapshot tomography that allows us to individuate volcanic structures without averaging them through time. However, for a better enlightening of the regional tectonic features, we propose further joint analyses including a larger passive dataset, as they should not change dramatically in time.

Another important issue revealed from our work is the remarkable "shadow" area western from Mt. Etna volcano where very poor resolution and ray coverage is found. Indeed, the seismic signals recorded in the nearby station where very difficult to be picked as most of the arrivals where highly attenuated or even impossible to recognize.

The interpretation of the low-velocity "ring" around the volcanic edifice, clearly visible in the shallower layers, is still under investigation, and requires further advanced analyses.

Besides its possible volcanic origin, anomaly 7 seems to disappear in depth, while a diffuse NW-SE alignment appears. This deep structure may be related with some major regional structures described by Barreca et al., (2016).

We present in figures 6.35, 6.36 and 6.37 preliminary 3D images of the high and low velocity anomalies. In these figures we clearly remark the main high and low velocity bodies and their connection in depth.

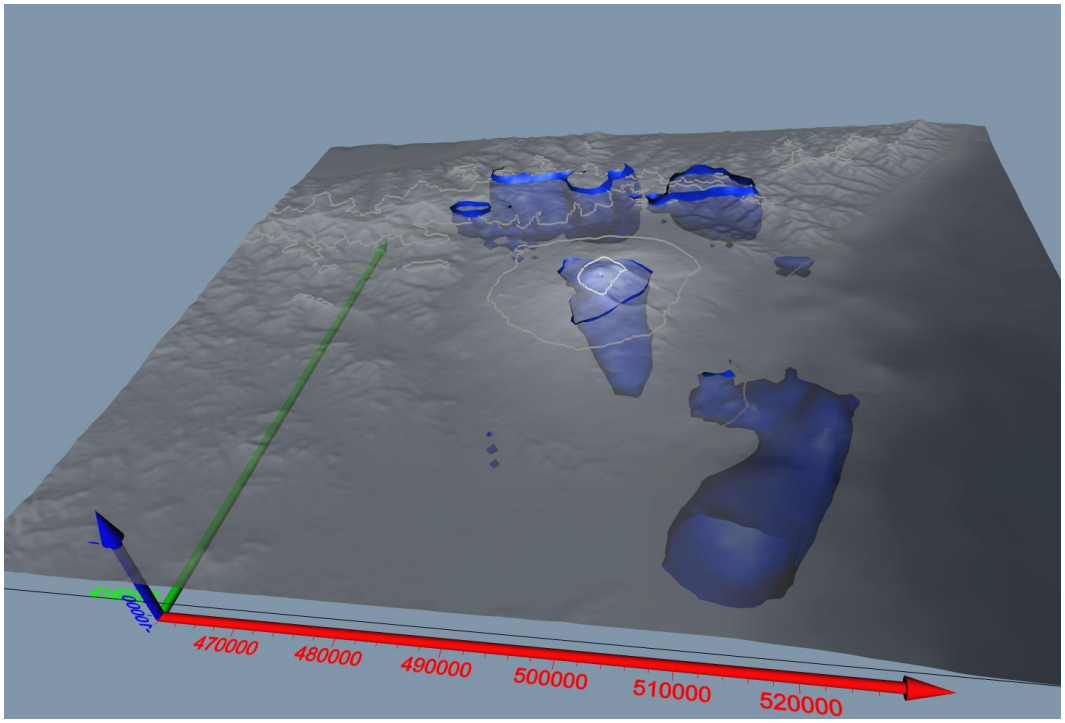

Figure 6.35. *3D P-wave absolute velocity maps for region 3. Blue volumes are those characterised by high P-wave velocities (Vp > 5.5 km/s). Green arrow points North.*

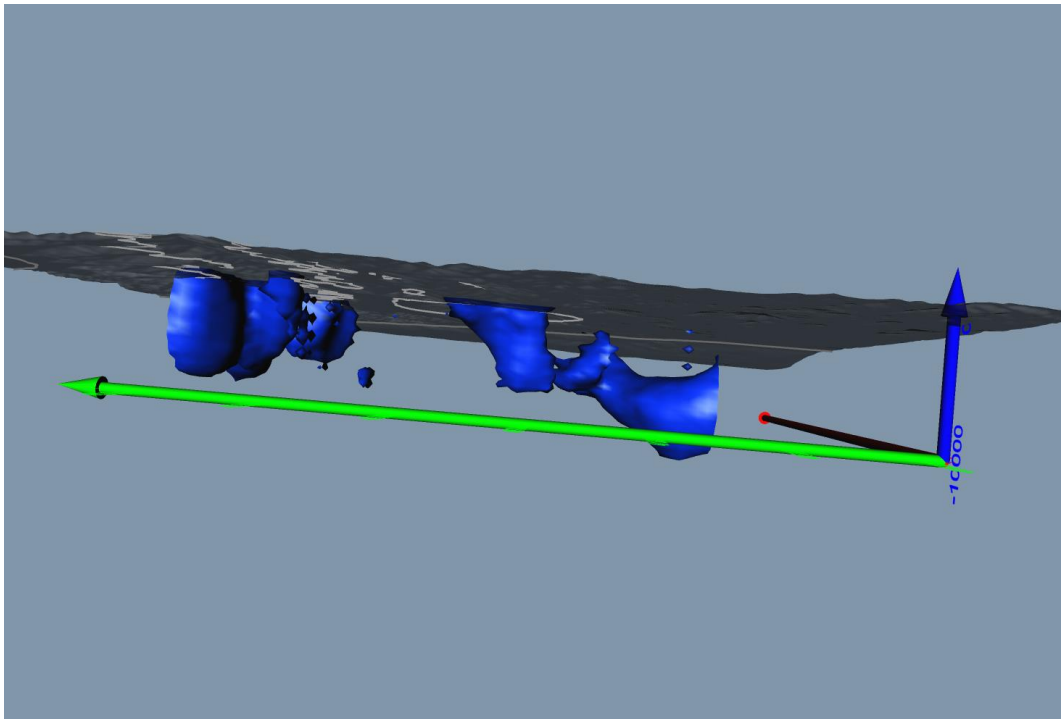

Figure 6.36. *3D P-wave absolute velocity maps for region 3. Almost YZ section. Blue volumes are those characterised by high P-wave velocities (Vp > 5.5 km/s).Green arrow points North.*

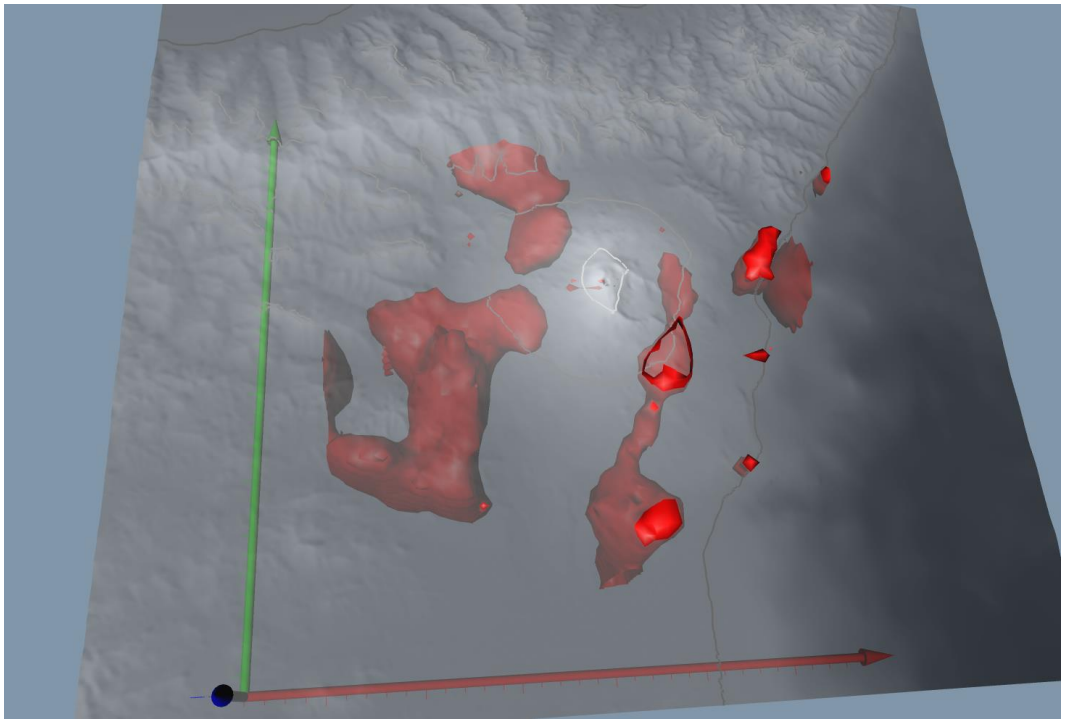

Figure 6.37. *3D P-wave absolute velocity maps for region 3. Almost XY section. Red volumes are those characterised by low P-wave velocities (Vp < 4 km/s).Green arrow points North.*

As final remarks we propose the presence of a series of anomalies of great relevance for both regional and local frameworks:

- *Anomalies 1 and 1b:* correspond to the well-known ATLFS, defined by many authors. Although its origin is still under debate, the most stable hypothesis is that of a dextral transfer zone separating a compressional regime on the western part of the Aeolian Archipelago, from an extensional regime to the northeast.
- *Anomaly 2:* Known as SAFS, this dextral strike-slip motion fault system accommodates the compression of the westernmost part of the Aeolian Archipelago. It easternmost limit reaches the mentioned ATLFS in the area of the Lipari-Vulcano complex.
- *Anomaly 3:* NW-SE discontinuity interpreted by many authors as a STEP fault related to the decoupling the subducting lithosphere from the non-subducting one.

- *Anomaly 4:* Large low velocity volume probably related to the active volcanism of the easternmost Aeolian Islands (Panarea and Stromboli).
- *Anomaly 5:* Probably the most well-known feature on the Etnean region. The HVB is enlightened, and as our results go deeper than previous tomographies, we observe the roots of this HVB connected in depth with new high velocity bodies located offshore.
- *Anomaly 6:* High velocity anomaly located near the coast of the eastern flank of Mt. Etna, that can be related with the HVB mentioned above. Other hypothesis is that these volume may be an effect of the Moho upwelling described by other authors.

There are some anomalies that never been interpreted and for which we present some preliminary ideas that must be further investigated. It is the case of anomalies 7, 8 and 9.

Finally, we want to remark that these seismic tomographic models are not just final results but also the key to carry out further advanced approaches as will be detailed in chapter 7.

7. An example of an Advanced Application: The analysis of The 2011–2013 seismic series associated to the volcanic activity of El Hierro Island on the light of a 3D high definition structural model

7.1. Advanced Applications of Velocity Models

To carry out many seismic analyses, the use of a velocity model that describes the different wave velocities at different depths becomes crucial. Thus, we could, for example, follow the ray path of a certain type of wave from its source to the receiver. Indeed, these velocities should be defined by considering both the regional geology and local structures. However, knowing the deep structures is not always possible, therefore seismic studies usually use simplified 1D velocity models to describe Earth Interior in order to perform further analysis. Nevertheless, these 1D velocity models do not always fit properly the studied region, especially in volcanic areas, which are known for their vertical and lateral heterogeneities. In these cases, differences between a simplified 1D velocity models and reality can be really large. To assess this problem, seismic velocity tomography provides a realistic 3D velocity model of the studied area that can be used for further analyses. These models, indeed, take into account vertical and lateral heterogeneities as they give velocity values for each cell of the defined 3D grid.

A wide range of studies can be enhanced using a 3D velocity model as initial input data: from routinely hypocentral location to more advanced seismic techniques.

The importance of obtaining realistic 3D velocity models throughout seismic tomography has been deeply described along this thesis. In this chapter we present a case of study with a complete set of seismic analyses for which we required a trustful tomographic velocity model. This case of study is focused on the island of El Hierro (Canary Islands, Spain) and the related seismo-volcanic crisis occurred on 2011. Additionally, further analyses derived from realistic relocation are described. Especially we present a new approach based on hydraulic fracturing and pore pressure diffusion modelling to study volcanic seismicity in order to better understand its origin.

7.2. Case of study: El Hierro seismo-volcanic crisis 2011-2013

In July 19th 2011 began a seismic unrest on the Island of El Hierro (Fig.7.1). This seismic activity leaded to a submarine eruption that last from October 2011 to January 2012. The seismic crisis registered in El Hierro was particularly large and intense starting on July 2011 and finishing on April 2013. A detailed description of the evolution and characteristics of this seismic crisis and submarine eruption is provided by López et al., (2012), Martí et al., (2013a) and Díaz-Moreno et al., (2015) among others.

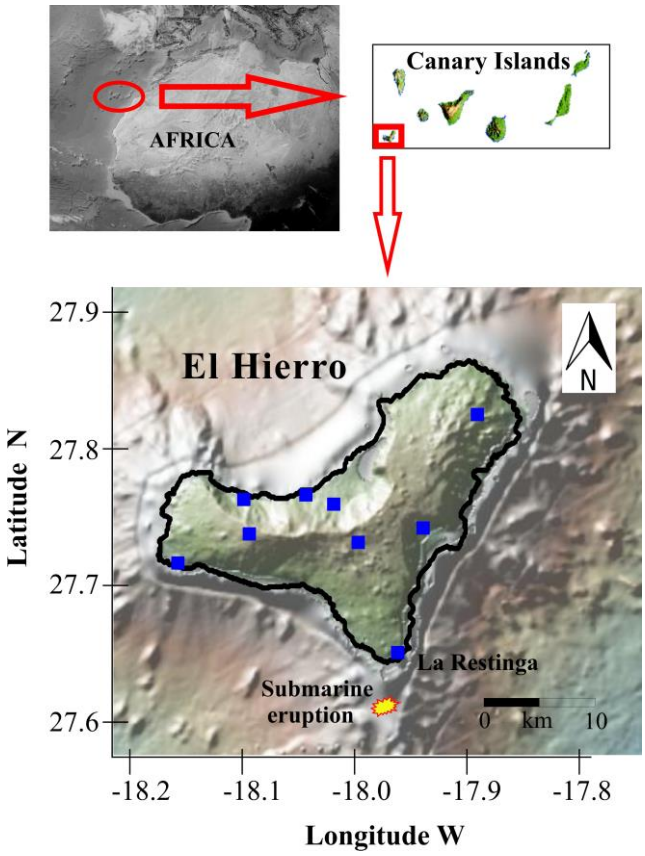

Figure 7.1. *Location of El Hierro Island, in the Canary archipelago, Atlantic Ocean. Blue squares represent the position of the seismic stations deployed by IGN. Red mark shows the eruptive area of October 2011 offshore La Restinga. The bathymetric map was obtained from http://www.geomapapp.org (see Ryan et al., 2009).*

7.2.1. Seismic Data and b-value estimation.

The dataset used in this study includes P- and S-wave phase readings from 18,902 earthquakes recorded between July 19th, 2011 and April 15th, 2013. These data are published in the revised earthquake bulletin of the "Instituto Geográfico Nacional" (IGN), the agency responsible for seismic monitoring in Spain (http://www.ign.es/ign/layoutIn/volcaFormularioCatalogo.do). The earthquake catalogue is based on data recorded by a network of 9 three-component, short-period seismometers with natural period of 1 second. In figure 7.2 we show earthquake rates throughout the period analysed in this manuscript and the cumulative energy release between Mid-July 2011 to Mid-April 2013.

Managing such a large catalogue implies to put great efforts in checking the quality of the data. One of the most popular methods in volcanic seismology is based on assessment of the seismic b-value and the magnitude of completeness (Mc) of the catalogue. The b-value is a parameter estimated from regression analyses of the frequency magnitude distribution (FMD) of earthquake catalogues. The FMD of earthquakes is scale-invariant and obeys the following power-law (Ishimoto and Iida, 1939; Gutemberg and Richter, 1944):

$$\text{Log } (N) = a - bM \qquad (7.1)$$

where N is the cumulative number of earthquakes with magnitude equal or greater than M, a and b are positive, real, constants characteristics of every earthquake catalogue. In particular, a corresponds to the logarithm of the number of earthquakes with M=0 (i.e. it is an index illustrative of the overall levels of seismicity), and b represents the relative amount of large to small events in a catalogue.

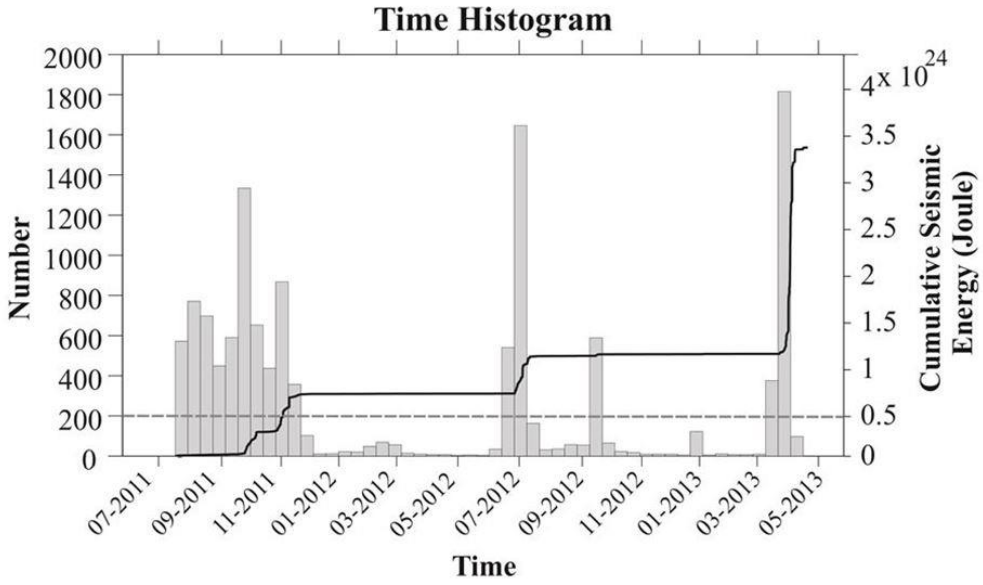

Figure 7.2. *Daily earthquake counts throughout the period analysed in the present work (mid July 2011 to May 2013). The cumulative seismic energy is plotted.*

The first, essential, step in b-value studies is the assessment of the magnitude of completeness (Mc) of the catalogue, i.e. the lowest magnitude at which 100% of the earthquakes in a given space-time volume are detected (Rydeleck and Sacks, 1989; Woessner and Wiemer, 2005). When a Gutemberg-Richter FMD is assumed, Mc is simply the magnitude at which the cumulative FMD curve departs from a linear trend. Calculations of magnitude of completeness in this study were performed using two different procedures, the Maximum Curvature Method (MCM) and the 90% Goodness-of-fit (GFT) method (Wyss et al., 1999; Wiemer and Wyss, 2002). In the MCM, Mc is defined as the point of maximum curvature of the FMD curve, which simply corresponds to the maximum of the first derivative of the cumulative FMD curve. The GFT method estimates Mc by comparison of the actual FMD with synthetic ones. A synthetic FMD for the El Hierro catalogue is generated for magnitudes between 0 and 4.6 (in bins of 0.1

magnitude units) and compared to the actual FMD by means of the GFT function (residual function):

$$R(a,b,M_i) = 100 - 100\frac{\sum_{M_i}^{Mmax}|B_i - S_i|}{\sum_i B_i} \qquad (7.2)$$

where Bi and Si are the actual and simulated cumulative number of events per magnitude, Mi is the minimum magnitude, a and b are the Gutemberg-Richter a- and b-values in eq. (7.1) for magnitudes greater than Mi. The minimum magnitude that corresponds to a value of the residual function, R, equal to 10% (i.e. 90% goodness of fit) is defined as Mc. The two methods consistently yielded similar results in all our calculations as expected for a catalogue that contains a large number of events and a uniform magnitude distribution such as the El Hierro seismic sequence. The Mc used was chosen as the best combination of MCM and 90% GFT (Wiemer and Wyss, 2000). The 90% GFT method had higher priority; if R in eq. (7.2) did not reach 10%, or 90% goodness of fit, the MCM value was used. The b-value was estimated by least square linear regression (LSR) on the FMD curve.

It has been suggested in the past that the b-value may depend on the stress conditions in the crust, material heterogeneity, and local thermal gradients (Mogi, 1962; Scholz, 1968; Wyss, 1973). Because of its diagnostic power, the b-value has been extensively employed in studies to identify active magma bodies, and track the spatial and temporal evolution of seismicity during periods of unrest. The b-value in regimes of high tectonic stress and material homogeneity is often less than 1; in contrast highly fractured rock is characterized by lower stresses, and thus, exhibits b-values appreciably greater than 1 (McNutt, 2005). A global average of the b-value for complete catalogues without departures from the linearity of eq. (7.1), is about 1 (Bridges and Gao, 2006). However, particularly in volcanic regions, b-values can be as high as 3. Several volcanoes display b-value anomalies at relatively shallow depth (~3-7 km) in relation with high degree of rock fracturing, and the presence of fluid-filled cracks, dykes and fractures

(McNutt, 2005). Farrel et al. (2009), for instance, analysed the seismicity recorded in the Yellowstone volcanic field between 1973 and 2008, a catalogue of about 30,000 earthquakes with magnitudes between -0.5 and 6. Spatial and temporal b-value mapping identified areas of high b-value in relation to the migration of magmatic fluids, and regions of low b-value attributed to high extensional stress regime. Jacobs and McNutt (2010) used the b-value to investigate the sequence of earthquakes leading to the 2006 eruption of Augustine volcano; they found evidence of high b-value anomalies related to changes in thermal gradients, pore pressure and stress, linked to the intrusion of a magmatic dike before the onset of the eruption.

Possible temporal variations of b-value were also investigated by means of a moving window technique (Wiemer and Wyss, 2000). This approach is known to be affected by intervals with low levels of seismicity, thus, producing uneven temporal sampling and smoothing of the b-value time series. The El Hierro catalogue, however, is characterized by high enough earthquake rates to ensure that, given the right choice of parameters, satisfactory results can be obtained. We tested multiple sets of input parameters, including variable catalogue time spans, window lengths and overlap, threshold magnitudes, and magnitude binning. The temporal variations in b-value were estimated using 200-event moving windows, with 10% overlap.

Ibáñez et al., (2012) observed that the b-value during seismic swarms is a powerful indicator of stress conditions. They reported changes in b-value from 2.25 during the early, pre-eruptive, period to 1.25 at the end of the eruptive phase. Their interpretation was that earthquakes during the first phase of unrest occurred as the consequence of stress transfer associated with magma migration from the upper mantle into the curst. The larger magnitude earthquakes recorded at the end of the analysed period were attributed to stress relaxation around the magma reservoir. In this section we will reanalyse the whole seismic series starting with a detailed study of the temporal variations of b-value.

In figure 7.3 we show temporal changes in b-value from which 6 seismic phases can be clearly identified. Phases 1, 2 and 3 coincide with those previously identified by Ibáñez et al. (2012) and correspond to the pre-eruptive and main submarine eruptive

period (July 2011–January 2012). However, three new seismic phases (phases 4, 5 and 6) were unidentified in previous works. During phase 4 a second eruptive event may have occurred as suggested by Pérez et al. (2014). Each phase is characterized by a sudden increase of the b-value, in some cases up to 3.0, and a progressive temporal decrease to values as low as 1.0. With the exception of the first and third phases (with a duration of three months), the duration of each seismic swarm is of the order of 1 month. In table 7.1 we summarize the characteristics of each phase, including their duration, number of earthquakes, and other significant observations.

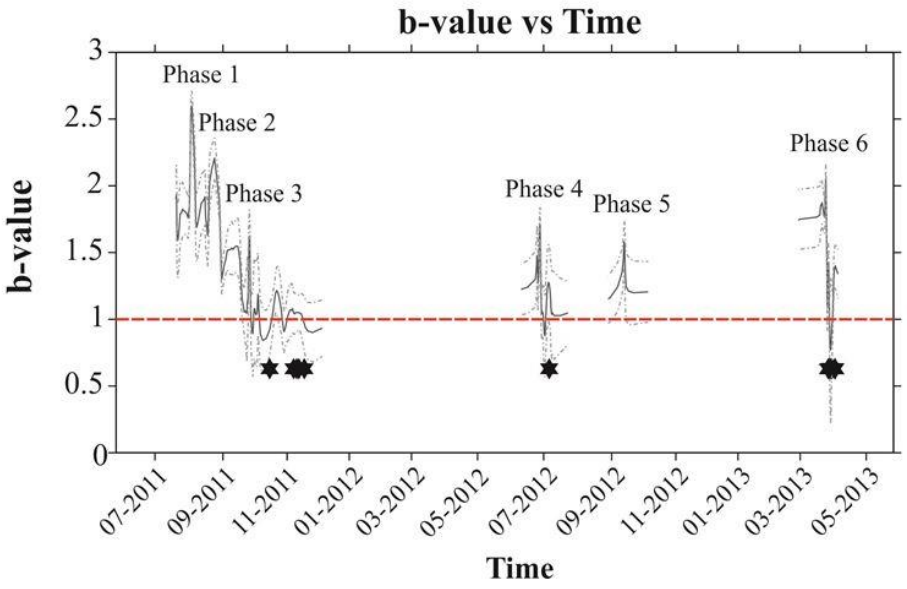

Figure 7.2. *Time dependent estimate of b-value using a moving window technique. b-values are calculated over successive windows of 200 events, with an overlap of 10%. Intervals with occurrence of less than 50 daily earthquakes were not considered for the present analysis.*

As high b-values can be interpreted in response to magma-related seismicity, b-values close to 1.0 define common pure-tectonic activity (see the above discussion). In

the case of El Hierro we detected periods of sudden increase in b-value followed by a decrease to reach values close to 1.0. Therefore, we interpreted the initial stages of each seismic swarm as a magma injection that is then followed by a more tectonic behaviour. This new tectonic response of the region will be analysed applying of hydraulic fracturing modelling and pore pressure diffusion.

Phase	**Time Interval**	**Highest b-value**	**Number of earthquakes (Magnitude > 1.3)**	**Number of earthquakes (Magnitude > 1.3) relocated with HypoDD**	**Number of earthquakes (Magnitude > 1.3) relocated with NLLoc**	**Main Geophysical and Geochemical observations**
1	07/19/2011 – 09/20/2011	2.8	3,408	3,037	3,153	Low magnitude seismicity.
2	09/21/2011- 10/12/2011	2.2	1,212	906	1,067	Hypocentre deepening trend. Change in b-value.
3	10/13/2011 – 03/05/2012	1.6	1,820	1,240	1,207	Onset of the submarine eruption. Volcanic tremor and higher magnitude events.
4	06/24/2012 – 07/15/2012	1.8	2,776	1,975	1,853	High deformation and gas emissions. High magnitude seismicity.
5	09/14/2012 – 09/23/2012	1.6	858	473	581	High deformation and gas emissions. Great number of events in short time.
6	03/18/2013 – 04/15/2013	2.3	2,330	280	2,122	High deformation and gas emissions. Great number of events in short time.

Table 7.1. *Stages of seismic unrest.*

7.2.2. Seismic relocation.

One straightforward application of a realistic 3D velocity model is the seismicity relocation. Location errors associated to routinely hypocentre location are usually large, as the main goal of this analysis is usually to obtain as fast as possible the location of an event in order to assess the risk. Differences on the location of the earthquakes using 1D and 3D velocity models are dramatic and may lead to a better understand of the processes and structures that are responsible of this seismic activity. To support this statement, we provide in this chapter, two different relocations using different algorithms to confront with an initial routinely hypocentre location. The difference between both will be shown and discussed in the following paragraphs.

In order to ensure that the best quality data are used in the following calculations, we removed all earthquakes with magnitudes M < 1.3, defined using b-value and Mc calculations previously described, from the original catalogue and those with less than 8 phase readings. The final data set consisted of 12,404 earthquakes with magnitudes between 1.3 and 4.9. Once we selected and characterized the high-quality data, a realistic relocation of the seismicity must be done. Performing a seismic relocation requires a realistic 3D velocity model of the region. Therefore we used the 3D velocity model obtained by García-Yeguas et al. (2014) calculated throughout the seismic passive tomography of this catalogue. We carried out the relocation by applying two different approaches: i) relative locations using HypoDD software proposed by Waldhauser (2001); and ii) probabilistic non-linear locations using NonLinLonc Software provided by Lomax et al., (2000). This relocation would enhance the quality of the hypocentre locations leading to the definition of different seismic patterns during the evolution of each series.

Preliminary earthquake locations published by IGN had average horizontal and vertical errors of 9 and 5 km, respectively. These values are large, and even more so in relation to the size of the region interested by volcanic activity; in Figure 7.4 we plot the original IGN locations available online. The vertical uncertainties are too large in order to distinguish any pattern or structure associated with the seismicity.

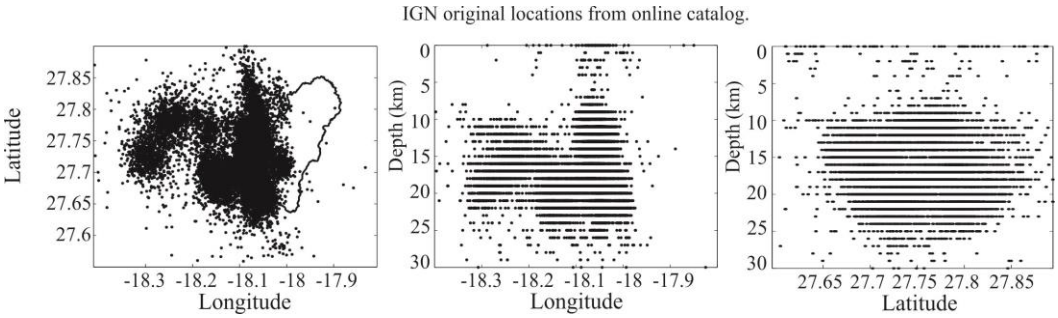

Figure 7.4. *Initial seismicity maps obtained from the original IGN online catalogue.*

Previous studies (e.g. López et al., 2012; Domínguez-Cerdeña et al., 2014 or Del Fresno et al., 2015) used the HypoDD (Waldhauser & Ellsworth, 2000) algorithm along with a regional, 1D, velocity model, which was not derived from inversion of local earthquake data. One of the main requirements of HypoDD is good azimuthal coverage. Due to the large amount of earthquakes located offshore, we prefer an earthquake location algorithm that is better suited for the task, NonLinLoc (Lomax et al., 2000). However, in order to compare and confirm results, we initially relocated the entire earthquake catalogue with both methods. We used a realistic velocity model (1D and 3D) derived ad-hoc for El Hierro using the results of a seismic tomography study by García-Yeguas et al. (2014) (Figure 7.5). These authors used 13,040 earthquakes in their inversion, including 89,583 P and 95,339 S-phases. As waveform data are not publicly available, only information from the IGN published bulletin, including P and S arrivals, could be used. Absolute and differential P- and S-wave arrival times were used for relocation with HypoDD and NLLoc.

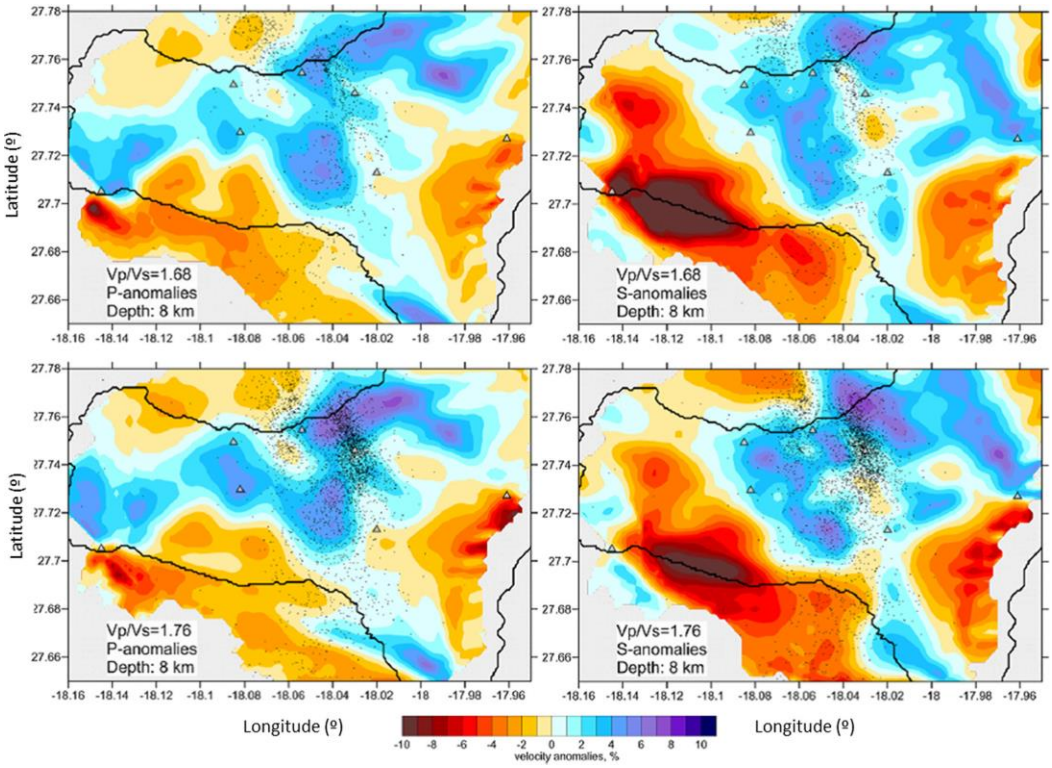

Figure 7.5. *V_p/V_s ratio anomalies described by Garcia-Yeguas et al., (2014).*

HypoDD solves a double-differences location problem, and locates pairs of events, starting from a 1D velocity model, assuming that the distance between their hypocentres is significantly smaller than the distance between the hypocentres and the recording stations. NLLoc is a probabilistic non-linear earthquake location method that allows the use of any available velocity model (1D, 2D or 3D). Further, with NLLoc it is possible to calculate an a-posteriori probability density function (PDF) that represents a complete probabilistic solution to the earthquake location problem, including information on uncertainty and resolution (Lomax et al., 2000; Mostaccio et al., 2013). The PDF can be computed via: i) a systematic Grid Search, which provides high accuracy to the expense of longer CPU time; ii) a stochastic Metropolis-Gibbs search, which is slower than linearized methods but faster than the grid search method; or iii) a hybrid Oct-Tree search method, which provides an optimal balance between CPU time and accuracy of

the results (for additional information see Lomax & Curtis, 2001). We adopted the Oct-Tree method. A probabilistic approach to earthquake location problems has been demonstrated to be more reliable than linear inversion with limited seismic network coverage (Presti et al., 2008), such as the case of El Hierro.

The results of relocations for each of the unrest phases are shown in figures 7.6a and 7.6b. Figure 7.6a shows relative relocations obtained from the NLLoc algorithm and Figure 7.6b illustrates the locations from HypoDD. Although in the previous section, based on b-value patterns, we identified at least 6 seismic phases, the spatial distribution of the VT earthquakes demonstrates that phases 1 and 2 are spatially indistinguishable. Therefore, for the purpose of the present study we will consider them together. The two algorithms produce comparable hypocentral distributions, an indication of the stability and reliability of our results. The new earthquake location maps, compared with previously published results (eg. López et al., 2012; Domínguez-Cerdeña et al., 2014 for phases 1, 2 and 3), display less scatter, and the five temporal phases are also clearly spatially separated. The lack of shallow (above 10 km depth) seismicity is noteworthy. The NLLoc algorithm, combined with a 3D v_P model and constant v_P/v_S ratio, yields precise and reliable hypocentre locations. NLLoc also provides a reliable means to identify poorly constrained hypocentre locations, and generally returns stable solutions for most seismic events. Comparing the results from NLLoc and HypoDD, the former exhibits more obvious clustering of seismicity and some linear features are also resolved. Moreover, the root mean square (RMS) residuals and hypocentral errors obtained with NLLoc are lower, less than 0.15 s and 0.5 km, respectively. The epicentres of events are spread over a relatively broad area, mostly in the south-west direction. The focal depths are constrained in the upper 25 km. Additional benefits of using 3D velocity models with NLLoc include that the probabilistic earthquake location algorithm provides a complete description of location uncertainties (Lomax et al., 2000). Conversely, hypocentral error estimates by HypoDD are only relative, as the algorithm only inverts for relative earthquake locations (e.g. Gambino et al., 2004).

In the NLLoc solutions, focal depths range between 5 and 25 km depth below sea level (b.s.l.), with more than 80% of the total seismicity being deeper than 12 km. The bulk of seismicity is located at depths of 12-16 km. General features of seismicity are that it is spread over a relatively large region below the island and distant from the site where the eruptions occurred. We also observe that no events were located south-east of the site of the October 2011 eruption. This region with absence of seismicity is highlighted in figure 7.6.

Figure 7.7a shows the Probability Density Function (PDF) of hypocentre locations estimated by NLLoc. The PDF represents a complete, probabilistic solution to the location problem, including information on uncertainty and resolution. This solution does not require a linearized theory, and the resulting PDF may be irregular and multi-modal because the forward calculation involves a non-linear relationship between hypocentre location and travel-times. This solution includes location uncertainties due to: a) the spatial relation between the network and the event; b) measurement of uncertainty in the observed arrival times, and c) errors associated with the estimation of theoretical travel times. The PDF values obtained via the grid-search procedure represents the complete, probabilistic spatial solution to the earthquake location problem. This solution indicates the uncertainty in spatial location due to Gaussian picking and travel-time calculation errors, the network-event geometry, and the incompatibility of the picks. The location uncertainty will in general be non-ellipsoidal (non-Gaussian) because the forward calculation involves a non-linear relationship between hypocentre location and travel-times. For each event, we calculated a complete map of the PDF of earthquake locations. The results were then stacked to obtain a composite location probability for all the located events (Saccorotti et al., 2001). The depth distribution of PDF reveals that the probability of earthquake occurrence is largest in the central sector of the island at depths between 10 and 20 km b.s.l.

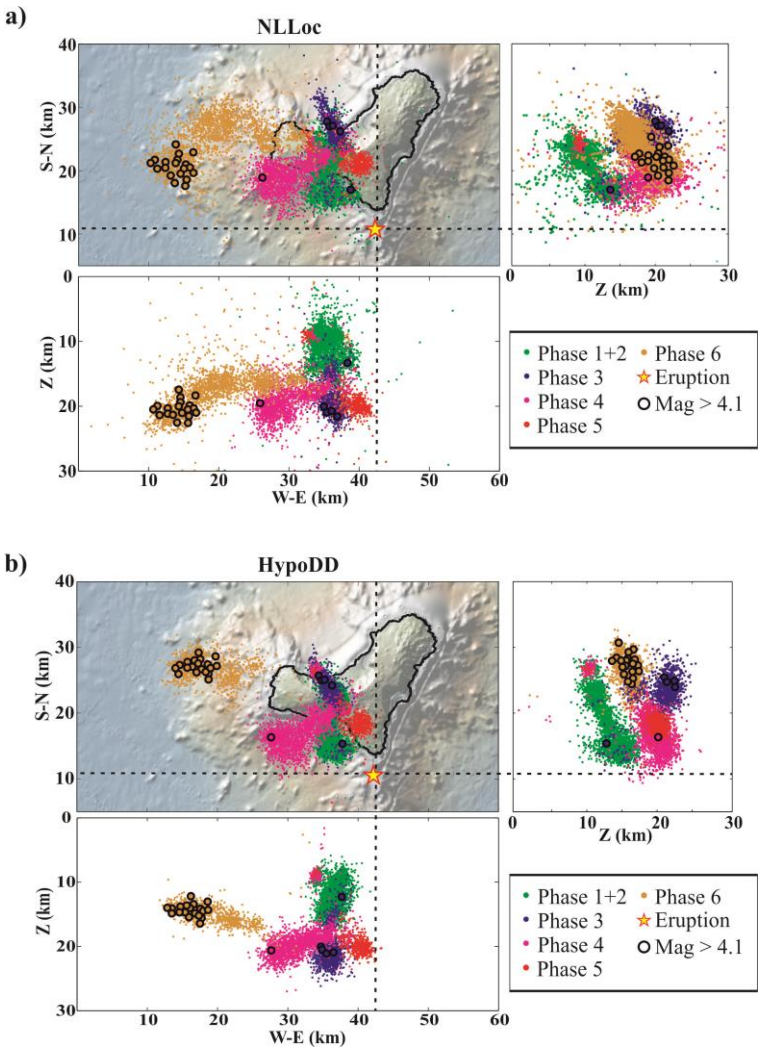

Figure 7.6. *a) Map of earthquake hypocentres at El Hierro obtained with NLLoc. b) Map of earthquake hypocentres at El Hierro obtained with HypoDD. Dashed lines mark the boundaries of the epicentral area toward South and East. The crossing point of these lines is the site of the La Restinga submarine eruption. The bathymetric map was obtained from http://www.geomapapp.org (see Ryan et al., 2009). The yellow start represents the site of La Restinga submarine eruption occurred in October 2011 – January 2012. Black circles represent the position of earthquakes with magnitudes above 4.1.*

In order to locate the point where each seismic series started, we do not use the location of the first earthquake in the sequence; instead, we calculate an average hypocentre from the first 10 earthquakes within each swarm. In figure 6b we illustrate the location of these points, and noted that they are located very close to one another, directly underneath El Hierro, and at very similar focal depths. The site where all seismic phases initiate coincides with the maximum of the earthquake locations PDF (Figure 7.7a).

For the purpose of investigating the spatial and temporal evolution of seismicity within the swarms we divided each phase into 12 equal-time periods (this time-windowing ensured that a large enough number of events was included within each interval). We, then, estimated the average location of all hypocentres within each period. This procedure allowed us to track the spatial and temporal evolution during each seismic phase (Figure 7.7b). In figure 7.7b we show the spatial and temporal evolution of the seismic clouds that track the average focal position of a large number of events within a short period of time. This plot reveals the evolution of the seismic clouds as well as any recurrent patterns between different seismic clouds. The main features of seismicity displayed in figure 7.7b are:

a) All seismic phases were triggered within a common, relatively small, volume located beneath El Hierro at depths of 12-14 km b.s.l.

b) Each seismic series evolves independently of all others, spanning different seismogenic volumes underneath El Hierro. There is no clear evidence of migration of the seismicity towards the surface. On the contrary, each series shows deepening of hypocentres with time. During all seismic series earthquake hypocentres migrate away (radially outwards) from the centre of El Hierro.

c) No preferential lineation is identified in the spatial evolution of seismicity. Hypocentre migration during each seismic series does not exhibit directivity.

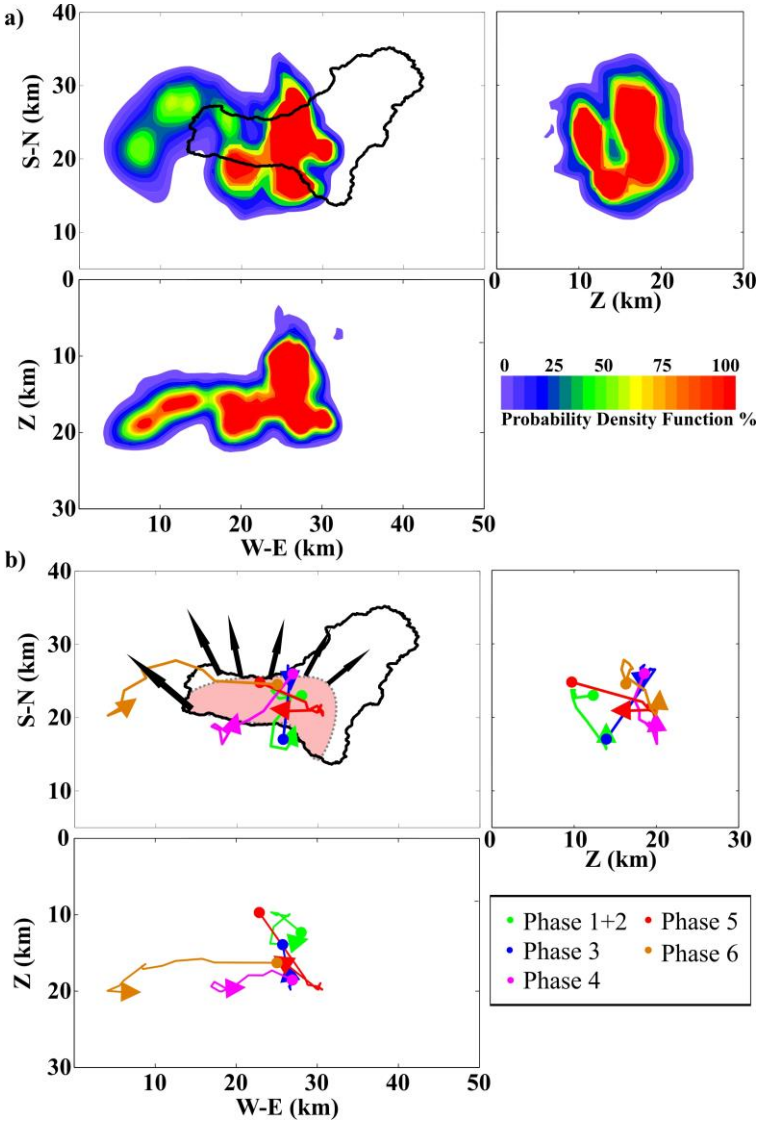

Figure 7.7. *a) Probability density function (PDF) image obtained from NLLoc relocation using the grid search method. b) Map of temporal and spatial evolution of seismicity representing the migration of each phase identified. Coloured arrows represent the final position of each series. Dots represent the average location for the first 10 earthquakes of each phase. Black arrows represent the observed horizontal deformation trends observed by García et al., (2014). Light pink area is the observation of the highest vertical deformation zone indicated by González et al., (2013).*

It is remarkable that the horizontal projection of the onset region of every seismic phase coincides with the area of highest deformation measured both using GPS and satellite observations (González et al., 2013; and García et al. 2014) as also illustrated in figure 7.7b. The light pink-coloured area represents the highest deformation values both in elevation and in the horizontal direction, as inferred from interferometry and GPS measurements published by Gonzalez et al. (2013) and Garcia et al. (2014). This observation suggests, potentially, a unique magmatic plume located directly underneath El Hierro.

It should be noted that the relocated seismicity does not exhibit any obvious spatial clustering around any potential pre-existing fracture systems, as observed in other studies (e.g. Deichmann and Giardini, 2009). In order to detect the existence of specific patterns in the spatial evolution the seismicity we study the differences in the relative position of a given earthquake, n, and the successive one, n+1 (figure 7.8). The main objective of this calculation is to understand whether there is any evidence of a preferential direction in the fracture process. Analysing the position of a given event relative to the next one, we investigate the existence of pre-existing fractures in the medium controlling the temporal evolution of the rupture. Figure 7.8 shows all seismic series sharing a similar characteristic: the lack of any preferential micro-fracture direction. This result supports a model of stress and hydraulic fracture diffusion to explain the mechanisms of seismogenic rupture in the El Hierro seismic series.

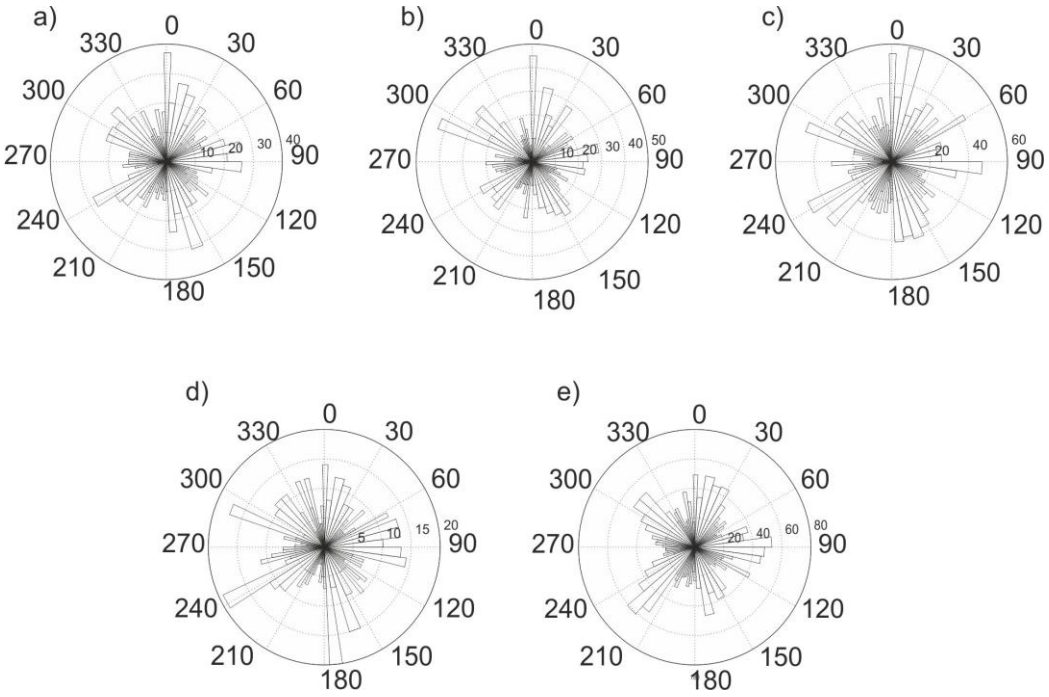

Figure 7.8. *Compass plot of azimuth between each pair of successive earthquakes. Each diagram represents one of the seismic phases. Note that the diagrams do not show any preferred rupture direction.*

7.2.3. Diffusivity Curves

It is noteworthy that injection of fluids, such as magma or water, can initiate seismic swarms (Pedersen et al., 2007). We infer that pore-pressure diffusion represents an important triggering mechanism of these series. Pore-pressure diffusion as trigger mechanism has been proposed in different studies: e.g. reservoir (large artificial lakes) induced seismicity (Talwani, 2000), water table changes or stream discharge connected with microseismicity (Lee and Wolf, 1998), earthquake swarms (Toda et al., 2002; Parotidis et al, 2003), fluid injections (Shapiro et al., 2002; Rothert and Shapiro, 2003; Parotidis et al, 2004; Deichmann and Giardini, 2009; Shapiro et al., 2010; Goertz-Allmann et al., 2011), and aftershocks of strong earthquakes (Bosl and Nur, 2002; Shapiro et al., 2003). As suggested by Shapiro et al., (2005) and Shapiro and Dinske

(2009), microseismic series associated to fluid injection (including magma) could be linked to a process of linear relaxation of pore pressure perturbations in a saturated medium with low or moderate permeability. When this phenomenon takes place within a short time period (hours or days), rupture propagation can be explained using linear pore pressure diffusion. The local diffusivity could condition the rupture mechanism and how it propagates, including the spatial distribution of hypocentres. In this section we follow the approach of Delepine et al. (2004) and Shapiro and Dinske (2009) to analyse the spatial evolution of El Hierro seismicity and test whether earthquake generation could be explained using the linear diffusivity model. Following Shapiro et al. (2002) the spatial and temporal features of the pressure-diffusion induced seismicity can be derived adopting the "triggering front" concept. If we can approximate the injection site as a point, or small in comparison to the size of the resulting cloud of hypocentres, it is likely that earthquakes could occur at distances smaller than the relaxation volume of the pore pressure. At larger distances seismicity will have lower probability of occurrence. The surface that characterizes this process is the triggering front (r_t). In the case of an isotropic and homogeneous medium, this triggering front is identified by the following relationship:

$$r_t = \sqrt{4\pi D t} \qquad (7.3)$$

where t is the time from the start of the seismic sequence and D is the hydraulic diffusivity.

Although Delepine et al. (2004) indicated that hydraulic diffusivity is frequently anisotropic, in some instances the diffusivity equations can still be applied for an isotropic media. In order to test the validity of the assumption of isotropic medium we scale the cloud of earthquakes using spherical shells centred at the location of the magma injection in every seismic phase. If the initial sphere has a dimension smaller than the size of the seismic cloud the assumption of isotropic medium can be applied within that volume. For this sphere we count the number of earthquakes included in it. Then, we build larger spherical shells centred at the same point and count the number of events within each shell. We build a "spatial density" of seismicity by normalizing earthquake

counts within each shell by the number of events included in the initial sphere. Under the assumption of a homogeneous and isotropic medium, the spatial density of seismicity should decrease with distance from the source. Since we do not know the size of the triggering stress propagation area, we can test this curves starting from an initial small radius of the sphere. If the nucleation region is smaller than the triggering stress area, the curve should initially grow and then decrease. If the size of this nucleation region is similar to the triggering stress area then the curve decreases homogeneously. In applying this procedure we started with an initial sphere of radius of 500 m centred at the initial point of every seismic phase. In figure 7.9 we plot how the normalized seismic cloud changes as a function of the radius of the nucleation region, from the common starting sphere of 500 m (left column) to the selected final nucleation sphere, were curve slopes decrease homogeneously (right column). Then we compared these nucleation spheres with the extension of the VT earthquake cloud and confirm the hypothesis of homogeneous and isotropic medium from the point of view of stress propagation. In table 7.2 we report the size of the nucleation spheres for every seismic phase along with the size of the associated seismic cloud. It can be observed that in all series the dimension of the nucleation spheres is smaller than the final length of the seismic cloud. Interestingly, the size of the nucleation sphere increases with time.

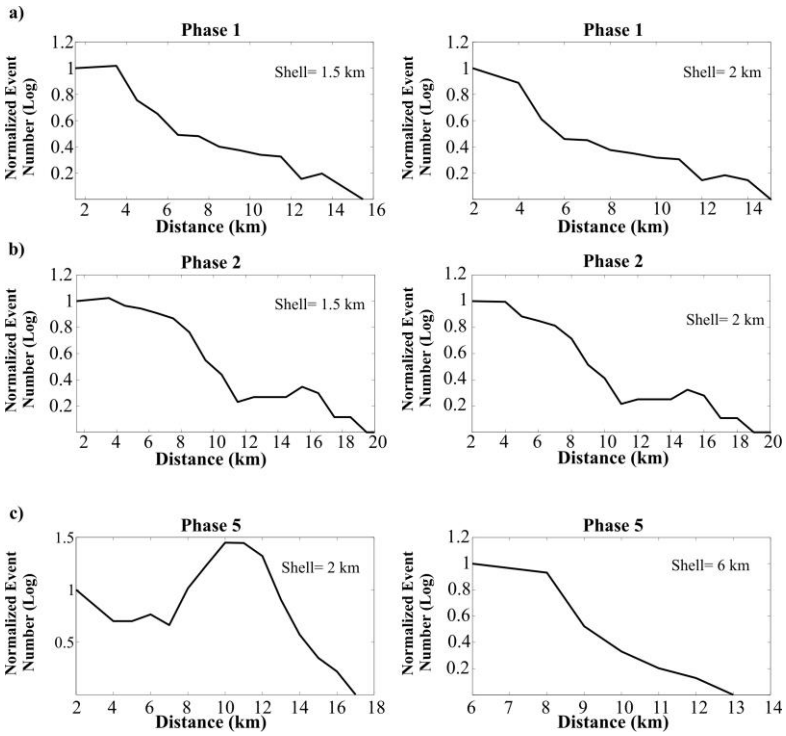

Figure 7.9. *Representation of the spatial density of the seismicity (normalized values from the initial sphere count) versus distance for the six seismic phases (See manuscript main text for a description of how these curves have been estimated. The left-hand side panels show the result with the value of the starting sphere size. The right-hand side panels show the spatial density of seismicity when the size of the shell presents a homogeneous decrease versus distance. During phases 1 and 2, the nucleation sphere is smaller (1.5 km of radius) than for other series. In general this radius grows for latest series, reaching values of 6 km for phase 6.*

Phase	Best Diffusivity value D (m^2 s^{-1})	Size of radio of the initial nucleation spheres (km)	Length of the associated seismic cloud (km)
1a	0.015	1.5	15
1b	0.03	1.5	15
1c	0.035	1.5	15
2	0.04	1.5	20
3	0.08	4	25
4	0.20	5	25
5	0.25	6	20
6	0.30	6	32

Table 7.2. *Best Diffusivity value D (m^2 s^{-1}) for every seismic series, the size of the radio of the initial nucleation spheres, and length of the associated seismic cloud.*

Equation 7.3 was applied to the previously identified seismic phases to calculate the triggering front and to estimate diffusivity. The process followed to estimate the best D-value was similar to those used by Akinci et al. (1995), albeit with a single variable, and could be summarized as: a) we calculated different triggering front (r_t) using different values of the diffusivity (D); b) the best D-value is the one for which triggering front curve produces the minimum residual and contains 90% of the earthquakes. In figure 9 we show an example of estimate of r_t versus time for different diffusivity coefficients during Phase 6 along with the evolution of b-value. When the diffusivity is estimated for the whole interval (400 hours) the fit of the different D values is less robust and large uncertainties are observed (Figure 7.10). The b-parameter (Figure 7.10a) increases to a maximum value of 2.25 at about 130 hours after the onset of the swarm. Then, at about 250 hours later, it decreases smoothly to values close to 1.0. Based on these observations we re-calculate the curve of r vs t for a shorter period (280 hours) during which the b-value is stable with values of around 1.0. The new curve provides a better fit to the data, and a diffusivity value of D= 0.3 m^2 s^{-1} is calculated. We performed similar fits to the rest

of the sequence for a selected period of time. We adopted the following criterion: the end-time interval is the time at which the b-value, after reaching its maximum value, decreases again close to 1.0.

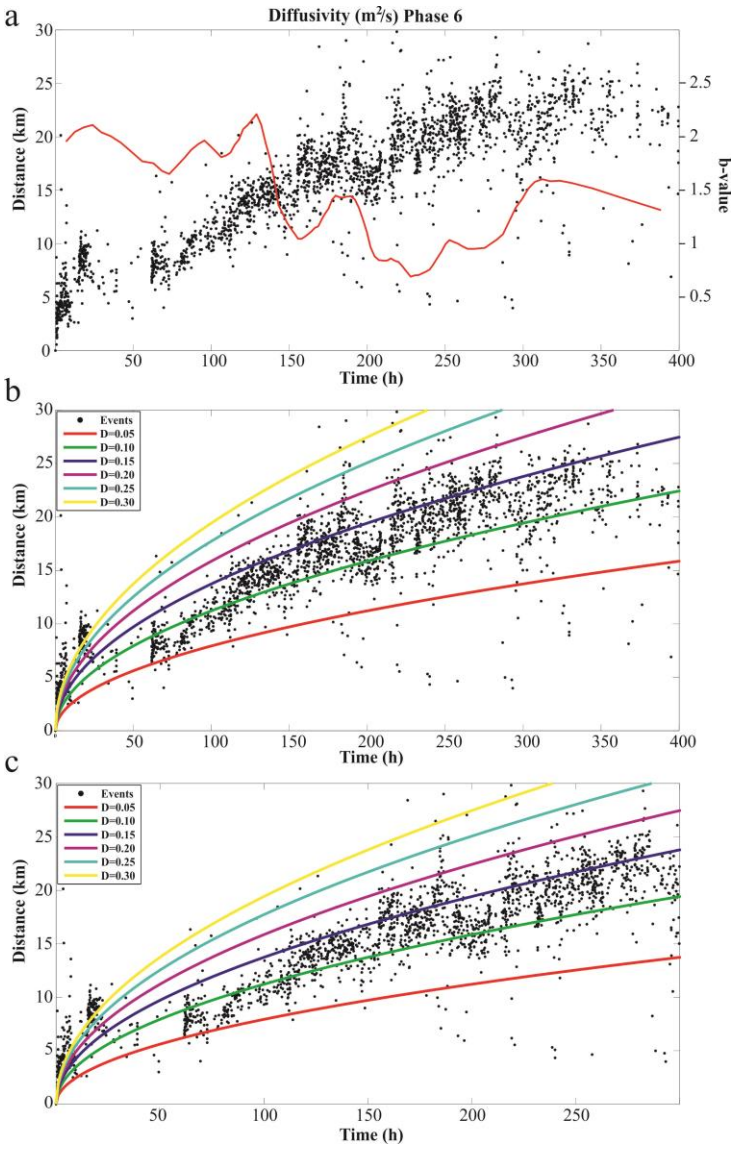

Figure 7.10. *Example of the procedure of diffusivity calculations. Results for Phase 6 are shown. a) Evolution of the distance of earthquakes as a function of the start time of the seismic swarm is plotted along with the evolution of the b-value. The start site of the series is calculated as the average hypocentre of the first 10 earthquakes as indicated in in figure 6b. b) Theoretical curves r vs t (eq. 7.3) for the whole duration of the series. c) Same curves as in figure 9b but truncated at the time when the b-value for this phase is minimum (see text for more details).*

In figures 7.11 and 7.12 we plot all the r vs t curves and the estimated best diffusivity. It is interesting to observe that for phases 1, 2 and 3 this estimate was more complex than for the rest of the series. This complexity is also reflected in the pattern of the b-value (see figure 7.2). Since these phases are associated to the onset of volcanic activity we could hypothesize the existence of more than three seismic phases. Phase 1 can be a combination of multiple magma injection processes. In figure 7.11 we plot 3 examples of r_t vs t for phase 1 (named 1a, 1b and 1c). We also note a temporal evolution of diffusivity, increasing with time. For the first seismic series, the best diffusivity value is D= 0.015 m^2 s^{-1}. For the rest of the series we obtained higher values ranging from D= 0.03 m^2 s^{-1} to D= 0.30 m^2 s^{-1}. In table 7.2 we summarize the best D values for each seismic series.

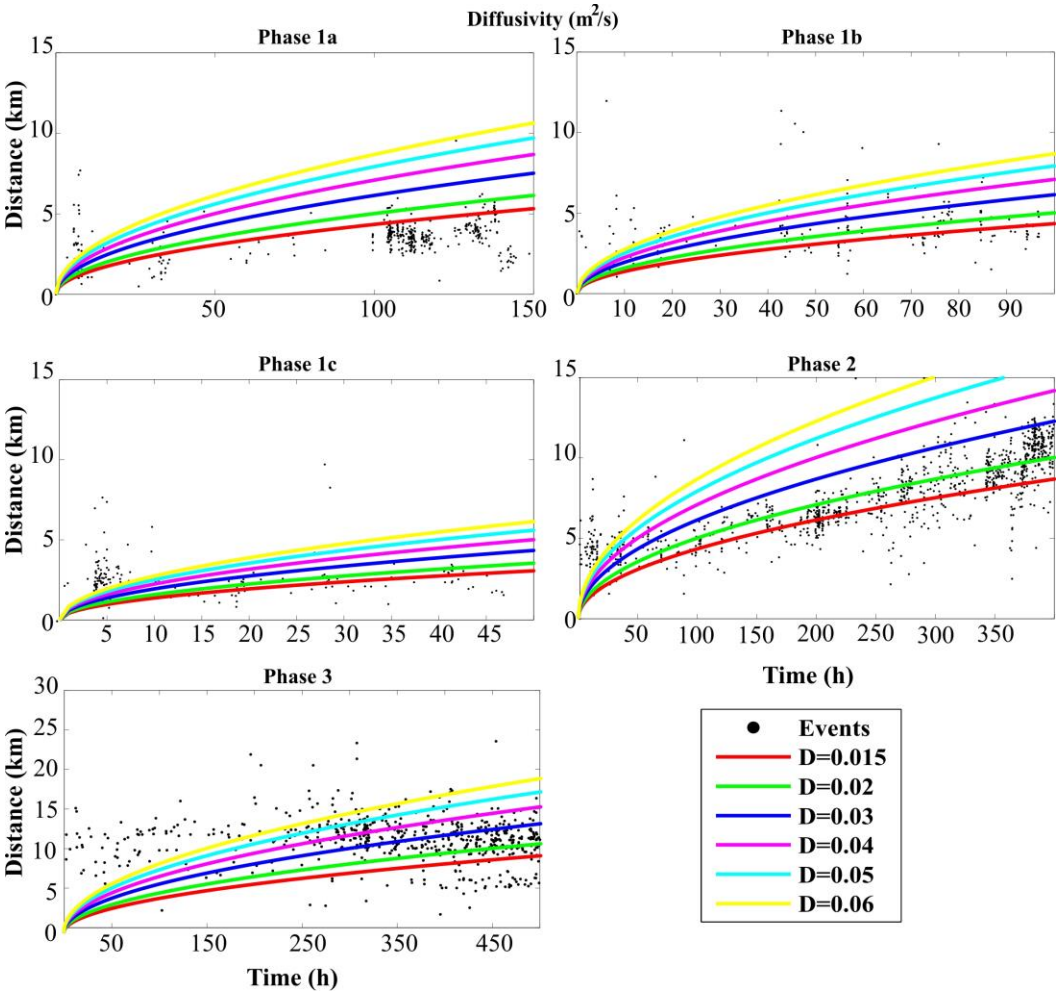

Figure 7.11. *Estimates of the best diffusivity value D (m2 s-1) for the seismic series associated to phases 1, 2 and 3. These estimates follow the procedure described in Figure 9. The best agreement of the curve r vs t is found for phase 2, coincident with the occurrence of the submarine eruption.*

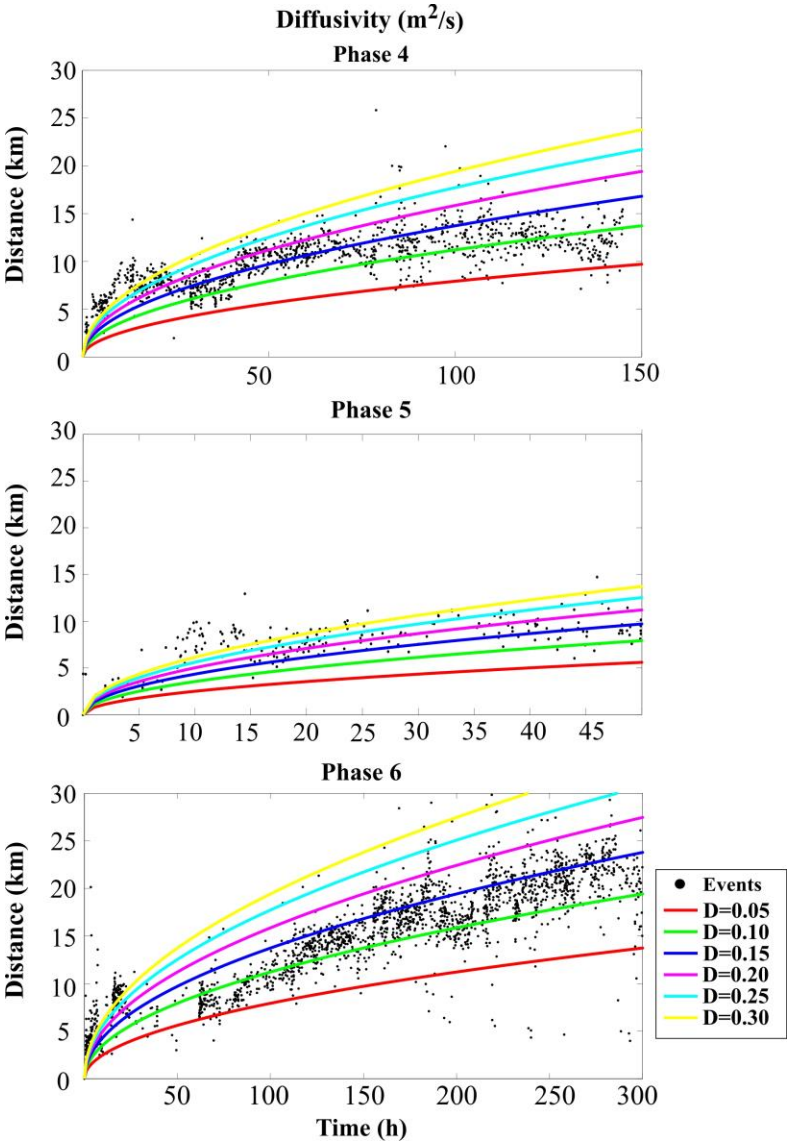

Figure 7.12. *Same as figure 7.10 for seismic swarms associated to phases 4, 5 and 6. Note as the best diffusivity value for every seismic swarm is one order of magnitude larger in comparison to earlier phases.*

The results suggest that the seismicity recorded at El Hierro is well described by a model of linear diffusivity, and thus, it may be explained using theory of linear pore pressure diffusion and hydraulic fracturing.

7.3. Discussion

The present case of study is a reanalysis of the seismicity recorded during seismic and volcanic activity on El Hierro Island (Canary Islands) between 2011 and 2013 (Ibáñez et al., 2012; Cerdeña-Domínguez et al. 2014; Díaz-Moreno et al., 2015). Here we focused our efforts on analysing the mechanisms that control the occurrence of VT earthquakes and on the applicability of models of pore-pressure diffusion and hydraulic fracturing. Temporal changes in b-value show the occurrence of at least 6 main different seismic swarms clearly associated to geochemical, geodetic and gravimetric observations previously presented. Each of these seismic phases exhibits an increase in b-value up to 3.0 followed by a temporal decrease to values close to 1.0. This pattern, common to all phases, suggests that the similar mechanisms were responsible for the seismic swarms: the injection of multiple magmatic pulses from the Upper Mantle into the Oceanic Crust.

Earthquake relocation revealed an overall absence of seismicity at shallow depth and around the site where eruptions took place. We also report lack any preferential rupture direction based on the absence of clustering of seismicity along any preferential direction, plane, or well-defined geological structure. As observed in figure 6, each seismic phase migrates independently of the previous phase, with the only recurring pattern being a tendency for hypocentres to deepen and expand radially outwards. Analyses of the location of the onset of each seismic phase suggest that they all share a common source region underneath the Island of El Hierro. Further, the hypocentral distribution of seismicity reveals substantial lack of seismicity to the South and to East of the eruption site in La Restinga Area. The eruption site is, indeed, located at the edge of the seismogenic region. Montesinos et al. (2006), Gorbatikov et al. (2013) and García-Yeguas et al. (2014) observed the presence of a high-velocity block centred underneath El Hierro (up to 15km depth) whose boundaries are found around the eruption site. In the same area, Blanco-Montenegro et al. (2008) observed before the 2011 eruption, a highly magnetized vertical structure that had been interpreted as complex deep intrusive bodies. Figure 6 in Gorbatikov et al., (2013) shows a nearly vertical high-velocity structure in the vicinity of La Restinga submarine eruption site of October 2011. They identified this structure surrounded by two main blocks of low shear-waves velocity and interpreted it as

the pre-existing feeding system that transported the magma aseismically from deep to the surface. In the three-dimensional velocity model of García-Yeguas et al. (2014) a similar vertical structure is identified with low body wave velocity. This vertical structure may correspond to a structural barrier for stress propagation towards the South and East. Such a block structure is a preferred model to explain the origin and evolution of the Canary Islands archipelago (e.g. Anguita and Hernán, 2000).

A diffusivity model (eq. 7.3) fits well the observed spatial distribution of the seismicity on El Hierro Island. The absence of any preferential rupture geometry or direction further supports our proposed conceptual model. In our model, pore pressure diffusion controls the generation of seismicity via hydraulic fracturing. When magma is injected into the lower crust, across the mantle-crust boundary, hydrostatic pressure conditions change in the region around the point of injection. Within this volume, which is common to all seismic phases, pore pressure increases (e.g. Delepine et al. 2004; Zang et al. 2014). As a result of this process, the effective normal stress across pre-existing cracks and fractures decreases, thus triggering many small-magnitude earthquakes (microseimicity), which spread out radially. The relatively high rates of smaller magnitude earthquakes result in comparatively high b-values (e.g. Riedel et al., 2003). The radial distribution of earthquake hypocentres generates a relatively homogeneous seismic cloud around the magma injection point. After its initial injection across the mantle-crust boundary, magma migrates either horizontally or upwards (see Martí et al., 2013a) and the volumetric component of seismicity becomes less important (e.g. Kraft and Deichmann, 2013; Zang et al., 2014). At this stage the effects of hydraulic fracturing, local and regional stress conditions, and stress concentration due to magma migration (pore-pressure diffusion),combine to control the spatial and temporal evolution of seismicity (e.g. Albino and Sigmundsson, 2013). Conditions of increased shear stress lead to larger magnitude earthquakes, an effect that is reflected in the overall decrease of the observed b-values. Finally, at larger distances the influence of hydraulic fracturing may become negligible, thus, preventing the generation of further seismicity. Similar seismic patterns have been reported by other authors (e.g. Majer et al. 2007; Deichman and Ernst 2009; Goertz-Allmann et al., 2011; Zang et al. 2014) in geothermal regions. Our analyses,

along with similarities with previous case studies, suggest that the distribution and evolution of earthquake hypocentres at El Hierro is not directly controlled by magma migration. We suggest that seismicity results from the combined effects of stress transfer pore pressure diffusion, hydraulic fracturing, and local and regional conditions, including crustal heterogeneity.

It is interesting to note how the estimated radii of the earthquake nucleation sphere, grow with time (see table 7.2). Combining such an increase with the observed changes in the diffusivity values we could infer that the area affected by stress propagation grew with times. This does not necessarily reflect an increase in the size of the magmatic pulses; it may represent pervasive fracturing due to an increase in background stress and deformation. During the initial stages of volcanic activity, magma injection in the oceanic crust was mainly controlled by stresses linked to the gravitational load of the island of El Hierro, and the overall tectonic regime in the region. As new magma was injected into the lower crust, stress increased in the region as demonstrated by deformation measured at the surface. Stress accumulation is reflected in the overall increase of diffusivity values. During the last seismic swarm, in phase 6, seismicity had the largest spatial extent and the largest earthquake magnitudes were recorded. The radius of the nucleation shell and the diffusivity were also the largest. A similar case is discussed in Murphy et al., (2013) and investigated by means of numerical modelling. The authors indicate that under the assumption that fluid injection induces seismicity, the triggering mechanism could be associated to two processes: i) increase in pore fluid pressure, effectively reducing the normal stress within the affected volume, or ii) changes in the Coulomb stress within the fault system. The extension of the seismogenic region and the duration of the seismic swarms are linked to the permeability of the rocks in the region. If low permeability is assumed, seismicity will be mostly located in the vicinity of the injection, as for El Hierro during phases 1 and 2. When the permeability increases, and Coulomb stress perturbations extend over a much larger area, pore diffusion will affect regions outside of the injection plume generating more extensive and energetic seismic swarms, as during phases 4, 5 and 6 (see energy evolution of figure 2 at El Hierro.

The observed temporal variations in b-value reflect changes in the earthquake triggering mechanisms. We observe that: i) the b-value decreases with time (figure 7.2) from values as high as 3 to values close to 1 (classical for tectonic regimes); ii) the larger magnitude earthquakes are located at large distance from the magna injection zone (figure 7.6). The latter observation suggests that spatial variations in b-value may follow a pattern similar to other regions with comparable seismic activity (e.g. Bachmann et al., 2012).

In order to study these variations we calculated the spatial distribution of b-value for every seismic series. We divided every seismic cloud in three segments of equal length, and calculated the b-value for them. In figure 7.13 we plot the horizontal projection of the spatial evolution of the b-values for every seismic series. Interestingly, for all seismic series the b-value reaches its maximum within the injection region and decreases progressively away from it. This observation reinforces our model of earthquake generation associated with periodic magma pulses beneath El Hierro. During the initial stages of each seismic series, pore-pressure quickly rises upon magma arrival near the region of magma injection, and diffusion controls the rupture process inducing micro-fracturing. Consequently, the observed b-value increases to relatively high values. Later, the cloud of earthquakes is observed to migrate from underneath the centre of the El Hierro outwards and seismicity becomes deeper. This process is controlled by propagation of hydraulic fracturing, and local and regional stress conditions. The pore-pressure front spreads, and the faults and fractures in the area experience a moderate increase in pore-pressure. Therefore, the b-value decreases due to the occurrence of earthquakes of increasing magnitude. The higher magnitudes are recorded towards the final stages of each seismic series due to the predominance of regional stress conditions over magma-driven processes. As suggested by Bachmann et al. (2012) the differential stresses across faults away from the magma injection region follow a typical tectonic earthquake-size distribution, and thus, the b-value lowers to values of about 1. Following Bachmann et al. (2012), we assume that differential stress is one of the governing parameters that influence the spatial and temporal change of b-values.

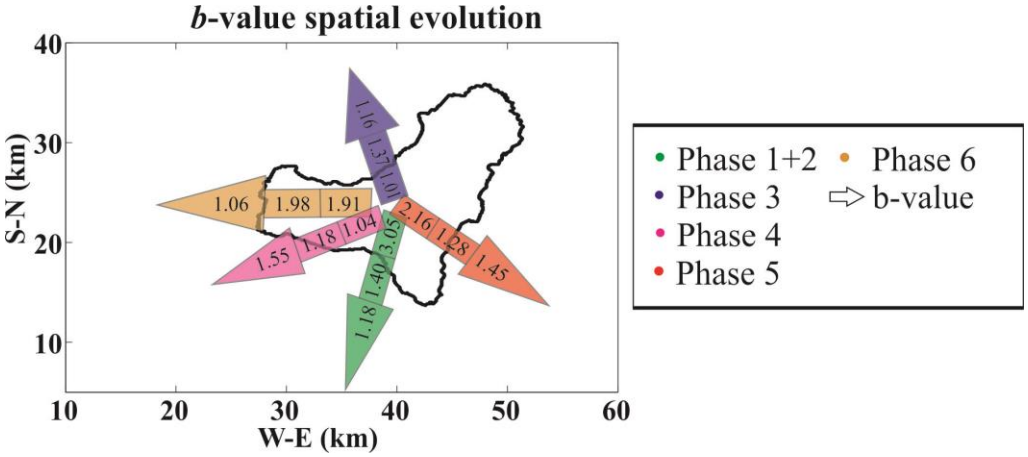

Figure 7.13. *Spatial evolution of b-values for each seismic swarm (see the main manuscript for details on spatial b-value calculations). Arrows portrait the spatial evolution of each seismic cloud.*

At El Hierro there was clear evidence of an eruption between October 2011 and January 2012, and another potential eruptive episode in June 2012 (discussed by Pérez et al., 2014, Blanco et al., 2015 and Pérez et al., 2015). It is well known that pre-eruptive magma migration produces high b-values (e.g. Riedel et al., 2003). The occurrence of eruptive activity at the surface confirms upward migration of magma. As the eruptions did not occur directly above the inferred location of magma injection across the mantle-crust boundary, several authors (e.g. Martí et al. 2013a; López et al., 2014 or Telesca et al. 2015) inferred horizontal magma migration. Magma movement is expected to produce changes in pore-pressure and should generate seismicity in the neighbouring regions; therefore, we cannot neglect these processes in the generation of seismicity and in explaining changes in b-value. However, the spatial evolution of phases 1 and 2, associated to the main eruptive episode in October 2011, suggests that there are discrepancies between horizontal migration of seismicity and the site of eruption. Furthermore, vertical migration of the magma towards the surface is entirely aseismic. Finally, we observe that all seismic series end with a tendency of earthquake hypocentres

to deepen, which is incompatible with mechanisms involving magma migration. Therefore, we hypothesize that despite evidence of magma movement after its initial injection, the influence of horizontal and vertical migration is secondary on earthquake triggering. We suggest that the seismic clouds map the effects of pore-pressure distribution and hydraulic fracturing rather than potential secondary magma migration.

The pattern of seismicity and the onset of every seismic series point to a model of periodic injection of magma from the Upper Mantle into the lower crust. For example, the evolution of b-values during phases 1 and 2 is complex. In these two periods, the b-value does not decrease as uniformly as observed in the other series. Following our proposed conceptual model, when the b-value is high pore-pressure diffusivity controls the rupture process, and earthquake generation is associated to near-field effects of magma injection. If the b-value exhibits increase-decrease cycles, it may be hypothesized that such pattern reflects multiple injection episodes. Additional evidence of multiple pulses is observed during phase 6 (figures 7.10 and 7.12). The pattern of seismicity recorded during the first 30 h of this series suggests a value of diffusivity much higher than expected. The b-value (figure 7.3) for the same series exhibits an initial high value, associated with the initial 30 hours, before decreasing and, once again, increasing at about hour 50. It, then, steadily decrease until the end of the series. This behaviour is compatible with multiple pulses of magma injection.

Martí et al, (2013 b) proposed a model to explain seismic and volcanic activity from June 2011 to January 2012. These authors combined petrological and geophysical observations to provide insights into the mechanisms of seismicity. In their model, seismicity during Phase 1 is generated by magma rising from the mantle into the Moho, and thus, it tracks magma propagation, the size, and the shape of a potential magma reservoir at about 15 km b.s.l. As the high velocity structure of El Hierro acts as a barrier to upwards migration, magma migrated horizontally, producing additional seismicity. Marti et al. (2013b) linked earthquake activity during this period to magma-driven fracturing via shear fracturing. Finally, magma ascended towards the surface resulting in an aseismic submarine eruption. The authors infer that the bulk of seismicity recorded

during Phase 3 could be associated to “gravitational and tectonic readjustments of the plumbing system”. This model is compatible with our observations of phases 1 to 3.

The model discussed in this chapter is described in figure 7.14. We plot the relocated seismicity together with the tomographic anomalies in order to image their spatial relation. Additionally we mark the beginning of the different magma pulses we have hypothesized in this discussion.

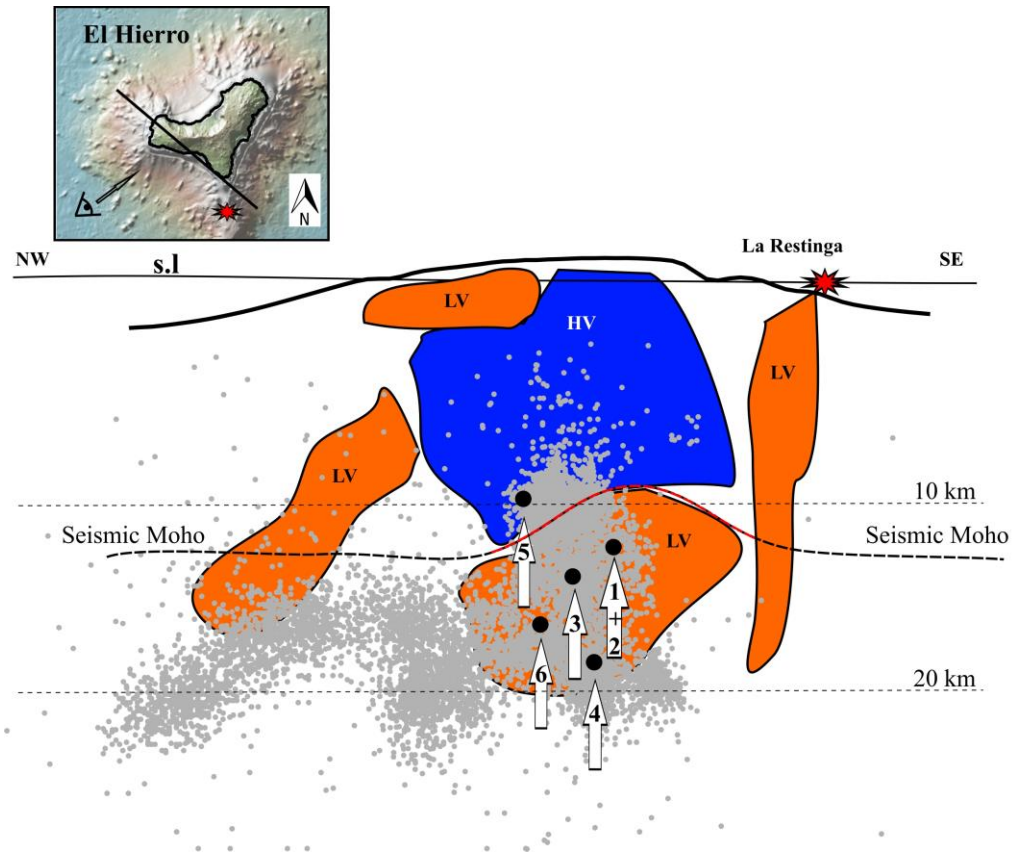

Figure 7.14. *Cartoon of the conceptual model proposed to explain the pattern of the seismic and volcanic unrest at El Hierro Island, presented in a NNW-SSW projection. The high-velocity body (blue color, HV) located underneath El Hierro Island is derived from the works of Gorbatikov et al. (2013) and García-Yeguas et al., (2014). The surrounding low-velocity regions (orange color, LV) and the position of the seismic Moho (black dashed line) in the area are derived from García-Yeguas et al., (2014) and references therein. The red dashed line outlines the eroded Moho as a consequence of the successive magma pulses. The vertical low-velocity structure located underneath of the La Restinga eruption defines the southernmost boundary of the crustal block where El Hierro is located. Each seismic phase throughout the period of unrest represents a new, distinct, magmatic pulse, depicted by vertical arrows. The bathymetric map was obtained from http://www.geomapapp.org (see Ryan et al., 2009).*

7.4. Preliminary applications on Mt. Etna

Mt. Etna, as described in Chapter 2, is a very active volcano, though, seismic swarms in this region have never been as large and intense as the one occurred in the seismic crisis of El Hierro Island. Nonetheless, we have a remarkable opportunity to study this volcano following the same methodologies described in this work. We selected a dataset of 300 events registered during the 2002-03 eruption already relocated using previous 3D models. These are very shallow events and were triggered by the magmatic ascent during the eruption. To analyse this new database we proceed following the same methodology as for the case of El Hierro. We first calculated the b-value evolution with time (figure 7.15) to identify the eruptive pattern. In this case we observe an increase in the b-vale to reach values of 1.3 and then a decrease to values of 0.6. There are important differences in terms of absolute values of *b*. However, the trend increase-decrease is the same.

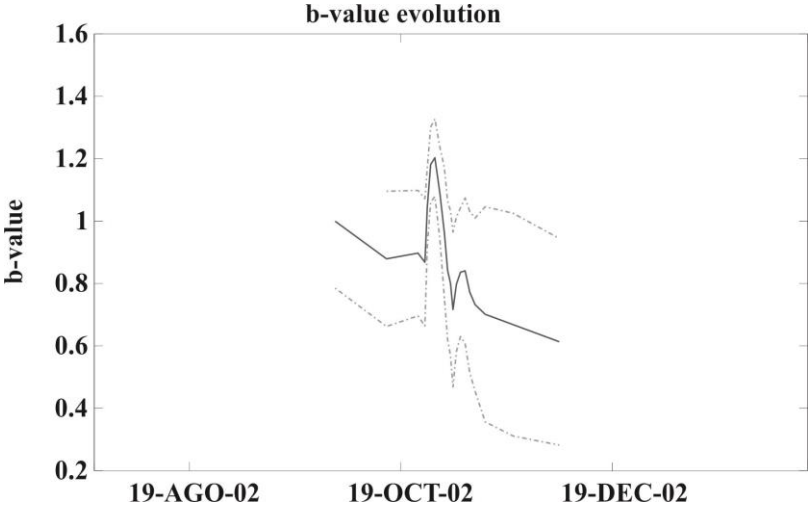

Figure 7.15*. b-value time evolution of 2002-03 eruption at Mt. Etna calculated using the same methodology describe in this chapter.*

Next step is the calculation of the diffusivity parameters for the seismic catalogue. Preliminary results are shown in figure 7.16. It is noteworthy that the

seismicity clearly adjust to a curve of D= 0.3 m^2s^{-1}, similar to that obtain for phase 6 for El Hierro catalogue.

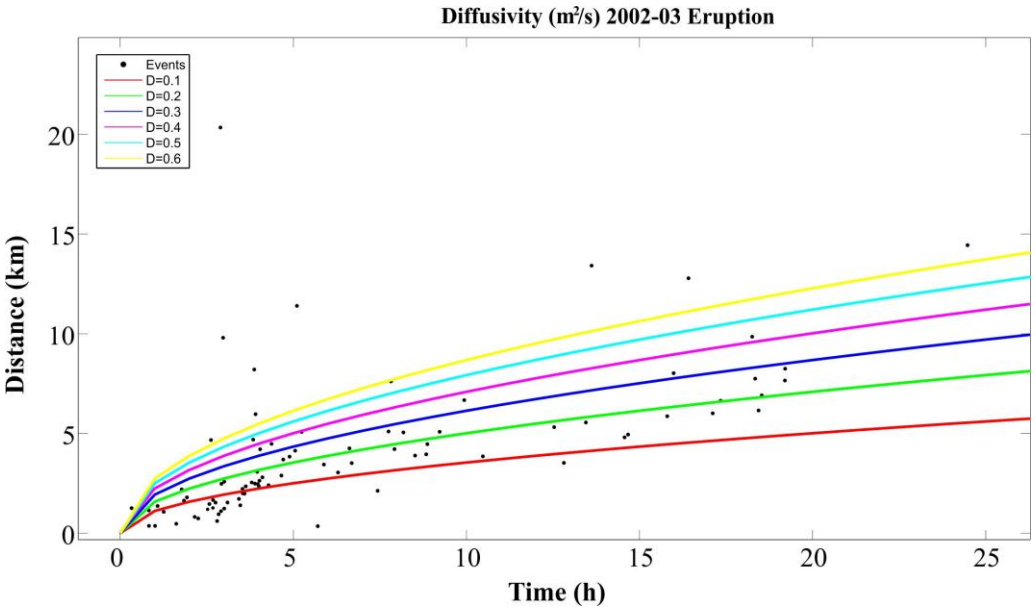

Figure 7.16. *Diffusivity curves calculated for the 300 events registered in Mt. Etna.*

Nonetheless it is important to note the difference in the number and magnitude of events comparing Mt. Etna and El Hierro catalogues. Thus, further analyses will be soon performed.

Along this chapter we demonstrated the utility of obtaining realistic 3D velocity models throughout seismic tomography as a first step to perform advanced seismic studies that allow us to enhance our present knowledge of volcanic dynamic and structure.

8. Conclusions

8.1 Conclusive Remarks

Along this chapter we present the main conclusions we extract from this Doctoral Thesis. We divide them into different sections according to Databases, Picking, Tomographic Inversion Code, Tomographic Images and Advanced Applications.

Additionally we provide a list of future works. Many of them are of immediate application (some are already in preparation).

8.1.1. Databases

- TOMO-ETNA Experiment is probably the most complex active-passive seismic survey carried out in the world. Especially when we consider the number of involved people, countries, international projects, etc.
- The wide distribution of the seismic sources, both active and passive, allows us to cover a very large region for an active experiment when compared to previous active surveys in volcanoes.
- Based on previous experiences on Deception Island, and Tenerife Island, we state that the dataset obtained will provide results over at least the next 10 years, by applying new techniques, approaches, etc.
- Regarding the TOMO-ETNA Experiment, we obtained more than three million seismic signals, from which we selected more than 180,000 P-phase travel times for the active sources and almost 12,000 P-phase travel times for the passive sources. These final dataset represent a very high quality data registered in seismic stations up to 50 km away from the active source.
- The final dataset consists on: i) 184,797 P-phase travel times for the active sources; ii) 11,802 P-phase travel times for the passive sources; iii) 267 stations.

8.1.2. Picking

- The automatic P-wave detection algorithm developed ad-hoc for the TOMO-ETNA dataset provides an accurate P-wave onset estimation using Multiband Frequency Analysis (AMPA).

- AMPA algorithm is a new fast, robust adaptable and reliable algorithm that allows us the processing of all three million seismic signals in less than 30 hours, providing also a set of quality assessment parameters.
- Additional confrontation between manual and automatic picking has been performed in order to estimate the possible discrepancies.

8.1.3. Tomographic Inversion Code

- Joint Active Passive Ray Tomography Software (PARTOS) has been developed ad-hoc for the TOMO-ETNA experiment dataset.
- The robustness, reliability and quality of the algorithms involved are strongly proved: i) it is based on two well-known tomographic codes developed for active and passive seismic inversion respectively; ii) Many synthetic tests have been carried out to validate the solutions.
- It is probably the first time that such robust and powerful joint active passive tomography software has been developed and openly shared within the scientific community.

8.1.4. Tomographic Images

- High resolution tomographic images are presented for three different relevant regions: i) North-eastern Sicily, comprising Ionian and Thyrrenian Seas (Region 1); ii) Aeolian Islands Archipelago (Region 2); and iii) Mt. Etna Volcano (Region 3).
- Stability, robustness and quality of the solutions are proved throughout a series of synthetic tests.
- The ray density maps show very high ray coverage within the areas of study, reaching in some cases more than 1,800 rays per cell.
- Region 1 main anomalies:
    - *Anomalies 1 and 1b:* correspond to the well-known ATLFS, defined by many authors. Although its origin is still under debate, the most stable hypothesis is that of a dextral transfer zone separating a compressional regime on the western part of the Aeolian Archipelago, from an extensional regime to the northeast.

- *Anomaly E:* Etnean volcanic region, characterised by low velocity anomalies.
- *Anomaly A:* Aeolian Islands region, characterised by a series of low velocity-high velocity anomaly distribution.

- Region 2 main anomalies:
- *Anomaly 2:* Known as SAFS, this dextral strike-slip motion fault system accommodates the compression of the westernmost part of the Aeolian Archipelago. It easternmost limit reaches the mentioned ATLFS in the area of the Lipari-Vulcano complex.
- *Anomaly 3:* NW-SE discontinuity interpreted by many authors as a STEP fault related to the decoupling the subducting lithosphere from the non-subducting one.
- *Anomaly 4:* Large low velocity volume probably related to the active volcanism of the easternmost Aeolian Islands (Panarea and Stromboli).
- Region 3 main anomalies:
  - *Anomaly 5:* Probably the most well-known feature on the Etnean region. The HVB is enlightened, and as our results go deeper than previous tomographies, we observe the roots of this HVB connected in depth with new high velocity bodies located offshore.
  - *Anomaly 6:* High velocity anomaly located near the coast of the eastern flank of Mt. Etna, that can be related with the HVB mentioned above. Other hypothesis is that these volume may be an effect of the Moho upwelling described by other authors.
  - *Anomalies 7, 8 and 9:* These are anomalies that have never been interpreted and for which we present some preliminary ideas that must be further investigated.

8.1.5. Advanced Applications

- We postulate 3D velocity models obtained throughout seismic tomography not just as final results, but as an important tool for advanced studies.
- We present a complete case of study using seismic velocity models as the base for further advanced applications. This study comprise the use of several procedures:
  - B-value estimation
  - Seismic precise location using relative and probabilistic non-linear algorithms.
  - Estimation of diffusivity curves
- Results enlighten new mechanisms of seismic migration in active volcanic regions.
- We state that seismic migration in volcanic environments do not necessary be directly related to magma migration.
- Hydraulic fracturing can be considered as an important mechanism controlling stress and seismic migration in volcanic areas, especially when magma intrusions occurred.

8.2. Future Work

8.2.1 Regarding Mt. Etna Volcano

- Joint Gravimetric and Seismic inversion. Combine both gravimetric and seismic velocity models in order to determine elastic parameters distribution (in preparation).
- Advanced applications of the new seismic velocity model on Mt. Etna in the light of Hydraulic Fracturing to better constrain the volcano-seismic swarms (in preparation).
- Seismic Attenuation tomography. It is a natural further step of the seismic velocity tomography as evidenced by several studies (i.e. Deception Island, Tenerife Island, Stromboli, etc.).
- Application of new advanced algorithm on seismic waves arrival detection in order to enhance the current high quality seismic database.

- New Joint Seismic Tomography of MT. Etna by including larger passive database. The current tomography represents a snapshot, which permits to enlighten volcanic structures that may change with time. However, structural regional features should not change with time and therefore we could improve our current knowledge of them by including more passive seismic information to the current joint tomographic inversion.

8.2.2. General applications

- Regarding the use of PARTOS, we pretend to carry out further joint tomographies in Tenerife Island, and Montserrat Island as immediate studies. Joint tomography of Deception Island is also on the focus for further studies.
- Use hydraulic fracturing approach in other active volcanic regions. For that purpose, we only need data from volcano-seismic swarms and a realistic 3D velocity model.
- Sharing Data, Results with the Scientific Community. We want to share with the rest of the community our results, databases and methodologies in order to allow other researchers to use them. This collaboration will also allow us to improve the results and techniques and therefore improve our knowledge of different volcanic regions. Sharing Data will be carried out throughout different ways:
    - Nature Scientific Data Publications.
    - KNOWAVES Spanish Research Project will provide necessary tools for sharing results throughout online cloud systems.
    - EPOS European Project will give us also the required tools to share databases and results with the scientific community.

9. Bibliography

Aiuppa, A., Cannata, A., Cannavò, F., Di Grazia, G., Ferrari, F., Giudice, G., ... & Patanè, D. (2010). Patterns in the recent 2007–2008 activity of Mount Etna volcano investigated by integrated geophysical and geochemical observations. *Geochemistry, Geophysics, Geosystems*, 11(9).

Aki, K., Christoffersson, A., Husebye, E. S., & Powell, C. (1974). Three-dimensional seismic velocity anomalies in the crust and upper-mantle under the USGS, California seismic array. *Eos Transactions. American Geophysical Union*, 56, 1145.

Albino, F. & Sigmundsson, F. (2013) Stress transfer between magma bodies: Influence of intrusions prior to 2010 eruptions at Eyjafjallajökull volcano, Iceland. *Journal of Geophysical Research: Solid Earth*, 119, 2964-2975, doi:10.1002/2013JB010510.

Alinaghi, A., Koulakov, I., & Thybo, H. (2007). Seismic tomographic imaging of P-and S-waves velocity perturbations in the upper mantle beneath Iran. *Geophysical Journal International*, 169(3), 1089-1102.

Allard, P., Behncke, B., D'Amico, S., Neri, M., & Gambino, S. (2006). Mount Etna 1993–2005: Anatomy of an evolving eruptive cycle. *Earth-Science Reviews*, *78*(1-2), 85–114. doi:10.1016/j.earscirev.2006.04.002.

Allen, R. V. (1978). Automatic earthquake recognition and timing from single traces. *Bulletin of the Seismological Society of America*, 68(5), 1521-1532.

Aloisi, M., Cocina, O., Neri, G., Orecchio, B., & Privitera, E. (2002). Seismic tomography of the crust underneath the Etna volcano, Sicily. *Physics of the Earth and Planetary Interiors*, *134*(3-4), 139–155. doi:10.1016/S0031-9201(02)00153-X.

Almendros, J., Alguacil, G., Del Pezzo, E., & Ortiz, R. (1997). Array tracking of the volcanic tremor source at Deception Island, Antarctica. *Geophysical Research Letters*, 24(23), 3069-3072.

Alparone, S., Barberi, G., Cocina, O., Giampiccolo, E., Musumeci, C., & Patanè, D. (2012). Intrusive mechanism of the 2008-2009 Mt. Etna eruption: Constraints by tomographic images and stress tensor analysis. *Journal of Volcanology and Geothermal Research, 229-230*, 50–63. doi:10.1016/j.jvolgeores.2012.04.001.

Alparone, S., Cocina, O., Gambino, S., Mostaccio, A., Spampinato, S., Tuvè, T., & Ursino, A. (2013). Seismological features of the Pernicana–Provenzana Fault System

(Mt. Etna, Italy) and implications for the dynamics of northeastern flank of the volcano. *Journal of volcanology and geothermal research*, 251, 16-26.

Alvarez, I., Garcia, L., Mota, S., Cortes, G., Benitez, C., & De la Torre, A. (2013). An Automatic P-Phase Picking Algorithm Based on Adaptive Multiband Processing. *Geoscience and Remote Sensing Letters, IEEE*, 10(6), 1488-1492.

Andronico, D., Branca, S., Calvari, S., Burton, M., Caltabiano, T., Corsaro, R. A., ... & Murè, F. (2005). A multi-disciplinary study of the 2002–03 Etna eruption: insights into a complex plumbing system. *Bulletin of Volcanology*, 67(4), 314-330.

Anguita, F., and Hernán, F. (2000). The Canary Islands origin: a unifying model. *Journal of Volcanology and Geothermal Research*, 103(1), 1-26.

Aoki, Y., Takeo, M., Aoyama, H., Fujimatsu, J., Matsumoto, S., Miyamachi, H., ... & Tanada, R. (2009). P-wave velocity structure beneath Asama Volcano, Japan, inferred from active source seismic experiment. *Journal of Volcanology and Geothermal Research*, 187(3), 272-277.

Argnani, A., Brancolini, G., Bonazzi, C., Rovere, M., Accaino, F., Zgur, F., & Lodolo, E. (2009). The results of the Taormina 2006 seismic survey: possible implications for active tectonics in the Messina Straits. *Tectonophysics*, 476(1), 159-169.

Armienti, P., Innocenti, F., Petrini, R., Pompilio, M., & Villari, L. (1989). Petrology and Sr-Nd isotope geochemistry of recent lavas from Mt. Etna: bearing on the volcano feeding system. *Journal of Volcanology and Geothermal Research*, 39(4), 315-327.

Auger, E., Gasparini, P., Virieux, J., & Zollo, A. (2001). Seismic evidence of an extended magmatic sill under Mt. Vesuvius. *Science*, 294(5546), 1510-1512.

Azzaro, R., Branca, S., Giammanco, S., Gurrieri, S., Rasà, R., & Valenza, M. (1998). New evidence for the form and extent of the Pernicana Fault System (Mt. Etna) from structural and soil–gas surveying. *Journal of volcanology and geothermal research*, 84(1), 143-152.

Azzaro, R. (1999). Earthquake surface faulting at Mount Etna volcano (Sicily) and implications for active tectonics. *Journal of Geodynamics*, 28(2), 193-213.

Azzaro, R., Branca, S., Gwinner, K., & Coltelli, M. (2012a). The volcano-tectonic map of Etna volcano, 1:100.000 scale: an integrated approach based on a morphotectonic

analysis from high-resolution DEM constrained by geologic, active faulting and seismotectonic data. *Italian Journal of Geosciences*, *131*(1), 153–170. doi:10.3301/IJG.2011.29.

Azzaro, R., D'Amico, S., Peruzza, L., & Tuvè, T. (2012a). Earthquakes and faults at Mt. Etna (southern Italy): problems and perspectives for a time-dependent probabilistic seismic hazard assessment in a volcanic region. *Bollettino di Geofisica Teorica ed Applicata,* 53(1), 75-88.

Bachmann, C. E., Wiemer, S., Goertz-Allmann, B. P., & Woessner, J. (2012). Influence of pore-pressure on the event-size distribution of induced earthquakes. *Geophysical Research Letters,* 39(9). DOI: 10.1029/2012GL051480.

Baer, M., & Kradolfer, U. (1987). An automatic phase picker for local and teleseismic events. *Bulletin of the Seismological Society of America*, 77(4), 1437-1445.

Balmforth, N. J., Craster, R. V., & Rust, A. C. (2005). Instability in flow through elastic conduits and volcanic tremor. *Journal of Fluid Mechanics*, 527, 353-377.

Barberi, F., Carapezza, M. L., Valenza, M., & Villari, L. (1993). The control of lava flow during the 1991–1992 eruption of Mt. Etna. *Journal of volcanology and geothermal research*, 56(1), 1-34.

Barberi, F., A. Gandino, A. Gioncada, P. La Torre, A. Sbrana, and C. Zenucchini (1994), The deep structure of the Eolian arc (Filicudi–Panarea–Vulcano sector) in light of gravity, magnetic and volcanological data, *J. Volcanol. Geotherm. Res*., 61,189–206.

Barberi, G., Cocina, O., Neri, G., Privitera, E., & Spampinato, S. (2000). Volcanological inferences from seismic-strain tensor computations at Mt. Etna Volcano, Sicily. *Bulletin of volcanology*, 62(4-5), 318-330.

Barberi, G., Cocina, O., Maiolino, V., Musumeci, C., & Privitera, E. (2004). Insight into Mt. Etna (Italy) kinematics during the 2002-2003 eruption as inferred from seismic stress and strain tensors. *Geophysical Research Letters*, *31*(21), 0–3. doi:10.1029/2004GL020918.

Barberi,G., Giampiccolo, E., Musumeci, C., Scarfi, L., Bruno, V., Cocina, O., Díaz-Moreno, A., Sicali, S., Tusa, G., Tuvè, T., Zuccarello, L., and Patanè, D., (2016). Seismic and Volcanic activity during 2014 in the región involved by TOMO-ETNA

seismic active experiment. . Special Volume: TOMOETNA. Eds. Morales J., and Puglisi G.. *Annals of Geophysics*. doi:10.4401/ag-7082.

Barclay, A. H., Wilcock, W. S. D., & Ibáñez, J. M. (2009). Bathymetric constraints on the tectonic and volcanic evolution of Deception Island Volcano, South Shetland Islands. *Antarctic Science*, 21(02), 153-167.

Barnard, S. T. (2004). Results of a reconnaissance trip to Mt. Etna, Italy: the effects of the 2002 eruption of Etna on the province of Catania. *Bulletin of the New Zealand Society for Earthquake Engineering*, 37(2), 47-61.

Barreca, G., Bruno, V., Cultrera, F., Mattia, M., Monaco, C., & Scarfì, L. (2014). New insights in the geodynamics of the Lipari–Vulcano area (Aeolian Archipelago, southern Italy) from geological, geodetic and seismological data. *Journal of Geodynamics*, 82, 150-167.

Barreca, G., Scarfì, L., Cannavò, F., Koulakov, I., & Monaco, C. (2016). New structural and seismological evidence and interpretation of a lithospheric scale shear zone at the southern edge of the Ionian subduction system (central-eastern Sicily, Italy). *Tectonics*.

Battaglia, J., & Aki, K. (2003). Location of seismic events and eruptive fissures on the Piton de la Fournaise volcano using seismic amplitudes. *Journal of Geophysical Research: Solid Earth*, (1978–2012), 108(B8).

Battaglia, J., Got, J. L., & Okubo, P. (2003). Location of long-period events below Kilauea Volcano using seismic amplitudes and accurate relative relocation. *Journal of Geophysical Research: Solid Earth*, (1978–2012), 108(B12).

Battaglia, M., Gottsmann, J., Carbone, D., & Fernández, J. (2008a). 4D volcano gravimetry. *Geophysics*, 73(6), WA3-WA18.

Battaglia, J., Zollo, A., Virieux, J., & Dello Iacono, D. (2008b). Merging active and passive data sets in traveltime tomography: the case study of Campi Flegrei caldera (Southern Italy). Geophysical Prospecting, 56(4), 555-573.

Beccaluva, L., G. Gabbianelli, F. Lucchini, P.L. Rossi, and C. Savelli (1985), Petrology and K/Ar ages of volcanic dredged from the Aeolian seamounts: implications for

geodynamic evolution of the southern Tyrrhenian basin, *Earth Planet. Sci. Lett*., 74, 187–208.

Behncke, B., & Neri, M. (2003a). Cycles and trends in the recent eruptive behaviour of Mount Etna (Italy). *Canadian Journal of Earth Sciences*, 40(10), 1405-1411.

Behncke, B., & Neri, M. (2003b). The July–August 2001 eruption of Mt. Etna (Sicily). *Bulletin of Volcanology*, 65(7), 461-476.

Bell, A. F., and Kilburn, C. R. (2012). Precursors to dyke-fed eruptions at basaltic volcanoes: insights from patterns of volcano-tectonic seismicity at Kilauea volcano, Hawaii. *Bulletin of volcanology*, 74(2), 325-339.

Ben-Avraham, Z., and M. Grasso (1991). Crustal structure variations and transcurrent faulting at the eastern and western margins of the eastern Mediterranean, *Tectonophysics*, 75, 269–277.

Ben-Zvi, T., Wilcock, W. S., Barclay, A. H., Zandomeneghi, D., Ibáñez, J. M., & Almendros, J. (2009). The P-wave velocity structure of Deception Island, Antarctica, from two-dimensional seismic tomography. *Journal of Volcanology and Geothermal Research*, 180(1), 67-80.

Benítez, M. C., Ramírez, J., Segura, J. C., Ibáñez, J. M., Almendros, J., García-Yeguas, A., & Cortes, G. (2007). Continuous HMM-based seismic-event classification at Deception Island, Antarctica. *Geoscience and Remote Sensing, IEEE Transactions on*, 45(1), 138-146.

Bianco, F., Scarfi, L., Del Pezzo, E., & Patanè, D. (2006). Shear wave splitting changes associated with the 2001 volcanic eruption on Mt Etna. *Geophysical Journal International*, 167(2), 959–967. doi:10.1111/j.1365-246X.2006.03152.x.

Billi, A., Barberi, G., Faccenna, C., Neri, G., Pepe, F., & Sulli, A. (2006). Tectonics and seismicity of the Tindari Fault System, southern Italy: crustal deformations at the transition between ongoing contractional and extensional domains located above the edge of a subducting slab. *Tectonics*, 25(2).

Billi, A., C. Faccenna, O. Bellier, L. Minelli, G. Neri, C. Piromallo, D. Presti, D. Scrocca, and E. Serpelloni (2011). Recent tectonic reorganization of the Nubia-Eurasia

convergent boundary heading for the closure of the western Mediterranean, *Bull. Soc. Géol. de France*, 182, 279–303.

Blanco, M. J., Fraile-Nuez, E., Felpeto, A., Santana-Casiano, J. M., Abella, R., Fernández-Salas, L. M., ... & Vázquez, J. T. (2015). Comment on "Evidence from acoustic imaging for submarine volcanic activity in 2012 off the west coast of El Hierro (Canary Islands, Spain)" by Pérez NM, Somoza L, Hernández PA, González de Vallejo L, León R, Sagiya T, Biain A, González FJ, Medialdea T, Barrancos J, Ibáñez J, Sumino H, Nogami K and Romero C [Bull Volcanol (2014) 76: 882-896]. *Bulletin of Volcanology*, 77(7):62, 882-896. doi: 10.1007/s00445-015-0947-6.

Blanco-Montenegro, I., Nicolosi, I., Pignatelli, A., and Chiappini, M. (2008). Magnetic imaging of the feeding system of oceanic volcanic islands: El Hierro (Canary Islands*). Geophysical Journal International*, 173(1), 339–350. doi:10.1111/j.1365-246X.2008.03723.x.

Blanco-Montenegro, I., Nicolosi, I., Pignatelli, A., García, A., & Chiappini, M. (2011). New evidence about the structure and growth of ocean island volcanoes from aeromagnetic data: The case of Tenerife, Canary Islands. *Journal of Geophysical Research: Solid Earth*, *116*(3), 1–17. doi:10.1029/2010JB007646.

Bonaccorso, A., Falzone, G., & Gambino, S. (1999). An investigation into shallow borehole tiltmeters. *Geophysical research letters*, 26(11), 1637-1640.

Bonaccorso, A., & Patanè, D. (2001). Shear response to an intrusive episode at Mt. Etna volcano (January 1998) inferred through seismic and tilt data. *Tectonophysics*, 334(2), 61-75.

Bonaccorso, A., Calvari, S., Coltelli, M., Del Negro, C., & Falsaperla, S. (Eds.). (2004). *Mt. Etna: Volcano Laboratory* (Vol. 143). Washington, D. C.: American Geophysical Union. doi:10.1029/GM143.

Bonaccorso, A., Bonforte, A., Guglielmino, F., Palano, M., & Puglisi, G. (2006). Composite ground deformation pattern forerunning the 2004–2005 Mount Etna eruption. *Journal of Geophysical Research: Solid Earth*, 111(B12).

Bonaccorso, A., Bonforte, A., Currenti, G., Del Negro, C., Di Stefano, A., & Greco, F. (2011). Magma storage, eruptive activity and flank instability: inferences from

ground deformation and gravity changes during the 1993–2000 recharging of Mt. Etna volcano. *Journal of Volcanology and Geothermal Research*, 200(3), 245-254.

Bonaccorso, A., Currenti, G., & Del Negro, C. (2013). Interaction of volcano-tectonic fault with magma storage, intrusion and flank instability: A thirty years study at Mt. Etna volcano. *Journal of Volcanology and Geothermal Research*, 251, 127-136.

Bonanno, A., Palano, M., Privitera, E., Gresta, S., & Puglisi, G. (2011). Magma intrusion mechanisms and redistribution of seismogenic stress at Mt. Etna volcano (1997-1998). *Terra Nova*, *23*(5), 339–348. doi:10.1111/j.1365-3121.2011.01019.x.

Bonforte, A., & Puglisi, G. (2003). Magma uprising and flank dynamics on Mount Etna volcano, studied using GPS data (1994–1995). *Journal of Geophysical Research: Solid Earth*, (1978–2012), 108(B3).

Bonforte, A., & Puglisi, G. (2006). Dynamics of the eastern flank of Mt. Etna volcano (Italy) investigated by a dense GPS network. *Journal of Volcanology and Geothermal Research*, 153(3), 357-369.

Bonforte, A., Bonaccorso, A., Guglielmino, F., Palano, M., & Puglisi, G. (2008). Feeding system and magma storage beneath Mt. Etna as revealed by recent inflation/deflation cycles. *Journal of Geophysical Research: Solid Earth*, 113(B5).

Bonforte, A., Gambino, S., & Neri, M. (2009). Intrusion of eccentric dikes: the case of the 2001 eruption and its role in the dynamics of Mt. Etna volcano. *Tectonophysics*, 471(1), 78-86.

Bonforte, A., Guglielmino, F., Coltelli, M., Ferretti, A., & Puglisi, G. (2011). Structural assessment of Mount Etna volcano from Permanent Scatterers analysis. *Geochemistry, Geophysics, Geosystems*, 12(2).

Bonforte, A., Federico, C., Giammanco, S., Guglielmino, F., Liuzzo, M., & Neri, M. (2013). Soil gases and SAR measurements reveal hidden faults on the sliding flank of Mt. Etna (Italy). *Journal of volcanology and geothermal research*, 251, 27-40.

Borgia, A., Ferrari, L., & Pasquarè, G. (1992). Importance of gravitational spreading in the tectonic and volcanic evolution of Mount Etna. *Nature*, 231-235.

Bosl, W. J. (2002). Aftershocks and pore fluid diffusion following the 1992 Landers earthquake. *Journal of Geophysical Research, 107*(B12), 2366. doi:10.1029/2001JB000155.

Bouillin, J.P., M. Duran-Delga, and P. Olivier (1986). Betic-Rifian and Tyrrhenian arcs: distinctive features, genesis and development stages, edited by F.C. Wezel, *"The origin of Arcs", Elsevier*: 281-304.

Bousquet, J. C., & Lanzafame, G. (2001). Nouvelle interpretation des fractures des eruptions laterales de l'Etna; consequences pour son cadre tectonique. *Bulletin de la Société Géologique de France*, 172(4), 455-467 (In French).

Bousquet, J. C., & Lanzafame, G. (2004). The tectonics and geodynamics of Mt. Etna: synthesis and interpretation of geological and geophysical data. *Mt. Etna: Volcano Laboratory* (Vol. 143). Bonaccorso, A., Calvari, S., Coltelli, M., Del Negro, C., & Falsaperla, S. (Eds.). Washington, D. C.: American Geophysical Union.

Branca, S., Carbone, D., & Greco, F. (2003). Intrusive mechanism of the 2002 NE-Rift eruption at Mt. Etna (Italy) inferred through continuous microgravity data and volcanological evidences. *Geophysical Research Letters*, 30(20).

Branca, S., Coltelli, M., & Groppelli, G. (2004). Geological evolution of Etna volcano. *Mt. Etna: Volcano Laboratory* (Vol. 143). Bonaccorso, A., Calvari, S., Coltelli, M., Del Negro, C., & Falsaperla, S. (Eds.). Washington, D. C.: American Geophysical Union, 49-63.

Branca, S., Coltelli, M., De Beni, E., & Wijbrans, J. (2008). Geological evolution of Mount Etna volcano (Italy) from earliest products until the first central volcanism (between 500 and 100 ka ago) inferred from geochronological and stratigraphic data. *International Journal of Earth Sciences*, 97(1), 135-152.

Branca, S., Coltelli, M., Groppelli, G., & Lentini, F. (2011). Geological map of Etna volcano, 1:50,000 scale. *Italian Journal of Geosciences*, 130(3), 265–291. doi:10.3301/IJG.2011.15.

Branca, S., & Ferrara, V. (2013). The morphostructural setting of Mount Etna sedimentary basement (Italy): Implications for the geometry and volume of the volcano and its flank instability. *Tectonophysics*, 586, 46-64.

Bridges, D. L., & Gao, S. S. (2006). Spatial variation of seismic b-values beneath Makushin Volcano, Unalaska Island, Alaska. *Earth and Planetary Science Letters*, 245(1), 408-415.

Buckingham, M. J., & Garcés, M. A. (1996). Canonical model of volcano acoustics. *Journal of Geophysical Research: Solid Earth*, (1978–2012), 101(B4), 8129-8151.

Busa, T., Clochiatti, R., & Cristofolini, R. (2002). The role of apatite fractionation and REE distribution in alkaline rocks from Mt. Etna, Sicily. *Mineralogy and Petrology*, 74(1), 95-114.

Caló, M., Dorbath, C., Luzio, D., Rotolo, S. G., & D'anna, G. (2009). Local earthquake tomography in the Southern Tyrrhenian region of Italy: Geophysical and petrological inferences on the subducting lithosphere. In *Subduction Zone Geodynamics* (pp. 85-99). Springer Berlin Heidelberg.

Calvari, S., & Pinkerton, H. (1998). Formation of lava tubes and extensive flow field during the 1991–1993 eruption of Mount Etna. *Journal of Geophysical Research: Solid Earth* (1978–2012), 103(B11), 27291-27301.

Calvari, S., Groppelli, G., & Pasquarè, G. (1994). Preliminary geological data on the south-western wall of the Valle del Bove, Mt. Etna, Sicily. *Acta Vulcanologica*. , 5, 15-30.

Calvari, S., Tanner, L. H., Groppelli, G., & Norini, G. (2004). Valle del Bove, eastern flank of Etna volcano: a comprehensive model for the opening of the depression and implications for future hazards. *Mt. Etna: Volcano Laboratory* (Vol. 143). Bonaccorso, A., Calvari, S., Coltelli, M., Del Negro, C., & Falsaperla, S. (Eds.). Washington, D. C.: American Geophysical Union, 65-75.

Cannata, A., Hellweg, M., Di Grazia, G., Ford, S., Alparone, S., Gresta, S., … Patanè, D. (2009). Long period and very long period events at Mt. Etna volcano: Characteristics, variability and causality, and implications for their sources. *Journal of Volcanology and Geothermal Research*, *187*(3-4), 227–249. doi:10.1016/j.jvolgeores.2009.09.007.

Cannata, A., Di Grazia, G., Montalto, P., Ferrari, F., Nunnari, G., Patanè, D., & Privitera, E. (2010). New insights into banded tremor from the 2008–2009 Mount Etna eruption. *Journal of Geophysical Research: Solid Earth*, (1978–2012), 115(B12).

Cannata, A., Montalto, P., Aliotta, M., Cassisi, C., Pulvirenti, A., Privitera, E., & Patanè, D. (2011). Clustering and classification of infrasonic events at Mount Etna using pattern recognition techniques. *Geophysical Journal International*, 185(1), 253-264.

Cannata, A., Montalto, P., & Patanè, D. (2013a). Joint analysis of infrasound and seismic signals by cross wavelet transform: detection of Mt. Etna explosive activity. *Natural Hazards and Earth System Sciences* (NHESS).

Cannata, A., Di Grazia, G., Aliotta, M., Cassisi, C., Montalto, P., & Patanè, D. (2013b). Monitoring seismo-volcanic and infrasonic signals at volcanoes: Mt. Etna case study. *Pure and Applied Geophysics*, 170(11), 1751-1771.

Caputo, M., G.F. Panza, and D. Postpischl (1972), New evidences about the deep structure of the Lipari arc, *Tectonophysics*, 15, 219–231.

Caracausi, A., Italiano, F., Paonita, A., Rizzo, A., & Nuccio, P. M. (2003a). Evidence of deep magma degassing and ascent by geochemistry of peripheral gas emissions at Mount Etna (Italy): assessment of the magmatic reservoir pressure. *Journal of Geophysical Research: Solid Earth*, 108(B10).

Caracausi, A., Favara, R., Giammanco, S., Italiano, F., Paonita, A., Pecoraino, G., ... & Nuccio, P. M. (2003b). Mount Etna: Geochemical signals of magma ascent and unusually extensive plumbing system. *Geophysical Research Letters*, 30(2).

Caracciolo, F. A., Nicolosi, I., Carluccio, R., Chiappini, S., De Ritis, R., Giuntini, A., ... & Chiappini, M. (2014). High resolution aeromagnetic anomaly map of Mount Etna volcano, Southern Italy. *Journal of volcanology and geothermal research*, 277, 36-40.

Carbone, D., Budetta, G., Greco, F., & Rymer, H. (2003). Combined discrete and continuous gravity observations at Mount Etna. *Journal of volcanology and geothermal research*, 123(1), 123-135.

Carbone, D., Zuccarello, L., & Saccorotti, G. (2008). Geophysical indications of magma uprising at Mt Etna during the December 2005 to January 2006 non-eruptive period. *Geophysical Research Letters*, 35(6).

Carbone, D., D'Amico, S., Musumeci, C., & Greco, F. (2009). Comparison between the 1994-2006 seismic and gravity data from Mt. Etna: New insight into the long-term behavior of a complex volcano. *Earth and Planetary Science Letters*, *279*(3-4), 282–292. doi:10.1016/j.epsl.2009.01.007.

Carbone, D., Aloisi, M., Vinciguerra, S., & Puglisi, G. (2014). New insight into the relationships between stress , strain and mass change at Mt . Etna during the period between the 1993-94 and 2001 eruptions. *Earth Science Reviews*, 16, 11012. doi:10.1016/j.earscirev.2014.07.004.

Cardaci, C., Coviello, M., Lombardo, G., Patanè, G., & Scarpa, R. (1993). Seismic tomography of Etna volcano. *Journal of volcanology and geothermal research*, 56(4), 357-368.

Carmona, E., Almendros, J., Serrano, I., Stich, D., & Ibáñez, J. M. (2012). Results of seismic monitoring surveys of Deception Island volcano, Antarctica, from 1999–2011. *Antarctic Science*, 24(05), 485-499.

Cassidy, J., France, S. J., & Locke, C. A. (2007). Gravity and magnetic investigation of maar volcanoes, Auckland volcanic field, New Zealand. *Journal of volcanology and geothermal research*, 159(1), 153-163.

Cassinis, R., Finetti, I., Giese, P., Morelli, C., Steinmetz, L., & Vecchia, O. (1969). Deep seismic refraction research on Sicily. *Bollettino di Geofisica Teorica ed Applicata*, 11(43/44), 140-160.

Castellano, M., Augusti, V., De Cesare, W., Favali, P., Frugoni, F., Montuori, C., ... & Ulivieri, G. (2008). Seismic tomography experiment at Italy's Stromboli Volcano. *Eos, Transactions American Geophysical Union*, 89(30), 269-270.

Catalano, R., Doglioni, C., & Merlini, S. (2001). On the mesozoic Ionian basin.Geophysical Journal International, 144(1), 49-64.

Cavallaro, D., Cocchi, L., Coltelli, M., Muccini, F., Carmisciano, C., Firetto-Carlino, M., Ibáñez, J.M., Patanè, D., Filippone, M. and Buttaro, E., (2016). Acquisition

procedures, processing methodologies and preliminary results of magnetic and ROV data, collected during the oceanographic cruises of the Tomo-Etna experiment. Special Volume: TOMOETNA. Eds. Morales J., and Puglisi G.. *Annals of Geophysics*. doi:10.4401/ag-7084.

Chester, D. K. (1985). *Mount Etna: the anatomy of a volcano*. Stanford University Press.

Chiarabba, C., Amato, A., Boschi, E., & Barberi, F. (2000). Recent seismicity and tomographic modeling of the Mount Etna plumbing system. *Journal of Geophysical Research: Solid Earth* (1978–2012), 105(B5), 10923-10938.

Chiarabba, C., De Gori, P., & Patane, D. (2004). The Mt. Etna plumbing system: the contribution of seismic tomography. *Mt. Etna: Volcano Laboratory* (Vol. 143). Bonaccorso, A., Calvari, S., Coltelli, M., Del Negro, C., & Falsaperla, S. (Eds.). Washington, D. C.: American Geophysical Union, 191-204.

Chiarabba, C., De Gori, P., & Speranza, F. (2008). The southern Tyrrhenian subduction zone: deep geometry, magmatism and Plio-Pleistocene evolution. *Earth and Planetary Science Letters*, 268(3), 408-423.

Chiodini, G., Frondini, F., Cardellini, C., Granieri, D., Marini, L., & Ventura, G. (2001). CO2 degassing and energy release at Solfatara volcano, Campi Flegrei, Italy. *Journal of Geophysical Research: Solid Earth*, 106(B8), 16213-16221.

Chouet, B. (1992). A seismic model for the source of long-period events and harmonic tremor. *Volcanic Seismology*, (pp. 133-156). Springer Berlin Heidelberg.

Chouet, B. A. (1996a). New methods and future trends in seismological volcano monitoring. *Monitoring and mitigation of volcano hazards* (pp. 23-97). Springer Berlin Heidelberg.

Chouet, B. A. (1996b). Long-period volcano seismicity: its source and use in eruption forecasting. *Nature*, 380(6572), 309-316, doi:10.1038/380309a0.

Chouet, B. (2003). Volcano seismology. *Pure and Applied Geophysics*, 160(3-4), 739-788.

Chouet, B., Dawson, P., & Martini, M. (2008). Shallow-conduit dynamics at Stromboli Volcano, Italy, imaged from waveform inversions. *Geological Society*, London, Special Publications, 307(1), 57-84.

Chouet, B. A., Dawson, P. B., James, M. R., & Lane, S. J. (2010). Seismic source mechanism of degassing bursts at Kilauea Volcano, Hawaii: Results from waveform inversion in the 10–50 s band. *Journal of Geophysical Research: Solid Earth* (1978–2012), 115(B9).

Chouet, B. A., and Matoza, R. S. (2013). A multi-decadal view of seismic methods for detecting precursors of magma movement and eruption. *Journal of Volcanology and Geothermal Research*, 252, 108-175, doi: 10.1016/j.jvolgeores.2012.11.013.

Cocina, O., Neri, G., Privitera, E., & Spampinato, S. (1997). Stress tensor computations in the Mount Etna area (southern Italy) and tectonic implications. *Journal of Geodynamics*, 23(2), 109-127.

Cocina, O., Neri, G., Privitera, E., & Spampinato, S. (1998). Seismogenic stress field beneath Mt. Etna (South Italy) and possible relationships with volcano-tectonic features. *Journal of volcanology and geothermal research*, 83(3), 335-348.

Cocina, O., Barberi, G., Giampiccolo, E., Milluzzo, V., Musumeci, C., Sicali, S., & Patanè, D. (2010). Seismic activity at Mt. Etna from July 2005 to January 2006: evidence of a deep magmatic intrusion leading to the 2006 eruption. *In EGU General Assembly Conference Abstracts* (Vol. 12, p. 9267).

Colombi, B., Guerra, I., Luongo, G., & Scarascia, S. (1979). Profilo sismico a rifrazione Acireale-Termini Imerese. *Contributi preliminari alla sorveglianza e rischio vulcanico (Etna-Eolie)*, 155-170 (In Italian).

Coltelli, M., Carlo, P. Del, & Vezzoli, L. (2000). Stratigraphic constraints for explosive activity in the past 100 ka at Etna Volcano, Italy. *International Journal of Earth Sciences*, 89(3), 665-677.

Coltelli, M., Cavallaro, D., Firetto Carlino, M., Cocchi, L., Muccini, F., D'alessandro, A., Claude, M.E, Monaco, C., Ibànez, J.M.,… and Rapisarda, S. (2016). The marine activities performed within the TOMO-ETNA experiment. Special Volume: TOMOETNA. Eds. Morales J., and Puglisi G.. *Annals of Geophysics*. doi:10.4401/ag-7081.

Corsaro, R. A., & Pompilio, M. (2004a). Buoyancy-controlled eruption of magmas at Mt Etna. *Terra Nova*, 16(1), 16-22.

Corsaro, R. A., & Pompilio, M. (2004b). Dynamics of magmas at Mount Etna. *Mt. Etna: Volcano Laboratory* (Vol. 143). Bonaccorso, A., Calvari, S., Coltelli, M., Del Negro, C., & Falsaperla, S. (Eds.). Washington, D. C.: American Geophysical Union, 91-110.

Corsaro, R. A., & Pompilio, M. (2004c). Magma dynamics in the shallow plumbing system of Mt. Etna as recorded by compositional variations in volcanics of recent summit activity (1995–1999). *Journal of volcanology and geothermal research*, 137(1), 55-71.

Corsaro, R. a., Métrich, N., Allard, P., Andronico, D., Miraglia, L., & Fourmentraux, C. (2009). The 1974 flank eruption of mount etna: an archetype for deep dike-fed eruptions at basaltic volcanoes and a milestone in etna's recent history. *Journal of Geophysical Research: Solid Earth*, *114*(7). doi:10.1029/2008JB006013.

Corsaro, R. a., Di Renzo, V., Distefano, S., Miraglia, L., & Civetta, L. (2013). Relationship between petrologic processes in the plumbing system of Mt. Etna and the dynamics of the eastern flank from 1995 to 2005. *Journal of Volcanology and Geothermal Research*, *251*, 75–89. doi:10.1016/j.jvolgeores.2012.02.010.

Corsaro, R. A., Rotolo, S. G., Cocina, O., & Tumbarello, G. (2014). Cognate xenoliths in Mt. Etna lavas: Witnesses of the high-velocity body beneath the volcano. *Bulletin of Volcanology*, 76(1), 1–18. doi:10.1007/s00445-013-0772-8.

Cortés, G., García, L., Álvarez, I., Benítez, C., de la Torre, Á., & Ibáñez, J. (2014). Parallel system architecture (PSA): An efficient approach for automatic recognition of volcano-seismic events. *Journal of Volcanology and Geothermal Research*, 271, 1-10.

Crisci, G. M., Rongo, R., Di Gregorio, S., & Spataro, W. (2004). The simulation model SCIARA: the 1991 and 2001 lava flows at Mount Etna. *Journal of Volcanology and Geothermal Research*, 132(2), 253-267.

Cristofolini, R., & Romano, R. (1982). Petrologic features of the Etnean volcanic rocks. *Mem. Soc. Geol. Ital*, 23, 99-115.

Cristofolini, R., Lentini, F., Patanè, G., & Rasà, R. (1979). Intergrazione di dati geologici, geofisici e petrologici per la stesura di un profilo crostale in corrispondenza dell'Etna. *Bollettino della Società Geologica Italiana*, 98(2), 239-247 (In Italian).

Cristofolini, R., Gresta, S., Imposa, S., & Patanè, G. (1988). Feeding mechanism of eruptive activity at Mt. Etna based on seismological and petrological data. *Modeling of Volcanic Processes* (pp. 73-93).

CristofoIini R, Corsaro RA, Ferlito C (1991). Variazioni petrochimiche nella successione etnea: un riesame in base a nuovi dati da campioni di superficie e da sondaggi. *Acta Vulc* 1, 25-37.

Currenti, G., & Williams, C. A. (2014). Numerical modeling of deformation and stress fields around a magma chamber: Constraints on failure conditions and rheology. *Physics of the Earth and Planetary Interiors*, 226, 14-27.

Dawson, P. B., Iyer, H. M., Evans, J. R., & Achauer, U. (1987). Inversion of teleseismic travel time residuals to investigate the three dimensional P velocity structure of the crust and upper mantle, the Long Valley, California, region [abs]: *International Union of Geodesy and Geophysics, General Assembly*. In Abstracts (Vol. 19, No. 1, p. 55).

Dawson, P., Chouet, B., & Pitt, A. (2016). Tomographic image of a seismically active volcano: Mammoth Mountain, California. *Journal of Geophysical Research: Solid Earth*.

De Astis, G., G. Ventura, and G. Vilardo (2003), Geodynamic significance of the Aeolian volcanism (Southern Tyrrhenian Sea, Italy) in light of structural, seismological and geochemical data, *Tectonics*, 22 (4), 1040, http://dx.doi.org/10.1029/2003TC001506.

De Barros, L., Bean, C. J., Lokmer, I., Saccorotti, G., Zuccarello, L., O'Brien, G. S., ... & Patane, D. (2009). Source geometry from exceptionally high resolution long period event observations at Mt Etna during the 2008 eruption. *Geophysical Research Letters*, 36(24).

De Barros, L., Martini, F., Bean, C. J., Garcia-Yeguas, A., & Ibáñez, J. (2012). Imaging magma storage below Teide volcano (Tenerife) using scattered seismic wavefields.

Geophysical Journal International, 191(2), 695–706. doi:10.1111/j.1365-246X.2012.05637.x.

De Beni, E., Branca, S., Coltelli, M., Groppelli, G., & Wijbrans, J. R. (2011). 40Ar/39Ar isotopic dating of Etna volcanic succession. *Italian Journal of Geosciences*, 130(3), 292-305.

De Boer, J. Z., & Sanders, D. T. (2002). Volcanoes in human history: the far-reaching effects of major eruptions. *Princeton University Press*.

De Gori P., Chiarabba C., Giampiccolo E., Martinez-Arèvalo C. and Patanè D. (2011). Body wave attenuation heralds incoming eruptions at Mt. Etna. *Geology*, 39, 503–506, doi:10.1130/G31993.1.

De Luca, G. Filippi, L., Patani, G., Scarpa, R., & Vinciguerra, S. (1997). Three-dimensional velocity structure and seismicity of Mt . Etna volcano , Italy. *Journal of Volcanology and Geothermal Research*, 0273(1993).

De Siena, L., Del Pezzo, E., & Bianco, F. (2010). Seismic attenuation imaging of Campi Flegrei: Evidence of gas reservoirs, hydrothermal basins, and feeding systems. *Journal of Geophysical Research: Solid Earth*, (1978–2012), 115(B9).

De Siena, L., Del Pezzo, E., & Bianco, F. (2011). A scattering image of Campi Flegrei from the autocorrelation functions of velocity tomograms. *Geophysical Journal International*, 184(3), 1304-1310.

Deichmann, N., & Ernst, J. (2009). Earthquake focal mechanisms of the induced seismicity in 2006 and 2007 below Basel (Switzerland). *Swiss Journal of Geosciences*, *102*(3), 457–466. doi:10.1007/s00015-009-1336-y.

Deichmann, N., & Giardini, D. (2009). Earthquakes Induced by the Stimulation of an Enhanced Geothermal System below Basel (Switzerland). *Seismological Research Letters*, *80*(5), 784–798. doi:10.1785/gssrl.80.5.784.

Del Fresno, C., Dominguez Cerdena, I., Cesca, S., & Buforn, E. (2014). The 8 October 2011 Earthquake at El Hierro (Mw 4.0): Focal Mechanisms of the Mainshock and Its Foreshocks. *Bulletin of the Seismological Society of America*, *105*(1), 330–340. doi:10.1785/0120140151.

Del Negro, C., & Ferrucci, F. (1998). Magnetic history of a dyke on Mount Etna (Sicily). *Geophysical Journal International*, 133(2), 451-458.

Del Negro, C., & Napoli, R. (2002). Ground and marine magnetic surveys of the lower eastern flank of Etna volcano (Italy). *Journal of volcanology and geothermal research*, 114(3), 357-372.

Del Negro, C., Napoli, R., & Sicali, A. (2002). Automated system for magnetic monitoring of active volcanoes. *Bulletin of volcanology*, 64(2), 94-99.

Del Negro, C., Currenti, G., Napoli, R., & Vicari, A. (2004). Volcanomagnetic changes accompanying the onset of the 2002–2003 eruption of Mt. Etna (Italy). *Earth and Planetary Science Letters*, 229(1), 1-14.

Del Pezzo, E., Godano, C., Gorini, A., & Martini, M. (1992). Wave polarization and location of the source of the explosion quakes at Stromboli Volcano. *Volcanic Seismology*, (pp. 279-296). Springer Berlin Heidelberg.

Delépine, N., Cuenot, N., Rothert, E., Parotidis, M., Rentsch, S., & Shapiro, S. A. (2004). Characterization of fluid transport properties of the Hot Dry Rock reservoir Soultz-2000 using induced microseismicity. *Journal of Geophysics and Engineering*, 1(1), 77–83. doi:10.1088/1742-2132/1/1/010.

Dellino, P., & Kyriakopoulos, K. (2003). Phreatomagmatic ash from the ongoing eruption of Etna reaching the Greek island of Cefalonia. *Journal of volcanology and geothermal research*, 126(3), 341-345.

Di Grazia, G., Falsaperla, S., & Langer, H. (2006). Volcanic tremor location during the 2004 Mount Etna lava effusion. *Geophysical research letters*, 33(4).

Di Lieto, B., Saccorotti, G., Zuccarello, L., La Rocca, M., & Scarpa, R. (2007). Continuous tracking of volcanic tremor at Mount Etna, Italy. *Geophysical Journal International*, 169(2), 699-705.

Di Stefano, A., & Branca, S. (2002). Long-term uplift rate of the Etna volcano basement (southern Italy) based on biochronological data from Pleistocene sediments. *Terra Nova*, 14(1), 61-68.

Di Stefano, R., & Chiarabba, C. (2002). Active source tomography at Mt. Vesuvius: constraints for the magmatic system. *Journal of Geophysical Research: Solid Earth* (1978–2012), 107(B11), ESE-4.

Di Stefano, R., Kissling, E., Chiarabba, C., Amato, A., & Giardini, D. (2009). Shallow subduction beneath Italy: Three-dimensional images of the Adriatic-European-Tyrrhenian lithosphere system based on high-quality P wave arrival times. *Journal of Geophysical Research: Solid Earth*, 114(B5).

Díaz-Moreno, A., Ibáñez, J. M., De Angelis, S., García-Yeguas, A., Prudencio, J., Morales, J., ... & García, L. (2015). Seismic hydraulic fracture migration originated by successive deep magma pulses: The 2011–2013 seismic series associated to the volcanic activity of El Hierro Island. *Journal of Geophysical Research: Solid Earth*, 120(11), 7749-7770.

Díaz-Moreno A., Koulakov I., García-Yeguas A., Cocina O, Barberi, G., Jakovlev A., Prudencio J., Zuccarello L., Álvarez I., García L., Benítez C., Scarfì, L., Patanè D., Ibáñez J.M., (2016). PARToS - Passive and Active Ray TOmography Software: Description and preliminary analysis using TOMO-ETNA experiment's dataset. Special Volume: TOMOETNA. Eds. Morales J., and Puglisi G.. *Annals of Geophysics*. doi:10.4401/ag-7088.

Dinc, A. N., Koulakov, I., Thorwart, M., Rabbel, W., Flueh, E. R., Arroyo, I., ... & Alvarado, G. (2010). Local earthquake tomography of central Costa Rica: transition from seamount to ridge subduction. *Geophysical Journal International*, 183(1), 286-302.

Doglioni, C., Innocenti, F., & Mariotti, G. (2001). Why Mt Etna?. *Terra Nova*,13(1), 25-31.

Domínguez-Cerdeña, I. D., Del Fresno, C., and Moreno, A. G. (2014). Seismicity patterns prior to the 2011 El Hierro eruption. *Bulletin of the Seismological Society of America*. 104 (1) doi: 10.1785/0120130200.

Dvorak, J. J., & Dzurisin, D. (1997). Volcano geodesy: The search for magma reservoirs and the formation of eruptive vents. *Reviews of Geophysics*, 35(3), 343-384.

Dzurisin, D. (2006). Volcano deformation: new geodetic monitoring techniques. *Springer-Verlag Berlin Heidelberg*. 1st Edition. XXXVI, pp. 442. doi: 10.1007/978-3-540-49302-0.

Eberhart-Phillips D.(1993). Local earthquake tomography: earthquake source regions. H.M. Iyer, Irahara (Eds.), Seismic Tomography: Theory and Practice, Chapman and Hall, New York, pp. 613–643.

Faccenna, C., Molin, P., Orecchio, B., Olivetti, V., Bellier, O., Funiciello, F., ... & Billi, A. (2011). Topography of the Calabria subduction zone (southern Italy): Clues for the origin of Mt. Etna. *Tectonics*, 30(1).

Faccenna, C., T.W. Becker, L. Auer, A. Billi, L. Boschi, J.P. Brun, F.A. Capitanio, F. Funiciello, F. Horvàth, L. Jolivet, C. Piromallo, L. Royden, F. Rossetti, and E. Serpelloni (2014). Mantle dynamics in the Mediterranean. *Reviews of Geophysics*, 52, 283–332, doi: 10.1002/2013RG000444.

Falsaperla, S., Privitera, E., Chouet, B., & Dawson, P. (2002). Analysis of long-period events recorded at Mount Etna (Italy) in 1992, and their relationship to eruptive activity. *Journal of volcanology and geothermal research*, 114(3), 419-440.

Falsaperla, S., Barberi, G., & Cocina, O. (2013). The failed eruption of Mt. Etna in December 2005: Evidence from volcanic tremor analyses. *Geochemistry, Geophysics, Geosystems*, *14*(12), 4989–5005. doi:10.1002/2013GC004976.

Farrell, J., Husen, S., & Smith, R. B. (2009). Earthquake swarm and b-value characterization of the Yellowstone volcano-tectonic system. *Journal of Volcanology and Geothermal Research*, 188(1), 260-276.

Farrell, J., Smith, R. B., Husen, S., & Diehl, T. (2014). Tomography from 26 years of seismicity revealing that the spatial extent of the Yellowstone crustal magma reservoir extends well beyond the Yellowstone caldera. *Geophysical Research Letters*, 41(9), 3068-3073.

Fialko, Y., Khazan, Y., & Simons, M. (2001). Deformation due to a pressurized horizontal circular crack in an elastic half-space, with applications to volcano geodesy. *Geophysical Journal International*, 146(1), 181-190.

Firetto-Carlino, M., Zgur, F., Bruno, P.P., Coltelli, M., Sormani, L., Cavallaro, D., Ibáñez, J.M. and Patanè, D., (2016). Acquisition and preliminary analysis of multi-channel seismic reflection data, acquired during the oceanographic cruises of the Tomo-Etna experiment. Special Volume: TOMOETNA. Eds. Morales J., and Puglisi G.. *Annals of Geophysics*. doi:10.4401/ag-7083.

Foulger, G. R., Julian, B. R., Pitt, A. M., Hill, D. P., Malin, P. E., & Shalev, E. (2003). Three-dimensional crustal structure of Long Valley caldera, California, and evidence for the migration of CO2 under Mammoth Mountain. *Journal of Geophysical Research: Solid Earth, (1978–2012), 108(B3).*

Francis, P. & Oppenheimer, C. (2004). Volcanoes. 2nd Edt. Oxford University Press, New York, Oxford, 521 p., ISBN 978-0199254699, ISBN 0199254699 (book),.

Froger, J. L., Merle, O., & Briole, P. (2001). Active spreading and regional extension at Mount Etna imaged by SAR interferometry. *Earth and Planetary Science Letters*, 187(3), 245-258.

Furuya, M., Okubo, S., Sun, W., Tanaka, Y., Oikawa, J., Watanabe, H., & Maekawa, T. (2003). Spatiotemporal gravity changes at Miyakejima Volcano, Japan: Caldera collapse, explosive eruptions and magma movement. *Journal of Geophysical Research: Solid Earth* (1978–2012), 108(B4).

Gambino, S., Mostaccio, A., Patanè, D., Scarfì, L., & Ursino, A. (2004). High-precision locations of the microseismicity preceding the 2002–2003 Mt. Etna eruption. *Geophysical research letters*, 31, L18604. doi: 10.1029/2004GL020499.

Garcés, M. A., & McNutt, S. R. (1997). Theory of the airborne sound field generated in a resonant magma conduit. *Journal of volcanology and geothermal research*, 78(3), 155-178.

Garcia, A., Fernandez-Ros, A., Berrocoso, M., Marrero, J. M., Prates, G., De la Cruz-Reyna, S., & Ortiz, R. (2014). Magma displacements under insular volcanic fields, applications to eruption forecasting: El Hierro, Canary Islands, 2011-2013. *Geophysical Journal International*, *197*(1), 322–334. doi:10.1093/gji/ggt505.

García, L., Álvarez, I., Benítez, C., Titos, M., Bueno, A., De la Torre, A., Alguacil, G., Díaz- Moreno, A., Prudencio, J., García-Yeguas, A., Ibáñez, J.M., Zuccarello, L.,

and Cocina, O. (2016). Advances on the automatic estimation of the P-wave onset time. Special Volume: TOMOETNA. Eds. Morales J., and Puglisi G.. *Annals of Geophysics*. doi:10.4401/ag-7087.

García-Yeguas, A., Almendros, J., Abella, R., & Ibáñez, J. M. (2011). Quantitative analysis of seismic wave propagation anomalies in azimuth and apparent slowness at Deception Island volcano (Antarctica) using seismic arrays. *Geophysical Journal International*, 184(2), 801-815.

García-Yeguas, A., Koulakov, I., Ibáñez, J. M., & Rietbrock, a. (2012). High resolution 3D P wave velocity structure beneath Tenerife Island (Canary Islands, Spain) based on tomographic inversion of active-source data. *Journal of Geophysical Research*, *117*(B9), B09309. doi:10.1029/2011JB008970.

García-Yeguas, A., Ibáñez, J.M., Koulakov, I., Jakovlev, A., Romero-Ruiz, M.C. and Prudencio, J. (2014). Seismic tomography model reveals mantle magma sources of recent volcanic activity at El Hierro Island (Canary Islands, Spain). *Geophysical Journal International*, 199, 1739-1750. doi: 10.1093/gji/ggu339.

Gasparini, P. (1998). Looking inside mt. vesuvius. *Eos, Transactions American Geophysical Union*, *79*(19), 229–229. doi:10.1029/98EO00165.

Gentili, S., & Michelini, A. (2006). Automatic picking of P and S phases using a neural tree. *Journal of Seismology*, 10(1), 39-63.

Gillot, P. Y., Kieffer, G., & Romano, R. (1994). The evolution of Mount Etna in the light of potassium-argon dating. *Acta Vulcanol*, 5, 81-87.

Goertz-Allmann, B. P., Goertz, A., & Wiemer, S. (2011). Stress drop variations of induced earthquakes at the Basel geothermal site. *Geophysical Research Letters*, 38(9). doi:10.1029/2011GL047498.

González, P. J., Samsonov, S. V., Pepe, S., Tiampo, K. F., Tizzani, P., Casu, F., ... & Sansosti, E. (2013). Magma storage and migration associated with the 2011–2012 El Hierro eruption: Implications for crustal magmatic systems at oceanic island volcanoes. *Journal of Geophysical Research: Solid Earth*, 118(8), 4361-4377.

Gorbatikov, A. V., Montesinos, F. G., Arnoso, J., Stepanova, M. Y., Benavent, M., & Tsukanov, A. A. (2013). New Features in the Subsurface Structure Model of El

Hierro Island (Canaries) from Low-Frequency Microseismic Sounding: An Insight into the 2011 Seismo-Volcanic Crisis. *Surveys in Geophysics*, 34(4), 463–489. doi:10.1007/s10712-013-9240-4.

Granieri, D., Carapezza, M. L., Chiodini, G., Avino, R., Caliro, S., Ranaldi, M., ... & Tarchini, L. (2006). Correlated increase in CO2 fumarolic content and diffuse emission from La Fossa crater (Vulcano, Italy): Evidence of volcanic unrest or increasing gas release from a stationary deep magma body?. *Geophysical Research Letters*, 33(13).

Greco, F., Currenti, G., D'Agostino, G., Del Negro, C., Di Stefano, A., Germak, A., ... & Sicali, A. (2010). Absolute and relative gravity measurements at etna volcano (italy). *IAG Symposium on Terrestrial Gravimetry: static and mobile measurements*.

Gresta, S., Bella, D., Musumeci, C., & Carveni, P. (1997). Some efforts on active faulting processes (earthquakes and aseismic creep) acting on the eastern flank of Mt. Etna (Sicily). *Acta Vulcanologica*, 9, 101-108.

Gresta, S., Longo, V., & Viavattene, A. (1990). Geodynamic behaviour of eastern and western sides of Mount Etna. *Tectonophysics*, 179(1), 81-92.

Gresta, S., Peruzza, L., Slejko, D., & Distefano, G. (1998). Inferences on the main volcano-tectonic structures at Mt. Etna (Sicily) from a probabilistic seismological approach. *Journal of Seismology*, 2(2), 105-116.

Guest, J. E., Chester, D. K., & Duncan, A. M. (1984). The Valle del Bove, Mount Etna: its origin and relation to the stratigraphy and structure of the volcano. *Journal of volcanology and geothermal research*, 21(1), 1-23.

Gutenberg, B., & Richter, C. F. (1944). Frequency of earthquakes in California. *Bulletin of the Seismological Society of America*, 34(4), 185-188.

Gutscher M.A., S. Dominguez, B. Mercier De Lepinay, L. Pinheiro, F. Gallais, N. Babonneau, A. Cattaneo, Y. Le Faou, G. Barreca, A. Micallef, and M. Rovere (2016), Tectonic expression of an active slab tear from high-resolution seismic and bathymetric data offshore Sicily (Ionian Sea), *Tectonics*, 35, 39-54, doi:10.1002/2015TC003898.

Gvirtzman, Z., & Nur, A. (1999). The formation of Mount Etna as the consequence of slab rollback. *Nature*, 401(6755), 782–785. doi:10.1038/44555.

Hagerty, M. T., Schwartz, S. Y., Garces, M. A., & Protti, M. (2000). Analysis of seismic and acoustic observations at Arenal Volcano, Costa Rica, 1995–1997. *Journal of Volcanology and Geothermal Research*, 101(1), 27-65.

Havskov, J., & Alguacil, G. (Eds.). (2016). *Instrumentation in earthquake seismology* (Vol. 22). 2nd Edition. Springer International Publishing. XVI, pp. 413. doi: 10.1007/978-3-319-21314-9.

Herring, T. A., King, R. W., & McClusky, S. C. (2006). Introduction to GAMIT/GLOBK, *Release 10.3, Dep. of Earth Atmos. and Planet. Sci., Mass. Inst. of Technol., Cambridge, Mass, 28*.

Hildyard, M. W., Nippress, S. E., & Rietbrock, A. (2008). Event detection and phase picking using a time-domain estimate of predominate period Tpd. *Bulletin of the Seismological Society of America*, 98(6), 3025-3032.

Hirn, a, Nercessian, a, Sapin, M., Ferrucci, F., & Wittlinger, G. (1991). Seismic Heterogeneity of Mt Etna - Structure and Activity. *Geophysical Journal International*, *105*(1), 139–153. doi:10.1111/j.1365-246X.1991.tb03450.x.

Hirn, A., Nicolich, R., Gallart, J., Laigle, M., Cernobori, L., & ETNASEIS Scientific Group. (1997). Roots of Etna volcano in faults of great earthquakes. *Earth and Planetary Science Letters*, *148*(1-2), 171–191. doi:10.1016/S0012-821X(97)00023-X.

Hofmann, A. W. (1988). Chemical differentiation of the Earth: the relationship between mantle, continental crust, and oceanic crust. *Earth and Planetary Science Letters*, 90(3), 297-314.

Ibáñez, J. M., Pezzo, E. Del, Almendros, J., La Rocca, M., Alguacil, G., Ortiz, R., & García, A. (2000). Seismovolcanic signals at Deception Island volcano, Antarctica: Wave field analysis and source modeling. *Journal of Geophysical Research*, *105*(B6), 13905. doi:10.1029/2000JB900013.

Ibáñez, J., Almendros, J., Carmona, E., Martínez-Arévalo, C., & Abril, M. (2003). The recent seismo-volcanic activity at Deception Island volcano. *Deep Sea Research*

Part II: Topical Studies in Oceanography, *50*(10-11), 1611–1629. doi:10.1016/S0967-0645(03)00082-1.

Ibáñez, J. M., Rietbock, A., & García-Yeguas, A. (2008). Imaging an active volcano edifice at Tenerife Island, Spain. *Eos, Transactions American Geophysical Union*, 89(32), 289-290.

Ibáñez, J. M., De Angelis, S., Díaz-Moreno, A., Hernández, P., Alguacil, G., Posadas, A., & Pérez, N. (2012). Insights into the 2011-2012 submarine eruption off the coast of El Hierro (Canary Islands, Spain) from statistical analyses of earthquake activity. *Geophysical Journal International*, 191(2), 659–670. doi:10.1111/j.1365-246X.2012.05629.x.

Ibáñez, J.M, Prudencio, J., Díaz-Moreno, A., Patané, D. , Puglisi, G. , Luehr, B.G. , Carrión, F., Dañobeitia, J.J., Coltelli, M., Bianco, F., Del Pezzo, E., Dahm, T., Willmott ,V., and Mazauric, V. (2016a). The TOMO-ETNA experiment: an imaging active campaign at Mt. Etna volcano. Context, main objectives, working-plans and involved research projects. Special Volume: TOMOETNA. Eds. Morales J., and Puglisi G. *Annals of Geophysics*. doi:10.4401/ag-7079.

Ibáñez, J.M., Díaz-Moreno, A., Prudencio, J.,…, Abramenkov, S.(2016b). TOMO-ETNA experiment at Etna volcano: activities on land. Special Volume: TOMOETNA. Eds. Morales J., and Puglisi G. *Annals of Geophysics*. doi:10.4401/ag-7080.

Ishimoto, M., & Iida, K. (1939). Observations of earthquakes registered with the microseismograph constructed recently. *Bulletin of Earthquake Research Institute*, 17, 443-478.

Iyer, H. M. (1993). *Seismic tomography: Theory and practice*. Springer Science & Business Media.

Jacobs, K. M., & McNutt, S. R. (2006). Using seismic b-values to interpret seismicity rates and physical processes during the preeruptive earthquake swarm at Augustine Volcano 2005-2006. The 2006 Eruption of Augustine Volcano, Alaska. Power, J.A., Coombs, M.L., and Freymueller, J.T., editors. U.S. Geological Survey Professional Paper 1769 59-83.

Jakovlev, A., Rümpker, G., Schmeling, H., Koulakov, I., Lindenfeld, M. and Wallner, H., 2013. Seismic images of magmatic rifting beneath the western branch of the East African rift. Geochemistry, Geophysics, Geosystems, 14(11), pp.4906-4920.

Jaxybulatov, K., Koulakov, I., Ibs-von Seht, M., Klinge, K., Reichert, C., Dahren, B., & Troll, V. R. (2011). Evidence for high fluid/melt content beneath Krakatau volcano (Indonesia) from local earthquake tomography. Journal of Volcanology and Geothermal Research, 206(3), 96-105.

Johnson, D. J., Eggers, A. A., Bagnardi, M., Battaglia, M., Poland, M. P., & Miklius, A. (2010). Shallow magma accumulation at Kīlauea Volcano, Hawai ʻi, revealed by microgravity surveys. *Geology*, 38(12), 1139-1142.

Johnston, M. J. S. (1997). Review of electric and magnetic fields accompanying seismic and volcanic activity. *Surveys in Geophysics*, 18(5), 441-476.

Jolivet, L., and C. Faccenna (2000). Mediterranean extension and the Africa-Eurasia collision, *Tectonics*, 19(6), 1095–1106, doi:10.1029/2000TC900018.

Jolly, A. D., Lokmer, I., Kennedy, B., Keys, H. J. R., Proctor, J., Lyons, J. J., & Jolly, G. E. (2014). Active seismic sources as a proxy for seismic surface processes: An example from the 2012 Tongariro volcanic eruptions, New Zealand. *Journal of Volcanology and Geothermal Research*, 286, 317-330.

Joron, J. L., & Treuil, M. (1984). Etude géochimique et pétrogenèse des laves de l'Etna, Sicile, Italie. *Bulletin Volcanologique*, 47(4), 1125-1144.

Judenherc, S., & Zollo, A. (2004). The Bay of Naples (southern Italy): Constraints on the volcanic structures inferred from a dense seismic survey. *Journal of Geophysical Research: Solid Earth*, (1978–2012), 109(B10).

Kamo, K., Ishihara, K., & Tahira, M. (1994). Infrasonic and seismic detection of explosive eruptions at Sakurajima Volcano, Japan, and the PEGASAS-VE early-warning system. *In Volcanic Ash and Aviation Safety, Proceedings of the First Int Symposium on Volcanic Ash and Aviation Safety* (pp. 357-365).

Kaneshima, S., Kawakatsu, H., Matsubayashi, H., & Sudo, Y. (1996). Mechanism of phreatic eruptions at Aso Volcano inferred from near-field broadband seismic observations. *Science*, 273(5275), 642.

Kasatkina, E., Koulakov, I., West, M., & Izbekov, P. (2014). Seismic structure changes beneath Redoubt Volcano during the 2009 eruption inferred from local earthquake tomography. *Journal of Geophysical Research: Solid Earth*, *119*(6), 4938–4954. doi:10.1002/2013JB010935.

Kato, A., Sakai, S., Iidaka, T., Iwasaki, T., & Hirata, N. (2010). Non-volcanic seismic swarms triggered by circulating fluids and pressure fluctuations above a solidified diorite intrusion. Geophysical Research Letters, 37(15).

Kauahikaua, J., Hildenbrand, T., & Webring, M. (2000). Deep magmatic structures of Hawaiian volcanoes, imaged by three-dimensional gravity models. *Geology*, 28(10), 883-886.

Kilburn, C. R. (2003). Multiscale fracturing as a key to forecasting volcanic eruptions. *Journal of Volcanology and Geothermal Research*, 125(3), 271-289.

Kiser, E., Levander, A., Harder, S., Abers, G., Creager, K., Vidale, J., ... & Malone, S. (2013, April). iMUSH: The design of the Mount St. Helens high-resolution active source seismic experiment. *EGU General Assembly Conference Abstracts* (Vol. 15, p. 12325).

Koulakov, I. (2009a). LOTOS Code for Local Earthquake Tomographic Inversion: Benchmarks for Testing Tomographic Algorithms. *Bulletin of the Seismological Society of America*, *99*(1), 194–214. doi:10.1785/0120080013.

Koulakov, I. (2009b). Code ATOM-3D for 3D tomographic inversion based on active refraction seismic data. *http://www.ivan-art.com/science/*.

Koulakov, I. (2012). Multiscale Seismic Tomography Imaging of Volcanic Complexes. *INTECH Open Access Publisher*.

Koulakov, I. (2013). Studying deep sources of volcanism using multiscale seismic tomography. *Journal of Volcanology and Geothermal Research*, *257*, 205–226. doi:10.1016/j.jvolgeores.2013.03.012.

Koulakov, I., Sobolev, S. V., & Asch, G. (2006). P - and S -velocity images of the lithosphere-asthenosphere system in the Central Andes from local-source tomographic inversion. *Geophysical Journal International*, *167*(1), 106–126. doi:10.1111/j.1365-246X.2006.02949.x.

Koulakov, I., Yudistira, T., & Luehr, B. G. (2009). P, S velocity and VP/VS ratio beneath the Toba caldera complex (Northern Sumatra) from local earthquake tomography. *Geophysical Journal International*, 177(3), 1121-1139.

Koulakov, I., Gordeev, E. I., Dobretsov, N. L., Vernikovsky, V. a., Senyukov, S., & Jakovlev, A. (2011). Feeding volcanoes of the Kluchevskoy group from the results of local earthquake tomography. *Geophysical Research Letters*, *38*(9), n/a–n/a. doi:10.1029/2011GL046957.

Koulakov, I., Gordeev, E. I., Dobretsov, N. L., Vernikovsky, V. a., Senyukov, S., Jakovlev, A., & Jaxybulatov, K. (2013a). Rapid changes in magma storage beneath the Klyuchevskoy group of volcanoes inferred from time-dependent seismic tomography. *Journal of Volcanology and Geothermal Research*. doi:10.1016/j.jvolgeores.2012.10.014.

Koulakov, I., West, M., & Izbekov, P. (2013b). Fluid ascent during the 2004–2005 unrest at Mt. Spurr inferred from seismic tomography. *Geophysical Research Letters*, 40(17), 4579-4582.

Koulakov, I., Jaxybulatov, K., Shapiro, N. M., Abkadyrov, I., Deev, E., Jakovlev, A., … Chebrov, V. (2014). Asymmetric caldera-related structures in the area of the Avacha group of volcanoes in Kamchatka as revealed by ambient noise tomography and deep seismic sounding. *Journal of Volcanology and Geothermal Research*, *285*, 36–46. doi:10.1016/j.jvolgeores.2014.08.012.

Koulakov I., E. Kukarina, E.I. Gordeev, V.N. Chebrov and V.A. Vernikovsky (2016), Magma sources in the mantle wedge beneath the Klyuchevskoy volcano group from seismic tomography inversion, *Russian Geology and Geophysics*.

Koulakov, I., Kaban, M. K., Tesauro, M., & Cloetingh, S. (2009). P - and S -velocity anomalies in the upper mantle beneath Europe from tomographic inversion of ISC data. *Geophysical Journal International*, *179*(1), 345–366. doi:10.1111/j.1365-246X.2009.04279.x.

Koulakov, I., & Sobolev, S. V. (2006a). A tomographic image of Indian lithosphere break-off beneath the Pamir-Hindukush region. *Geophysical Journal International*, *164*(2), 425–440. doi:10.1111/j.1365-246X.2005.02841.x.

Koulakov, I., & Sobolev, S. V. (2006b). Moho depth and three-dimensional P and S structure of the crust and uppermost mantle in the Eastern Mediterranean and Middle East derived from tomographic inversion of local ISC data. *Geophysical Journal International*, *164*(1), 218–235. doi:10.1111/j.1365-246X.2005.02791.x.

Koulakov I and Shapiro N (2015) Seismic Tomography of Volcanoes. In Beer M, Kougioumtzoglou IA, Patelli E and Au S (Ed.) Encyclopedia of Earthquake Engineering. Springer, Dordrecht, pp 3117-3134. DOI 10.1007/978-3-642-36197-5_51-1.

Kraft, T. and Deichmann, N. (2013). High-precision relocation and focal mechanism of the injection-induced seismicity at the Basel EGS. *Geothermics*, 52, 59-73.

Kumagai, H., Chouet, B. A., & Nakano, M. (2002). Waveform inversion of oscillatory signatures in long-period events beneath volcanoes. *Journal of Geophysical Research: Solid Earth*, (1978–2012), 107(B11), ESE-7.

Küperkoch, L., Meier, T., Lee, J., Friederich, W., & EGELADOS Working Group. (2010). Automated determination of P-phase arrival times at regional and local distances using higher order statistics. *Geophysical Journal International*, 181(2), 1159-1170.

Küperkoch, L., Meier, T., & Diehl, T. (2012). Automated event and phase identification. *New manual of seismological observatory practice*, 2, 1-52.

Kurzon, I., Vernon, F. L., Rosenberger, A., & Ben-Zion, Y. (2014). Real-time automatic detectors of P and S waves using singular value decomposition. *Bulletin of the Seismological Society of America*, 104(4), 1696-1708.

Kuznetsov, P. Y., & Koulakov, I. Y. (2014). The three-dimensional structure beneath the Popocatépetl volcano (Mexico) based on local earthquake seismic tomography. *Journal of Volcanology and Geothermal Research*, *276*, 10–21. doi:10.1016/j.jvolgeores.2014.02.017.

Laigle, M., & Hirn, A. (1999). Explosion-seismic tomography of a magmatic body beneath Etna: Volatile discharge and tectonic control of volcanism. *Geophysical Research Letters*, *26*(17), 2665. doi:10.1029/1998GL005300.

Laigle, M., Hirn, A., Sapin, M., Lépine, J. C., Diaz, J., Gallart, J., & Nicolich, R. (2000). Mount Etna dense array local earthquake P and S tomography and implications for volcanic plumbing. *Journal of Geophysical Research: Solid Earth* (1978–2012), 105(B9), 21633-21646.

Langer, H., Falsaperla, S., Masotti, M., Campanini, R., Spampinato, S., & Messina, A. (2009). Synopsis of supervised and unsupervised pattern classification techniques applied to volcanic tremor data at Mt Etna, Italy. *Geophysical Journal International*, 178(2), 1132-1144.

Langet, N., Maggi, A., Michelini, A., & Brenguier, F. (2014). Continuous Kurtosis-Based Migration for Seismic Event Detection and Location, with Application to Piton de la Fournaise Volcano, La Réunion. *Bulletin of the Seismological Society of America*, 104(1), 229-246.

Lanzafame, G., Neri, M., & Rust, D. (1996). Active tectonics affecting the eastern flank of Mount Etna: structural interactions at a regional and local scale. *Etna: fifteen years on*, 1861740018, 25-33.

Lanzafame, G., & Bousquet, J. C. (1997). The Maltese escarpment and its extension from Mt. Etna to Aeolian Islands (Sicily): importance and evolution of a lithosphere discontinuity. *Acta Vulcanologica*, 9, 113-120.

Lee, M. K., & Wolf, L. W. (1998). Analysis of fluid pressure propagation in heterogeneous rocks: Implications for hydrologically-induced earthquakes. *Geophysical Research Letters*, 25(13), 2329-2332.

Lees, J. M. (2007). Seismic tomography of magmatic systems. *Journal of Volcanology and Geothermal Research*, *167*(1-4), 37–56. doi:10.1016/j.jvolgeores.2007.06.008.

Lentini, F., Carbone, S., & Guarnieri, P. (2006). Collisional and postcollisional tectonics of the Apenninic-Maghrebian orogen (southern Italy). *Geological Society of America Special Papers*, 409, 57-81.

Leonard, G. S., Johnston, D. M., Paton, D., Christianson, A., Becker, J., & Keys, H. (2008). Developing effective warning systems: Ongoing research at Ruapehu volcano, New Zealand. *Journal of Volcanology and Geothermal Research*, 172(3), 199-215.

Levander, A., Kiser, E., Palomeras, I., Zelt, C., Schmandt, B., Hansen, S., ... & Abers, G. (2015, April). Preliminary Results from the iMUSH Active Source Seismic Experiment. *EGU General Assembly Conference Abstracts* (Vol. 17, p. 7550).

Lin, G., Amelung, F., Lavallee, Y., & Okubo, P. G. (2014a). Seismic evidence for a crustal magma reservoir beneath the upper east rift zone of Kilauea volcano, Hawaii. *Geology*, *42*(3), 187–190. doi:10.1130/G35001.1.

Lin, G., Shearer, P. M., Matoza, R. S., Okubo, P. G., & Amelung, F. (2014b). Three-dimensional seismic velocity structure of Mauna Loa and Kilauea volcanoes in Hawaii from local seismic tomography. *Journal of Geophysical Research : Solid Earth Three*, *119*, 4377–4392. doi:10.1002/2013JB010820.

Lo Giudice, E., Patanè, G., Rasà, R., & Romano, R. (1982). The structural framework of Mount Etna. *Memorie delle Società Geologica Italiana*, 23, 125-158.

Lo Giudice, E., & Rasà, R. (1992). Very shallow earthquakes and brittle deformation in active volcanic areas: The Etnean region as an example. *Tectonophysics*, 202(2), 257-268.

Lodge, A., Nippress, S. E. J., Rietbrock, A., García-Yeguas, A., & Ibáñez, J. M. (2012). Evidence for magmatic underplating and partial melt beneath the Canary Islands derived using teleseismic receiver functions. *Physics of the Earth and Planetary Interiors*, 212, 44-54.

Lomax, A., Virieux, J., Volant, P., and Berge-Thierry, C. (2000). Probabilistic earthquake location in 3D and layered models. *Advances in seismic event location*, Springer Netherlands, 101-134, doi: 10.1007/978-94-015-9536-0_5.

Lomax, A., and Curtis, A. (2001). Fast, probabilistic earthquake location in 3D models using oct-tree importance sampling. *Geophysical Research Abstracts*, 3, 955.

Lomax, A., Zollo, A., Capuano, P., & Virieux, J. (2001). Precise, absolute earthquake location under Somma–Vesuvius volcano using a new three-dimensional velocity model. Geophysical Journal International, 146(2), 313-331.

López, C., Blanco, M. J., Abella, R., Brenes, B., Cabrera Rodríguez, V. M., Casas, B., … and Villasante-Marcos, V. (2012). Monitoring the volcanic unrest of El Hierro

(Canary Islands) before the onset of the 2011-2012 submarine eruption. *Geophysical Research Letters*, 39(13), n/a–n/a. doi:10.1029/2012GL051846.

López, C., Martí, J., Abella, R., & Tarraga, M. (2014). Applying fractal dimensions and energy-budget analysis to characterize fracturing processes during magma migration and eruption: 2011–2012 El Hierro (Canary Islands) submarine eruption. *Surveys in Geophysics*, 35(4), 1023-1044.

Lu, Z., Wicks, C., Dzurisin, D., Thatcher, W., Freymueller, J. T., McNutt, S. R., & Mann, D. (2000). Aseismic inflation of Westdahl volcano, Alaska, revealed by satellite radar interferometry. *Geophysical Research Letters*, 27(11), 1567-1570.

Lu, Z., Wicks, C., Dzurisin, D., Power, J. A., Moran, S. C., & Thatcher, W. (2002). Magmatic inflation at a dormant stratovolcano: 1996–1998 activity at Mount Peulik volcano, Alaska, revealed by satellite radar interferometry. *Journal of Geophysical Research: Solid Earth*, (1978–2012), 107(B7), ETG-4.

Lundgren, P., Berardino, P., Coltelli, M., Fornaro, G., Lanari, R., Puglisi, G., ... & Tesauro, M. (2003). Coupled magma chamber inflation and sector collapse slip observed with synthetic aperture radar interferometry on Mt. Etna volcano. *Journal of Geophysical Research: Solid Earth*, (1978–2012), 108(B5).

Maercklin, N., Riedel, C., Rabbel, W., Wegler, U., Lühr, B. G., & Zschau, J. (2000). Structural investigation of Mt. Merapi by an active seismic experiment. *Deutsche Geophys*, 13-16.

Majer, E. L., Baria, R., Stark, M., Oates, S., Bommer, J., Smith, B., & Asanuma, H. (2007). Induced seismicity associated with enhanced geothermal systems. *Geothermics*, 36(3), 185-222.

Malinverno, A., and W.B.F. Ryan (1986). Extension in the Tyrrhenian Sea and shortening in the Apennines as result of arc migration driven by slab sinking in the lithosphere, *Tectonics*, 5, 227–245.

Mantovani, E., D. Albarello, C. Tamburelli, and D. Babbucci (1996), Evolution of the Tyrrhenian basin and surrounding regions as a result of the Africa–Euroasia convergence, *J. Geodyn*., 21, 35–72.

Marsella, E., Favali, P., Castellano, M., Aiello, G., Bortoluzzi, G., Di Fiore, V., ... & Rinke, N. R. (2007). The Stromboli geophysical experiment. Preliminary report on wide angle refraction seismics and morphobathymetry of Stromboli island (Southern Tyrrhenian sea, Italy) based on integrated offshore-onshore data acquisition (cruise STRO-06 R/V Urania).

Martí, J., Pinel, V., López, C., Geyer, A., Abella, R., Tárraga, M., Blanco, M.J., Castro, A. and Rodríguez, C. (2013a). Causes and mechanisms of the 2011–2012 El Hierro (Canary Islands) submarine eruption. *Journal of Geophysical Research: Solid Earth*, 118(3), 823-839. DOI: 10.1002/jgrb.50087.

Martí, J., Castro, A., Rodriguez, C., Costa, F., Carrasquilla, S., Pedreira, R., and Bolos, X. (2013b). Correlation of Magma Evolution and Geophysical Monitoring during the 2011-2012 El Hierro (Canary Islands) Submarine Eruption. *Journal of Petrology*, 0(0). doi:10.1093/petrology/egt014.

Martínez-Arévalo, C., Patanè, D., Rietbrock, A., & Ibánez, J. M. (2005). The intrusive process leading to the Mt. Etna 2001 flank eruption: Constraints from 3-D attenuation tomography. *Geophysical Research Letters*, *32*(21), 1–5. doi:10.1029/2005GL023736.

Marty, B., Trull, T., Lussiez, P., Basile, I., & Tanguy, J. C. (1994). He, Ar, O, Sr and Nd isotope constraints on the origin and evolution of Mount Etna magmatism. *Earth and Planetary Science Letters*, 126(1), 23-39.

Mattia, M., Patane, D., Aloisi, M., & Amore, M. (2007). Faulting on the western flank of Mt Etna and magma intrusions in the shallow crust. *Terra Nova*, 19(1), 89-94.

Métaxian, J. P., Lesage, P., & Valette, B. (2002). Locating sources of volcanic tremor and emergent events by seismic triangulation: Application to Arenal volcano, Costa Rica. *Journal of Geophysical Research: Solid Earth*, (1978–2012), 107(B10), ECV-10.

McNutt, S. R. (1992). Volcanic tremor. *Encyclopedia of earth system science*, 4, 417-425.

McNutt, S. R. (2002). Volcano seismology and monitoring for eruptions. *International Geophysics Series*, 81(A), 383-406.

McNutt, S. R. (2005). Volcanic Seismology. *Annual Review of Earth and Planetary Sciences*, *33*(1), 461–491. doi:10.1146/annurev.earth.33.092203.122459.

Melián, G., Barrancos, J., Padilla, G., Dionis, S., Rodríguez, F., Nolasco, D., ... and Peraza, M. D. (2012, April). Spatial and temporal variations of soil CO2 degassing rate at El Hierro volcanic system and relation to the 2011 submarine eruption. *EGU General Assembly Conference Abstracts*,14, 8903.

Michel, S., & Zlotnicki, J. (1998). Self-potential and magnetic surveying of La Fournaise volcano (Réunion Island): Correlations with faulting, fluid circulation, and eruption. *Journal of Geophysical Research: Solid Earth* (1978–2012), 103(B8), 17845-17857.

Mogi, K. (1962). Magnitude frequency relation for elastic shocks accompanying fractures of various materials and some related problems in earthquakes, *Bull. Earthquake Res. Inst.* 40, 831- 853.

Monaco, C., Petronio, L., & Romanelli, M. (1995). Tettonica estensionale nel settore orientale del Monte Etna (Sicilia): dati morfotettonici e sismici. *Studi Geol. Camerti*, 2, 363-374 (In Italian).

Monaco, C., Tapponnier, P., Tortorici, L., & Gillot, P. Y. (1997). Late Quaternary slip rates on the Acireale-Piedimonte normal faults and tectonic origin of Mt. Etna (Sicily). *Earth and Planetary Science Letters*, 147(1), 125-139.

Monaco, C., Catalano, S., Cocina, O., De Guidi, G., Ferlito, C., Gresta, S., ... & Tortorici, L. (2005). Tectonic control on the eruptive dynamics at Mt. Etna Volcano (Sicily) during the 2001 and 2002–2003 eruptions. *Journal of Volcanology and Geothermal Research*, 144(1), 211-233.

Monaco, C., De Guidi, G., & Ferlito, C. (2010). The morphotectonic map of Mt. Etna. *Italian journal of geosciences*, 129(3), 408-428.

Monaco, C., Ibáñez, J.M., Carrión, F. and Tringali, L. M., (2016). Cetacean behavioural responses to noise exposure generated by seismic surveys: how to mitigate better?. Special Volume: TOMOETNA. Eds. Morales J., and Puglisi G. *Annals of Geophysics*. doi:10.4401/ag-7089.

Monteiller, V., Got, J.-L., Patanè, D., Barberi, G., Cocina, O., & Others. (2009). Double-difference tomography at Mt Etna volcano: Preliminary results. *The VOLUME*

Project--VOLcanoes: Understanding Subsurface Mass moveMEnt, *9*(October 2002), 7962.

Montesinos, F. G., Arnoso, J., Benavent, M., and Vieira, R. (2006). The crustal structure of El Hierro (Canary Islands) from 3-D gravity inversion. *Journal of Volcanology and Geothermal Research*, 150(1-3), 283–299. doi:10.1016/j.jvolgeores.2005.07.018.

Montuori, C., Cimini, G. B., & Favali, P. (2007). Teleseismic tomography of the southern Tyrrhenian subduction zone: New results from seafloor and land recordings. *Journal of Geophysical Research: Solid Earth*, 112(B3).

Mostaccio, A., Tuvè, T., Patanè, D., Barberi, G., and Zuccarello, L. (2013). Improving Seismic Surveillance at Mt. Etna Volcano by Probabilistic Earthquake Location in a 3D Model. *Bulletin of The Seismological Society Of America*, 103, 4, 2447–2459, doi: 10.1785/0120110202.

Murphy, S., O'Brien, G. S., McCloskey, J., Bean, C. J., and Nalbant, S. (2013). Modelling fluid induced seismicity on a nearby active fault. Geophysical Journal International, 194(3), 1613-1624.

Murru, M., Montuori, C., Wyss, M., & Privitera, E. (1999). The locations of magma chambers at Mt. Etna, Italy, mapped by b- values. Geophysical research letters, 26(16), 2553-2556.

Musumeci, C. (2002). Magma system recharge of Mount St. Helens from precise relative hypocenter location of microearthquakes. Journal of Geophysical Research, 107(B10), 2264. doi:10.1029/2001JB000629.

Musumeci, C., Cocina, O., De Gori, P., & Patanè, D. (2004). Seismological evidence of stress induced by dike injection during the 2001 Mt. Etna eruption. Geophysical Research Letters, 31(7), n/a–n/a. doi:10.1029/2003GL019367.

Napoli, R., Currenti, G., Del Negro, C., Greco, F., & Scandura, D. (2008). Volcanomagnetic evidence of the magmatic intrusion on 13th May 2008 Etna eruption. *Geophysical Research Letters*, 35(22).

Neri, M., & Acocella, V. (2006). The 2004–2005 Etna eruption: implications for flank deformation and structural behaviour of the volcano. Journal of Volcanology and Geothermal Research, 158(1), 195-206.

Neri, M., Acocella, V., & Behncke, B. (2004). The role of the Pernicana Fault System in the spreading of Mt. Etna (Italy) during the 2002–2003 eruption. Bulletin of Volcanology, 66(5), 417-430.

Neri, M., Guglielmino, F., & Rust, D. (2007). Flank instability on Mount Etna: Radon, radar interferometry, and geodetic data from the southwestern boundary of the unstable sector. Journal of Geophysical Research: Solid Earth, (1978–2012), 112(B4).

Neri, G., B. Orecchio, C. Totaro, G. Falcone, and D. Presti (2009). Subduction beneath southern Italy close the ending: results from seismic tomography, Seismol. Res. Lett., 80, 63–70., 2002.

Neuberg, J., Luckett, R., Baptie, B., & Olsen, K. (2000). Models of tremor and low-frequency earthquake swarms on Montserrat. Journal of Volcanology and Geothermal Research, 101(1), 83-104.

Neuberg, J. W., Tuffen, H., Collier, L., Green, D., Powell, T., & Dingwell, D. (2006). The trigger mechanism of low-frequency earthquakes on Montserrat. Journal of Volcanology and Geothermal Research, 153(1), 37-50.

Nicolich, R., Laigle, M., Hirn, a., Cernobori, L., & Gallart, J. (2000). Crustal structure of the ionian margin of Sicily: Etna volcano in the frame of regional evolution. Tectonophysics, 329(1-4), 121–139. doi:10.1016/S0040-1951(00)00192-X.

Nicolosi, I., Caracciolo, F. A., Branca, S., Ventura, G., & Chiappini, M. (2014). Volcanic conduit migration over a basement landslide at Mount Etna (Italy). Nature Scientific Reports, 4.

Nippress, S. E. J., Rietbrock, A., & Heath, A. E. (2010). Optimized automatic pickers: application to the ANCORP data set. Geophysical Journal International, 181(2), 911-925.

Nishimura, T., N. Uchida, H. Sato, M. Ohtake, S. Tanaka, and H. Hamaguchi, (2000). Temporal changes of the crustal structure associated with the M6.1 earthquake on

September 3, 1998, and the volcanic activity of Mount Iwate, Japan, Geophysical Research Letters, 27, 269–272.

Nishimura, T., Tanaka, S., Yamawaki, T., Yamamoto, H., Sano, T., Sato, M., ... & Sato, H. (2005). Temporal changes in seismic velocity of the crust around Iwate volcano, Japan, as inferred from analyses of repeated active seismic experiment data from 1998 to 2003. Earth, planets and space, 57(6), 491-505.

Nolet, G. (1981). Linearized inversion of (teleseismic) data. In The solution of the inverse problem in geophysical interpretation (pp. 9-37). Springer US. 2,11, pp 9-37. DOI: 10.1007/978-1-4684-3962-5_2

Nugraha, A. D., Widiyantoro, S., Gunawan, A., & Suantika, G. (2013). Seismic Velocity Structures beneath the Guntur Volcano Complex, West Java, Derived from Simultaneous Tomographic Inversion and Hypocenter Relocation. Journal of Mathematical and Fundamental Sciences, 45(1), 17-28.

Ohminato, T., Chouet, B. A., Dawson, P., & Kedar, S. (1998). Waveform inversion of very long period impulsive signals associated with magmatic injection beneath Kilauea Volcano, Hawaii. Journal of Geophysical Research: Solid Earth, (1978–2012), 103(B10), 23839-23862.

Ort, M. H., Porreca, M., & Geissman, J. W. (2015). The use of palaeomagnetism and rock magnetism to understand volcanic processes: introduction. Geological Society, London, Special Publications, 396(1), 1–11. doi:10.1144/SP396.17.

Onizawa, S. Y., Oshima, H., Aoyama, H., Mori, H. Y., Maekawa, T., Suzuki, A., ... & Okada, H. (2007). P-wave velocity structure of Usu volcano: Implication of structural controls on magma movements and eruption locations. Journal of volcanology and geothermal research, 160(1), 175-194.

Padilla, G. D., Hernández, P. A., Padrón, E., Barrancos, J., Pérez, N. M., Melián, G., … and Hernández, I. (2013). Soil gas radon emissions and volcanic activity at El Hierro (Canary Islands): The 2011-2012 submarine eruption. Geochemistry, Geophysics, Geosystems, 14(2), 432-447. doi:10.1029/2012GC004375.

Padrón, E., Perez, N. M., Hernandez, P. A., Sumino, H., Melian, G. V., Barrancos, J., … and Nagao, K. (2013). Diffusive helium emissions as a precursory sign of volcanic unrest. Geology, 1–4. doi:10.1130/G34027.1.

Paige, C. C., & Saunders, M. a. (1982). LSQR: An Algorithm for Sparse Linear Equations and Sparse Least Squares. ACM Transactions on Mathematical Software, 8(1), 43–71. doi:10.1145/355984.355989.

Palano, M., Puglisi, G., & Gresta, S. (2008). Ground deformation patterns at Mt. Etna from 1993 to 2000 from joint use of InSAR and GPS techniques. Journal of Volcanology and Geothermal Research, 169(3), 99-120.

Palano, M., Rossi, M., Cannavò, F., Bruno, V., Aloisi, M., Pellegrino, D., ... & Mattia, M. (2010). Etn@ ref: a geodetic reference frame for Mt. Etna GPS networks. Annals of Geophysics.

Parotidis, M. (2003). Pore-pressure diffusion: A possible triggering mechanism for the earthquake swarms 2000 in Vogtland/NW-Bohemia, central Europe. Geophysical Research Letters, 30(20), 2075. doi:10.1029/2003GL018110.

Parotidis, M. (2004). Back front of seismicity induced after termination of borehole fluid injection. Geophysical Research Letters, 31(2), L02612. doi:10.1029/2003GL018987.

Patanè, D., & Privitera, E. (2001). Seismicity related to 1989 and 1991–93 Mt. Etna (Italy) eruptions: kinematic constraints by fault plane solution analysis. Journal of volcanology and geothermal research, 109(1), 77-98.

Patanè, D., Ferrari, F., & Ferrucci, F. (1999). First application of ASDP software: a case study at Mt. Etna volcano and in the Acri region (Southern Italy). Physics of the earth and planetary interiors, 113(1), 75-88.

Patane, D., Chiarabba, C., Cocina, O., De Gori, P., Moretti, M., & Boschi, E. (2002). Tomographic images and 3D earthquake locations of the seismic swarm preceding the 2001 Mt. Etna eruption: evidence for a dyke intrusion. Geophysical Research Letters, 29(10), 135-1.

Patanè, D., De Gori, P., Chiarabba, C., & Bonaccorso, A. (2003). Magma ascent and the pressurization of Mount Etna's volcanic system. *Science*, 299(5615), 2061-2063.

Patanè, D., Cocina, O., Falsaperla, S., Privitera, E., & Spampinato, S. (2004). Mt. Etna volcano: a seismological framework. *Mt. Etna: Volcano Laboratory* (Vol. 143). Bonaccorso, A., Calvari, S., Coltelli, M., Del Negro, C., & Falsaperla, S. (Eds.). Washington, D. C.: American Geophysical Union, 147-165.

Patanè, D., Barberi, G., Cocina, O., De Gori, P., & Chiarabba, C. (2006). Time-resolved seismic tomography detects magma intrusions at Mount Etna. *Science (New York, N.Y.), 313*(5788), 821–3. doi:10.1126/science.1127724.

Patanè, D., Di Grazia, G., Cannata, A., Montalto, P., & Boschi, E. (2008). Shallow magma pathway geometry at Mt. Etna volcano. *Geochemistry, Geophysics, Geosystems*, 9(12).

Patanè, D., M.Aliotta, A. Cannata, C. Cassisi, M. Coltelli, G. Di Grazia, P. Montalto, and L. Zuccarello (2011), Interplay between Tectonics and Mount Etna's Volcanism: Insights into the Geometry of the Plumbing System, in New Frontiers in *Tectonic Research-At the Midst of Plate Convergence*, Edited by Uri Schattner, pp. 73-104, ISBN 978-953-307-594-5.

Patanè, D., Aiuppa, A., Aloisi, M., Behncke, B., Cannata, A., Coltelli, M., ... & Salerno, G. (2013). Insights into magma and fluid transfer at Mount Etna by a multiparametric approach: a model of the events leading to the 2011 eruptive cycle. *Journal of Geophysical Research: Solid Earth*, 118(7), 3519-3539.

Paulatto, M., Minshull, T. A., Baptie, B., Dean, S., Hammond, J. O. S., Henstock, T., ... & Voight, B. (2010). Upper crustal structure of an active volcano from refraction/reflection tomography, Montserrat, Lesser Antilles. *Geophysical Journal International*, 180(2), 685-696.

Pedersen, R., Sigmundsson, F., & Einarsson, P. (2007). Controlling factors on earthquake swarms associated with magmatic intrusions; Constraints from Iceland. *Journal of volcanology and geothermal research*, 162(1), 73-80.

Pérez, N. M., Hernández, P. A., Padrón, E., Melián, G., Marrero, R., Padilla, G., ... & Nolasco, D. (2007). Precursory subsurface 222Rn and 220Rn degassing signatures of the 2004 seismic crisis at Tenerife, Canary Islands. *Pure and Applied Geophysics*, 164(12), 2431-2448.

Pérez, N. M., Padilla, G. D., Padrón, E., Hernández, P. A., Melián, G. V., Barrancos, J., ... and Hernández, Í. (2012). Precursory diffuse CO2 and H2S emission signatures of the 2011–2012 El Hierro submarine eruption, Canary Islands. *Geophysical Research Letters*, 39(16).

Pérez N. M., Somoza L., Hernández P. A., González de Vallejo L., León R., Sagita T., Biain A., González F. J., Medialdea T., Barrancos J., Ibáñez J., Sumino H., Nogami K. and Romero C. (2014). Evidence from acoustic imaging for submarine volcanic activity in 2012 off the west coast of El Hierro (Canary Islands, Spain). *Bulletin of Volcanology*, 76:882. doi: 10.1007/s00445-014-0882-y.

Pérez, N. M., Somoza, L., Hernández, P. A., de Vallejo, L. G., León, R., Sagiya, T., ... & Romero, C. (2015). Reply to comment from Blanco et al.(2015) on "Evidence from acoustic imaging for submarine volcanic activity in 2012 off the west coast of El Hierro (Canary Islands, Spain) by Pérez et al.[Bull. Volcanol.(2014), 76: 882–896]. *Bulletin of Volcanology*, 77(7):63, 1-8. doi: 10.1007/s00445-015-0948-5.

Piromallo, C., & Morelli, A. (2003). P wave tomography of the mantle under the Alpine-Mediterranean area. *Journal of Geophysical Research: Solid Earth*, 108(B2).

Polonia, A., L. Torelli, A. Artoni, M. Carlini, C. Faccenna, L. Ferranti, L. Gasperini, R. Govers, D. Klaeschen, C. Monaco, G. Neri, N. Nijholt, B. Orecchio, R. Wortel (2016). The Ionian and Alfeo-Etna fault zones: New segments of an evolving plate boundary in the central Mediterranean Sea?, *Tectonophysics*, 675, 69–90, doi:10.1016/j.tecto.2016.03.016.

Powell, T. W., & Neuberg, J. (2003). Time dependent features in tremor spectra. *Journal of Volcanology and Geothermal Research*, 128(1), 177-185.

Presti, D., Orecchio, B., Falcone, G., and Neri, G. (2008). Linear versus non-linear earthquake location and seismogenic fault detection in the southern Tyrrhenian Sea, Italy. *Geophysical Journal International*, 172(2), 607–618. doi:10.1111/j.1365-246X.2007.03642.x.

Prudencio, J., Ibáñez, J. M., García-Yeguas, A., Del Pezzo, E., & Posadas, A. M. (2013a). Spatial distribution of intrinsic and scattering seismic attenuation in active volcanic

islands–II: Deception Island images. *Geophysical Journal International*, 195(3), 1957-1969.

Prudencio, J., Del Pezzo, E., García-Yeguas, A., & Ibáñez, J. M. (2013b). Spatial distribution of intrinsic and scattering seismic attenuation in active volcanic islands–I: model and the case of Tenerife Island. *Geophysical Journal International*, ggt361.

Prudencio, J., De Siena, L., Ibáñez, J. M., Del Pezzo, E., García-Yeguas, A., & Díaz-Moreno, A. (2015a). The 3D Attenuation Structure of Deception Island (Antarctica). *Surveys in Geophysics*, 36(3), 371-390.

Prudencio, J., Ibáñez, J. M., Del Pezzo, E., Martí, J., García-Yeguas, A., & De Siena, L. (2015b). 3D Attenuation Tomography of the Volcanic Island of Tenerife (Canary Islands). *Surveys in Geophysics*, 36(5), 693-716.

Prudencio, J., Del Pezzo, E., Ibáñez, J. M., Giampiccolo, E., & Patané, D. (2015c). Two-dimensional seismic attenuation images of Stromboli Island using active data. *Geophysical Research Letters*, 42(6), 1717-1724.

Puglisi, G., & Bonforte, A. (2004). Dynamics of Mount Etna Volcano inferred from static and kinematic GPS measurements. *Journal of Geophysical Research: Solid Earth*, (1978–2012), 109(B11).

Puglisi, G., Briole, P., & Bonforte, A. (2004). Twelve years of ground deformation studies on Mt. Etna volcano based on GPS surveys *Mt. Etna: Volcano Laboratory* (Vol. 143). Bonaccorso, A., Calvari, S., Coltelli, M., Del Negro, C., & Falsaperla, S. (Eds.). Washington, D. C.: American Geophysical Union, 321-341.

Puglisi, G., Bonforte, A., Ferretti, A., Guglielmino, F., Palano, M., & Prati, C. (2008). Dynamics of Mount Etna before, during, and after the July–August 2001 eruption inferred from GPS and differential synthetic aperture radar interferometry data. *Journal of Geophysical Research: Solid Earth*, (1978–2012), 113(B6).

Rawlinson, N., & Urvoy, M. (2006). Simultaneous inversion of active and passive source datasets for 3-D seismic structure with application to Tasmania. Geophysical Research Letters, 33(24).

Reading, A. M., Mao, W., & Gubbins, D. (2001). Polarization filtering for automatic picking of seismic data and improved converted phase detection. *Geophysical Journal International*, 147(1), 227-234.

Riedel, C., Petersen, T., Theilen, F., & Neben, S. (2003). High b-values in the leaky segment of the Tjörnes Fracture Zone north of Iceland: are they evidence for shallow magmatic heat sources?. *Journal of volcanology and geothermal research*, 128(1), 15-29.

Rittmann, A., & Sato, M. (1973). Structure and Evolution of Mount Etna [and Discussion]. *Philosophical Transactions of the Royal Society of London A: Mathematical, Physical and Engineering Sciences*, 274(1238), 5-16.

Roman, D. C., Cashman, K. V., Gardner, C. A., Wallace, P. J., & Donovan, J. J. (2006). Storage and interaction of compositionally heterogeneous magmas from the 1986 eruption of Augustine Volcano, Alaska. *Bulletin of Volcanology*, 68(3), 240-254.

Ross, Z. E., & Ben-Zion, Y. (2014). Automatic picking of direct P, S seismic phases and fault zone head waves. *Geophysical Journal International*, 199(1), 368-381.

Rothert, E., and Shapiro S. A. (2003), Microseismic monitoring of borehole fluid injections: data modelling and inversion for hydraulic properties of rocks, *Geophysics*, 68(2), 685– 689.

Roure, F., D.G. Howell, C. Muller, and I. Moretti (1990).Late Cenozoic subduction complex of Sicily, *Journ. Struct. Geol.*, 12, 259-266.

Rust, D., & Neri, M. (1996). The boundaries of large-scale collapse on the flanks of Mount Etna, Sicily. *Geological Society*, London, Special Publications, 110(1), 193-208.

Ryan, W.B.F., S.M. Carbotte, J.O. Coplan, S. O'Hara, A. Melkonian, R. Arko, R.A. Weissel, V. Ferrini, A. Goodwillie, F. Nitsche, J. Bonczkowski, and R. Zemsky (2009), Global Multi-Resolution Topography synthesis. *Geochemistry, Geophysics, Geosystems*, 10, Q03014, doi:10.1029/2008GC002332.

Rydelek, P. A., & Sacks, I. S. (1989). Testing the completeness of earthquake catalogues and the hypothesis of self-similarity. *Nature*, 337(6204), 251-253.

Rymer, H., & Brown, G. C. (1986). Gravity fields and the interpretation of volcanic structures: geological discrimination and temporal evolution. *Journal of volcanology and geothermal research*, 27(3), 229-254.

Saccorotti, G., Bianco, F., Castellano, M., & Del Pezzo, E. (2001). The July–August 2000 seismic swarms at Campi Flegrei volcanic complex, Italy. *Geophysical Research Letters*, 28, L13053, 2525-2528. doi: 10.1029/2001GL013053.

Saccorotti, G, Zuccarello, L., Del Pezzo, E., Ibáñez, J.M, and Gresta, S. (2004). Quantitative analysis of the tremor wavefield at Etna volcano, Italy. *Journ. Vol. Geo. Res.* , 136, 223-245.

Saccorotti, G., Lokmer, I., Bean, C. J., Di Grazia, G., & Patanè, D. (2007). Analysis of sustained long-period activity at Etna Volcano, Italy. *Journal of volcanology and geothermal research*, 160(3), 340-354.

Saragiotis, C. D., Hadjileontiadis, L. J., & Panas, S. M. (2002). PAI-S/K: a robust automatic seismic P phase arrival identification scheme. *Geoscience and Remote Sensing, IEEE Transactions*, 40(6), 1395-1404.

Scarfì L., Barberi G., Musumeci C., Patanè D. (2016). Seismotectonics of northeastern Sicily and southern Calabria (Italy): New constraints on the tectonic structures featuring in a crucial sector for the central Mediterranean geodynamics, *Tectonics*, 35, 812–832, doi:10.1002/2015TC004022.

Scollo, S., Del Carlo, P., & Coltelli, M. (2007). Tephra fallout of 2001 Etna flank eruption: analysis of the deposit and plume dispersion. *Journal of Volcanology and Geothermal Research*, 160(1), 147-164.

Schiano, P., Clocchiatti, R., Ottolini, L., & Busà, T. (2001). Transition of Mount Etna lavas from a mantle-plume to an island-arc magmatic source. *Nature*, 412(6850), 900-904.

Scholz, C. H. (1968). The frequency-magnitude relation of microfracturing in rock and its relation to earthquakes. *Bulletin of the Seismological Society of America*, 58(1), 399-415.

Shahrukh, M., Soupios, P., Papadopoulos, N., & Sarris, A. (2012). Geophysical investigations at the Istron archaeological site, eastern Crete, Greece using seismic

refraction and electrical resistivity tomography. Journal of Geophysics and Engineering, 9(6), 749.

Shalev, E., Kenedi, C. L., Malin, P., Voight, V., Miller, V., Hidayat, D., … Mattioli, G. (2010). Three-dimensional seismic velocity tomography of Montserrat from the SEA-CALIPSO offshore/onshore experiment. *Geophysical Research Letters*, *37*(19). doi:10.1029/2010GL042498.

Shapiro, S. A., & Dinske, C. (2009). Scaling of seismicity induced by nonlinear fluid-rock interaction. *Journal of Geophysical Research*, *114*(B9), B09307. doi:10.1029/2008JB006145.

Shapiro, S. A., Rothert, E., Rath, V., & Rindschwentner, J. (2002). Characterization of fluid transport properties of reservoirs using induced microseismicity. *Geophysics*, 67(1), 212-220.

Shapiro, S. A., Patzig, R., Rothert, E., & Rindschwentner, J. (2003). Triggering of Seismicity by Pore-pressure Perturbations: Permeability-related Signatures of the Phenomenon. *Pure and Applied Geophysics*, *160*(5), 1051–1066. doi:10.1007/PL00012560.

Shapiro, S. A., Rentsch, S., & Rothert, E. (2005). Characterization of hydraulic properties of rocks using probability of fluid-induced microearthquakes. *Geophysics*, 70(2), F27-F33.

Shapiro, S. A., Dinske, C., Langenbruch, C., & Wenzel, F. (2010). Seismogenic index and magnitude probability of earthquakes induced during reservoir fluid stimulations. *The Leading Edge*, 29(3), 304-309.

Sharp, A. D. L., Davis, P. M., & Gray, F. (1980). A low velocity zone beneath Mount Etna and magma storage. *Nature*, *287*, 587–591.

Shinohara, H., Aiuppa, A., Giudice, G., Gurrieri, S., & Liuzzo, M. (2008). Variation of H2O/CO2 and CO2/SO2 ratios of volcanic gases discharged by continuous degassing of Mount Etna volcano, Italy. *Journal of Geophysical Research: Solid Earth*, 113(B9).

Solaro, G., Acocella, V., Pepe, S., Ruch, J., Neri, M., & Sansosti, E. (2010). Anatomy of an unstable volcano from InSAR: Multiple processes affecting flank instability at

Mt. Etna, 1994–2008. *Journal of Geophysical Research: Solid Earth*, (1978–2012), 115(B10).

Spakman, W., and R. Wortel (2004). A tomographic view on western Mediterranean geodynamics, *in The TRANSMED Atlas: The Mediterranean Region From Crust to Mantle, pp. 31–52, Springer*, Berlin.

Spilliaert, N., Allard, P., Métrich, N., & Sobolev, a. V. (2006). Melt inclusion record of the conditions of ascent, degassing, and extrusion of volatile-rich alkali basalt during the powerful 2002 flank eruption of Mount Etna (Italy). *Journal of Geophysical Research: Solid Earth*, *111*(4). doi:10.1029/2005JB003934.

Sturkell, E., Einarsson, P., Sigmundsson, F., Geirsson, H., Olafsson, H., Pedersen, R., ... & Stefánsson, R. (2006). Volcano geodesy and magma dynamics in Iceland. *Journal of Volcanology and Geothermal Research*, 150(1), 14-34.

Takanami, T., & Kitagawa, G. (1988). A new efficient procedure for the estimation of onset times of seismic waves. *Journal of Physics of the Earth*, 36(6), 267-290.

Talwani, P. (2000). Seismogenic properties of the crust inferred from recent studies of reservoir-induced seismicity—Application to Koyna. *Current Science*, 79(9), 1327-1333.

Tanaka, S., Hamaguchi, H., Nishimura, T., Yamawaki, T., Ueki, S., Nakamichi, H., ... & Aizawa, K. (2002). Three-dimensional P-wave velocity structure of Iwate volcano, Japan from active seismic survey. *Geophysical research letters*, 29(10), 59-1.

Tanguy, J. C. (1978). Tholeiitic basalt magmatism of Mount Etna and its relations with the alkaline series. *Contributions to Mineralogy and Petrology*, 66(1), 51-67.

Tanguy, J. C. (1980). L'Etna: étude petrologique et paléomagnétique: Implications volcanologiques. *These doc d'Etat*, University of Paris, 618 pp.

Tanguy, J. C., Condomines, M., & Kieffer, G. (1997). Evolution of the Mount Etna magma: constraints on the present feeding system and eruptive mechanism. *Journal of Volcanology and Geothermal research*, 75(3), 221-250.

Telesca, L., Lovallo, M., Molist, J. M., Moreno, C. L., & Meléndez, R. A. (2015). Multifractal investigation of continuous seismic signal recorded at El Hierro volcano

(Canary Islands) during the 2011–2012 pre-and eruptive phases. *Tectonophysics*, 642, 71-77.

Thorwart, M., Dzierma, Y., Lieser, K., Buhs, H., & Rabbel, W. (2015). Shear-wave velocity structure of the Chilean subduction zone (39–40° S) based on Rayleigh wave dispersion: evidence of fluid release and melts in the mantle beneath the Villarrica volcano. *Geological Society, London, Special Publications*, 410(1), 59-70.

Thurber C.H. (1983). Earthquake locations and three-dimensional crustal structure in the Coyote Lake area, Central California. Journal of Geophysical Research. 88, pp. 8226–8236.

Thurber, C. H. (1984). Seismic detection of the summit magma complex of Kilauea volcano, Hawaii. *Science*, 223(4632), 165-167.

Tibaldi, A., & Groppelli, G. (2002). Volcano-tectonic activity along structures of the unstable NE flank of Mt. Etna (Italy) and their possible origin. *Journal of Volcanology and Geothermal Research*, 115(3), 277-302.

Tilling, R. I. (2011). Volcanic hazards and early warning. In Extreme Environmental Events (pp. 1135-1145). *Springer New York*. p. 1135-1145.

Toda, S., Stein, R. S., & Sagiya, T. (2002). Evidence from the AD 2000 Izu islands earthquake swarm that stressing rate governs seismicity. *Nature*, 419(6902), 58-61.

Tomatsu, T., Kumagai, H., & Dawson, P. B. (2001). Tomographic inversion of P-wave velocity and Q structures beneath the Kirishima volcanic complex, southern Japan, based on finite difference calculations of complex traveltimes. *Geophysical Journal International*, 146(3), 781-794.

Tonarini, S., Armienti, P., D'Orazio, M., & Innocenti, F. (2001). Subduction-like fluids in the genesis of Mt. Etna magmas: evidence from boron isotopes and fluid mobile elements. *Earth and Planetary Science Letters*, 192(4), 471-483.

Toomey, D. R., & Foulger, G. R. (1989). Tomographic inversion of local earthquake data from the Hengill-Grensdalur central volcano complex, Iceland. *Journal of Geophysical Research: Solid Earth*, 94(B12), 17497-17510.

Uhira, K., & Takeo, M. (1994). The source of explosive eruptions of Sakurajima volcano, Japan. *Journal of Geophysical Research: Solid Earth*, (1978–2012), 99(B9), 17775-17789.

Um, J., & Thurber, C. (1987). A fast algorithm for two point seismic ray tracing. *Bulletin of the Seismological Society of America*, *77*(June), 972–986.

Vanorio, T., Virieux, J., Capuano, P., & Russo, G. (2005). Three-dimensional seismic tomography from P wave and S wave microearthquake travel times and rock physics characterization of the Campi Flegrei Caldera. *Journal of Geophysical Research: Solid Earth*, (1978–2012), 110(B3).

Vargas, C. A., & Torres, R. (2015). Three-dimensional velocity structure of the Galeras volcano (Colombia) from passive local earthquake tomography. *Journal of Volcanology and Geothermal Research*, 301, 148-158.

Ventura, G., G. Vilardo, G. Milano, and N.A. Pino (1999), Relationship among crustal structure, volcanism and strike-slip tectonics in the Lipari–Vulcano volcanic complex (Aeolian Islands, Southern Tyrrhenian Sea, Italy), *Phys. Earth Planet. Int.*, 116, 31–52.

Vergniolle, S., & Brandeis, G. (1994). Origin of the sound generated by Strombolian explosions. *Geophysical Research Letters*, 21(18), 1959-1962.

Vergniolle, S., & Brandeis, G. (1996). Strombolian explosions: 1. A large bubble breaking at the surface of a lava column as a source of sound. *Journal of Geophysical Research: Solid Earth*, (1978–2012), 101(B9), 20433-20447.

Vergniolle, S., Boichu, M., & Caplan-Auerbach, J. (2004). Acoustic measurements of the 1999 basaltic eruption of Shishaldin volcano, Alaska: 1. Origin of Strombolian activity. *Journal of Volcanology and Geothermal Research*, 137(1), 109-134.

Villaseñor, A., Benz, H. M., Filippi, L., Luca, G. De, Scarpa, R., Patang, G., & Vinciguerra, S. (1998). Three-dimensional of Mt. Etna, Italy P-wave velocity structure. *Geophysical Research Letters*, *25*(11), 1975–1978.

Voight, B., Sparks, R. S. J., Shalev, E., Minshull, T., Paulatto, M., Annen, C., ... & Zamora, W. (2014). The SEA-CALIPSO volcano imaging experiment at Montserrat:

plans, campaigns at sea and on land, scientific results, and lessons learned. *Geological Society, London, Memoirs*, 39(1), 253-289.

Wagner, D., Koulakov, I., Rabbel, W., Luehr, B. G., Wittwer, A., Kopp, H., ... & Asch, G. (2007). Joint inversion of active and passive seismic data in Central Java. Geophysical Journal International, 170(2), 923-932.

Waite, G. P. (2002). Seismic evidence for fluid migration accompanying subsidence of the Yellowstone caldera. *Journal of Geophysical Research*, *107*(B9), 2177. doi:10.1029/2001JB000586.

Waldhauser, F. (2001). hypoDD - A Program to Compute Double-Difference Hypocenter Locations by. *US Geological Survey*. Open File Rep., 1–25.

Waldhauser, F., & Ellsworth, W. L. (2000). A double-difference earthquake location algorithm: Method and application to the northern Hayward fault, California. *Bulletin of the Seismological Society of America*, 90(6), 1353-1368.

Walter, T. R., Wang, R., Zimmer, M., Grosser, H., Lühr, B., & Ratdomopurbo, A. (2007). Volcanic activity influenced by tectonic earthquakes: static and dynamic stress triggering at Mt. Merapi. *Geophysical Research Letters*, 34(5).

Wassermann, J. (2002). Volcano seismology. *IASPEI New Manual of Seismological Observatory Practice*, 1(13), 662-703.

Wegler, U., Lühr, B. G., & Ratdomopurbo, A. (1999). A repeatable seismic source for tomography at volcanoes. *Annals of Geophysics*, 42(3).

Wegler, U., & Lühr, B.-G. (2001). Scattering behaviour at Merapi volcano (Java) revealed from an active seismic experiment. *Geophysical Journal International*, *145*(3), 579–592. doi:10.1046/j.1365-246x.2001.01390.x.

Westaway, R. (1993). Quaternary uplift of southern Italy. *Journal of Geophysical Research: Solid Earth*, 98(B12), 21741-21772.

Wicks, C., de La Llera, J. C., Lara, L. E., & Lowenstern, J. (2011). The role of dyking and fault control in the rapid onset of eruption at Chaitén volcano, Chile. *Nature*, 478(7369), 374-377.

Wiemer, S., & Wyss, M. (2000). Minimum magnitude of completeness in earthquake catalogs: examples from Alaska, the western United States, and Japan. *Bulletin of the Seismological Society of America*, 90(4), 859-869.

Wiemer, S., & Wyss, M. (2003). Reply to "Comment onMinimum Magnitude of Completeness in Earthquake Catalogs: Examples from Alaska, the Western United States, and Japan,'by Stefan Wiemer and Max Wyss," by Paul A. Rydelek and IS Sacks. *Bulletin of the Seismological Society of America*, 93(4), 1868-1871.

Woessner, J., & Wiemer, S. (2005). Assessing the quality of earthquake catalogues: Estimating the magnitude of completeness and its uncertainty. *Bulletin of the Seismological Society of America*, 95(2), 684-698.

Wyss, M. (1973). Towards a physical understanding of the earthquake frequency distribution. *Geophysical Journal International*, 31(4), 341-359.

Wyss M., Hasegawa A., Wiemer S., Umino N., 1999. Quantitative mapping of precursory seismic quiescence before the 1989, M7.1 off-Sanriku earthquake, Japan, *Ann. Geofis.*, 42, 851–869.

Yamamoto, M., & Sato, H. (2010). Multiple scattering and mode conversion revealed by an active seismic experiment at Asama volcano, Japan. *Journal of Geophysical Research: Solid Earth*, (1978–2012), 115(B7).

Yamawaki, T., Tanaka, S., Ueki, S., Hamaguchi, H., Nakamichi, H., Nishimura, T., ... & Yamaguchi, S. (2004). Three-dimensional P-wave velocity structure of Bandai volcano in northeastern Japan inferred from active seismic survey. *Journal of volcanology and geothermal research*, 138(3), 267-282.

Zabelina, I., Ruppert, N. A., & Freymueller, J. T. (2014). Velocity structure of the Saint Elias, Alaska, Region from local earthquake tomography. *Bulletin of the Seismological Society of America*, 104(5), 2597-2603

Zandomeneghi, D., Almendros, J., Ibáñez, J. M., & Saccorotti, G. (2008). Seismic tomography of Central Sao Miguel, Azores. *Physics of the Earth and Planetary Interiors*, 167(1), 8-18.

Zandomeneghi, D., Barclay, A., Almendros, J., Ibañez Godoy, J. M., Wilcock, W. S., & Ben-Zvi, T. (2009). Crustal structure of Deception Island volcano from P wave

seismic tomography: Tectonic and volcanic implications. *Journal of Geophysical Research: Solid Earth*, (1978–2012), 114(B6).

Zandomeneghi, D., Kyle, P., Miller, P., Passcal, I., Snelson, C., & Aster, R. (2010). Seismic Tomography of Erebus Volcano, Antarctica. *Eos, Transactions American Geophysical Union*, 91(6), 53-55.

Zandomeneghi, D., Aster, R., Kyle, P., Barclay, A., Chaput, J., & Knox, H. (2013). Internal structure of Erebus volcano, Antarctica imaged by high-resolution active-source seismic tomography and coda interferometry. *Journal of Geophysical Research: Solid Earth*, 118(3), 1067-1078.

Zelt, C. A., & Barton, P. J. (1998). Three-dimensional seismic refraction tomography: A comparison of two methods applied to data from the Faeroe Basin. Journal of Geophysical Research: Solid Earth (1978–2012), 103(B4), 7187-7210.

Zhang, H., & Thurber, C. H. (2003). Double-difference tomography: The method and its application to the Hayward fault, California. Bulletin of the Seismological Society of America, 93(5), 1875-1889.

Zhang, H., Thurber, C., & Rowe, C. (2003). Automatic P-wave arrival detection and picking with multiscale wavelet analysis for single-component recordings. *Bulletin of the Seismological Society of America*, 93(5), 1904-1912.

Zhao, D., & Hasegawa, A. (1993). P wave tomographic imaging of the crust and upper mantle beneath the Japan Islands. *Journal of Geophysical Research: Solid Earth*, 98(B3), 4333-4353.

Zhao, D., Mishra, O. P., & Sanda, R. (2002). Influence of fluids and magma on earthquakes: seismological evidence. *Physics of the Earth and Planetary Interiors*, *132*(4), 249–267. doi:10.1016/S0031-9201(02)00082-1.

Zieger, T., Sens-Schönfelder, C., Ritter, J., Luehr, B.-G. and Dahm, T., (2016). P-wave Scattering and the Distribution of Heterogeneity around Etna Volcano. Special Volume: TOMOETNA. Eds. Morales J., and Puglisi G. *Annals of Geophysics*. doi:10.4401/ag-7085.

Zobin, V. M. (2011). Introduction to volcanic seismology. *Elsevier*.

Zollo, A. E. A., Gasparini, P., Virieux, J., & Le Meur, H. (1996). Seismic evidence for a low-velocity zone in the upper crust beneath Mount Vesuvius. *Science*, 274(5287), 592.

Zollo, A., Gasparini, P., Virieux, J., Biella, G., Boschi, E., Capuano, P., ... & Iannaccone, G. (1998). An image of Mt. Vesuvius obtained by 2D seismic tomography. *Journal of Volcanology and Geothermal Research*, 82(1), 161-173.

Zollo, A., Marzocchi, W., Capuano, P., Lomax, A., & Iannaccone, G. (2002). Space and time behavior of seismic activity at Mt. Vesuvius volcano, southern Italy. *Bulletin of the Seismological Society of America*, 92(2), 625-640.

Zollo, A., Judenherc, S., Auger, E., D'Auria, L., Virieux, J., Capuano, P., ... & Musacchio, G. (2003). Evidence for the buried rim of Campi Flegrei caldera from 3-d active seismic imaging. *Geophysical Research Letters*, 30(19).

Zschau, J., Sukhyar, R., Purbawinata, M.A., Luehr, B. &Westerhaus, M., 1998. Project MERAPI—interdisciplinary research at a high-risk volcano, in *Decade-Volcanoes under Investigation*, Vol. Sonderband III/1998 of DGG-Mitteilungen, pp. 3–8, eds Zschau, J. &Westerhaus,M., Deutsche Geophysikalische Gesellschaft.

Zuccarello, L., Burton, M. R., Saccorotti, G., Bean, C. J., & Patanè, D. (2013). The coupling between very long period seismic events, volcanic tremor, and degassing rates at Mount Etna volcano. *Journal of Geophysical Research: Solid Earth*, 118(9), 4910-4921.

Zuccarello, L. (2015). Volcanic activity of Mt. Etna during the quiescent October 2005-January 2006 period, inferred through very long period seismic events, volcanic tremor, degassing rates and gravity. *PhD Thesis at UCD School of Geological Sciences, University College Dublin*.

Zuccarello, L., Paratore, M., La Rocca, M., Ferrari, F., Messina, A., Branca, S., Contrafatto, D., Galluzzo, D., Rapisarda, S., García, L., (2016). Shallow velocity model in the area of Pozzo Pitarrone, Mt. Etna, from single station, array methods and borehole data. Special Volume: TOMOETNA. Eds. Morales J., and Puglisi G. *Annals of Geophysics*. doi:10.4401/ag-7086.

A. Appendix 1

A.1 .Funding and associated research projects

The TOMO-ETNA experiment was evolved between 2011 and 2014, and mainly integrates the European Union project "MEDiterranean SUpersite Volcanoes (MED-SUV)" efforts with the resources of the EU project "EUROFLEETS2". However other funding agencies from Italy, Spain, and Germany supported this experiment. In addition, the Italian Navy and the "Dipartimento di Protezione Civile della Regione Siciliana" actively participated in the experiment. This such a long time interval includes several negotiations with different research and civil agencies and the application of various additional research project and parallel aids, including economic, equipment and human additional support. Both main research projects (MED-SUV and EUROFLEETS2) will be specifically described in next sections. The number of associated projects and other negotiations is large, and a full description of then is reported in Appendix A3. Next we will mention some of these negotiations processes and support obtained from them.

A.2. MED-SUV Project the core project of the TOMO-ETNA experiment

The TOMO-ETNA experiment was conceived, planned and carried out in the framework of the EC-FP7 MEDiterranean Supersite Volcanoes (MED-SUV) project, which overarching objective was to apply the Supersite rationale to the Italian active volcanoes. The Supersite initiative born on 2007 at the conclusion of the 3rd International Geohazards workshop of GEO held in November 2007 in Frascati, Italy, with the aims "to stimulate an international and intergovernmental effort to monitor and study selected reference sites by establishing open access to relevant datasets according to Group Of Earth Observation (GEO) principles to foster the collaboration between all various partners and end-users" (Frascati Declaration). Selected sites (Supersites) are areas prone to earthquake, volcano or other hazards and for which significant Earth Observation and ground-based data sets are available. Thus, although not explicitly declared, Supersite initiative is intrinsically multiplatform being based on the use of data provided by research infrastructures belonging to Space and Earth domains. On 2011 the European Commission promoted the application of the Supersite approach in Europe though a specific call; MED-SUV was one of the projects which positively responded to this call, focused their activities on Mt. Etna and Campi Flegrei / Vesuvius volcanoes. Since 2013 these two areas have been appointed as Permanent Supersites from the Scientific Advisory

Committee (SAC) of GEO Geohazards Supersites and Natural Laboratories (GSNL), also considering the existence of MED-SUV project. Indeed, more than 3 million of people are exposed to potential volcanic hazards in a large region in the Mediterranean Sea, where these two volcanic areas are located. The wide range of styles and intensities of volcanic phenomena observed on these volcanoes, which can be assumed as archetypes of 'closed' and 'open conduit' volcano, together with the long-term multidisciplinary data sets give an exceptional opportunity to improve the understanding of a very wide spectrum of geohazards, as well as implementing a large variety of innovative models for investigating the volcanic processes.

The improvement of the knowledge of the Supersites and the sharing of the relevant data sets are two key principles of the Frascati Declaration, which are the base for the enhancement of the hazard assessment and the risk reduction. MED-SUV adopted these two principles in the work plan definition, by attempting to cope with the main gaps in the knowledge in both areas and to improve the sharing of the data relevant to the two Supersites (either provided by the ground-based monitoring institutions, Space Agencies or collected during the project). The project proposes the development and implementation of a state-of-the-art infrastructure for the volcanic risk management life-cycle, from the observation to people preparedness. Thus, MED-SUV project offers the opportunity to operate in natural laboratories by using cutting-edges technologies and carrying out in-field and laboratories experiments.

Indisputably Mt. Etna and Campi Flegrei / Vesuvius are among the most well-known volcanoes worldwide. However, one of the most relevant gaps in the knowledge of Mt. Etna consisted in the relatively poor information concerning the deep structure of this volcano. Indeed, this inadequacy in the knowledge of the crust limits the capability of the models to investigate the dynamic of this volcano, despite through the last decades the computational capacity improved dramatically and many sophisticated numerical modelling approaches have been implemented.

A.3. EUROFLEETS2. TOMO-ETNA experiment and marine implications

EUROFLEETS2 "New operational steps towards an alliance of European research fleets" (01-03-2013 to 28-02-2017, Grant Agreement n° 312762) is a project funded in the frame of the 7th Framework Programme of the European Commission. The project is the extension and expansion of the first initiative, EUROFLEETS "Towards an Alliance of

European Research Fleets" (01-09-2009 to 31-08-2013, Grant Agreement n° 228344). Both projects were granted under the funding schemes of Research Infrastructures and respectively a combination of Collaborative Project and Coordination and Support Actions for Integrating Activities.

Research Vessels (RVs) and their embarked equipment are crucial infrastructures necessary for marine sciences. They provide sea access to the whole community of researchers, enable all kinds of observations, in-situ measurements, sampling and mapping, and are necessary to maintain deep sea observatories. Over the years, the missions assigned to RVs became more complex and technically sophisticated. This encourages national marine institutions to increase their coordination and collaboration, and to share their facilities in order to optimize the cost in operating their marine infrastructures and to efficiently meet the scientific ever increasing demands.

By bringing together European research fleet owners and operators, EUROFLEETS2 (http://www.eurofleets.eu) contributes to enhance operational coordination between RVs and associated equipment. It has the aim of developing a new pan-European distributed infrastructure with common strategic vision and coordinated access to RVs and associated equipment, in order to facilitate the access to these rare floating laboratories and maximize their contribution to the scientific knowledge

Through operational initiatives such as regional virtual fleets or the development of common tools or methodologies, this project promotes more inter-operable and cost-effective European research fleets for sustainable management of regional seas and oceans. EUROFLEETS2 aims also to develop the impact of research infrastructures on innovation by establishing links with industry and fostering the involvement of the industrial sector on specific activities.

EUROFLEETS2 involves multi-disciplinary expertise from thirty-one marine institutes, universities, foundations and small and medium enterprises (SMEs) from twenty member states of the European Union, four associated countries, and one Overseas Country and Territory. The Project has ambitious objectives and the 31-member consortium works together in three structured and complementary research activities:

i) the TransNational Access (TNA), as core activity of the project, to coordinate access to European RVs and associated equipment for all European scientists and their partners;

ii) the Joint Research Activity (JRA) for joint development of common equipment or software;

iii) the Networking Activity (NA) with a range of actions for an enhanced coordination of European research fleets including the polar components. This activity includes also the opening of TNA calls and the evaluation of submitted proposals by a European panel of experts. Specific tasks are undertaken as well for the training of young marine scientists.

Within the innovative EUROFLEETS2 TNA activity, three different types of calls were opened: i) three calls offering access to 22 European RVs operating in targeted maritime regions (call 1 for polar and sub-polar regions, call 2 for North Atlantic and Nord Sea, call 3 for Mediterranean Sea, Black Sea and Red Sea), ii) one "Embarked Equipment" call aiming to deploy pieces of equipment from their non-usual RVs or underwater vehicles, so contributing to higher inter-operability within European research fleets, and iii) the so called "Super-Integration" call in which the MEDSUV.ISES proposal was selected for funding.

With the "Super-Integration" call, EUROFLEETS2 wanted to further develop its integrating actions by proposing a multi-platform experiment as an innovative way of integrating European and international infrastructures. Such multi-platform experiments are very rare as they require a high level of anticipation and coordination and the objective was to allow the realization of a single multinational, large-scale scientific project able to attract international scientific leaders and non-traditional end users on board European RVs.

To achieve this, an expression of interest was opened very early in the project to allow potential candidates to check if their proposals were fitting with the "Super-Integration philosophy", and in that case, to check that EUROFLEETS2 could cover their needs. A dedicated unique call for proposals was launched afterwards, but very early in the project's life, to seek a scientific project which needed to mobilize a combination of EUROFLEETS2 TNA vessels, nationally funded RVs, together with other appropriate scientific tools like research planes or shore infrastructures proposed with their own EC or national funding. This call sought to identify a truly cross cutting proposal, able to prove its scientific excellence and to mobilize private and public funding structures on top of EUROFLEETS2 EC funding. High impact

proposals with a significant cross cutting theme could seek to develop a multi-annual programme focused on one European location or develop a proposal which requires the deployment of several vessels and platforms with their associated equipment to a number of locations with a common theme.

The MEDSUV.ISES project was successfully selected for funding among a total of four scientific proposals submitted within the "Super-Integration" call. The support brought by EUROFLEETS2 to the TOMO-ETNA experiment of the MEDSUV project represented a total of 25 days of ship-time in 2014 on board the Spanish RV "Sarmiento de Gamboa" and the Greek RV "Aegaeo".

A.4. Additional research projects and parallel negotiations

In this section we detail additional research projects that have supported the TOMO-ETNA experiment and other parallel negotiations focused in the acquisition of human and material resources.

a. Spanish COCSABO project. In order to use the Spanish Oceanographic vessel "Sarmiento de Gamboa" the UGR team leaders by Jesús Ibáñez applied for a project named MED-SUV (COC-DI-2011-08) in November of 2011. The proposal was applied to "La Comisión de Coordinación y Seguimiento de las Actividades de los Buques Oceanográficos (COCSABO)" belonging to "La Secretaría General de Ciencia y Tecnología del Ministerio de Economía y Competitividad" of the Spanish government. The proposal was approved in January 2014 and allowed to program 25 days of activities of the vessel "Sarmiento de Gamboa – CSIC" for the summer of 2014. It is important to note that the negotiations of this applications started before that the core project MED-SUV were approved and granted.

b. European project EUROFLEETS2. In order to complement the use of the Spanish vessel "Sarmiento de Gamboa" and to include other additional oceanographic vessels, the consortium INGV-Catania and UGR leaders by G. Puglisi, D. Patané and J. Ibáñez applied for the project "MED-SUV. Integration of on-shore and off-shore passive and active Seismic Experiments in South Italy (MED-SUV.ISES)" within the EUROFLEETS2 "Super-Integration" call opened in June of 2013 (a more detailed description of EUROFLEETS2 is provided in the next section). Successfully evaluated by

a European panel of experts, the scientific proposal was selected for funding in April 2014, permitting to complement the activities programmed by the "Sarmiento de Gamboa" and to include new geophysical activities using the Greek Research Vessel "Aegaeo" in November of 2014. Once the use of the oceanographic vessels was secured by these two projects, the final dates of the experiment were fixed definitively to start at the end of June of 2014.

c. German project TOMO-ETNA (Seismic TOMOgraphy of ETNA volcano and Eolian Islands, Italy, using active and passive seismic data). In order to obtain and homogeneous set of portable seismic stations, a proposal was submitted to the German Geophysical Instrument Pool Potsdam (GIPP). This pool belongs to the Helmholtz-Centre Potsdam - GFZ German Research Centre of Germany. In June 2013 the consortium comprising the GFZ-Postdam, INGV-Catania and the UGR prepared a proposal for the use of instruments that was submitted in August 2013. The leaders of this project were B. Luehr and T. Dahm from GFZ, G. Puglisi and D. Patané from INGV-Catania and J.M. Ibáñez from UGR. In February 2014 we obtained the final confirmation of the availability of 100 seismic stations, including 80 short period seismic stations and 20 BB, to be used in the period June-November 2014.

d. Negotiation with Dipartimento Regionale della Protezione Civile, Regione Siciliana for the use of their different resources in the TOMO-ETNA experiment. The INGV-Catania leader D. Patané prepared a preliminary agreement with the Department that was signed. In this first document additional grants for the expected onland chemical explosions were included. The working period of this process was November 2013 to June 2014. Due to economical restrictions the final support for the performing of chemical explosions on land was eliminated in July 2014, just when the experiment started, and these activities were cancelled in the last minute.

e. Agreement with the INGV_Centro Nazionale Terremoti "Osservatorio di Gibilmanna" to use Italian OBSs in the experiment. INGV-Catania leader D. Patané requested to this institution the use of at least 12-14 OBSs. This agreement was closed and they prepared the instrument to be deployed in the TOMO-ETNA experiment, three of them remained

deployed for around 6 months and were recovered by the Greek vessel "Aegaeo". The working period of this process was November 2013 to June 2014.

f. Negotiation with the Unidad de Tecnología Marina-CSIC in Barcelona (Spain) to use Spanish OBSs in the experiment. The UGR leader J. Ibáñez and INGV-Catania leader D. Patané requested to this institution the use of at least 12-15 OBSs. This agreement was confirmed and the CSIC team prepared the instruments that were deployed in the TOMO-ETNA experiment. The working period of this process was November 2013 to June 2014.

g. Negotiation with the Italian Navy (Italian Navy General Staff and Command in Chief of the Fleet) for the use of a hydrographic vessel. In order to deploy the Italian OBSs and to perform high definition bathymetry and magnetic profiles the INGV-Catania leader D. Patané and M. Coltelli and INGV-Roma 2 (Porto Venere) leader C. Carmisciano applied for an agreement between MED-SUV and the Italian Navy. In this agreement allowed us to use, free of charges, the hydrographic vessel "Galatea" for a period of 10 days starting on June 25, 2014.

h. Negotiation with the Italian Navy Command of Sicily in Augusta, for the use of a logistic support ship and the use of a military dock during the experiment. The INGV-Catania leader D. Patané and M. Coltelli, and UGR leader J.M. Ibáñez negotiated with this institution the use of a support ship that would have helped the "Sarmiento de Gamboa" during the Seismic Reflection Experiment with the 3 km long streamer. Additionally, in order to save cost, a negotiation to use the military dock for ship berthing was opened. The working period of this process was October 2013 to June 2014.

i. Bilateral negotiation between Spanish, Greek and Italian Foreign Offices to request authorization of marine scientific work in the economic exclusive zones of Italy. The UGR leader J.M. Ibáñez with the collaboration of D. Patane and M. Coltelli from INGV-Catania prepared an official document and memorandum to obtain this authorization. This negotiation implied the participation of the Spanish embassy in Rome. The working period of this process was March 2014 to October 2014.

j. Negotiation with OGS, Trieste (Italy). M. Coltelli and D. Patané from INGV-Catania established an agreement with the OGS institution in order to have access to multichannel seismic instruments to be deployed from the "Aegaeo" vessel. These instruments were:

two GI guns in linear array and its air compressor arranged in TEU-20 container, and a 96 channels, 300 m long digital streamer. This negotiation started in September 2014, including a further negotiation with Italian Coast Guard of Messina to obtain the local authorization to use air-gun without damage marine mammals.

B. Appendix 2

B.1. List of the TOMO-ETNA working group

Here it is the list of people who currently form the working group with a short description of their contribution to the experiment.

UGR, Spain:
General coordinator of the experiment: Jesús M. Ibáñez.
Spanish marine coordinator: Francisco Carrión.
Onland activities Coordinator: Alejandro Díaz-Moreno; Janire Prudencio.
Onland seismic stations: Rafael Abreu; Gerardo Alguacil; Isaac Alvarez; Carolina Aranda; Carmen Benitez; Luisa Buontempo; Mercedes Feriche; Luz García; Daniel García; Cristina González; José Benito Martín; José Morales; Inmaculada Serrano; Manuel Titos; Lucia Urbano.
Onboard marine activities: Judit González Santana; Nuria Gutiérrez Luna; Ana Isabel Lozano Martínez; Diego Martín Jiménez; José Manuel Muñoz Hermosilla; Mayte Pedrosa; Elsa María Alfonso Sánchez; Teresa Teixidó;

INGV-OE, Catania, Italy:
INGV General Coordinator: Domenico Patané.
Italian marine coordinator: Mauro Coltelli.
MED-SUV coordinator: Giuseppe Puglisi.
Onland activities coordinator: Ornella Cocina; Luciano Zuccarello.
Onland Seismic stations: Giampiero Aiesi; Raffaele Azzaro; Graziella Barberi; Massimo Cantarero; Pasqualino Cappuccio; Danilo Contraffatto; Graziano La Rocca; Sergio Di Prima; Susanna Falsaperla; Elisabetta Giampiccolo; Carla Musumeci; Daniele Pellegrino; Mario Pulvirenti; Salvatore Rapisarda; Marco Sassano; Luciano Scarfì; Luciano Scuderi; Antonino Sicali; Giuseppina Tusa; Tiziana Tuvè.
Onboard marine activities: Eloisa Claude; Marco Firetto Carlino; Salvatore Rapisarda.

INGV-OV, Napoli, Italy:
INGV-OV coordinator: Francesca Bianco;

INGV-OV scientific coordinator: Edoardo Del Pezzo;
Onland seismic stations: Stefano Fiore; Danilo Galluzzo; Mario La Rocca; Mariantonietta Longobardi; Luciano Nocerino; Solange Scognamiglio.

INGV-CNT, Roma, Italy:
Italian OBS coordinator: Giuseppe D'Anna;
Marine and onland activities: Pier Paolo Bruno; Fabio Criscuoli; Antonino D'Alessandro; Roberto D'Anna; Pasquale De Gori; Gioacchino Fertitta; Lucian Giovani; Giuseppe Passafiume; Marcello Silvestri; Stefano Speciale.

INGV-Roma2, Italy:
Project-Italian Navy coordinator: Cosmo Carmisciano;
Marine and onland activities: Carla Bottari; P. Bruno; Luca Cocchi; Filippo Muccini.

INGV-BO, Bologna, Italy:
Onland seismic stations: Simone Salimbeni.

OGS, Trieste, Italy:
Marine activities coordinator: Fabrizio Zgur.
Marine activities: Lorenzo Facchin; Giampaolo Visnovic; Lorenzo Sormani; Diego Cotterle; Rita Blanos; Paolo Mansutti

GFZ, Potsdam, Germany:
Portable seismic stations coordinators: Birger-G. Luehr; Torsten Dahm

Univ. Catania, Italy:
Marine activities: Fabrizio Cultrera; Danilo Cavallaro; Clara Monaco.

Univ. La Coruña, Spain:
Onland seismic stations: Pedro Gea.

Univ. Cádiz, Spain:
Onland seismic stations: Araceli García-Yeguas.

Univ. Jaén, Spain:
Onland seismic stations: Alfonso Ontiveros.

Univ. La Laguna, Spain:
Onland seismic stations: Enrique Coello; María Cordero; Cayetano Guillén; Carmen Romero.

Univ. College of Dublin, Ireland:
Onland seismic stations: Hannah McCann.

Univ. Colima, Mexico:
Onland seismic stations: Mauricio Bretón.

Berckley Seismological Lab., USA:
Scientific coordinator: Margaret Hellweg.
Onland seismic stations: Sierra Boyd.

IPGG SB, Novrosibirsk, Russia:
Software coordinator: Ivan Koulaikov
Onland seismic stations: Sergey Abramenkov.

C. Appendix 3

C.1. International collaborations

The objective of TOMO-ETNA experiment will contribute to part of the EU Project MED-SUV objectives and therefore is integrated by a large set of members associated to this FP7 EU project. Additionally, other institutions that have been collaborated in similar previous experiments have been integrated to the present one.

The MED-SUV consortium that support this project is composed by 21 research institutions from Italy, Germany, UK, France, Spain, Portugal and Malta, and 4 private companies from Italy and UK. As partners of the present experiment we have researcher from the following institutions: INGV Catania, Rome, Rome2, Bologna and Naples (Italy), University of Granada-UGR (Spain), GFZ-Potsdam (Germany), OGS, Trieste (Italy), University of California-Berkeley-BSL (USA), University of College of Dublin-UCD (Ireland), Universidad de Colima (Mexico), Universidad de La Laguna (Spain), Universidad de Jaén (Spain), Universidad de Cádiz (Spain), University of Catania (Italy) CSIC-Spain and Institute of Petroleum, Geology and Geophysics-IPGG (Russia).

The role, in term of responsibilities, of the different partners of the project was:

- UGR was the main coordinator of the experiment, both marine and on-land, and is the scientific coordinator of the future data analysis.
- INGV-Catania was the general coordinator of MED-SUV project and was be the connecting link between this project and the other projects. Additionally, the on-land and part of the offshore operations were coordinated by this partner.
- GFZ was the responsible of the portable seismic network.
- IPGG is the responsible of the elaboration of joint inversion software that integrates passive and active seismic data in both environments to obtain the tomographic images.

In order to recognize the work performed by the several researchers involved in the organization, materialization and future analysis of the data, TOMO-ETNA Working group was created. The list of the names of the persons involved in this working group was enlarged with time according with new contributions and contributors. This list will be used as reference of the authors for the different scientific products that will be produced in the future such as

presentation in international conferences. In Appendix B we present the full list of this working group.

D. Appendix 4

D.1. Data management and control

Such a complex experiment like TOMO-ETNA has generated a big amount of data in both terrestrial and marine environments. The data base can be divided according to the type of instruments and data recording systems but also according to the environment, marine or terrestrial. The division of the data base was done as follow: Short Period Portable Seismic Stations; Portable Broadband Stations; OBSs Stations, Spanish and Italian; INGV Permanent Seismic Network; Seismic Streamer Data; other Marine Data. In total around 6.5 Tb of data in the raw format have been collected divided as follow: 1.5 Tb for portable short-period and Broadband seismic stations; 1 Tb for the permanent seismic network of the INGV; 0.5 Tb for the OBSs; 3 Tb for marine streamer data in both legs ("Sarmiento de Gamboa" and "Aegaeo" vessels); 0.5 Tb for the rest of geophysical and marine data, such as magnetic, bathymetric or robot images, among others. The policy of the data is indicated by following the policy of the MED-SUV Consortium. The use of the data is currently restricted to the MED-SUV consortium, until the end of the project. Data set will be available at the MED-SUV portal. After the end of the project, the data policy has to follow the EUROFLEET rules, which foresee an open access. Access rules should be still defined. In the follow we describe were physically these data are storage and in the future available.

1.1 Short period portable seismic stations

The project has several copies of the short period portable seismic station data and they are stored in Catania, Naples, Potsdam and Granada in the raw data format. There are some teams that have converted data formats to miniseed and SAC format in Granada, Catania and Potsdam.

1.2 Portable broadband stations

Data of these stations have the same processing and storage policy that the short period stations.

1.3 OBS data

1.3.1 Spanish OBS

The original OBS data are in CSIC-UTM, Catania and Granada in the raw format. UGR transformed them into SEGY format. These data are distributed to Catania, Naples, and Potsdam.

1.3.2 Italian OBS

The original OBS data are stored in INGV-CNT in Gibilmana. Later the data will be distributed to Catania, Naples Granada and Potsdam.

1.4 INGV permanent seismic network

A copy of the whole data from the period April-November 2014 is available in Catania and Granada in dmx format. Naples can access to this copy via internal server. Researchers from UGR converted this format to SAC.

1.5 Seismic streamer data

A copy of data associated to the "Sarmiento de Gamboa" vessel is available in Catania and Granada (also in Barcelona as owner of the vessel). Data from "Aegaeo" campaign is available in Catania and Trieste (as owner of the streamer).

1.6 Other marine data

This data base was obtained during the experiment by "Sarmiento de Gamboa", "Galatea" and "Aegaeo" vessels, and it is composed by: bathymetry data, magnetic data and other measurements. This information is stored together with the MCS streamer data and is available in Catania and Granada.

E. Appendix 5

E.1. PARTOS User Guide

Along this section we present a user guide to start using PARTOS code.

The program runs is set to run in windows (not yet available to linux operative systems). It is composed by a series of executable files (.exe), thus no installation procedure is needed. The program main directory ‘./PARTOS/’ must be copied the in the computer. The root directory structure is shown in figure A.1, and comprises a series of folders and files. The mentioned executable files are saved in the ‘./PROG/’ directory.

E.1.1. General Folder Structure in PARTOS:

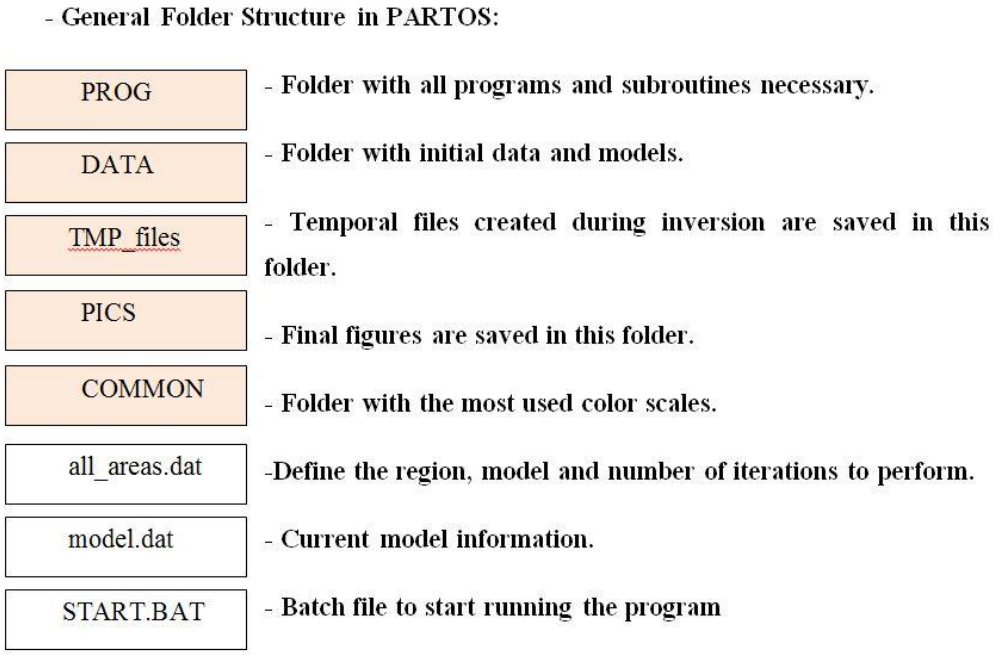

Figure A.1*. Root directory structure of PARTOS software. Orange boxes represent folders and white boxes represent files.*

The data folder saves the input data for the different regions of study. First of all we must create our own AREA directory with an 8-character name (eg. AREA_001). This folder will contain input data from our study region and the different inversion models and synthetic tests (Figures A.2). Additional files (sethor.dat and setver.dat) must be configured and set in this directory. These files contain the information needed to perform horizontal and vertical sections of the results (see 'input file' section for an extended description of these files). Figure A.3 shows the directory scheme for the DATA and MODEL folders. One of the most important folders is 'inidata', which is located within then AREA folder and contains the main input files with our datasets (Figure A.3).These input files include the observed travel times for active and passive data, station coordinates, bathymetry file, etc., and are described along the 'input files' section.

The map directory is optional and it contains coastal lines and political boundaries files used to plot the resulting figures.

The other main directory is MODEL_01 (Figure A.3). In case of a real inversion, this folder must contain 2 essential files for the inversion that are: i) MAJOR_PARAM.dat, which is a file containing all the necessary parameter for the different steps of the tomographic inversion (ray_tracing, grid construction, inversion, etc.); and ii) refmod.dat, which defines the initial 1D velocity model. Additionally, a folder (initially empty) named 'files' must be created. This folder will save all the files calculated during the inversion procedure.

- DATA folder:

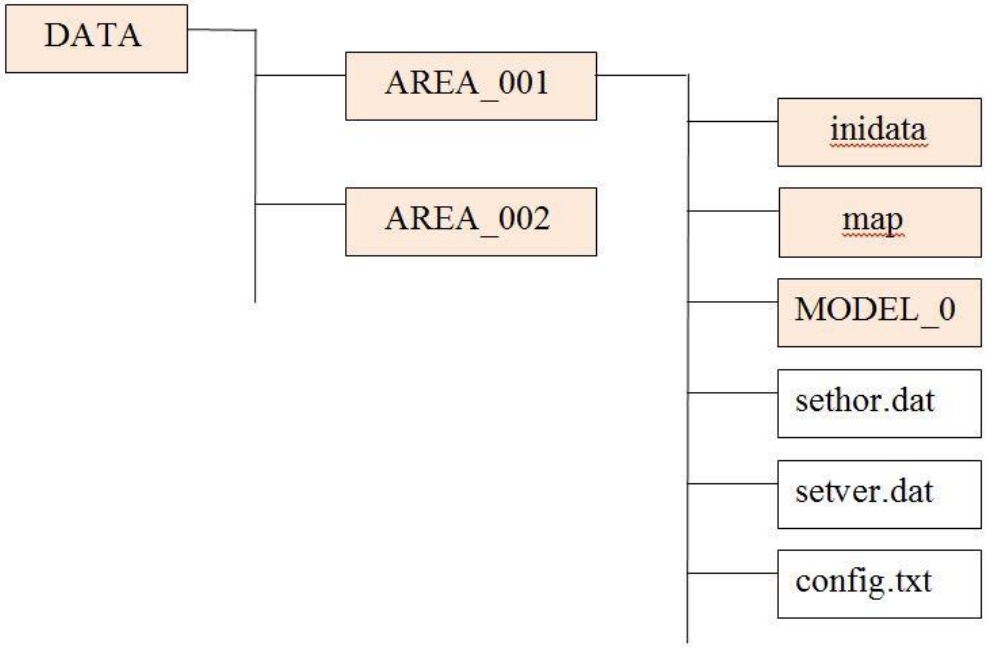

Figure A.2. *Directory scheme of the DATA folder.*

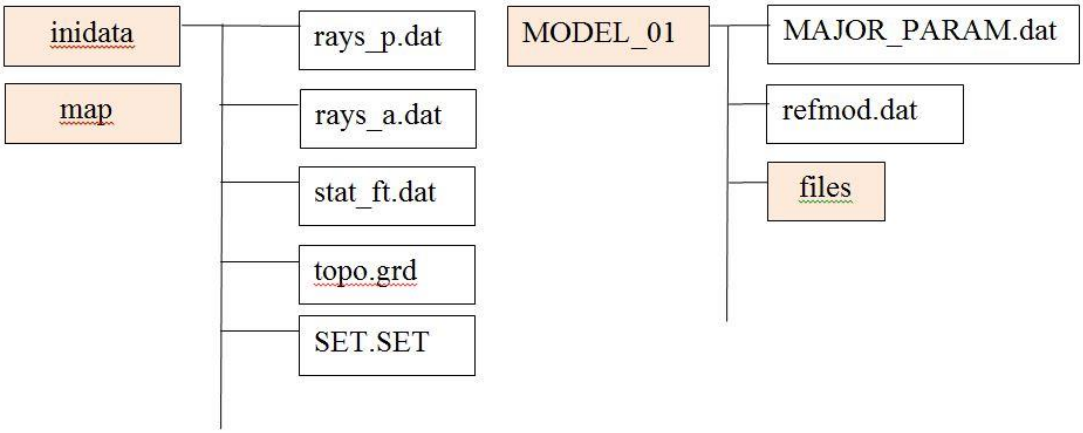

Figure A.3*. Inidata and MODEL_01 directories scheme.*

In case of synthetic modelling, the MODEL folder must contain the same MAJOR_PARAM.dat file and refmod.dat as the real model directory (Figure A.4). Additionally, 2 files must be prepared: i) refysn.dat, which must be the same as refmod.dat; and 'anomaly.dat', which contains information about the type of synthetic calculations to be performed (checkerboard, vertical or horizontal anomaly). An example of these files is described in 'input files section'.

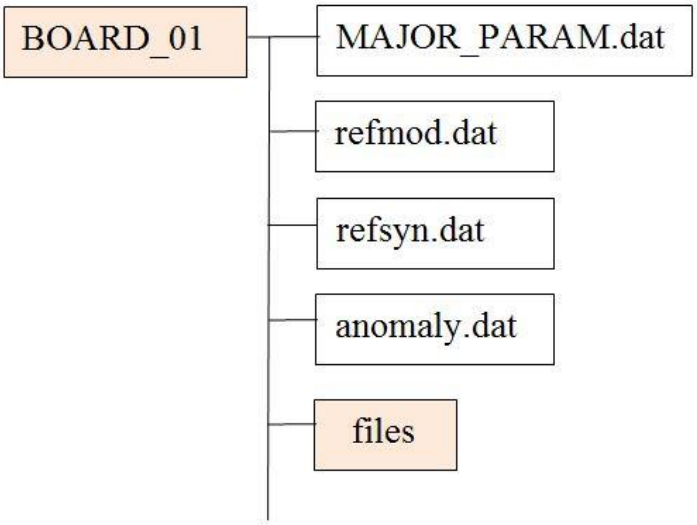

Figure A.4. *Description of the synthetic modelling directory.*

E.1.3. Input files:

The files that should be defined in 'inidata' folder are:

- Topography file: topo.grd
- Stations coordinates: stat_ft.dat
- Rays file for active and passive separately: rays_a.dat (Active); rays_p.dat (Passive).
- Center of Coordinates: set.set

All these files should be prepared in geographical coordinates and are saved in the inidata folder. The format of each of these files is explained in the following paragraphs together with some explanatory figures.

SET.SET: file with the geographical coordinates (Longitude and Latitude) of the center of the studied region:

```
15.00 37.80      Fi0, Tet0, Center of conversion to XY
```

Stat_ft.dat: file with the stations coordinates.

1st column: longitude of the station

2nd column: latitude of the station

3rd column: altitude of the station (altitudes above sea level must be negative)

```
15.05900        37.39500        -0.00500
15.05200        37.42400        -0.00600
14.94300        37.45600        -0.02600
14.80000        37.43100        -0.04400
14.68700        37.39900        -0.31700
```

Rays_a.dat: Rays file with the active data:

1st column: longitude of the station

2nd column: latitude of the station

3rd column: altitude of the station (altitudes above sea level must be negative)

4th column: longitude of the shot

5th column: latitude of the shot

6th column: depth of the shot

7th column: travel time

15.05900	37.39500	-0.00500	15.30630	37.28030	0.01000	5.92000
15.05900	37.39500	-0.00500	15.30990	37.27830	0.01000	5.92000
15.05900	37.39500	-0.00500	15.32050	37.27230	0.01000	6.37000
15.05900	37.39500	-0.00500	15.32230	37.27130	0.01000	5.94000
15.05900	37.39500	-0.00500	15.33990	37.26150	0.01000	6.77000

Rays_p.dat: Rays file with the passive data (same format as for LOTOS code):

1st column: longitude of the earthquake.

2nd column: latitude of the earthquake.

3rd column: depth of the earthquake.

4th column: number of phase readings.

Then one line for each phase readings with the following columns:

1st column: Phase identification (1 for P-phase or 2 for S-phase).

2nd column: number of the station (line of the station coordinates in the stat_ft.dat file).

3rd column: travel time.

```
15.5630   38.4520   131.82     10
       1   213     18.230
       2   213     31.930
       1   211     18.740
       2   211     32.530
       1   198     18.760
       2   198     32.600
       1   202     19.890
       1   216     19.920
       1   207     20.550
       1    91     20.790
 13.6352   37.1840    19.75     31
       1   170      3.890
       2   170      6.880
       1    94      6.610
       1    97      9.730
```

Topo.grd: topography file in geographical coordinates (Surfer format)

```
DSAA
801 1167
   13.29875217616705300     16.49875217616705200
   36.00032324433125600     39.49832324433125300
-3852.78 3265.42
1.70141e38 1.70141e38 1.70141e38 1.70141e38 1.70141e38 1.70141e38 1.70141e38 1.70141e38
1.70141e38 1.70141e38 1.70141e38 1.70141e38 1.70141e38 1.70141e38 1.70141e38 1.70141e38
1.70141e38 1.70141e38 1.70141e38 1.70141e38 1.70141e38 1.70141e38 1.70141e38 1.70141e38
```

Additional files must be set within the AREA folder (figure 2). These files are used to prepare the output figures and their format is explained in the following paragraphs.

Sethor.dat: file to adjust the number and depths of the horizontal sections figures.

```
4     Number of horizontal sections
0 3 6 10   Depths of sections
-0.5 0.5 0.02 -0.5 0.5 0.02 fi1, fi2, dfi, tet1, tet2, dtet
3                    distance from nearest node
0                    Smoothing factor1              Number of summary
5.8                  Velocity to create depth contours
```

Setver.dat: file to adjust the number and coordinates of the vertical sections figures.

```
2                       Number of different sections (use digitize tool from surfer to get the section coordinates)
14.1325548125, 38.3308707537
15.4391780962, 37.4943131635
14.7938336695, 37.2074934183
15.1284567056, 38.3627396143
5  distance from section for visualization of events
0.5                             dx
-5 30 0.5               zmin,zmax,dz
10              Marks for indication of position of section
3                       Distance to the nearest node
0                       Smoothing factor
1                       If 0, no sources are visualized
```

refmod.dat: file to define the initial 1D velocity model. The first line indicates the V_p/V_s ratio. The next part is divided in 3 columns:

1st column: Depth

2nd column Velocity of the P-waves

3rd column (optional): Velocity of S-waves. This column if not defined is automatically calculated using the V_p/V_s ratio.

```
1.75                    Ratio vp/vs
-3.000    4.5       2.57
10.000    5.4       3.09
30.000    7.0       4.00
55.000    8.100     4.63
70.000    8.200     4.538
240.000   8.4       4.793
700.000   10        4.793
```

MAJOR_PARAM.dat: file that contains the necessary parameters for each step of the inversion.

```
**********************************************************
GENERAL INFORMATION :
1          KEY 1: REAL; KEY 2: SYNTHETIC
1          KEY FOR ACTIVE DATA: 0 - no data
1          KEY FOR PASSIVE DATA: 0 - no data
0          KEY 0: all data, KEY 1: odd events, KEY 2: even events
**********************************************************
Parameters for tracing in 3D model using bending tracing
**********************************************************
TRACING_PARAMETERS:
! Parameters for BENDING:
0.5                ds_ini: basic step along the rays
5                  min step for bending
0.03               min value of bending
10                 max value for bending in 1 step
20                 k_reduce: frequency of data to be selected
100                nfreq_print: frequency of printing on console
8. 3 0.7           dtmax_1it, niter_change, dtmax_others
0                  minimal S-R distance, km (optional)
2                  Tolerance for the gather identification (km)

**********************************************************
ORIENTATIONS OF GRIDS:
4                  number of grids
0 22 45 67         orientations
**********************************************************
INVERSION PARAMETERS :
100                LSQR iterations
1 1.               Weights for the P and S models
0.3000 1.000       Weight ACTIVE and PASSIVE
0.5 1.5            HORIZONTAL smoothing (P, S)
0.5 1.0            VERTICAL smoothing (P, S)
1.0 1.0            regularization level (P, S and crust)

0.5                weight of the gather correction (Active)
1.0001   0.0001    weight of the station corrections (P and S) (Passive)
5.0                wzt_hor (Passive source, horizontal shift)
5.0                wzt_ver (Passive source, vertical shift)
2.0                wzt_time (Passive source, origin time)
```

```
************************************************************
Parameters for location in 3D model using bending tracing
************************************************************
LOC_PARAMETERS:
! Parameters for BENDING:
1                   ds_ini: basic step along the rays
10                  min step for bending
0.05                min value of bending
10                  max value for bending in 1 step

! Parameters for location
30                  dist_limit=100      : within this distance the weight is equal
1                   n_pwr_dist=1        : power for decreasing of W with distance
30                  ncyc_av=10

0.                  res_loc1=0.2        : lower limit for location (for LT residuals, W=1)
1.5                 res_loc2=1.5        : upper limit for location (for GT residuals, W=0)
2.                  w_P_S_diff=2 (+ causes better coherency of P and S)
10.                 stepmax
0.3                 stepmin

10                  Frequency for output printing

************************************************************
Parameters for 3D model with regular grid
************************************************************
3D_MODEL PARAMETERS:
-150. 150. 6  xx1, xx2, dxx,
-150. 150. 6  yy1, yy2, dyy,
-5. 30. 2     zz1, zz2, dzz
12                  distance from nearest node
0                   Smoothing factor1
************************************************************
Parameters for grid construction
************************************************************
GRID_PARAMETERS:
-150. 150. 6        grid for ray density calculation (X)
-150. 150. 6        grid for ray density calculation (Y)
-5. 30. 2.          min and max levels for grid
0.05 100.0          !plotmin, plotmax= maximal ray density, relative to average
```

```
DATA FOR PASSIVE TOMOGRAPHY:
************************************************************
1D LOCATION KEY :
1    1: using reference table (large areas);
     2: using straight lines (small areas with high relief)
************************************************************
Parameters for calculation of the reference table:
************************************************************
REF_PARAM:
1                    min step
700.                 max depth
500.                 max distance
4                    number of depth steps
-5 0.5               depth, s   tep
20 1                 depth, step
50 3                 depth, step
200 10               depth, step
700                  maximal depth
************************************************************
Parameters for location in 1D model using reference table
and data selection:
************************************************************
LIN_LOC_PARAM :
7                    Minimal number of records
100                  km, maximum distance to nearest station
1.5                  S max resid with respect to P max resid
100                  dist_limit=100       : within this distance the weight is equal
1                    n_pwr_dist=1         : power for decreasing of W with distance
30                   ncyc_av=10

! For output:
30                   bad_max=30                  : maximal number of outliers
1          maximal dt/distance
2                    distance limit

10                   Frequency for output printing
```

```
3                   Number of different grids
_____________________________________________________
10 10 10            dx,dy,dz
0.                  res_loc1=0.2        : lower limit for location (for LT residuals, W=1)
6.                  res_loc2=1.5        : upper limit for location (for GT residuals, W=0)
2.                  w_P_S_diff=2 (+ causes better coherency of P and S)
_____________________________________________________
2 2 2               dx,dy,dz
0.                  res_loc1=0.2        : lower limit for location (for LT residuals, W=1)
3.                  res_loc2=1.5        : upper limit for location (for GT residuals, W=0)
2.                  w_P_S_diff=2 (+ causes better coherency of P and S)
_____________________________________________________
0.5 0.5 0.5                 dx,dy,dz
0.                  res_loc1=0.2        : lower limit for location (for LT residuals, W=1)
1.5                 res_loc2=1.5        : upper limit for location (for GT residuals, W=0)
2.                  w_P_S_diff=2 (+ causes better coherency of P and S)
```

Refysn.dat: file with the 1D velocity model used during the synthetic modelling. The format is exactly the same as file 'refmod.dat'.

Anomaly.dat: file with the description of the synthetic anomalies to be performed during the synthetic tests.

```
1           1 - board, 2 - horiz. anom, 3 - vert. anom
_____________________________________________________
15.00       P-anomalies
-800. 800. 15. 0.0
-800. 800. 15. 0.0
-10. 100. 90. 0.5
-15.00      S-anomalies
-800. 800. 15. 0.0
-800. 800. 15. 0.0
-10. 100. 90. 0.5
```

Once all the input files are properly set in their folders, the next step is to prepare the 'all_areas.dat' and 'model' file which are used to start the inversion procedure. These files are saved in the main directory (figure 1).

all_areas.dat: file specifying the name of the area, model and number of iterations to invert.

```
1: name of the area
2: name of the model
3: number of iterations
*****************************************
ETNA_inv    PASSIVE5     6
```

Model.dat: file with the current name of area, model, iteration and grid number.

```
ETNA_inv
PASSIVE5
1
1
```

Finally, starting the inversion procedure needs only to launch the batch file 'START.BAT' located in the main directory (figure A.1).

F. Appendix 6

In this appendix we show some of the tomographic images regarding the different tests, varying the parameters of smoothing to illustrate how this parameter affects the results.

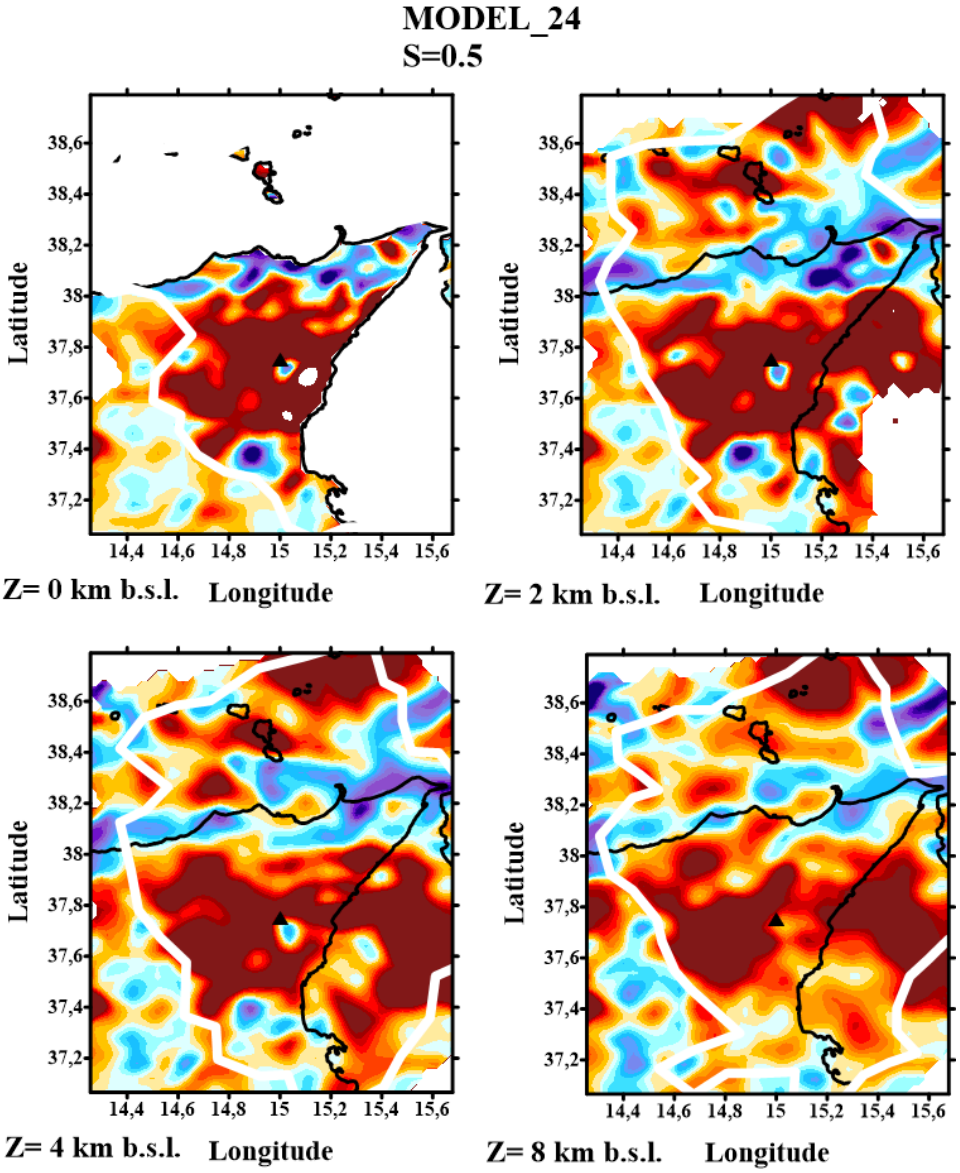

Figure F.1: *Tomographic Images of Region 1 using smoothing value of 0.5. From 0 to 8 km b.s.l..*

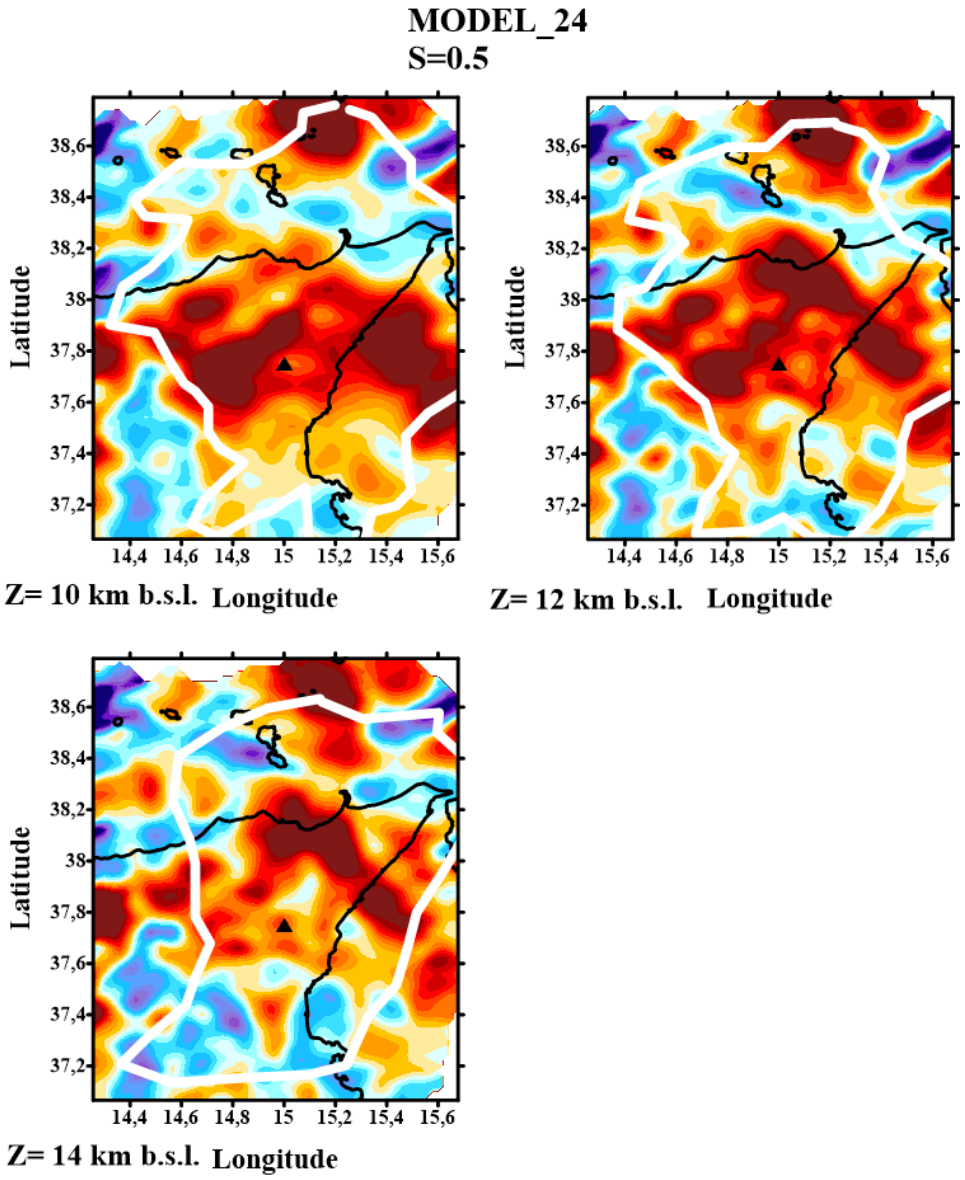

Figure F.2: *Tomographic Images of Region 1 using smoothing value of 0.5. From 10 to 14 km b.s.l..*

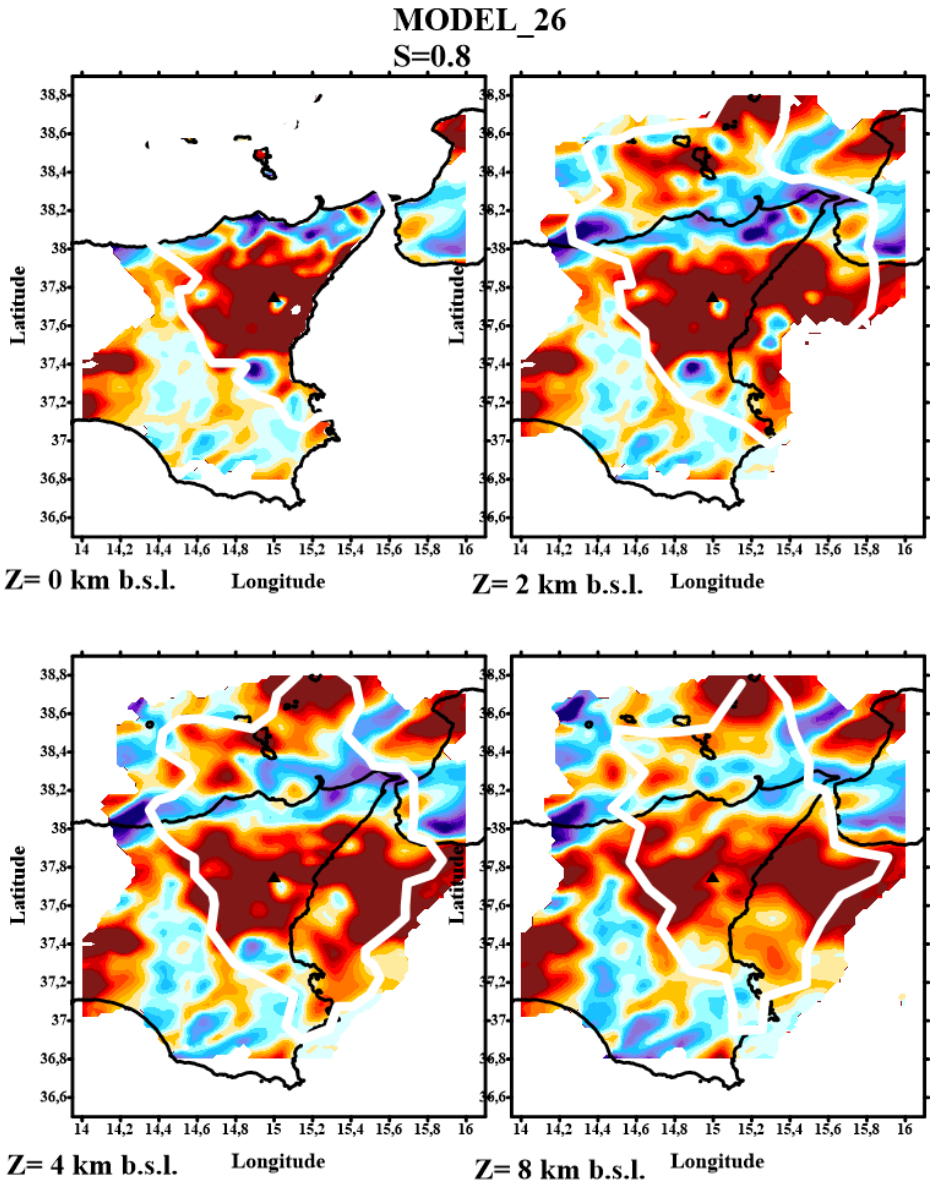

Figure F.3: *Tomographic Images of Region 1 using smoothing value of 0.8. From 0 to 8 km b.s.l..*

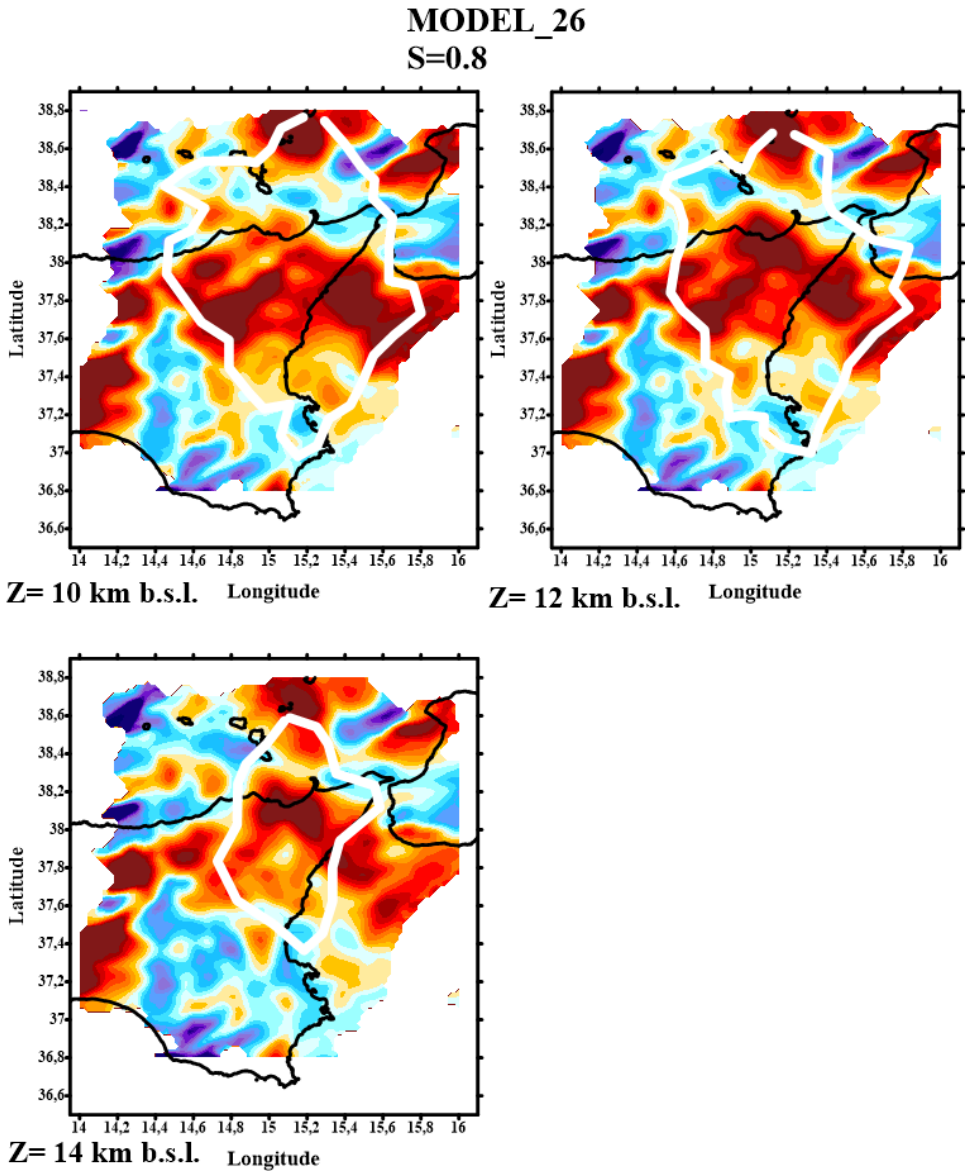

Figure F.4: *Tomographic Images of Region 1 using smoothing value of 0.8. From 0 to 8 km b.s.l..*

The following images presented are a set of tests regarding the grid spacing and dimensions varying also the smoothing parameter. In this case, the images shown are from Region 3 and plotting the absolute velocities

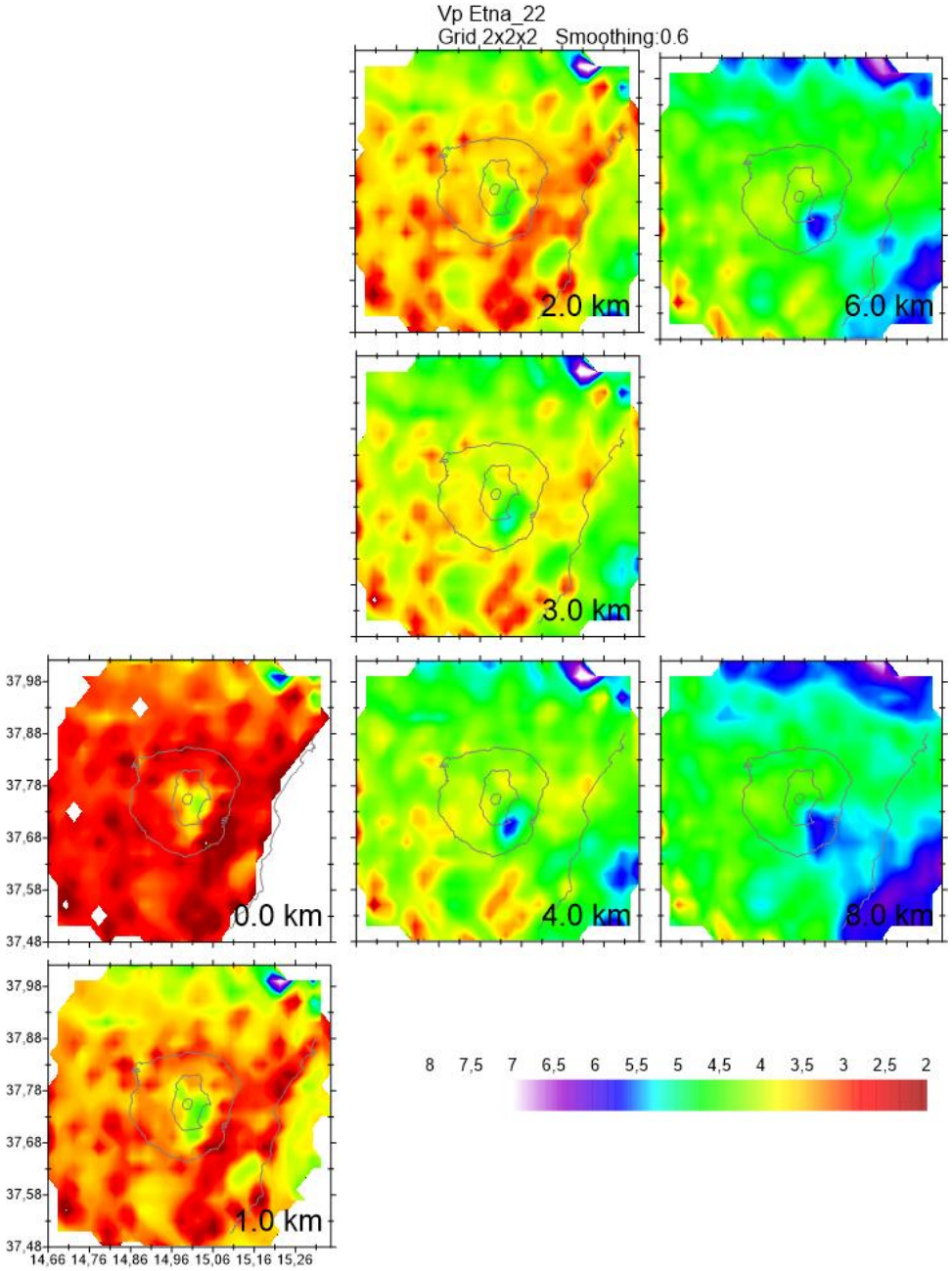

Figure F.5: *Absolute velocity maps of Region 3 using smoothing value of 0.6, and grid spacing ok 2 km in horizontal and 2 km in vertical.*

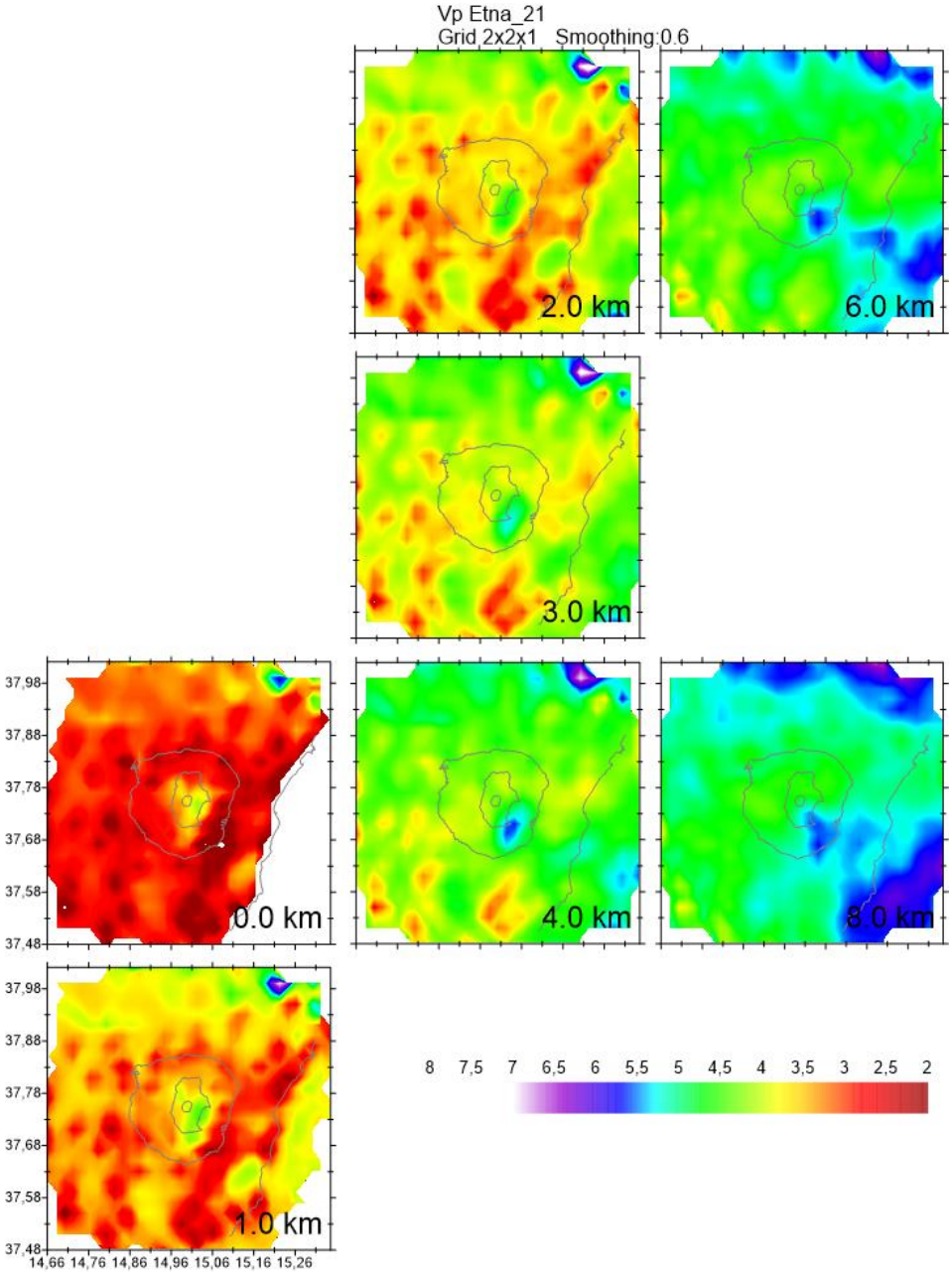

Figure F.6: *Absolute velocity maps of Region 3 using smoothing value of 0.6, and grid spacing ok 2 km in horizontal and 1 km in vertical.*

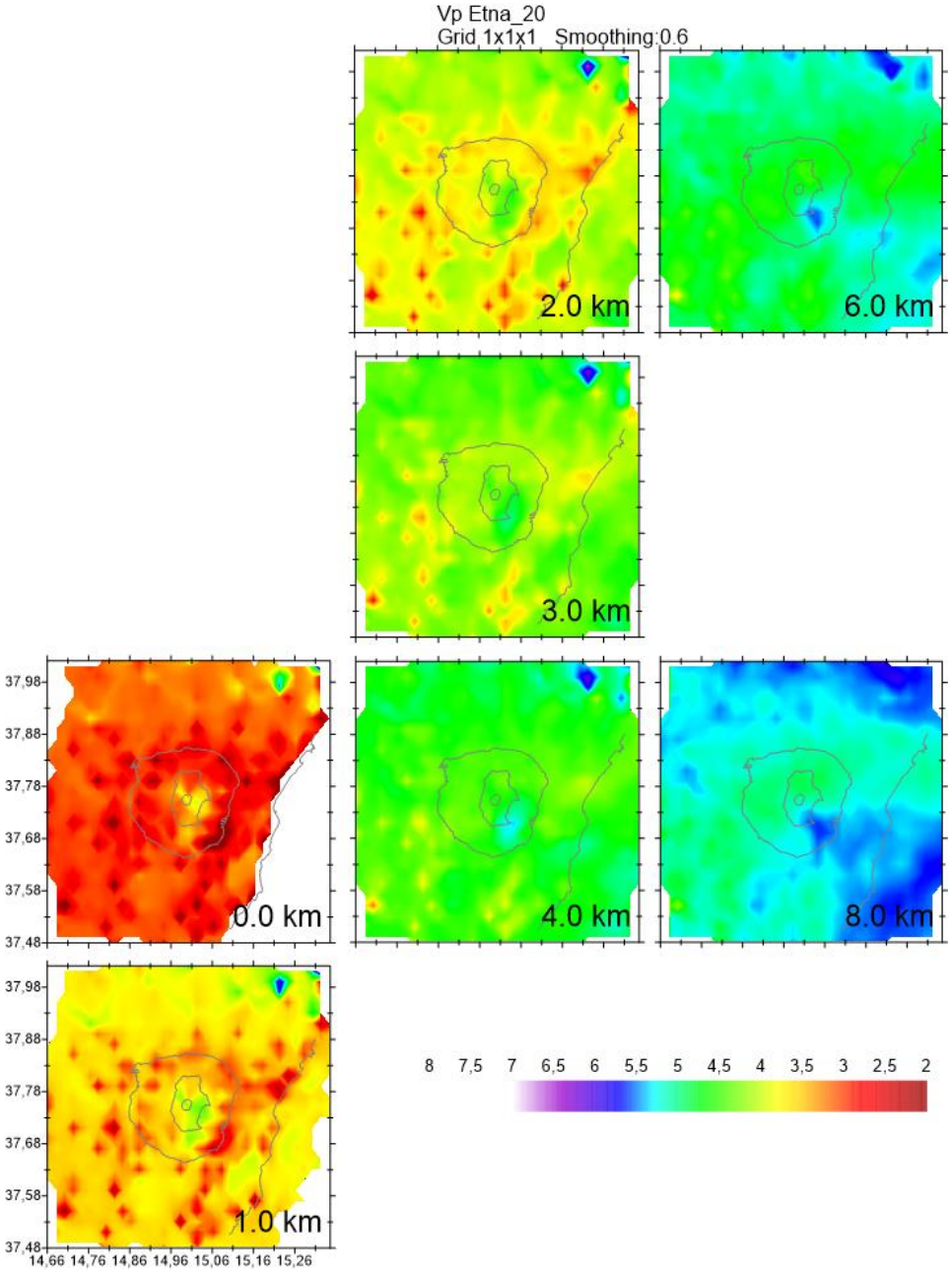

Figure F.7: *Absolute velocity maps of Region 3 using smoothing value of 0.6, and grid spacing ok 1 km in horizontal and 1 km in vertical.*

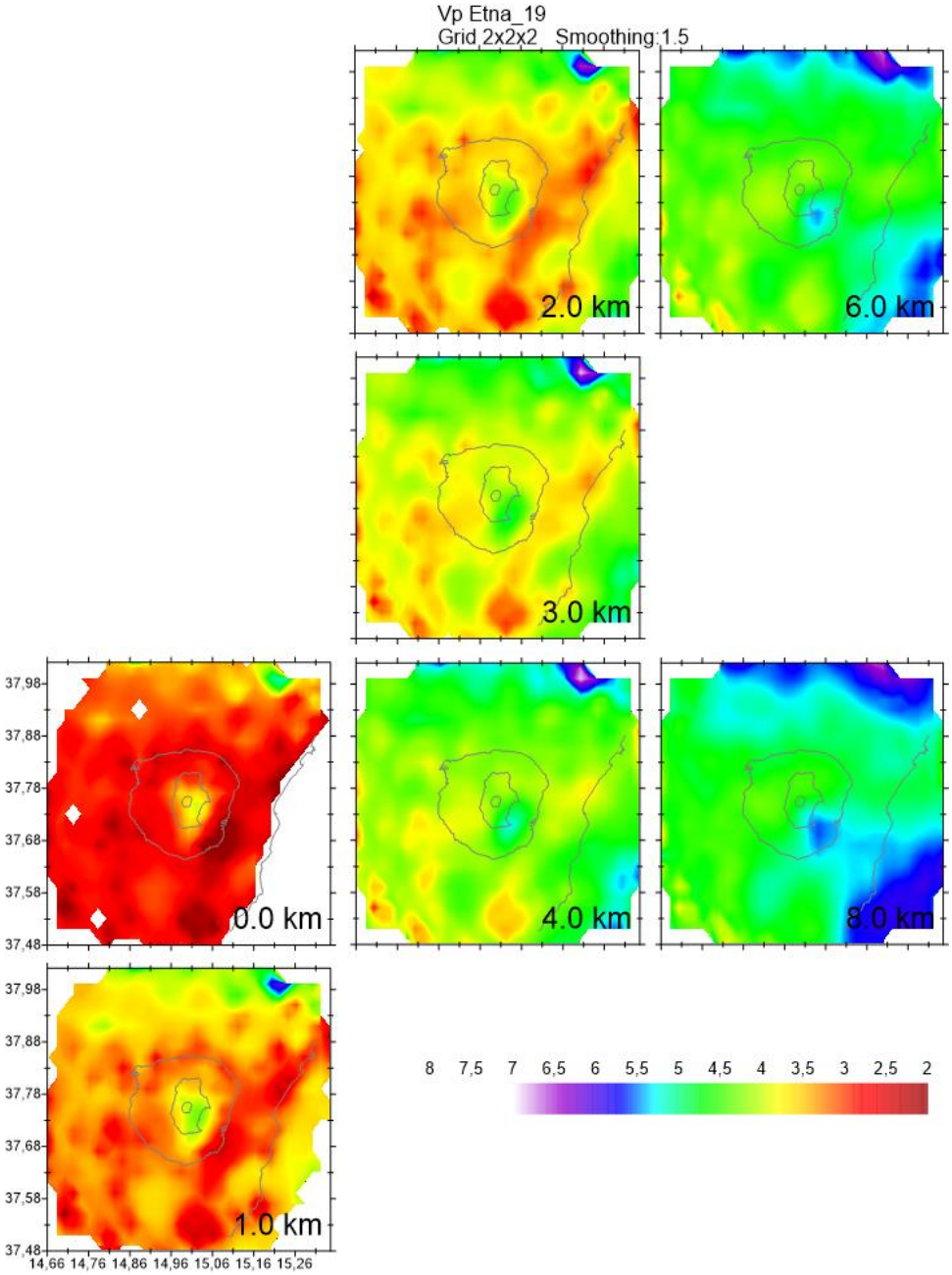

Figure F.8: *Absolute velocity maps of Region 3 using smoothing value of 1.5, and grid spacing ok 2 km in horizontal and 2 km in vertical.*

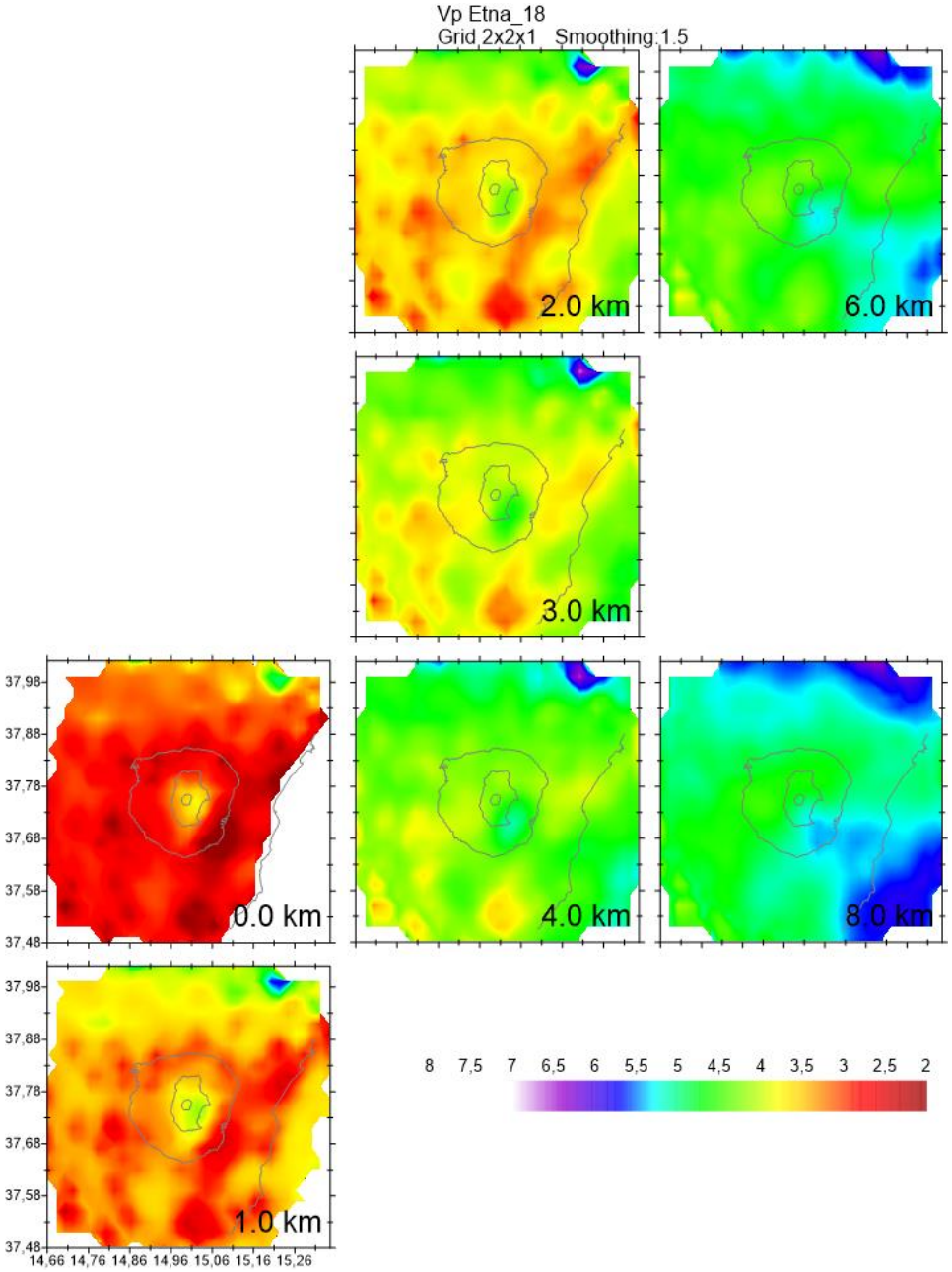

Figure F.9: *Absolute velocity maps of Region 3 using smoothing value of 1.5, and grid spacing ok 2 km in horizontal and 1 km in vertical.*

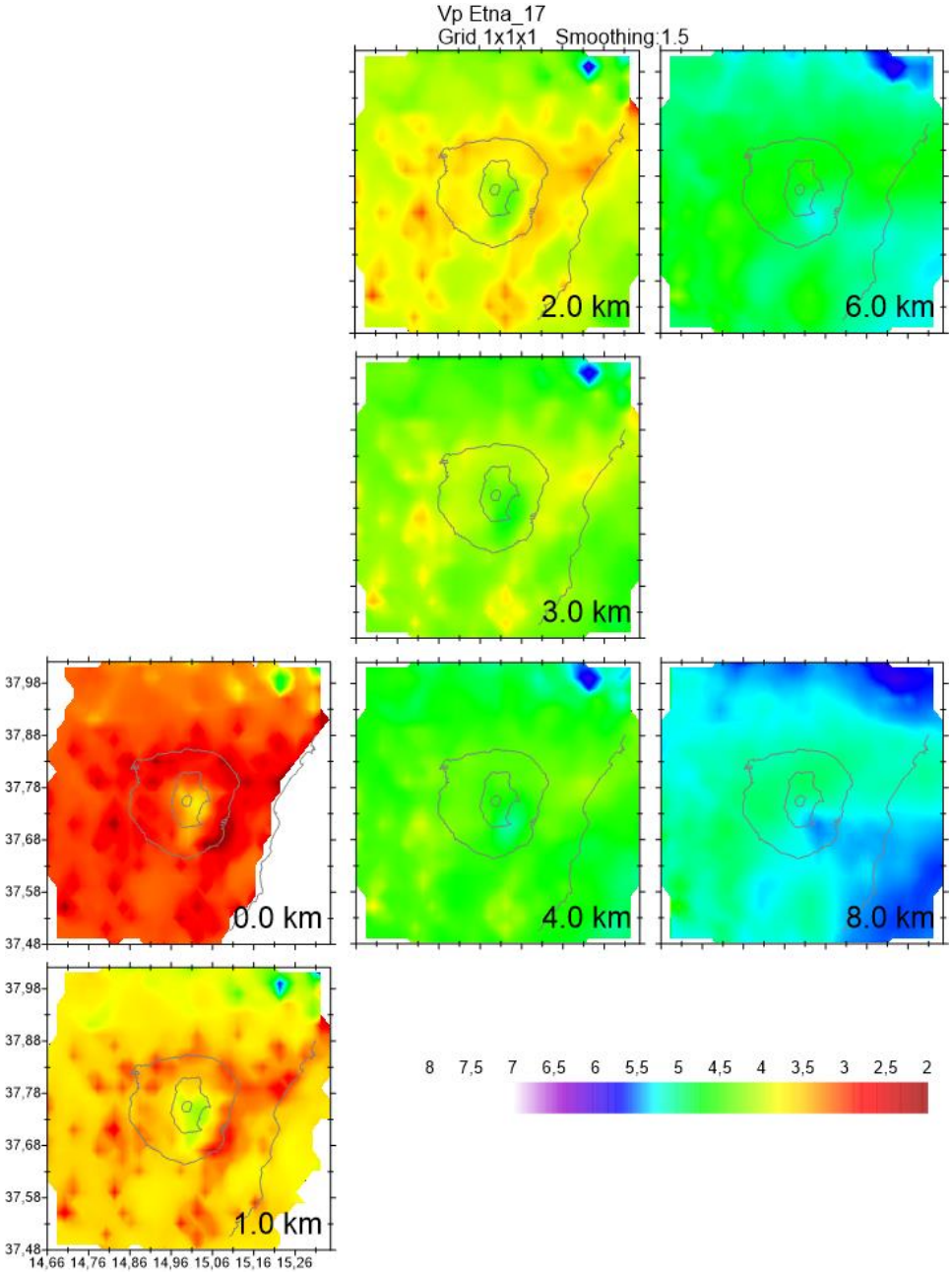

Figure F.10: *Absolute velocity maps of Region 3 using smoothing value of 1.5, and grid spacing ok 1 km in horizontal and 1 km in vertical.*

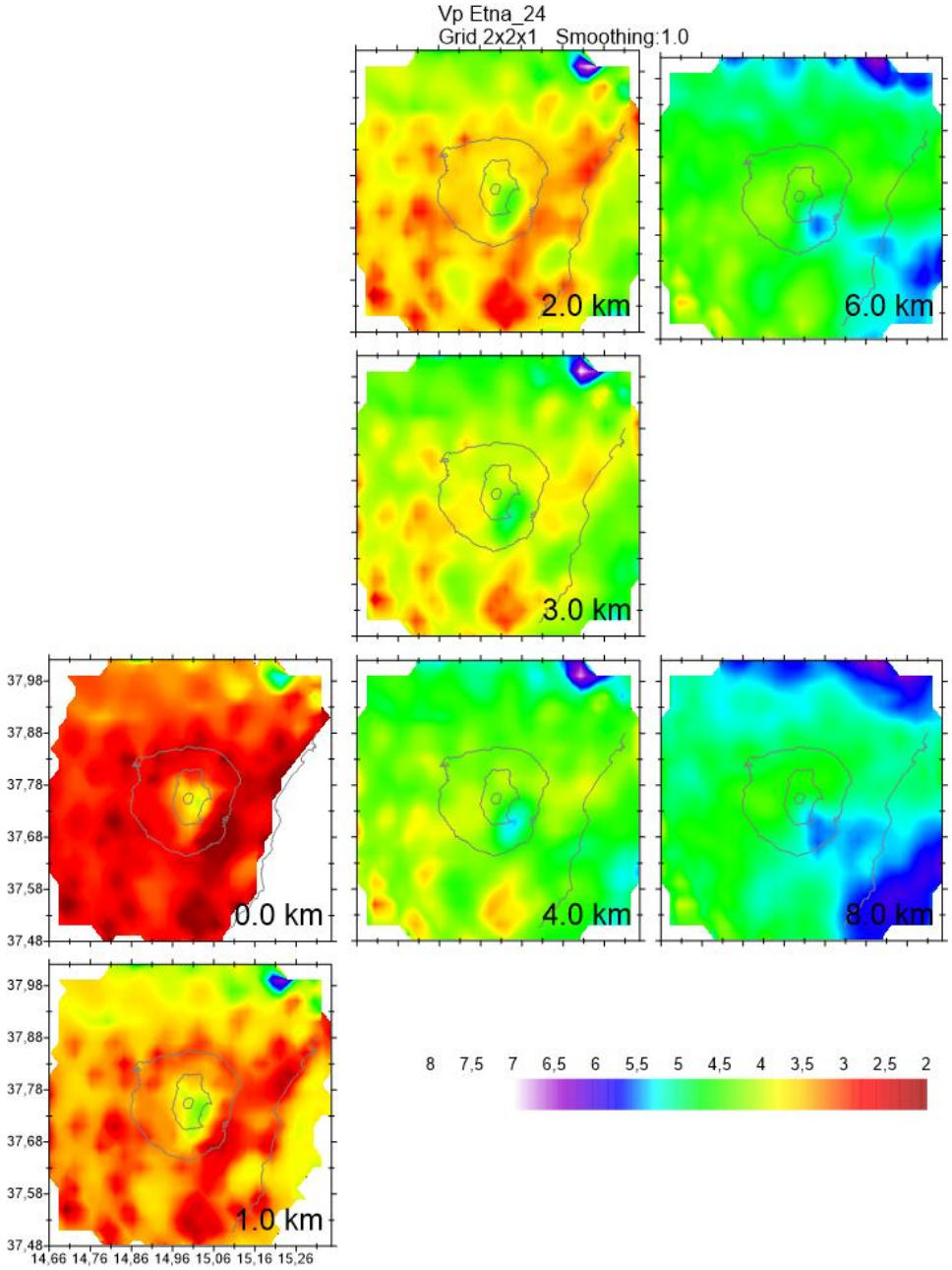

Figure F.11: *Absolute velocity maps of Region 3 using smoothing value of 1.0, and grid spacing ok 2 km in horizontal and 1 km in vertical.*

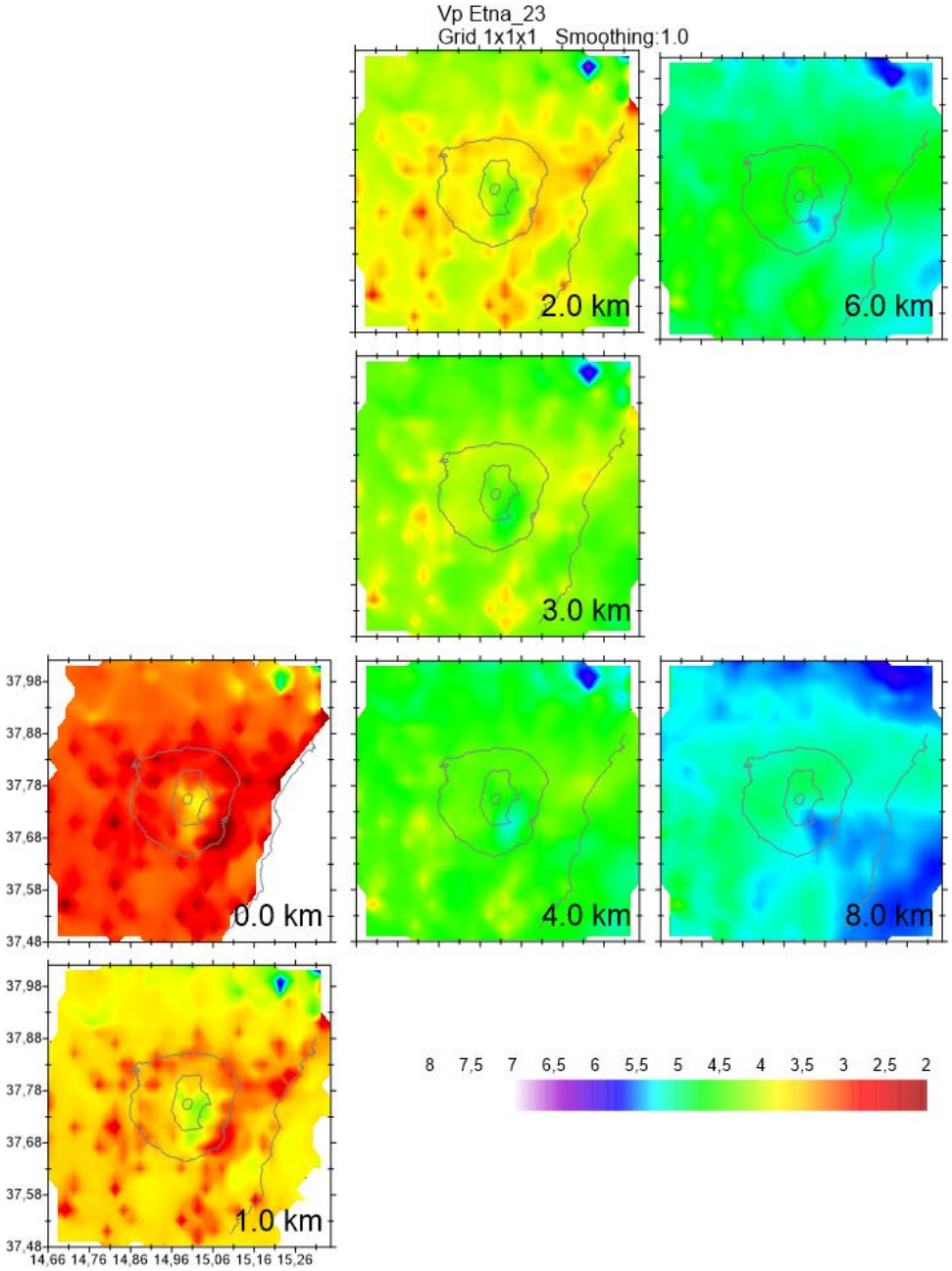

Figure F.12: *Absolute velocity maps of Region 3 using smoothing value of 1.0, and grid spacing ok 1 km in horizontal and 1 km in vertical.*

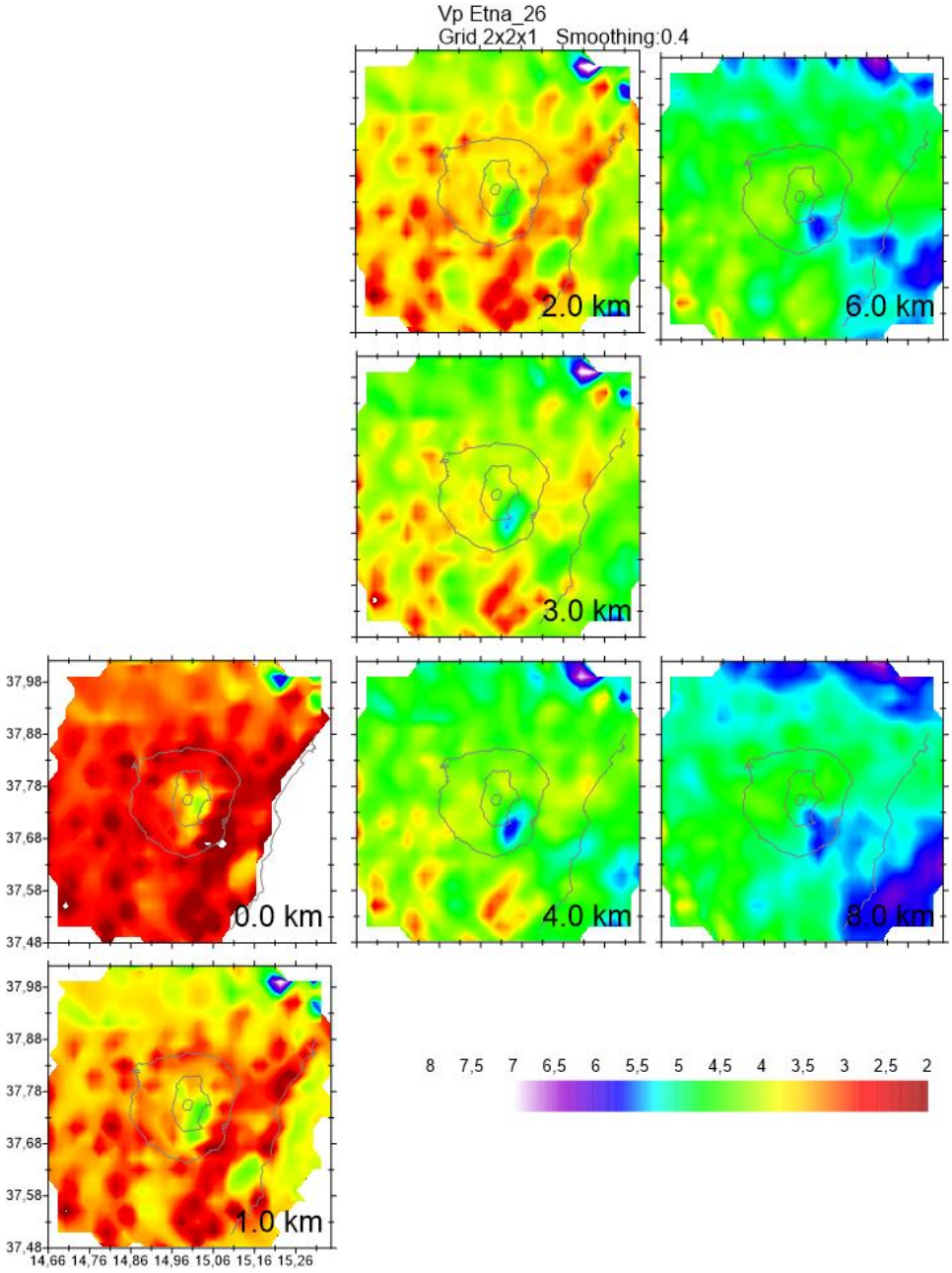

Figure F.13: *Absolute velocity maps of Region 3 using smoothing value of 0.4, and grid spacing ok 2 km in horizontal and 1 km in vertical.*

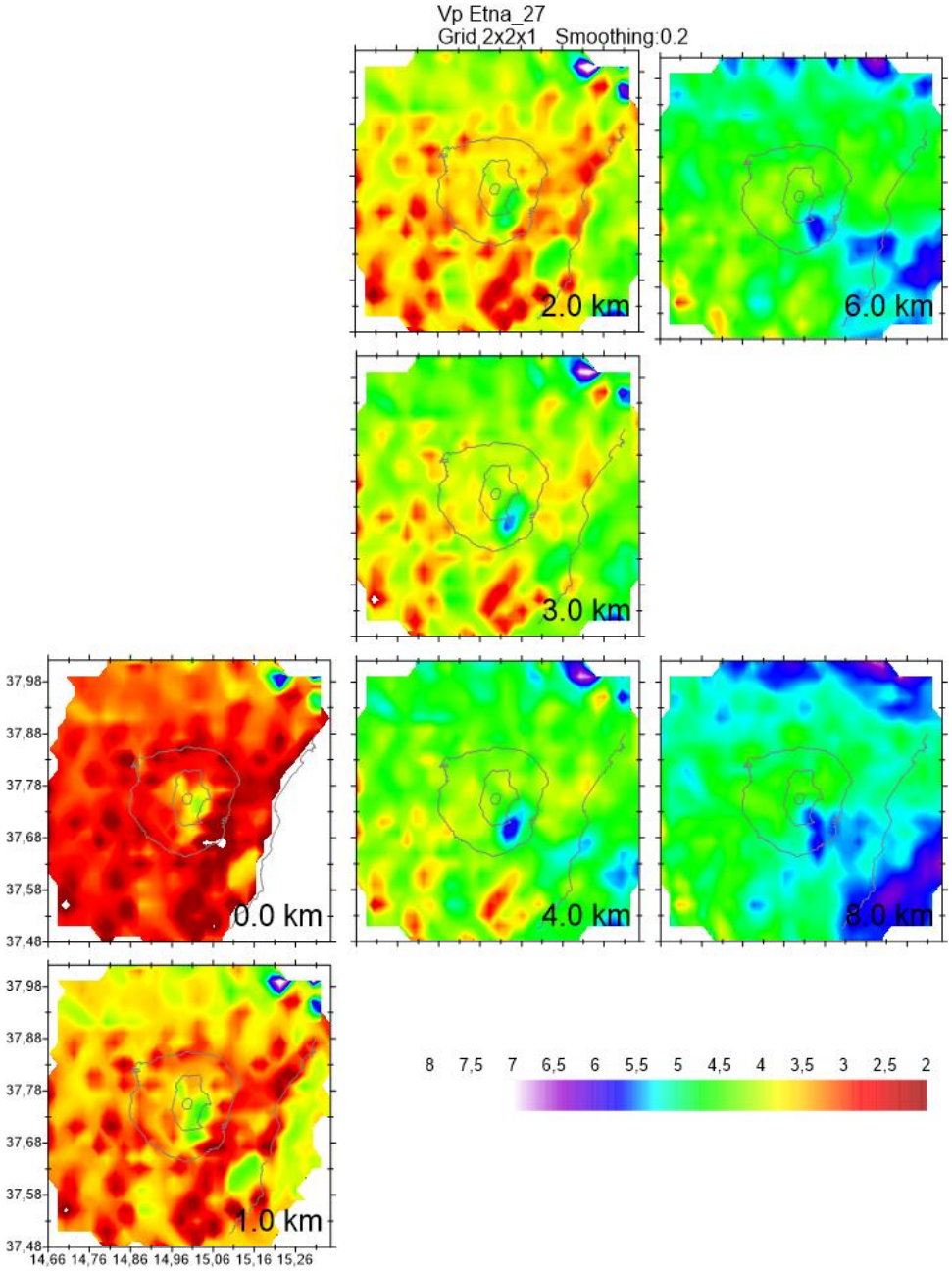

Figure F.14: *Absolute velocity maps of Region 3 using smoothing value of 0.2, and grid spacing ok 2 km in horizontal and 1 km in vertical.*